Continental-scale Landscape Evolution: A Multi-Proxy Approach

Victoria Milanez Fernandes

Imperial College London

Department of Earth Science and Engineering

Supervisors: Dr. Gareth Roberts & Dr. Alex Whittaker

This dissertation is submitted for the degree of
Doctor of Philosophy
in Earth Science and Engineering Research
.

January 20, 2021

Abstract

Earth's topography results from complex interactions between deep and surface processes operating on a range of spatio-temporal scales. To quantify the evolution of long-wavelength (>100 km) vertical motions caused by sub-plate support, for which generating sufficient geological observations is challenging, I combine novel approaches across global, continental and regional scales.

In Chapter 2, I exploit a paleobiological database to generate a new compilation of $> 24,000$ spot measurements of uplift across all continents. Records from western North America and eastern South America are combined with geophysical observations and isostatic calculations to explore how lithospheric thinning and mantle thermal anomalies may generate uplift of the observed wavelengths and amplitudes.

In Chapter 3, the uplift inventory developed in Chapter 2 is augmented by additional stratigraphic markers and is subsequently used to estimate post-depositional uplift of the North American Continent. To bridge the gaps between these measurements, an inverse modelling scheme is used to calculate the smoothest spatio-temporal pattern of rock uplift rate that yields the smallest misfit between 4161 observed and calculated longitudinal river profiles. A landscape evolution model driven by this calculated rock uplift history is used to determine drainage patterns, denudation and sedimentary flux from Late Cretaceous times until present. These patterns are consistent with stratigraphic and thermochronologic observations.

In Chapter 4, I combine geophysical observations and isostatic calculations with 27 backstripped wells in the Baltimore Canyon Trough to propose upper mantle drawdown produced ∼600 m excess water-loaded subsidence between ∼20–0 Ma. Using the landscape evolution model from Chapter 3, well data and published isopachs, I explore the contribution of source region uplift to increased Neogene basin-wide sediment accumulation. Results suggest the Middle Miocene sediments might not be sourced from the Appalachians, or models are too simplistic to predict the increased sedimentary flux.

Declaration

Declaration of Originality

I hereby declare that this dissertation, submitted for the degree of Doctor of Philosophy at Imperial College London and Associateship of the Royal School of Mines, is original research undertaken by me. Unless explicitly stated in the text, this thesis is the result of my own work.

Copyright Declaration

The copyright of this thesis rests with the author and is made available under a Creative Commons Attribution Non-Commercial No Derivatives licence. Researchers are free to copy, distribute or transmit the thesis on the condition that they attribute it, that they do not use it for commercial purposes and that they do not alter, transform or build upon it. When reusing or sharing this work, ensure you make the licence terms clear to others by naming the licence and linking to the licence text.

Acknowledgements

First, I would like to express my sincere gratitude for my supervisors Gareth Roberts and Alex Whittaker. I don't think I would have finished this degree without their support, guidance and reassuring confidence in my work and my abilities. Their patience and efforts have helped me produce research that I am truly proud of. I cannot thank them enough for this opportunity. Their encouragement and inspiration goes far beyond the work contained in this thesis, and my esteem for them goes far beyond the academic realm. I also wish to thank Becky Bell for her critical feedback on my work as my assessor throughout the years.

A special thank you goes to Gaia Stucky de Quay, Carla Pont and Alex Lipp for taking me on such incredible fieldwork experiences, engaging in long academic discussions about how everyone else is wrong, and making day-to-day life at Imperial so great. It has been true privilege to be able to work with such talented and driven peers. I wish to thank Sinéad Lyster, Andy Procter and Hamish Mitchell providing a friendly ear to my work stresses, great chat at the end of a long field day, letting me crash on their sofas, and much needed reminders to relax every once in a while. I would not have made it through without the motivation and encouragement from Kenny Wong, Newnham girls and friends from Rio. To Alistair Boyce, my deepest appreciation for the unwavering care and support throughout my degree, especially during the writing of this thesis.

Finally, I would like to deeply thank my parents, Gustavo Fernandes and Adriana Milanez, who have wholeheartedly encouraged and supported me in my academic pursuits from the other side of the Atlantic. I could not have done it without them. Obrigada.

Contents

Abstract **3**

1 Introduction **17**

1.1 Overview . . . 17

1.2 Motivation . . . 19

1.3 Expected topographic signals of geological processes . . . 20

1.3.1 Sub-plate support . . . 21

1.4 Measuring vertical motions of continents . . . 23

1.5 Aims & Objectives . . . 25

1.6 Thesis outline . . . 27

2 Uplift Patterns from a Global Paleobiology Inventory **30**

2.1 Chapter overview . . . 30

2.2 Introduction . . . 31

2.2.1 Previous work . . . 31

2.3 Calculation of Vertical Motions . . . 34

2.3.1 Paleobiology Database (PBDB) . . . 35

2.3.2 Bathymetric model . . . 36

2.3.3 Sea-level . . . 49

2.3.4 Compaction correction . . . 50

2.3.5 Elevation . . . 54

2.4 Global Patterns of Uplift . . . 55

2.4.1 Western North America . . . 57

2.4.2 Borborema Province, northeast Brazil . . . 60

2.4.3 Summary . . . 64

2.5 Discussion . . . 64
2.5.1 Isostatic considerations . . . 66
2.5.2 Western North America . . . 72
2.5.3 Borborema . . . 75
2.5.4 Summary . . . 77
2.5.5 Remarks on limitations and further work . . . 78

3 The Ups and Downs of a Continent - Evolution of the North American Landscape 80
3.1 Chapter Overview . . . 80
3.2 Introduction . . . 81
3.2.1 A Role for Large-Scale Crustal and Lithospheric Thickening? . . . 83
3.2.2 Epeirogeny and the Role of Dynamic Support . . . 85
3.3 North American Landscape Evolution: Existing Constraints . . . 87
3.3.1 Birth of the Western Interior Seaway . . . 87
3.3.2 Regression of Western Interior Seaway . . . 89
3.3.3 Post-Cretaceous Events . . . 90
3.3.4 Neogene Uplift and Denudation . . . 94
3.4 Stratigraphic Constraints on Uplift . . . 95
3.4.1 Regressive stratigraphic sequences . . . 96
3.4.2 Net Uplift of North America . . . 104
3.5 River Profile Inversion . . . 108
3.5.1 Drainage Inventory . . . 108
3.5.2 Erosional Parameterisation . . . 110
3.5.3 Inverse Modelling . . . 112
3.5.4 Calculated Rock Uplift History . . . 115
3.5.5 Independent Tests . . . 117
3.6 Landscape Evolution Modelling . . . 125
3.6.1 Badlands Algorithm . . . 125
3.6.2 Calculated Landscape . . . 127
3.6.3 Denudational History . . . 133
3.7 Discussion . . . 137
3.7.1 Continental Epeirogeny . . . 137

3.7.2 Consequences for Landscape Evolution . . . 139
3.7.3 Geodynamic Implications . . . 142

4 Uplift, Subsidence and Evolution of the U.S. Mid-Atlantic Region 144

4.1 Chapter overview . . . 144
4.2 Introduction . . . 145
4.3 Passive Margin Subsidence and Sub-Plate Support . . . 146
4.3.1 Geophysical observations . . . 147
4.3.2 Data . . . 151
4.3.3 Stratigraphic framework . . . 152
4.3.4 Backstripping methodology . . . 154
4.3.5 Theoretical thermal subsidence . . . 161
4.3.6 Subsidence history . . . 164
4.3.7 Seismic reflection data . . . 167
4.3.8 Causes of subsidence in the Baltimore Canyon Trough . . . 172
4.4 Appalachian Uplift and Sedimentary Flux . . . 178
4.4.1 Measuring sediment accumulation rate . . . 180
4.4.2 Assessment of sediment volumes . . . 184
4.4.3 Sediment Flux Prediction from Landscape Evolution Modelling . . . 190
4.4.4 Causes for data-model mismatch . . . 196
4.4.5 Implications for Neogene topographic growth of the Appalachian Mountains . . . 198

5 Discussion 199

5.1 General Conclusions . . . 199
5.2 Cross-cutting Themes . . . 201
5.2.1 Different methods for measuring vertical motions of the Earth's surface . . . 202
5.2.2 What about tectonics? . . . 207
5.3 Future Work . . . 208

Bibliography 211

List of Tables

2.1 Bathymetric model, descriptions of environments as given in the PBDB documentation, and attributed paleo-bathymetric ranges 37
2.2 Comparison of paleobathymetric models. 40
2.3 Benchmarking PBDB and independently reference paleoenvironmental interpretations. 45
2.4 Parameters used in isostatic calculations 69

3.1 References for generalised stratigraphic columns 103
3.2 References for state-wide geological maps 104

4.1 List of wells 151

List of Figures

1.1 Global map of topography 18
1.2 Diagram illustrating the contributions of isostatic and dynamic topography 20
1.3 Global map of crustal thickness from CRUST1.0. 21
1.4 Global shear wavespeed anomalies 22

2.1 Paleobiology inventory 33
2.2 Schematic illustrating methodology to calculate uplift 35
2.3 Bathymetric model 37
2.4 Paleobathymetries for best-constrained samples 49
2.5 Simplified global sea-level compilation 50
2.6 Compaction correction parameter space 52
2.7 Example compaction correction 53
2.8 Comparison between different resolution DEMs 54
2.9 Elevation consistency test 55
2.10 Global measurements of uplift 56
2.11 Calculated uplift of Western Interior of North America 59
2.12 Uplift of the Borborema Plateau, NE Brazil 62
2.13 Cross sections through uplift and geophysical measurements 65
2.14 Schematic illustrating isostatic calculations. 66
2.15 Parameterisation of isostatic calculations 70
2.16 Comparison of a steady-state (equilibrated) and a disequilibrated geotherm on the generation of uplift by lithospheric thinning 71
2.17 Geophysical observations from the Western Interior of North America 74
2.18 Geophysical observations from the Borborema Province, northeast Brazil 76
2.19 Schematic paleogeographies and uplift patterns from PBDB measurements 78

3.1 Topography and physiographic provinces of North America 83
3.2 Geological map of North America 84
3.3 Shear wavespeed anomalies beneath North America 85
3.4 Distribution of Cretaceous to Recent magmatism 86
3.5 Western Interior Seaway and Cretaceous outcrop 88
3.6 Constraints on Landscape Evolution 89
3.7 North American solid sedimentary flux 91
3.8 Sediment provenance for Gulf of Mexico drainage 91
3.9 Chronostratigraphic framework of Western Interior of the United States 96
3.10 Location of reference stratigraphic columns 99
3.11 Stratigraphic columns showing marine to terrestrial transitions 99
3.12 Paleobathymetry and net uplift 105
3.13 Stratigraphic and biostratigraphic constraints 105
3.14 Topography and drainage of North America. 109
3.15 Inverted longitudinal river profiles 110
3.16 Inverse model parameterisation 113
3.17 Residual misfit 114
3.18 Calculated uplift history for North America 116
3.19 Data coverage as a function of model time 117
3.20 Calculated uplift history at grid nodes 118
3.21 Calculated uplift history with spatial smoothing $\lambda_s = 0.05$ 119
3.22 Calculated uplift history with spatial smoothing $\lambda_s = 5$ 120
3.23 Comparison uplift history with stratigraphic data. 120
3.24 Comparison uplift history with PBDB data. 121
3.25 Testing results of inverse modelling, v 122
3.26 Testing effect of reducing erosional parameter 123
3.27 Testing effect of increasing erosional parameter 124
3.28 Predicted landscape evolution 128
3.29 Landscape evolution model, flat initial condition 129
3.30 Landscape evolution model, 1% DEM initial condition 130
3.31 Landscape evolution model, 10% DEM initial condition 131

3.32 Testing impact of alternative uplift history used to externally force landscape evolution model. 132
3.33 Distribution of thermochronology data 134
3.34 Comparison of thermochronmetric and calculated denudation rates 136
3.35 Paleogeography model of North America 138

4.1 Eastern North America and Atlantic Ocean. 148
4.2 Elastic thickness of eastern North America 149
4.3 Location of well data 151
4.4 Chronostratigraphy of the Baltimore Canyon Trough. 154
4.5 History of New Jersey subsidence from the COST B-2 well 157
4.6 Time-depth relationships for wells 158
4.7 Testing compaction parameterisation 159
4.8 Compaction parameterisation and porosity. 160
4.9 Best-fitting instantaneous rifting subsidence histories. 164
4.10 History of passive margin subsidence 165
4.11 History of passive margin subsidence (continued) 166
4.12 Spatial patterns of tectonic subsidence 167
4.13 Location of seismic profiles 168
4.14 Seismic stratigraphy of the New Jersey margin 169
4.15 Seismic strike line A-148, located offshore New Jersey 170
4.16 Seismic line MMG16, located on Georges Bank. 171
4.17 Seismic line LMG18, located on Georges Bank. 172
4.18 Flexural analysis for an Appalachian load 174
4.19 Trade-off between average excess temperature, $\overline{T}$, and mantle layer thickness, h. . . . 176
4.20 Geomorphic constraints on the evolution of the Appalachian Mountains 179
4.21 Sediment accumulation rate at each well 181
4.22 Sediment accumulation rate at each well (continued) 182
4.23 Isopach maps of allostratigraphic units in the Baltimore Canyon Trough 185
4.24 Isopach maps of allostratigraphic units in the Baltimore Canyon Trough (continued) . 186
4.25 Comparison of Middle Miocene isopach maps 187
4.26 Comparisons of sediment flux to the BCT 188

4.27 Location of sedimentary flux swath profile 191
4.28 Predicted landscape evolution of Appalachian Mountains 192
4.29 Landscape evolution model for decaying topography 193
4.30 Landscape evolution model with paleotopography and uplift 194
4.31 Predicted and observed sedimentary flux, uplift and subsidence of the North American middle Atlantic margin 195

Chapter 1

Introduction

1.1 Overview

Understanding the history of the Earth's surface is of fundamental concern to the Earth Sciences. The patterns and tempo of surface uplift and erosion provide a framework for understanding long-term processes and feedbacks relating to crustal deformation and orogenesis (e.g., *Meyer et al.*, 1998; *Willett*, 1999; *Roe et al.*, 2008; *Whipple*, 2009), global climate and atmospheric circulation (e.g., *Ruddiman and Kutzbach*, 1989; *Kitoh*, 2004; *Mitrovica et al.*, 2020), oceanic geochemical cycles (e.g., *Raymo et al.*, 1988; *Goddéris and François*, 1995; *Hilton et al.*, 2011), the evolution of biota (e.g., *Gallen et al.*, 2013; *Perrigo et al.*, 2019), as well as constraints on mantle viscosity and rates of convection (e.g., *Fjeldskaar*, 1994; *Gurnis et al.*, 2000). Histories of surface uplift and subsidence can help discern mechanisms responsible for generating the observed topography, as these often have specific rates and patterns specific to the driving forces (*Rohrman et al.*, 2002; *Lovell*, 2010).

Despite their importance, measurements of surface uplift and topographic growth on geological timescales are difficult to obtain, as they require the use of proxies (e.g., thermochronology, paleoaltimetry, cosmogenic radionuclide dating *Blisniuk and Stern*, 2005; *Sahagian and Proussevitch*, 2007; *Chamberlain et al.*, 2012; *Schildgen et al.*, 2018). These methods require careful field and laboratory work, and thorough assessment of uncertainties, assumptions and interpretations (e.g. constraints on lapse rates, cooling rates, distribution of cosmic rays). These difficulties mean that obtaining the large, precise inventories of uplift required to constrain growth and decay of topography at continental scales is challenging. One way to circumvent problems and uncertainties associated with obtaining uplift rates from single methods is to employ a multidisciplinary approach, combining data and observations from

different fields, such as erosion rates, age and pattern of magmatism, crustal deformation structures, geophysical data and models (e.g., gravity, seismic tomography), as well as geomorphic modelling and provenance studies.

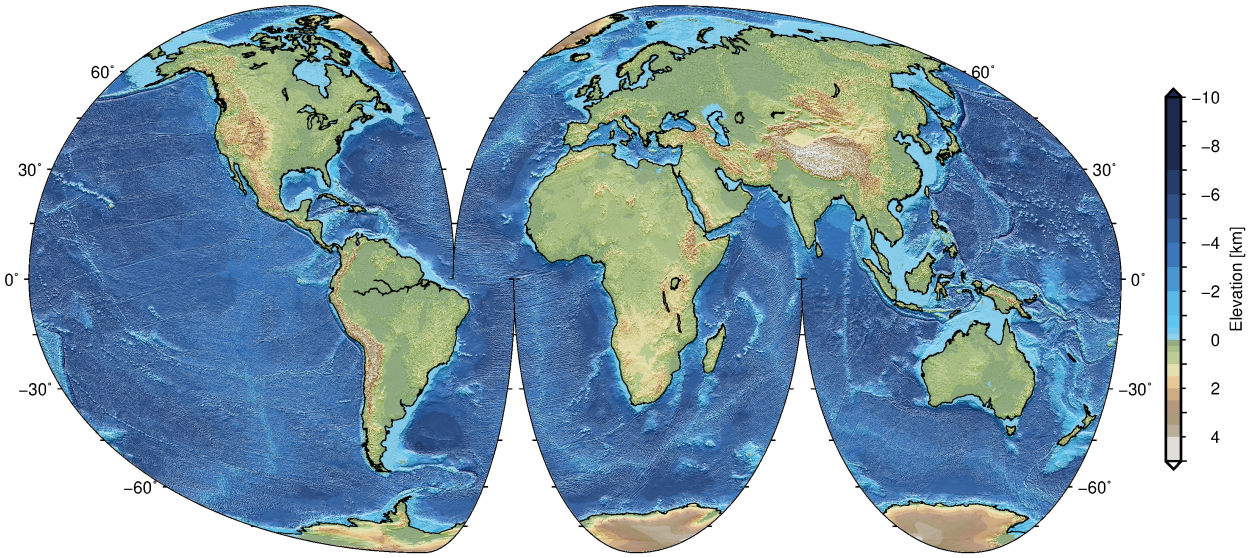

Figure 1.1: **Global map of topography** from ETOPO1 dataset.

This dissertation describes my work developing datasets and methodologies to constrain histories of uplift, subsidence and landscape evolution of Earth's surface. I focus on North America because of its considerable spatial extent, the presence of marine sedimentary deposits across the continent, large fluvial catchments draining most of the landmass, and the availability of big data inventories. I start by exploring how spot records of marine fossils can be combined on a global scale to measure net uplift of continents from Cretaceous to Recent times. I then focus on constraining the uplift history of North America, where these measurements are particularly dense. I augment the inventory of net uplift measurements by including stratigraphic successions of regressive marine sequences. I then fill in the gaps between spot measurements by using inverse and forward modelling techniques to extract uplift histories from longitudinal river profiles, and predict long-term erosion and sedimentary flux at a continental-scale. These predictions are tested using independent datasets of thermochronometric and sedimentary flux data. Finally, I investigate the subsidence of the eastern North American middle Atlantic margin and whether simple continental-scale forward landscape evolution models can predict the observed sedimentary flux to the margin.

1.2 Motivation

The present day shape of the Earth's surface, shown in Figure 1.1, is the result of complex interactions between deep and surface processes operating on a range of spatial and temporal scales. Much of the observed topography is isostatic in nature, controlled by density and thickness variations within the Earth's crust and lithosphere caused by, for example, cooling, crustal thinning, shortening, or magmatic emplacement (e.g. *Parsons and Sclater*, 1977; *McKenzie*, 1978; *Reymer and Schubert*, 1984; *Tapponnier et al.*, 2001). Additionally, isostatic support of topography also depends on the buoyancy of the lithosphere and underlying convecting mantle, where both composition and temperature play significant roles (e.g. *Hager et al.*, 1985; *Gaherty and Hager*, 1994; *Colli et al.*, 2016). However, some proportion of the Earth's topography is not readily explained by isostatic effects, and the role of transient changes in isostatic support, such as those arising from temperature dependent buoyancy, is poorly understood (e.g., *Flament et al.*, 2013; *Molnar et al.*, 2015). Instead, transient asthenospheric mantle flow, related to vertical stresses exerted by sub-plate convection or glacio-eustatic rebound, control recent topographic evolution in a number of regions (e.g. *Hager et al.*, 1985; *Mitrovica et al.*, 1989; *Gurnis*, 1990; *Forte*, 2000; *Flament et al.*, 2013; *Winterbourne et al.*, 2014; *Arnould et al.*, 2018). The interaction of these isostatic and dynamic processes, which can operate on multiple length and timescales, directly links Earth's deep interior to the evolution of surface environments through erosion and deposition (e.g. *Whipple*, 2009; *Molnar et al.*, 2015).

Observations of paleo-topography, surface and rock uplift rates, and how they have varied over geological time, may help distinguish between the tectonic and mantle-driven processes responsible for shaping the Earth's surface (e.g., *Schildgen et al.*, 2012; *Austermann et al.*, 2017). Therefore, by constraining histories of surface vertical motions, one may find important clues about geological processes (e.g., *Hager and Richards*, 1989; *England and Molnar*, 1990; *Gurnis et al.*, 2000; *Liu*, 2015). Doing so, however, is challenging because superposition of different processes with varying amplitudes and rates complicates interpretations (Figure 1.2). Different geological processes will variably affect rock uplift, surface uplift and erosion. Climatic variability can also affect rates of erosion, which can, in turn, contribute to further rock uplift (e.g., *Molnar and England*, 1990; *Willett*, 1999; *Beaumont et al.*, 2001; *Willett et al.*, 2001; *Bonnet and Crave*, 2003; *Whipple and Meade*, 2006; *Bishop*, 2007). Tectonic subsidence and base-level fall also contribute to the generation of relief, and create accommodation space for the erosional products of uplift, acting to enhance geomorphic processes that shape the landscape (e.g. *Burov and Cloetingh*, 1997; Gran et al., 2013). Additionally, erosion acts to remove

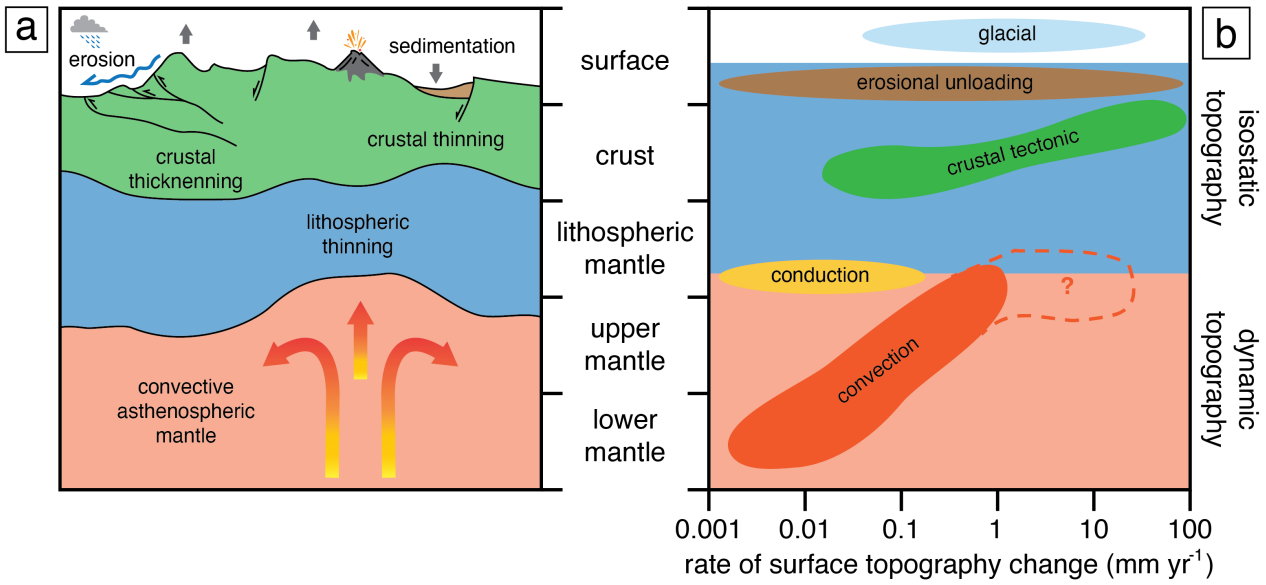

Figure 1.2: **Diagram illustrating the contributions of isostatic and dynamic topography,** modified after *Faccenna and Becker* (2020). (a) Illustration (not to scale) of the different processes that might contribute to the generation of topography. (b) Summary of relevant rates of surface deformation associated with these processes, and the depths at which they originate. The ? refers to the unresolved debate on the maximum rates of topographic change associated with mantle convection (e.g., *Flament et al.*, 2013; *Molnar et al.*, 2015).

much of the measurable record of past uplift. Furthermore, whether erosive processes responsible for shaping topography on a reach or stream scale, such as lithology, can be scaled-up whole-catchment or continental scale in an analytical, predictive manner remains unclear (e.g., *Kooi and Beaumont*, 1996; *Roberts et al.*, 2019). Therefore, understanding the interaction and interplay between uplift, erosion and subsidence on a continental scale, and how they affect landscape evolution is paramount for understanding the driving forces behind the evolution of Earth's surface.

1.3 Expected topographic signals of geological processes

The length-scales, timescales and amplitudes of the different processes contributing to the generation of topography span multiple orders of magnitude (Figure 1.2). In general, contrasts in crustal thickness generate most of the variation in Earth's observed topography (Figure 1.3; *Lachenbruch and Morgan*, 1990; *Faccenna and Becker*, 2020). Crustal thickening as a result of tectonic shortening, or crustal thinning by extension, is known to generate uplift, or subsidence, up to order 1 km in amplitude (e.g., *McKenzie*, 1978; *DeCelles et al.*, 2002). Similarly to the crust, variations in lithospheric composition and thickness can generate isostatic topography (e.g., *Crough and Thompson*, 1976; *Le Stunff and Ricard*, 1995; *Ávila and Dávila*, 2020). In this scenario, the isostatic elevation is a direct consequence

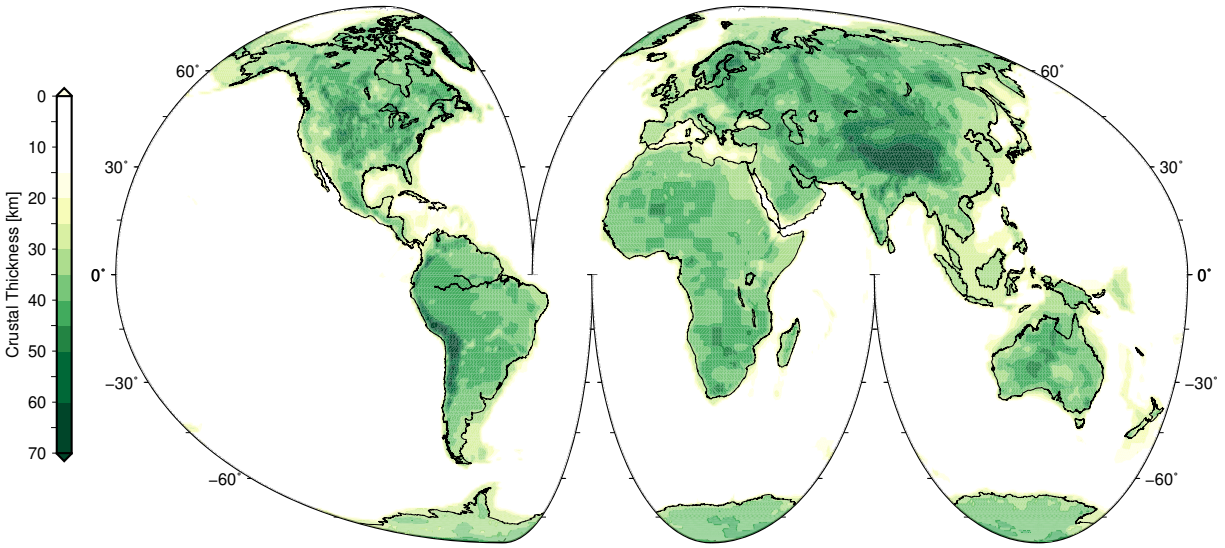

Figure 1.3: **Global map of crustal thickness from** CRUST1.0 (*Laske et al.*, 2013). Uncertainties in crustal thickness are laterally heterogeneous due to sampling variability. In specific regions of interest, improved Moho depth (i.e., crustal thickness) constraints can be derived from teleseismic receiver functions (e.g., *Luz et al.*, 2015a).

of structural deformation by plate motion, which generates localised belts of high topography, ranging from a few kilometres (e.g. throw on single faults) to 1000 km (e.g. Himalayas and Tibetan Plateau). Regions of tectonically-generated topography are directly associated with geological structures, such as faults and folds, where rates of deformation can be measured directly (e.g., *Suppe et al.*, 1992; *Mitchell et al.*, 2001; *Walker et al.*, 2009). The dynamic component associated with these tectonic processes, which operates on larger length-scales and timescales determined by mantle viscosity and convection patterns, is harder to detect in the geological record.

1.3.1 Sub-plate support

In this project, I work to understand how the convecting mantle directly beneath tectonic plates affects vertical motions, as this has direct implications for understanding chemistry of magmatism, ice-sheet stability, continental-scale ecology and biodiversity, the long-term carbon cycle, and water flux across oceanic gateways (e.g., *Kutzbach et al.*, 1989; *Crosby and McKenzie*, 2009; *Parnell-Turner et al.*, 2015; Roberts and Mannion, 2019; *Mitrovica et al.*, 2020). Here, I take sub-plate support to mean vertical motions, positive and negative, arising from the convecting mantle, and make no distinction between those associated with forces arising from mantle convection or the buoyancy contribution from temperature anomalies.

The timescales, wavelengths and amplitudes of topography generated by sub-plate support can be

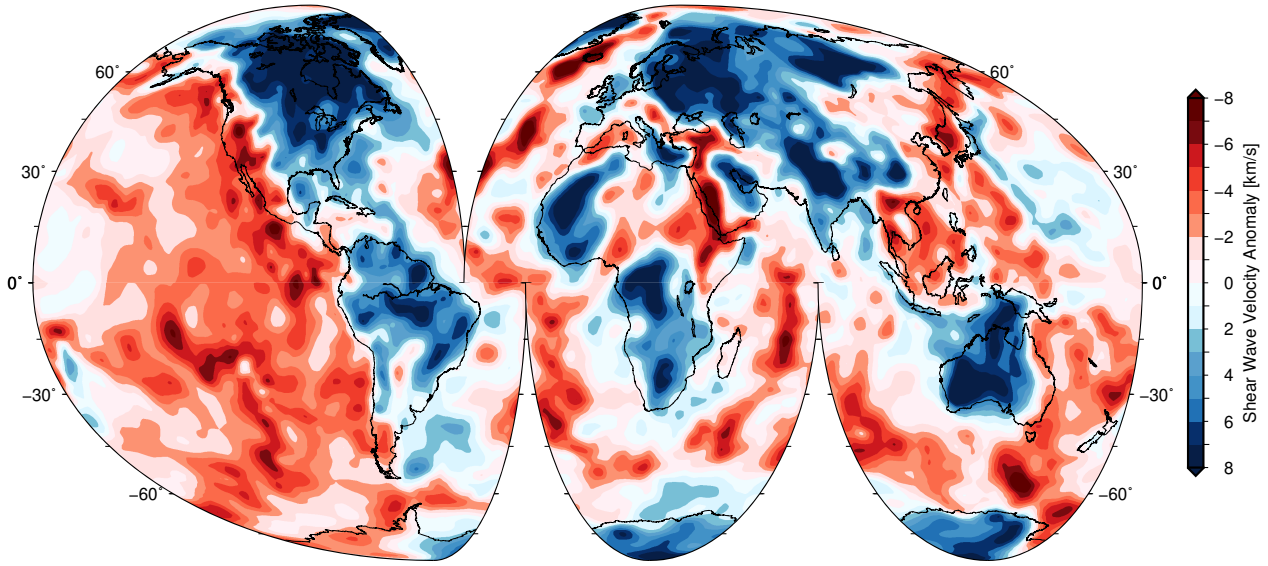

Figure 1.4: **Global shear wavespeed anomalies** at 125 km depth (*Schaeffer and Lebedev*, 2013).

estimated by different methods. For example, observations of buried fluvial landscapes, combined with fluid dynamical models, suggest transient uplift, of 300–1000 m amplitude and length-scales $\sim$ 400 km, can be generated on timescales of 1–10 Ma by thermal anomalies in the convecting mantle (*Rudge et al.*, 2008; *Hartley et al.*, 2011; *Stucky de Quay et al.*, 2017). Independent geophysical observations, such as shear-wave tomographic models, provide a useful guide to the present-day configuration of mantle convection, as density variations, and therefore buoyancy of the convective mantle can be inferred from perturbations in seismic velocity (Figure 1.4; e.g., *Forte et al.*, 1993; *Conrad and Gurnis*, 2003; *Steinberger*, 2016). Geodynamic modelling suggests that the length scales over which changes are observed is of order 10^3–10^4 km, although maximum predicted amplitudes range from 0.6–3 km (*Ricard et al.*, 1993; *Steinberger*, 2007; *Conrad and Husson*, 2009; *Spasojević and Gurnis*, 2012; *Flament et al.*, 2013). These predictions are highly dependent on the assumptions about the mantle viscosity structure and model boundary conditions, so require testing against independent geological observations.

A different method of measuring sub-plate support is estimating residual topography by removing isostatic contributions from sediments, variable crust and lithsophere thickness, and ice loading from the present-day topography (e.g., *Winterbourne et al.*, 2014; *Hoggard et al.*, 2016). Such measurements provide key observational constraints for geodynamic model results. Estimates of residual topography from oceanic lithosphere suggest convectively supported vertical motions can be generated at smaller length-scales, of 100 to a few hundred kilometres, with amplitudes < 2 km. The lack of consensus on wavelengths and amplitudes of sub-plate support of topography is an outstanding issue in global

geodynamic modelling, especially when concerning the continents (*Davies et al.*, 2019). An outstanding issue is development of datasets that constrain the temporal evolution of sub-plate support.

1.4 Measuring vertical motions of continents

There is no general consensus on how convection-driven vertical motions on continents should be measured through deep time. Previous works have used paleogeographic interpretations to generate estimates of epeirogenic motions of continents since the mid-Cretaceous (*Ziegler et al.*, 1985; *Sahagian*, 1987). However the geological data used to generate observations of uplift is unclear, and so reproducing such results and adequately assessing uncertainties is challenging.

The residual topography measurements compiled by *Hoggard et al.* (2016) are limited to the oceanic realm where the lithospheric structure, controlled primarily by a well-understood age-dependent behaviour, is relatively simple when compared to continents. Signals of sub-plate support are, therefore, more easily isolated. Generating such residual elevation datasets on continents is limited by the present-day understanding of how lithospheric composition, extent of melting, and other processes such as lithospheric delamination, contribute to the evolution of topography (e.g., *Davies et al.*, 2019). Conversion of free air anomalies can also be used to infer "dynamic", i.e. uncompensated, topography by scaling the gravity anomalies with an "admittance" factor. By assuming a linear (admittance) transform function between gravity and non-isostatically compensated topography, free-air gravity anomalies can be used infer sub-plate support on continents (e.g., *Roberts et al.*, 2012a). However, the choice of admittance factor is not generally agreed upon (*Colli et al.*, 2016; *Hoggard et al.*, 2016; *Yang and Gurnis*, 2016). Improved documentation of the temporally and spatially variable behaviour of the continental surface is required.

The present-day topography of the Earth's surface is increasingly well mapped, and available with increasing resolution, owing to higher resolution satellite based digital elevation models (e.g., SRTM, ASTER, AW3D30; *Jarvis et al.*, 2008; *Tachikawa et al.*, 2011; *Tadono et al.*, 2014). The GPS observational networks and advances in InSAR, as well as other methods of satellite geodesy, now provide a robust estimate of the short-term variations in surface elevation in specific areas. These observations have provided significant advances on our understanding of the earthquake mechanics and ground motions (*Elliott et al.*, 2016; *Wang et al.*, 2019). On timescales of 100 ka, vertical motions can be measured using dated raised shorelines or emerged coral atolls, which can be used to constrain long-term variability of seismic cycles, slip distribution on faults, or the timing of glacial loading-unloading

Merritts et al. (1999); *Pedoja et al.* (2006); *Westway et al.* (2006); *Binnie et al.* (2016); *Austermann et al.* (2017); *Hoffmann et al.* (2020).

At longer, million-year time scales, the timing and magnitude of uplift, denudation and subsidence on continents can be reconstructed using geological approaches. The age of magmatic events, low-temperature thermochronology, subsidence histories, river incision rates, sedimentary flux, isotope geochemistry, paleobotany, geomorphologic, stratigraphic and paleontological observations can all independently provide constraints on the history of vertical motions on continents (e.g. *Sahagian*, 1987; *Dickinson et al.*, 1988; *Gregory and Chase*, 1992; *Rohrman et al.*, 2002; *Matmon et al.*, 2003; *Chapin et al.*, 2004; *Colgan and Henry*, 2009; *Liu and Gurnis*, 2010; *Galloway et al.*, 2011; *Chamberlain et al.*, 2012; *McKeon et al.*, 2014). This data, however, is not always readily available or uniformly distributed across all continents, thus making the assembly of a coherent continental paleogeographic history a challenging task. Recently, significant effort has been expended into compiling large databases of geological observations that can be used to infer histories of vertical motions, such as fossil assemblages (PBDB, paleobiodb.org), age and composition data of volcanic rocks (NAVDAT, navdat.org), reflection seismic surveys (NAMSS, *Triezenberg et al.*, 2016), thermochronology (*Herman et al.*, 2013), ^{10}Be denudation rates (*Covault et al.*, 2013; *Harel et al.*, 2016), and oceanic residual depth (*Hoggard et al.*, 2016), to name a few. The use of these geological 'big-data' in scientific research has the advantage of allowing the automation of computational processes, significant statistical analysis and investigation of processes on a global scale. Generation of large-scale, self-consistent compilations of geological data is therefore of timely relevance.

Spot measurements of uplift and denudation are often spatially restricted by sampling biases or their geological occurrence and preservation, and often give little or no indication of changing rates of vertical motions. Further, disagreements still exist on how some of these data should be interpreted and how to avoid resulting biases (e.g., *Deng and Ding*, 2015; *Schildgen et al.*, 2018). Fluvial landscapes provide an alternative opportunity to investigate large scale continental vertical motions (Whittaker, 2012). Rivers are a ubiquitous feature of low-mid latitude terrestrial topography. Shapes of rivers are the geomorphic expression of the interaction between tectonic, climatic and erosive processes, therefore we can use their shape as an archive of the processes that have shaped them (*Howard*, 1994; *Whipple and Tucker*, 1999; *Snyder et al.*, 2000; *Kirby and Whipple*, 2001; *Wobus et al.*, 2006). Continent-wide drainage patterns can provide useful information about regional uplift history, and fill in the gaps where geological data is lacking, consequently helping reveal causal mechanisms of elevation change

(*Roberts et al.*, 2012a; *Goren et al.*, 2014; *Rudge et al.*, 2015). Similarly, the sedimentary flux into basins provide a spatially averaged estimate of the erosional and geomorphic evolution of its source drainage systems. Therefore sediments preserved at the continental margins provide an alternative approach to resolving the tectonic, erosional and geomorphic histories of their onshore counterpart (e.g. *Pazzaglia and Brandon*, 1996; *Poag and Sevon*, 1989).

Subsidence histories of offshore continental margins also play a significant role in the accumulation and preservation of sediments. Ultimately, the offshore sedimentary record can also be used to measure vertical motions at continental margins. Typically, quantitative passive margin basin studies have relied on constraining the subsidence history and the deeper crustal structure, resulting in models where the development of the basins is expressed in terms of the isostatic response to crustal/lithospheric thinning (*McKenzie*, 1978; *Watts and Thorne*, 1984). However, stratigraphic sequences recorded at passive margins might also contain signals of sub-plate support (e.g., *Moucha et al.*, 2008; *Czarnota et al.*, 2013; *Lodhia et al.*, 2018). Processes linking the the onshore and offshore regions also influence the development of margin stratigraphy, and is therefore directly relevant to the exploration of natural resources, or inference of sea-level variations from passive margins (e.g., *Miller*, 2005). Landscape evolution models, combined with known histories of continental uplift and denudation, can provide means to quantitatively predict the effects of a changing source region to the sediment delivery to the margin of continents (*Kooi and Beaumont*, 1996; *Tucker and Slingerland*, 1996; *Braun and Sambridge*, 1997; *Salles*, 2015). Thus, understanding the history of offshore subsidence, onshore uplift and the resulting sedimentary flux to passive margins is essential for a comprehensive understanding of continental landscape evolution.

1.5 Aims & Objectives

This dissertation addresses the following questions: What does the geological record tell us about global patterns of uplift? How can we improve the spatial and temporal resolution of spot measurements of uplift? Are simple mathematical models of landscape evolution successful on a continental scale? Can geological 'big-data' be used to test model predictions? How does subsidence of continental margins compare to growth of topography onshore, and what is the significance for deep-Earth processes?

To answer these questions, the major challenge that arises is generating enough geological observations, of sufficient precision, and over a large enough geographic extent such that topographic signals of

mantle convective processes can be picked out. This challenge cannot be resolved by using a single methodology over a small geographic area, but rather requires the synthesis of multiple techniques, modelling approaches and data sources. A few factors contribute to the timeliness of this study. First, the accessibility of global databases of multiple types, which require great effort to compile and did not exist a decade ago, allows such multi-disciplinary, continental-scale studies to be achieved. The increasing efficiency and accessibility of inverse and forward models of landscape evolution has created an opportunity to investigate landscape change in ways that were previously not possible. Finally, recent work by *Austermann et al.* (2017) and *Hoggard et al.* (2016) highlight the importance of global and continental-scale datasets for investigating the surface expression of mantle convection. This dissertation will focus on the evolution of long-wavelength ($>$ 100 km) vertical motions on a global, continental and regional setting, taking the North American continent and adjacent continental platforms as the main field of study. A key element is to develop observations and methods that link processes across the range of length- and time-scales from the Late Cretaceous to present-day.

The overarching goal of this research project is to understand continental tectonic motions and their causal drivers by integrating approaches at a large scale. I wish to develop a thorough understanding of Cenozoic landscape evolution, with a special focus on North America, through the use of large geological databases, inverse and forward modelling of drainage, subsidence analysis and histories of sedimentary flux. My specific objectives are to:

1. Formalise a methodology for deriving net uplift on continents from new, large inventories of marine fossil and paleoenvironmental data (Paleobiology Database, paleobiodb.org), and apply this methodology on a global scale.

2. Explore how these measurements of net uplift, combined with isostatic calculations, can be used to generate insight into the regional history of sub-plate support.

3. Use computational methods to extract and invert large drainage inventories from North America to derive a best-fitting, smooth uplift rate history from the Late Cretaceous to Recent. The resulting models will be tested using independent geological data.

4. Predict the denudation and sedimentary flux for North America resulting from the inverse model by combining these outputs with a forward landscape evolution model. Use low-temperature thermochronology data and sediment accumulation rates in offshore basins to test these predictions.

5. Derive a subsidence history for the Baltimore Canyon Trough Basin, offshore eastern North America, in order to investigate the timing and amplitude of sub-plate support affecting the passive margin.

6. Review the existing record of sediment accumulation in the Baltimore Canyon Trough, compare these to predictions of sedimentary flux derived from a landscape evolution model, and consider the implications for Neogene uplift of the Appalachian Mountains.

1.6 Thesis outline

- **Chapter 1:** *Introduction* This chapter provides a background to the significance of understanding of uplift and landscape evolution on continents and adjacent passive margins.

- **Chapter 2:** *Uplift Patterns from a Global Paleobiology Inventory* addresses Objectives 1 and 2. I present a method for adapting modern inventories of paleobiological and paleoenvironmental data to generate a new compilation of $> 24,000$ spot measurements of uplift atop all continents and numerous ocean islands. The compilation provides self-consistent, and in places, high-resolution (< 100 km, < 1 Ma), measurements of Cretaceous to Recent cumulative (post-deposition) uplift across significant tracts of most continents. Records from western North America and eastern South America are combined with geophysical observations (e.g. free-air gravity, shear and Pn-wave tomography) and simple isostatic calculations to determine origins of topography. Uncertainties associated with paleobathymetry, post-deposition compaction and glacio-eustasy are assessed. Isostatic calculations are used to explore how lithospheric thinning and mantle thermal anomalies may generate uplift of the observed wavelengths and amplitudes. The results emphasise the importance of large inventories of paleobiological data for understanding the history of tectonic and mantle convective processes. The work presented in this chapter has been published in GSA Bulletin.

  All of the published research was conceptualised, carried-out and written up by me, with supervision, review and editing by Dr. Gareth Roberts (co-author).

- **Chapter 3:** *The Ups and Downs of a Continent - Evolution of the North American Landscape* addresses Objectives 3 and 4. This chapter explores how inventories of stratigraphic and geomorphic observations can be combined with inverse and forward modelling approaches to determine how the North American landscape evolved. First, the biostratigraphic inventory developed in

Chapter 2 is augmented by stratigraphic markers and used to estimate post-depositional regional uplift. Secondly, to bridge the gaps between these measurements, an inverse modelling scheme is used to calculate the smoothest spatio-temporal pattern of rock uplift rate that yields the smallest misfit between 4161 observed and calculated longitudinal river profiles. Results suggest that Cenozoic regional uplift occurred in a series of stages, in agreement with independent stratigraphic observations. Finally, a landscape evolution model driven by this calculated rock uplift history is used to determine drainage patterns, denudation and sedimentary flux from Late Cretaceous times until the present day. These patterns are broadly consistent with stratigraphic and thermochronologic observations. We conclude that a calibrated inverse modelling strategy can be used to reliably extract the temporal and spatial evolution of the North American landscape at geodynamically useful scales.

This chapter has been published in the Journal of Geophysical Research: Earth Surface. All of the published research was conceptualised, carried-out and written up by me, with supervision, review and editing by my co-authors Dr. Gareth Roberts, Dr. Alex Whittaker and Prof. Nicky White (co-author).

- **Chapter 4:** *Uplift, Subsidence and Evolution of the U.S. Mid-Atlantic Region* tackles Objectives 5 and 6. First, I build on existing analyses to backstrip 27 wells, which, combined with seismic data, constrain timing and extent of Cenozoic subsidence of the Baltimore Canyon Trough, offshore eastern North America. Results indicate up to $\sim$ 600 m of water-loaded subsidence between $\sim$ 20–0 Ma centred on the Baltimore Canyon Trough. Seismic data from the trough shows Neogene aggrading clinoforms. There is little evidence for faulting or stratigraphic growth, which indicates that Neogene lithospheric strain rates were low. Amplitude and spatial extent of Neogene subsidence are difficult to explain by glacio-eustasy or glacio-isostatic adjustment. Secondly, I explore whether forward modelling of landscape evolution, developed in Chapter 3, can give new insight into Late Cretaceous to Recent evolution of the Middle US Atlantic margin. Predictions of sedimentary flux are compared to sediment accumulation rates measured from well data and published basin-wide isopach maps.

  The first part of this chapter (Section 4.3) has been published in Earth and Planetary Science Letters. The preliminary data processing and analysis for this publication, conceptualised by me, was carried out by Matthew Morris under my supervision. Their work was completely re-done by me, including more data, a revised methodology, figures, improved validation of results, and

new text, such that my work forms the principal contribution to the publication. Dr. Gareth Roberts provided supervision to this project. I have not included text, results or analysis from the published article that have not been the direct result of my own work. The second part of this chapter (Section 4.4) has not yet been published, and is entirely my own work.

- **Chapter 5:** *Discussion* This chapter synthesises results presented in this dissertation, evaluates the overall shortcomings, successes and implications of results, and is followed by a discussion of future work.

Chapter 2

Uplift Patterns from a Global Paleobiology Inventory

All of the material in this chapter has been published as

Fernandes, V.M., and Roberts, G.G. (2020). Cretaceous to Recent Net Continental Uplift from Paleobiological Data: Insights into Sub-Plate Support, *Geological Society of America Bulletin*, doi:10.1130/B35739.1.

Copyright (2020), Geological Society of America.

2.1 Chapter overview

There are many geoscience problems for which constraining histories of uplift or subsidence of Earth's surface are of direct or indirect importance, for example reconstructing tectonics, mantle convection, geomorphology, sedimentary and chemical flux, biodiversity, glacio-eustasy and climate change. The least equivocal constraints on timing and amplitude of vertical motions on geological timescales come from the distribution of rock formed in shallow marine environments. However, obtaining enough observations at sufficiently large spatial and temporal scales ($\sim 10^2$–10^4 km, $\sim$ 1–100 Ma) to constrain histories of regional topographic evolution remains challenging. To address this issue I adapted modern inventories of paleobiological and paleoenvironmental data to generate a new compilation of $> 24,000$ spot measurements of uplift atop all continents and numerous ocean islands. The compilation provides self-consistent, and in places, high-resolution (< 100 km, < 1 Ma), measurements of Cretaceous to Recent cumulative (post-deposition) uplift across significant tracts of most continents. Records from western North America and eastern South America are combined with geophysical observations (e.g.

free-air gravity, shear and Pn-wave tomography) and isostatic calculations to determine origins of topography. Uncertainties associated with paleobathymetry, post-deposition compaction and glacio-eustasy are assessed. Isostatic calculations are used to explore how lithospheric thinning and mantle thermal anomalies may generate uplift of the observed wavelengths and amplitudes. The results emphasise the importance of large inventories of paleobiological data for understanding the history of tectonic and mantle convective processes as expressed at the Earth's surface.

2.2 Introduction

Vertical motions of Earth's surface are used to inform almost all branches of the Earth Sciences. They are used to understand, for example, growth of mountain ranges, deep Earth rheology, natural hazards, histories of mantle convection, glacio-eustasy and sedimentary basin formation (e.g., *Ziegler et al.*, 1985; *White and McKenzie*, 1988; *Molnar and England*, 1990; *Densmore and Hovius*, 2000; *Copley and McKenzie*, 2007; *Hoggard et al.*, 2016). Understanding how topography grows and decays is a fundamental geologic concern but also important for understanding chemical fluxes, the distribution of natural resources and biodiversity. For example, the elevation, history and erosion of topography are crucial components for understanding chemical fluxes to the oceans, weathering, atmospheric and oceanic circulation and biotic distributions (e.g., *Raymo and Ruddiman*, 1992; *Anderson and Anderson*, 2010; *Herman et al.*, 2013; *Perrigo et al.*, 2019). As such, topographic evolution plays a central role in understanding climate change throughout geological time (*Mitrovica et al.*, 2020). Despite more than 100 years of study, defining and understanding histories of topographic growth and decay on geologic timescales remain important topics of research (e.g., *Davis*, 1899; *Suess*, 1906; *Hack*, 1975; *Ziegler et al.*, 1985; *Sahagian*, 1987; *Mitrovica et al.*, 1989; *McDonough and Cross*, 1991; *Rowley*, 2013). In this chapter, I make use of existing paleobiological databases to produce 24,372 individual measurements of net uplift since Cretaceous times. These measurements are used to consider how lithospheric and sub-plate processes generate observed timings, amplitudes, and wavelengths of uplift.

2.2.1 Previous work

In general, subsidence is better preserved in the geological record than uplift because erosion tends to remove the rock record one wishes to measure. Uplift and associated landscape evolution is often estimated indirectly using proxies. For example, a consequence of uplift is increased potential energy, which results in the erosion, transport and deposition of clastic material. As such, histories of solid

sedimentary efflux at continental margins have been qualitatively and quantitatively related to patterns of uplift in most continents (e.g., *Walford and White*, 2005; *Guillocheau et al.*, 2012; *Galloway et al.*, 2011; *Lodhia et al.*, 2018). Thermal and compaction histories of rocks can be linked to uplift via inferred histories of denudation (e.g., thermochronometry, vitrinite reflectance, sonic velocities; see *Walford and White*, 2005; *Schildgen et al.*, 2009; *Anderson and Anderson*, 2010). Radiometric and biostratigraphic techniques can be used to date eroded surfaces, which in many places can be related to changes in base-level generated by, say, uplift (e.g., *Bierman and Steig*, 1996; *Aciego et al.*, 2007; *Finnegan et al.*, 2014; *Stucky de Quay et al.*, 2019). Isotopic data, basalt morphology and paleobotany are also used to constrain elevation of topography via functions (lapse rates) that correlate, for example, temperature, or isotopic compositions, with elevation (e.g., *Gregory and Chase*, 1992; *Garzione et al.*, 2000; *Ghosh et al.*, 2006; *Sahagian and Proussevitch*, 2007; *Chamberlain et al.*, 2012).

A suite of geodetic and geologic observations exists to directly measure uplift and subsidence at a range of scales. For example, contemporary measurements of vertical motion from geodetic data (e.g., InSAR, GPS) have improved understanding of active tectonics and associated seismic hazards (e.g., *Reilinger et al.*, 2010; *Elliott et al.*, 2016). Uplifted, radiometrically dated Holocene terraces and historical records at tide gauges are crucial constraints on the viscoelastic response of the lithosphere and mantle to unloading (e.g., *Lambeck et al.*, 1998; *Pedoja et al.*, 2014; *Watts*, 2001). The least equivocal constraints on the history of uplift on timescales of tens of thousands to millions of years come from dated marine rock. Pioneering work, by for example *Ziegler et al.* (1985) and *Sahagian* (1987), showed that Cretaceous marine sedimentary strata across North America and Africa provide evidence for kilometre-scale, long wavelength, uplift during the last 100 million years (see also *Holmes*, 1965; *Burke and Gunnell*, 2008). Using these observations to determine uplift histories relies on accurate identification of marine lithologies and paleoenvironments. To be able to use these inventories to constrain histories of sub-plate support, a general challenge is their sparsity. In contrast, stratigraphy along passive margins and the relationship between age and depth of the oceans provide well resolved estimates of modern and ancient sub-plate support (see e.g., *Czarnota et al.*, 2013; *Hoggard et al.*, 2016; *Lodhia et al.*, 2018).

Recent studies measuring vertical motions of continental topography on geologic timescales have similarly focused on mapping the difference between modern and paleo-elevations of dated sea-level markers (e.g., *Bétard*, 2010; *Dorsey et al.*, 2011; *Schildgen et al.*, 2012; *Peulvast and Bétard*, 2015; *Bessin et al.*, 2017). These studies understandably tend to focus on regional scales (e.g., tens to hundreds of

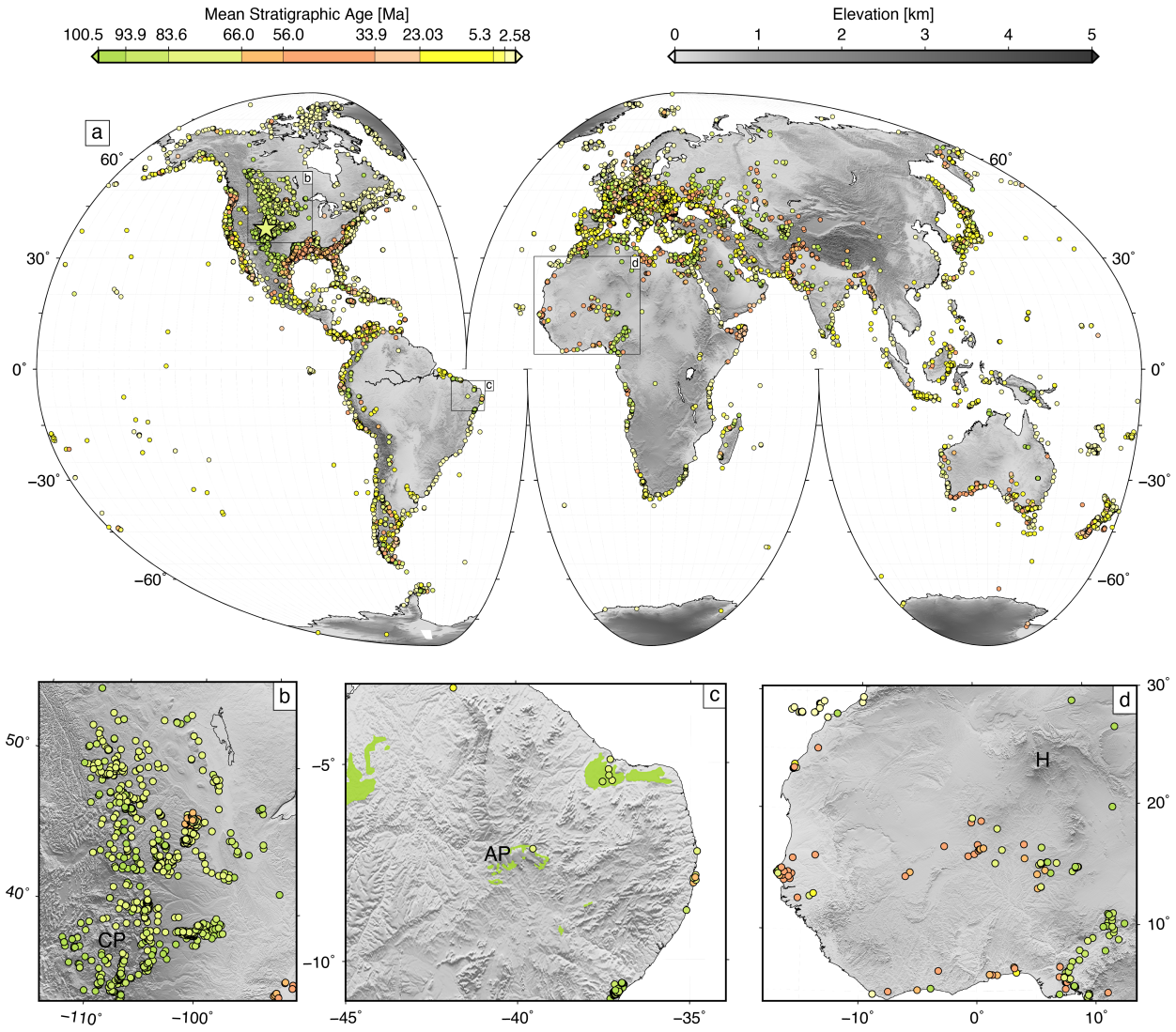

Figure 2.1: **Paleobiology inventory.** (a) Circles = Cretaceous to Recent marine fossils contained within the Paleobiology Database (PBDB) used to measure uplift; colours indicate mean stratigraphic age. Gray scale = hill-shaded topography (ETOPO1). Star (central western North America) = location of example shown in Figure 2.2. (b/c/d) Distribution of uplift constraints in western North America/Borborema Province, Brazil/NW Africa. CP = Colorado Plateau, AP = Araripe Plateau, H = Hoggar Mountains. Green polygons in panel (c) show distribution of Cretaceous marine rock including the Araripe Plateau, which is shown in the centre of the panel.

kilometres). Recently, the paleobiology community has assembled large inventories of paleontological data from across the globe to address large-scale paleobiological questions (e.g., `paleodb.org`; `geobiodiversity.com`). For example, genera in the Paleobiology Database (PBDB) include 24,372 records of Cretaceous to Recent marine fossil assemblages from all continents and many ocean islands. In this study I make use of that inventory and coincident elevation measurements to constrain uplift at $> 24,000$ localities, which includes estimates for all continents and many ocean islands (Figure 2.1).

This chapter has three parts. First, the simple methodology for measuring net uplift is explained using

an example from western North America. The scheme used to assess the veracity of records in the PBDB, and, in particular, the approach used to identify extraneous records is explained. Uncertainties generated by paleobathymetry, post-deposition compaction and denudation, and sea level change are estimated. Second, amplitude, wavelength and timing of vertical motions for two case studies — the Western Interior of North America and Borborema Province, northeastern Brazil — are given. Finally, an example is provided of how net uplift measured using the PBDB can be used to give insight into the geologic evolution of continents. The uplift measurements are combined with geophysical observations (e.g., free-air gravity, shear and Pn-wave tomography) and simple isostatic calculations to elucidate the mechanisms responsible for generating the present-day elevation of continental topography.

2.3 Calculation of Vertical Motions

In many cases the current elevation of fossil assemblages on continents provides a reasonably good (minimum) constraint on net uplift since deposition. This result is a consequence of paleo-water depths in epicontinental seaways typically being small (less than a few hundred meters), post-deposition compaction tending to reduce elevations of uplifted marine rock, and far-field glacio-eustatic sea-level changes being of small amplitude (<200 m) compared to many (kilometre-scale) uplift estimates. However, in some places (e.g., where there is significant structural relief) these uncertainties can be important. Therefore the following sections describe procedures to calculate uplift and uncertainties from PBDB records. In its simplest form net uplift, U, is calculated as

$$U = E + B - S + \Delta C, \tag{2.1}$$

where E is present-day elevation of the marine fossil assemblage, B is paleobathymetry, S is sea-level at the time of deposition and ΔC is a correction that accounts for post-depositional compaction of sediments. Maximum and minimum estimates of uplift can be simply calculated using extreme uncertainties in elevation, paleobathymetry, sea level and compaction (e.g., $U_{max} = E_{max} + B_{max} - S_{min} + \Delta C$; $U_{min} = E_{min} + B_{min} - S_{max}$). If these quantities are measured with uncorrelated and random uncertainties (i.e. δE, δB, δS, $\delta \Delta C$) then uplift uncertainties, δU, can be calculated by quadrature, i.e. $\delta U = [(\delta E)^2 + (\delta B)^2 + (\delta S)^2 + (\delta \Delta C)^2]^{1/2}$. Similarly, uncertainties in average uplift rate, $U' = U/A$ where A is sample age (with associated uncertainty δA), can be expressed as $\delta U' = |U'|[(\delta E/E)^2 + (\delta B/B)^2 + (\delta S/S)^2 + (\delta \Delta C/\Delta C)^2 + (\delta A/A)^2]^{1/2}$. I note that I calculate surface uplift and that associated rock uplift can be significantly higher in denuded regions (e.g., *England and*

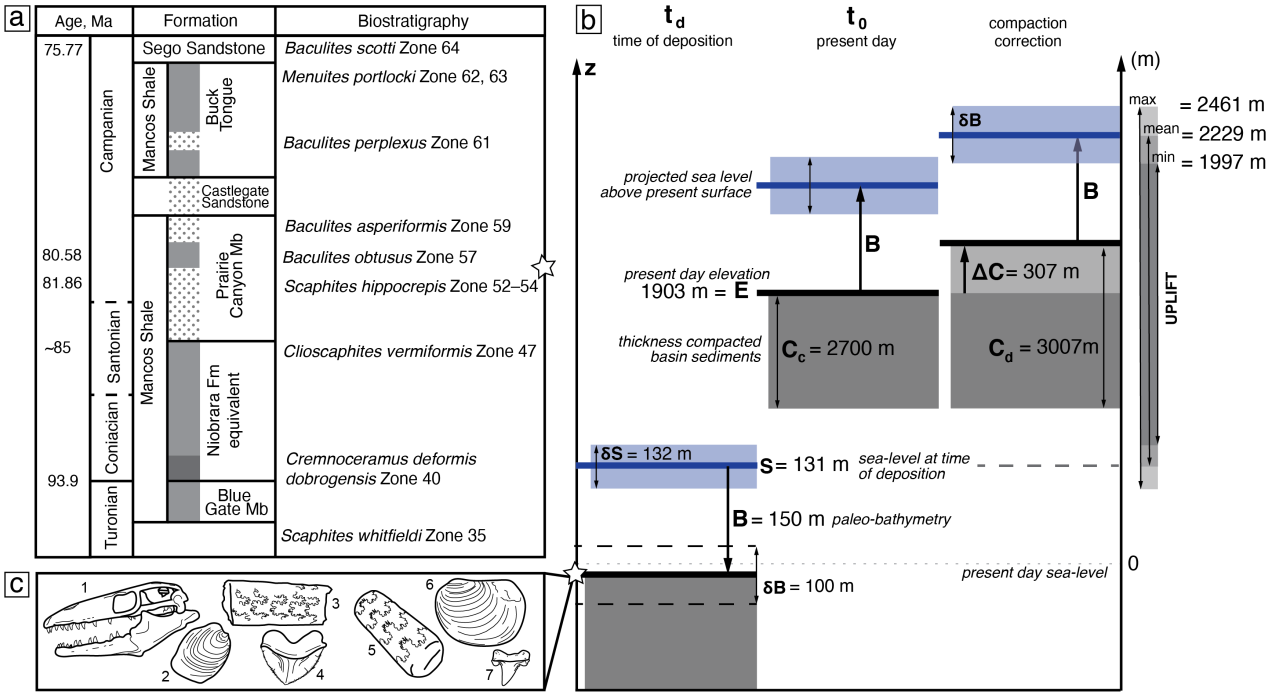

Figure 2.2: **Schematic illustrating methodology to calculate uplift.** (a) Generalised stratigraphic column of Mancos Shale successions in western Colorado (see star in Figure 2.1a). Age constraint is based upon ammonite zones (see Biostratigraphy pane) and radiometric dating in some places (*Obradovich and Cobban*, 1975; *Merewether and McKinney*, 2015); dotted/light/dark gray bars = sand/sandy-shale/shale. Star = location of fossil assemblage shown in panel (c). (b) Schematic diagram shows information used to calculate uplift and its uncertainty. Gray = solid Earth and associated compaction (ΔC) and paleobathymetric (B) corrections; blue = sea-level correction. (c) Fossil assemblage used to constrain age and paleoenvironment of Prairie Canyon Member of the Mancos Shale (see star in panel a) from PBDB: 1–*Prognathodon* [mosasaur], 2–*Platyceramus cycloides* [bivalve], 3–*Baculites haresi* [ammonite], 4–*Squalicorax pristodontus* [shark], 5–*Baculites aquilaensis* [ammonite], 6–*Innoceramus balticus* [bivalve], 7–*Cretolamna* [shark].

Molnar, 1990).

The following sections describe the methodology used to calculate uplift with the aid of an example from the Prairie Canyon Member of the Mancos Shale, western Colorado (Figure 2.2; *Kass*, 1999). The key fossil assemblages at this locality are preserved within the siltstone part of this member and include shark teeth, *Bacculites* ammonites, inoceramid bivalves and mosasaur skull fragments. This stratigraphy was interpreted as Campanian in age based on the fossil assemblage and regional chronostratigraphic correlations (*Obradovich and Cobban*, 1975; *Merewether and McKinney*, 2015).

2.3.1 Paleobiology Database (PBDB)

Fossil occurrences were retrieved from the PBDB on 8th July 2019 using the following filters: Maximum Age = 100.5 Ma, Minimum Age = 0 Ma (Cenomanian to Recent). The total number of records (fos-

sils) downloaded was 580,637. This inventory contains information about age, location, stratigraphic origin (i.e. formation, unit, member), lithology, paleoenvironment and tectonic setting at the time of deposition and references to original source material. The inventory also identifies fossil assemblages, i.e., fossils that are located at the same site and stratigraphic level, which are usually obtained from cited studies.

The records obtained from the PBDB required modification prior to generating uplift constraints. The three most important modifications were as follows. First, all fossils identified as non-marine (i.e. '*terrestrial*'), or those with no information about paleoenvironment, were removed from the database. Assemblages containing genera that do not necessarily represent marine conditions were also removed (e.g., birds that fly inland). For example, four records from inland Australia that document assemblages containing only species of the Pelecanidae family (pelicans) were removed. The total number of remaining marine fossil assemblages is 24,372. Each assemblage will subsequently be referred to as a point, and used to calculated uplift. Second, in general most points are accurately located. However, a small number are assigned incorrect locations in the database and must be corrected manually (e.g., whales off the coast of Hawaii were incorrectly assigned locations in Australia and Brazil). Locations of all key assemblages shown in this paper were checked and $< 1\%$ required manual intervention. Finally, qualitative paleoenvironmental information is converted into quantitative estimates of paleobathymetry. Paleoenvironmental information is recorded in the PBDB as, for example, '*shallow subtidal*', '*estuary/bay*', '*slope/basin*', as is information about the tectonic setting, for example, '*passive margin*', '*foreland basin*'. The PBDB identifies 37 different paleoenvironments and 14 tectonic settings, accompanied by descriptions (see following section for names and descriptions). The approach used to generate quantitative estimates of paleobathymetry is described in detail in the following section. Finally, points with poorly constrained paleobathymetry were corrected, where possible, using the methodology outlined below.

2.3.2 Bathymetric model

A variety of schemes exist to convert paleoenvironment descriptors into quantitative estimates of paleo-water depth (e.g., *Sahagian et al.*, 1996; *Immenhauser*, 2009). I used Immenhauser's (2009) scheme as it tends to yield conservative estimates of paleo-water depth, especially for shallow water environments (see Figure 2.3, Table 2.1). For example, I define water depths for '*very shallow marine*' as $0-50$ m, '*shallow marine*' as $0-100$ m, '*shelf*' as $0-250$ m, '*upper bathyal*' as $250-500$ m, '*middle bathyal*' as $500-2000$ m, and '*lower bathyal*' as $2000-4000$ m. Attributing a paleo-water depth range

to any given paleoenvironment is obviously subject to uncertainties, but is necessary to be able to use qualitative descriptions of depositional environments for quantitative analyses of elevation change.

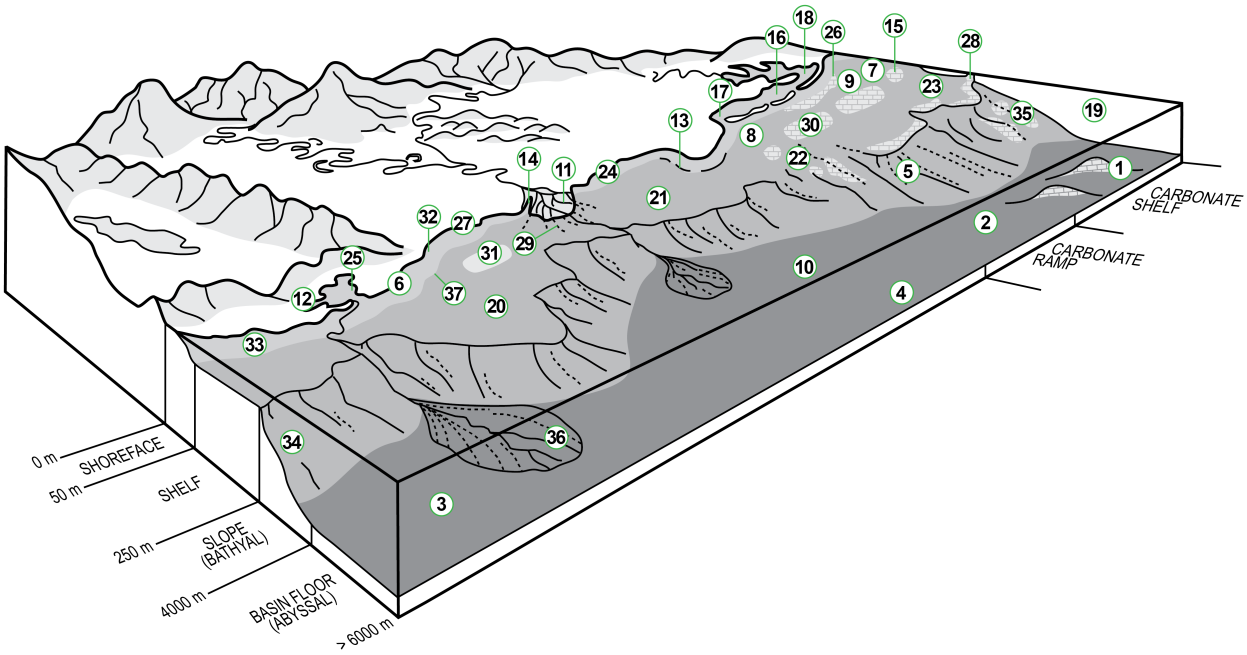

Figure 2.3: **Bathymetric model**. Cartoon illustrates the distribution of marine paleoenvironments recorded in the PBDB. 1–basin reef, 2–basinal (carbonate), 3–basinal (siliciclastic), 4–basinal (siliceous), 5–carbonate indet., 6–coastal indet., 7–deep subtidal, 8–deep subtidal ramp, 9–deep subtidal shelf, 10–deep-water indet., 11–delta front, 12–estuary/bay, 13–foreshore, 14–interdistributary bay, 15–intrashelf/intraplatform reef, 16–lagoonal, 17–lagoonal/restricted shallow subtidal, 18–marginal marine indet., 19–marine indet., 20–offshore, 21–offshore indet., 22–offshore ramp, 23–offshore shelf, 24–open shallow subtidal, 25–paralic indet., 26–perireef or subreef, 27–peritidal, 28–platform/shelf-margin reef, 29–prodelta, 30–reef, buildup or bioherm, 31–sand shoal, 32–shallow subtidal indet., 33–shoreface, 34–slope, 35–slope/ramp reef, 36–submarine fan, 37-transition zone/lower shoreface. A description of paleoenvironments is given in Table 2.1.

Table 2.1: Bathymetric model, descriptions of environments as given in the PBDB documentation, and attributed paleo-bathymetric ranges

No.	Environment	Description	min B [m]	max B [m]
1	Basin Reef	Deep water reef growing close to basin floor	500	1000
2	Basinal (carbonate)	On slope, basinal oozes that are predominantly carbonate, deep-sea.	500	3000
3	Basinal (siliciclastic)	On slope, terriginous mud, deep-sea.	500	4000
4	Basinal (siliceous)	On slope, cherty deposits, deep-sea.	500	4000

5	Carbonate indet.	All carbonate deposits where environment of deposition cannot be determined.	0	3000
6	Coastal indet.	Coastal environment where a specific non-deltaic setting cannot be identified.	0	50
7	Deep Subtidal	Deposited between normal wave base and typical storm wave base.	15	50
8	Deep Subtidal Ramp	Ramp between normal and storm weather wave base.	15	50
9	Deep Subtidal Shelf	On flat shelf or platform between normal and storm weather wave base.	15	50
10	Deep-water indet.	Unspecified deep sea.	250	4000
11	Delta Front	Marine delta portion, more open marine, with significant fresh water input.	1	15
12	Estuary/Bay	Shallow water with fresh water influence; perpendicular to shore, including wave base.	0	15
13	Foreshore	Coastal. Sandstone with gently dipping planar cross lamination with minimal bioturbation.	0	1
14	Interdistributary Bay	Delta with marine influence, at sea level and may contain marine to brackish water faunas.	0	2
15	Intraplatform Reef	Shallow-water portion of a platform, but not near its margin.	0	100
16	Lagoonal/Restricted Shallow Subtidal	Up to a few meters of water depth, hyposaline, restricted water movement.	0	2
17	Lagoonal	Up to a few meters of water depth, hypersaline. Shallow marine with fresh water; influence parallel to shore, including wave base. Carbonate or siliciclastic.	0	5
18	Marginal Marine indet.	Shallow setting, dominated by wave, river and tidal processes. Depositional settings include delta, beach, barrier island, estuarine, lagoonal, tidal flat.	0	15
19	Marine indet.	All marine siliciclastic deposits.	0	4000
20	Offshore	Below typical storm wave base, although can be affected by exceptionally strong storms. On the continental slope. Shale with storm sand beds, pervasive bioturbation of *Cruziana*.	50	250
21	Offshore indet.	Below typical storm wave base, although can be affected by exceptionally strong storms. On the continental slope. Unknown platform geometry.	50	250

22	Offshore Ramp	Carbonate platforms which have a very low gradient depositional slope (commonly less than 0.1) from a shallow-water shoreline or lagoon to a basin floor.	50	250
23	Offshore Shelf	The term shelf is more widely used in geological context for any broad, gently-sloping surface, clastic or carbonate, which has a break in slope in deeper water.	50	250
24	Open Shallow Subtidal	Up to a few meters of water depth, normal marine salinities.	1	15
25	Paralic indet.	Shallow marine cannot distinguish between lagoon or estuary, including wave base.	0	15
26	Peri-reef or Sub-reef	Carbonate deposits in the vicinity of a reef, however not containing in situ reef growth.	1	250
27	Peritidal	Shallow marine. Includes supratidal and intertidal settings and may be characterised in arid climates by evaporite minerals, dolomite, and desiccation cracks, but in humid climates by bioturbated mudstones with fenestral pores.	0	2
28	Platform/Shelf-margin Reef	Located on a carbonate platform margin.	0	250
29	Prodelta	Deeper marine delta portion, mud-dominated, difficult to distinguish from offshore deposits.	15	100
30	Reef, Buildup or Bioherm	Reef of uncertain geographical position relative to the shore or continental shelf margin.	0	250
31	Sand Shoal	Strong wave or tidal currents and consequently displays large-scale trough cross-stratification of well-sorted grainstone, but may also display seaward-inclined laminae where it is developed in a foreshore setting.	0	15
32	Shallow Subtidal indet.	Up to a few meters of water depth, salinity undetermined.	1	15
33	Shoreface	Coastal. Sandstone with large-scale trough cross-bedding and *Skolithos*. On weak wave climate, may be highly bioturbated with wave-ripple laminae.	1	50
34	Slope	Slumps, slides, debrites, turbidites.	250	4000
35	Slope/Ramp Reef	Growing on a shelf slope or carbonate ramp.	50	250
36	Submarine Fans	Deep water depositional systems generated by turbidity currents, often associated with a delta system.	1500	4000

37	Transition Zone/ Lower Shoreface	Coastal. Mudstone and hummocky cross-stratified sandstone, mixed *Skolithos–Cruziana*.	15	70

I compared paleobathymetries calculated using this approach to 13 other schemes (see Table 2.2). Each depositional environment was matched to the equivalent description in Table 2.1. I find that there is generally close agreement between approaches. The most significant discrepancies are for shallow water environments (< 200 m), for which the Immenhauser conversion scheme tends to be more conservative (i.e. has the greatest range of water depths; see Table 2.2).

Table 2.2: Comparison of paleobathymetric models.

Reference, Location	Environment & Description	B min [m]	B max [m]	PBDB Environment	No.	Tectonic Setting	B min [m]	B max [m]
Ziegler et al. (1985), Global	ocean trenches; turbidites or pelagic	6000	12000	deep-water indet.	10	none	250	4000
	ocean floor; pelagic sequence on ocean floor	4000	6000	basinal (silicicalstic)	3	none	500	4000
	continental slope-rise	200	4000	slope	34	none	250	4000
	prodelta fans	200	4000	basinal (silicicalstic)	3	none	500	4000
	outer shelf	50	200	offshore indet.	21	none	50	250
	prodelta	50	200	prodelta	29	none	15	100
	inner shelf	0	50	shoreface	33	none	1	50
	delta front	0	50	delta front	11	none	1	15
Sahagian and Jones (1993), Russian platform	shoreface; beach oolites, mudcracks, evaporites, fossils	0	2	shoreface	33	passive margin	1	150
	lagoon; mud, fossils	0	2	lagoonal	16	passive margin	0	2
	reef; fossils	0	2	reef, buildup or bioherm	30	passive margin	0	250
	transition zone; storm beds, fossils	2	10	transition zone/lower shoreface	37	passive margin	45	200

	offshore; fossils	10	25	offshore	20	passive margin	150	250
	deep; fossils	25	50	deep-water indet.	10	passive margin	250	4000
Sahagian et al. (1996), Russian Platform	deep water	100	200	deep-water indet.	10	passive margin	250	4000
Read (1985), Global	deep shelf and ramp; diverse open marine biota, upward fining, storm-generated beds, dominantly fair weather base	10	40	deep subtidal ramp	8	none	45	150
He et al. (2017), Pearl River Mouth	littoral; sea-level to fair weather-wave base	0	20	shallow subtidal indet.	32	passive margin	1	45
	inner shelf; fair to storm-wave base	20	100	deep subtidal indet.	7	passive margin	45	150
	outer shelf; storm-wave base to shelf break	100	200	offshore	20	passive margin	150	250
	continental slope; bathyal	200	3000	slope	34	passive margin	250	3000
	basin plain; abyssal	3000	5000	basinal (silicicalstic)	3	passive margin	2000	4000
Katz et al. (2013), New Jersey Shelf	upper shoreface	0	5	shallow subtidal indet.	32	passive margin	1	45
	lower shoreface	5	10	deep subtidal indet.	7	passive margin	45	150
	shoreface-offshore transition zone	10	30	transition zone/lower shoreface	37	passive margin	45	200
	inner neritic shelf	0	30	shoreface	33	passive margin	1	150

	middle-outer neritic shelf	30	200	offshore	20	passive margin	150	250
	offshore	20	200	offshore	20	passive margin	150	250
El-Azabi and El-Araby (2007), Gulf of Suez	foreshore intertidal	0	2	foreshore	13	rift	0	1
	shoreface / shallow subtidal	0	5	shallow subtidal indet.	32	rift	1	15
	deep subtidal	5	30	deep subtidal indet.	7	rift	15	50
	offshore transition zone	5	25	transition zone/lower shoreface	37	rift	15	70
	offshore; lower deep subtidal	25	30	offshore	20	rift	50	250
Short (2014), southern Australia Shelf	inner shelf; benthic species	0	70	shoreface	33	passive margin	1	150
	middle-outer shelf; benthic species	70	250	offshore	20	passive margin	150	250
	intertidal	0	3	foreshore	13	passive margin	0	1
	middle-deep neritic	60	140	offshore	20	passive margin	150	250
Allen (1970), modern Niger delta	delta front	0	30	delta front	11	passive margin	1	45
	prodelta	0	60	prodelta	29	passive margin	45	100
	nearshore/shoreface	0	20	shoreface	33	passive margin	1	150
	upper shoreface	0	7	shallow subtidal indet.	32	passive margin	1	45

	lower shoreface	7	20	deep subtidal indet.	7	passive margin	45	150
	offhsore	20	200	offshore	20	passive margin	150	250
	continental slope; bathyal	200	3000	slope	34	passive margin	250	3000
Adegoke et al. (2017), Niger delta	nearshore; includes shoreline, marsh and estuary	0	8	foreshore	13	passive margin	0	1
	marsh	0	8	marginal marine indet.	18	passive margin	0	45
	estuary	0	8	estuary/bay	12	passive margin	0	45
	inner neritic	8	55	shoreface	33	passive margin	1	150
	continental shelf	8	250	offshore	20	passive margin	150	250
	slope; bathyal	250	2000	slope	34	passive margin	250	3000
	basin floor; abyssal	2000	4000	basinal (siliciclastic)	3	passive margin	2000	4000
Davies et al. (2002), Arabian Plate	outer platform	50	200	offshore shelf	23	foreland basin	50	250
	middle platform	10	50	deep subtidal shelf	9	foreland basin	15	50
	inner platform	0	10	shallow subtidal indet.	32	foreland basin	1	15
Olson and Leckie (2003), northern Gulf of Mexico	marsh; benthic foraminifera zonations	0	5	marginal marine indet.	18	passive margin	0	45
	bay; benthic foraminifera zonations	0	5	estuary/bay	12	passive margin	0	45
	lagoon; benthic foraminifera zonations	0	5	lagoonal	16	passive margin	0	2

	inner neritic; benthic foraminifera zonations	0	50	shoreface	33	passive margin	1	150
	middle-outer neritic; benthic foraminifera zonations	50	150	offshore	20	passive margin	150	250
Brigaud et al. (2018), Paris basin	upper offshore; storm dominated, poorly sorted, bioturbation	10	40	transition zone/lower shoreface	37	cratonic basin	12	50
	shoal (shoreface); high energy, ooids, cross-bedding, well sorted	2	30	shoreface	33	cratonic basin	1	40
	lagoonal	0	2	lagoonal/ restricted shallow subtidal	17	cratonic basin	0	5
	intertidal; restricted and protected environment	0	2	peritidal	27	cratonic basin	0	2
	supratidal; brackish, brine ponds and episodic flux of normal marine waters	0	2	marginal marine indet.	18	cratonic basin	0	12

An important concern is whether the paleoenvironment of a given fossil assemblage reported in the PBDB is consistent with other paleoenvironmental interpretations for the same unit. To address this question I have benchmarked 14 randomly chosen points from North America, Africa and Europe against independent references (see Table 2.3). For example, PBDB entry number 23,864 is an Eocene assemblage from the Bashi Member of the Hatchetigbee Bluff Formation of Alabama, US. It is reported in the PBDB as a sandstone deposited within a peri-reef or sub-reef environment by *Palmer and Brann* (1965). These deposits probably formed within a shelf environment in the vicinity of a reef but do not contain direct evidence of in situ reef growth. Using the preferred conversion scheme they yield a paleo-water depth of 1–250 m (Table 2.1). An independent paleoenvironmental classification of the

Bashi-Hatchetigbee Bluff deposits, which crops out as an East-West band in northern Alabama and Georgia, is given by *Gibson and Bybell* (1981). Based on foraminifera assemblages and sedimentology (e.g., the occurrence of shelly glauconitic silt and very fine grained sand, commonly including a thin sequence of laminated silt and clay at the top), they identify the depositional facies as inner shelf (inner to middle neritic, i.e. < 150 m; *Olson and Leckie*, 2003). The other benchmarks are similarly consistent (see Table 2.3).

Table 2.3: Benchmarking PBDB and independently reference paleoenvironmental interpretations.

Location	Age [Ma]	Stratigraphy	Reference, Environment	Benchmark Reference, Environment
Saudi Arabia; 46.824, 25.203	83.5–70.6	Hajajah Mb, Aruma Fm	*El-Sorogy et al.* (2016): basin reef, intra-shelf basin.	*Gameil et al.* (2020): intra-shelf basin reef, fore-reef, back-reef – based on fossils (corals, solitary corals, bivalves, rudists, gastropods, echinoids).
Skane, Sweden; 12.816, 55.566	66–61.6	Stevens Klint Fm	*Bjerager et al.* (2010): basin reef, deep-water coral reef complex, reefs are 20 m high, 200 m long, formed on a first order paleo-seafloor high.	*Schøder and Surlyk* (2020): cool-water, coral-bryozoan mound complex within a chalk seaway continental platform – based on fossil assemblage and associated sediments.
Colorado, USA; 104.717, 38.283	100.5–93.9	Bridge Creek Limestone Mb, Greenhorn Limestone	*Elder* (1987): basinal carbonate, cratonic basin, chalky, very well indurated. Section C2 constitutes interbedded limestones and shales.	*Elderbak and Leckie* (2016): deposition in deep axis of Greenhorn seaway, in anoxic event – based on benthic and planktonic foraminifera.
England, 0.267, 51.950	99.6–93.5	Totternhoe Stone Mb, Zig Zag Chalk	*Newton* (1892): basinal carbonate.	*Woods* (2015): sea floor pelagic carbonate – based on foraminifera, coccoliths, sedimentology.

110.094, 36.525	99.6–93.5	Mancos Shale	*Kirkland* (1996): basinal siliciclastic, foreland basin.	*Leckie et al.* (1991): basinal to neritic (oxygen minimum zone) – based on kaolinite abundances, benthic and planktonic calcareous forams. Indicates deeper water at peak transgression, transition into arenaceous benthic foraminifera assemblage, hummocky cross-beds (below fair weather wave base = 5–15 m).
Bern, Swizerland: 7.517, 46.867	20.44–15.97	Upper Marine Molasse, Belpberg Beds	*Kroh and Menkveld-Gfeller* (2006): sandstone, delta front.	*Schlunegger et al.* (1997): Foreland basin deltaic shoreface, offshore bay, nearshore, foreshore, shoreface with 0–130 m PWD (given in text) – based on sedimentology.
Alabama, USA; 85.317, 32.126	85.8–70.6	Blufftown	*Schwimmer et al.* (1993): estuary/bay, most likely back-barrier or estuarine settings during relatively high sea-level stands.	*Case and Schwimmer* (1988): back-barrier marine or estuarine environment, near-normal salinity, with considerable fluvial input, shallow – based on sedimentology.
Alberta, Canada; 110.470, 49.120	83.5–70.6	Dinosaur Park	*Eberth and Brinkman* (1997): mudstone, estuary/bay.	*Beavan and Russell* (1999): paralic with increasing marine influence, brackish water marginal marine – based on fossils (shark teeth, marine reptiles) and sedimentology (inclined heterolithic stratification, characterised by alternating sand, mud, and carbonaceous shale laminae, with localised ironstone concretion suggestive of a lateral accretion surface).

South Dakota, USA; 103.220, 43.270	99.6–93.5	Hartland shale, Greenhorn Fm	*Sageman and Bina* (1997): offshore, foreland basin. Deposited during widespread marine flooding of the Western Interior U.S., the Greenhorn Formation is renowned for its organic carbon-rich shales and limestone-marlstone cycles	*Sageman* (1989): offshore, low-energy anoxia occasionally oxygenated by storm events, cratonic basin – based on geochemical analysis, benthic fossil assemblages, other fossil associations (e.g. ammonites).
Alabama, USA; 87.475, 32.141	56–47.8	Bashi Mb, Hatchetigbee Bluff Fm	*Palmer and Brann* (1965): perireef or subreef.	*Gibson and Bybell* (1981): inner shelf deposits, inner to middle neritic – based on foraminifera and sedimentology (shelly glauconitic silt and very fine grained sand, commonly including a thin sequence of laminated silt and clay at the top).
New Mexico, USA; 105.893, 35.492	93.5–89.3	Carlile Shale, Blue Hill	*Coates and Kauffman* (1973): bafflestone, reef, buildup or bioherm.	*Shimada* (2006): Comparing to the laterally equivalent in Kansas. Offshore to nearshore – based on distribution of fossil fish and sedimentary structures.
Maryland, USA; 76.516, 38.531	13.82–11.62	Choptank, Drumcliff	*Shattuck* (1904): shoreface sandstone. Mollusk-dense pale yellow-brown to pale orange well-sorted sand. Sub-tropical to temperate, in a current-swept channel-like basin.	*Kidwell et al.* (2015): shoreface to marine shelf – based on fossil assemblage (sedimentary structures are rare/absent). Densely packed shells and fine sand, onshore portions of a marine shelf, including sandy and shelly seafloors of a few meters to 10–20 m PWD (given in text).

Arizona, USA; 110.819, 35.745	93.5–89.3	Toreva Fm, Blue Point Tongue	*Kirkland* (1996): transition zone/lower shoreface, foreland basin.	*Olesen* (1991): shoreface – based on sedimentology and fossils. Fine-grained, non-calcareous sandstone, stratification obscured by bioturbation but consists of small-scale, very low angle, planar-tabular cross-bedding or ripple laminations.

At face value the largest paleo-water depth uncertainties are associated with 11,447 assemblages recorded as forming in indeterminate marine environments (i.e. '*marine indet.*'). However, many records contain comments that provide additional information that can be used to improve estimates of paleo-water depth. These '*geologic comments*' are often excerpts from publications from which the database entries were made. This additional information was also used to ensure consistency between the database and original publications. For example, the point numbered 10,119 is a fossil assemblage from the Gram Formation, Denmark (Tortonian; $11.6 - 7.2$ Ma). It was recorded in the database as '*marine indet.*' and no indication of tectonic setting was given. However, the '*geologic comments*' noted that "*[the] Gram Formation was deposited in a marine environment at a depth between 50 and 100 m, as indicated by the marine flora associated with terrestrial material, foraminifera and the marine fauna*". These more precise estimates were used to modify the database entry. All entries corrected in this way are labelled 'b' in the inventory of uplift constraints. If the '*geologic comments*' did not provide additional information on the source of the data (e.g., the original paper) then other publications were consulted. These points are labelled 'c' in the data tables. Any points that were not corrected using either of these two methodologies are labelled 'a'. Of the 12,765 points that have accurate paleo-water depth records $> 90\%$ have minimum paleo-water depth estimates of 50 m or less, and maximum paleo-water depth estimates of 250 m or less (see Figure 2.4).

As another example, consider the fossil assemblage shown in Figure 2.2. The PBDB entry is consistent with the original publication, which places the assemblage near Cedaredge, Colorado, on the eastern-most portion of the Book Cliffs and states that it is contained within the "Mancos B" (the Prairie Canyon) Member of the Mancos Shale (*Cole et al.*, 1997). The depositional environment is interpreted as offshore marine based on sedimentary architecture and fossil assemblage (mosasaur, shark teeth, ammonites and bivalves). This interpretation is consistent with that of *Hampson* (2010) who examined the sedimentology of distal portions of the Prairie Canyon Member in western Colorado.

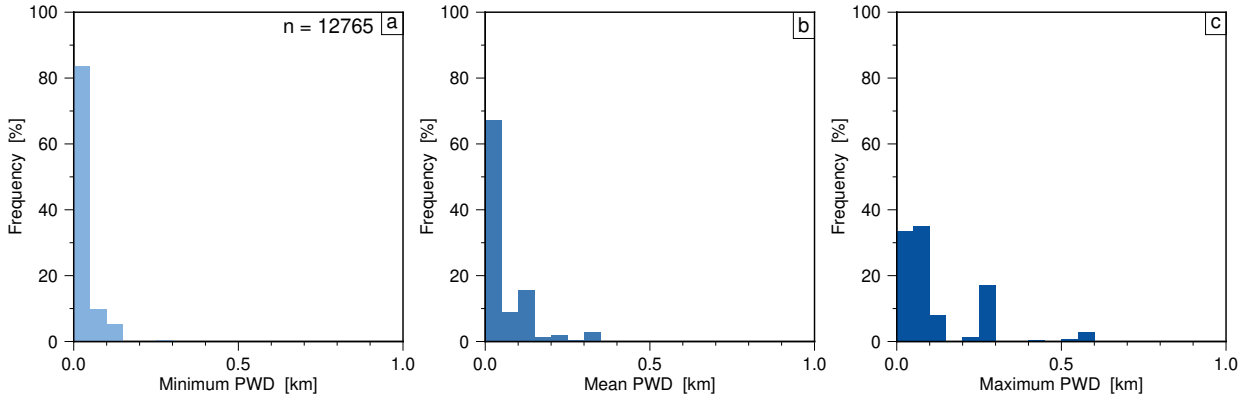

Figure 2.4: **Paleobathymetries for best-constrained samples**. (a) Minimum paleo-water depth (PWD), (b) mean and (c) maximum. These histograms exclude samples with tag 'a' and identified as '*marine indet.*', '*carbonate indet.*' or '*deep-water indet.*'. See body text of main manuscript for discussion of these results.

Using my preferred conversion scheme (Table 2.1) the paleo-water depth range for this assemblage is 150 ± 100 m (see Figure 2.2). In the following sections I examine two other potentially significant sources of error: sea-level and compaction.

2.3.3 Sea-level

Global changes in sea-level are challenging to constrain accurately on geological timescales. Many previous attempts have made use of two techniques. The first is identifying anomalous subsidence patterns from backstripped stratigraphy in regions with supposedly well understood tectonic histories (e.g., rifting and cooling of passive margins; *Watts and Steckler*, 1979). The second correlates stratigraphy from supposedly stable, or well understood, continental margins or interiors (e.g., *Vail et al.*, 1977). *Bessin et al.* (2017) presented a compilation of global sea-level curves produced using a suite of different methodologies (coastal onlap analysis, continental flooding, backstripping, ocean floor age-depth-area and isotope proxies; *Haq et al.*, 1987; *Haq and Al-Qahtani*, 2005; *Scotese and Golonka*, 1992; *Smith et al.*, 1994; *Miller*, 2005; *Kominz et al.*, 2008; *Müller et al.*, 2008; *Miller et al.*, 2011; *Rowley*, 2013). The compilation shows significant discrepancies between estimates of eustasy ($100 - 200$ m for some stages). These discrepancies are not surprising given that many estimates of glacio-eustasy are based on regional datasets in places where the stability (or predictability) of continental vertical motions is assumed. The role of mantle convection and complex hydrodynamic processes in modifying the vertical motions of supposedly stable continents and sea level is generally poorly understood on geological timescales but important (e.g., ocean syphoning: migration of water caused by surface deflections; *Mitrovica and Milne*, 2002; *Moucha et al.*, 2008; *Flament et al.*, 2013;

Austermann et al., 2017). Amplitudes of global sea-level change are estimated to vary by as much as as 200 m, whilst mantle-driven processes can produce changes in vertical motions of similar or greater amplitudes, and comparable timescales (*Miller*, 2005; *Lovell*, 2010). For example, backstripping of stratigraphy along passive margins combined with upper mantle shear wave tomographic models indicate that sub-plate support can generate up to ~ 1 km of uplift or subsidence at $\sim 10 - 10,000$ km wavelengths, on timescales of $1 - 100$ Ma (e.g., *Czarnota et al.*, 2013; *Flament et al.*, 2013; *Lodhia et al.*, 2018).

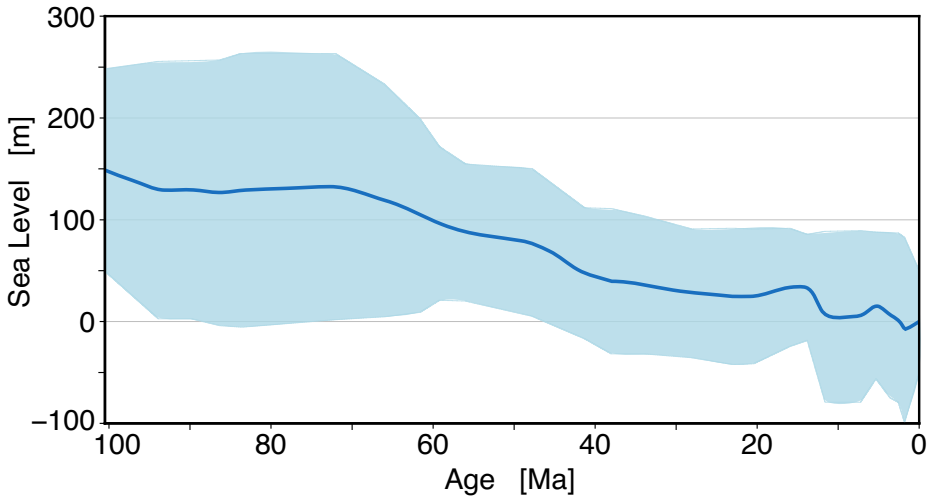

Figure 2.5: **Simplified global sea-level compilation from *Bessin et al.* (2017).** Solid blue curve is mean sea-level, light blue band indicates minimum and maximum values. These curves were used to correct uplift estimates using Equation 1 in the main manuscript.

A pragmatic way to assess the impact of sea-level on calculated uplift is to use the range of values given for each stage in the compilation of *Bessin et al.* (2017). The extrema for each stage are used to define sea-level uncertainties, δS, and uplift is corrected by the mean value. Present-day sea-level is used as the reference frame for all measurements and paleo-sea level uncertainties are between a minimum of -99 m and maximum of $+264$ m over the time period of interest (Figure 2.5).

2.3.4 Compaction correction

Post-deposition compaction of strata means that measurements of net uplift from elevations of fossil assemblages are minima (Figure 2.2). Correcting for compaction is not necessary for sedimentary rock that satisfies two criteria. First, they were deposited directly upon rock that will not compact significantly (e.g., crystalline basement; previously compacted rock). Second, they were not subsequently buried. However, many of the fossil assemblages within the database are contained within stratigraphy from sedimentary basins that accumulated significant stratal thicknesses before and after

their deposition. Therefore a strategy for correcting for compaction is required.

The compaction correction, ΔC, is calculated by decompacting the thickness of underlying sedimentary rock, C_c, by removing overlying rock of thickness D. Porosity is parameterised using the well-known formulation by *Athy* (1930)

$$\phi(z) = \phi_\circ \exp\left(-\frac{z}{\lambda}\right), \tag{2.2}$$

where $\phi_\circ$ and λ are initial porosity and compaction wavelength, respectively, z is depth. Assuming that the solid fraction remains constant during compaction, the decompacted thickness is given by

$$\int_D^{D+C_c} [1-\phi(z)]\mathrm{d}z = \int_0^{C_d} [1-\phi(z)]\mathrm{d}z, \tag{2.3}$$

where D is the amount of denudation, C_c and C_d are compacted and decompacted sedimentary layer thicknesses, respectively. Substitution with Equation 4.1 and solving the integral gives

$$C_d = C_c + \phi_\circ\lambda\left[\exp\left(-\frac{D+C_c}{\lambda}\right) - \exp\left(-\frac{D}{\lambda}\right) + 1 - \exp\left(-\frac{C_d}{\lambda}\right)\right]. \tag{2.4}$$

C_d is solved iteratively for each layer using the Newton-Raphson method. The resulting compaction correction is $\Delta C = C_d - C_c$.

Compaction parameter values can be obtained from well data, for example, from direct measurements of porosity or via indirect means (e.g., the relationship between velocity and porosity; *Wyllie et al.*, 1956). Values of $\phi_\circ$ and λ can range from $0.25 - 0.7$ and $1.4 - 3.7$ km, respectively, in siliciclastic sediments, and $0.4 - 0.8$ and $1.2 - 6.0$ km in carbonates (*Magara*, 1980; *Sclater and Christie*, 1980; *Goldhammer*, 1997). Figure 2.6 shows the expected compaction correction for a plausible range of $\phi_\circ$ and λ. The correction can be significant, exceeding 2.4 km, in regions where initial porosity is high and large thicknesses of sedimentary rock are decompacted. Notwithstanding these constraints, estimates of C_c and D are usually minima because it is usually not possible to constrain how much of the sedimentary pile has been lost by erosion.

Figure 2.7 shows an example of applying a compaction correction to the test case in western North America. This fossil assemblage was deposited within the Piceance basin, which contains thick Cambrian to Pliocene sedimentary rock (*Johnson*, 1992). The stratigraphy consists of predominantly siliciclastic deposits (sandstones and shales; *UUPA Team*, 2003). The exact value of C_c depends on whether all Mesozoic sedimentary rock or only Cretaceous deposits ought to be decompacted

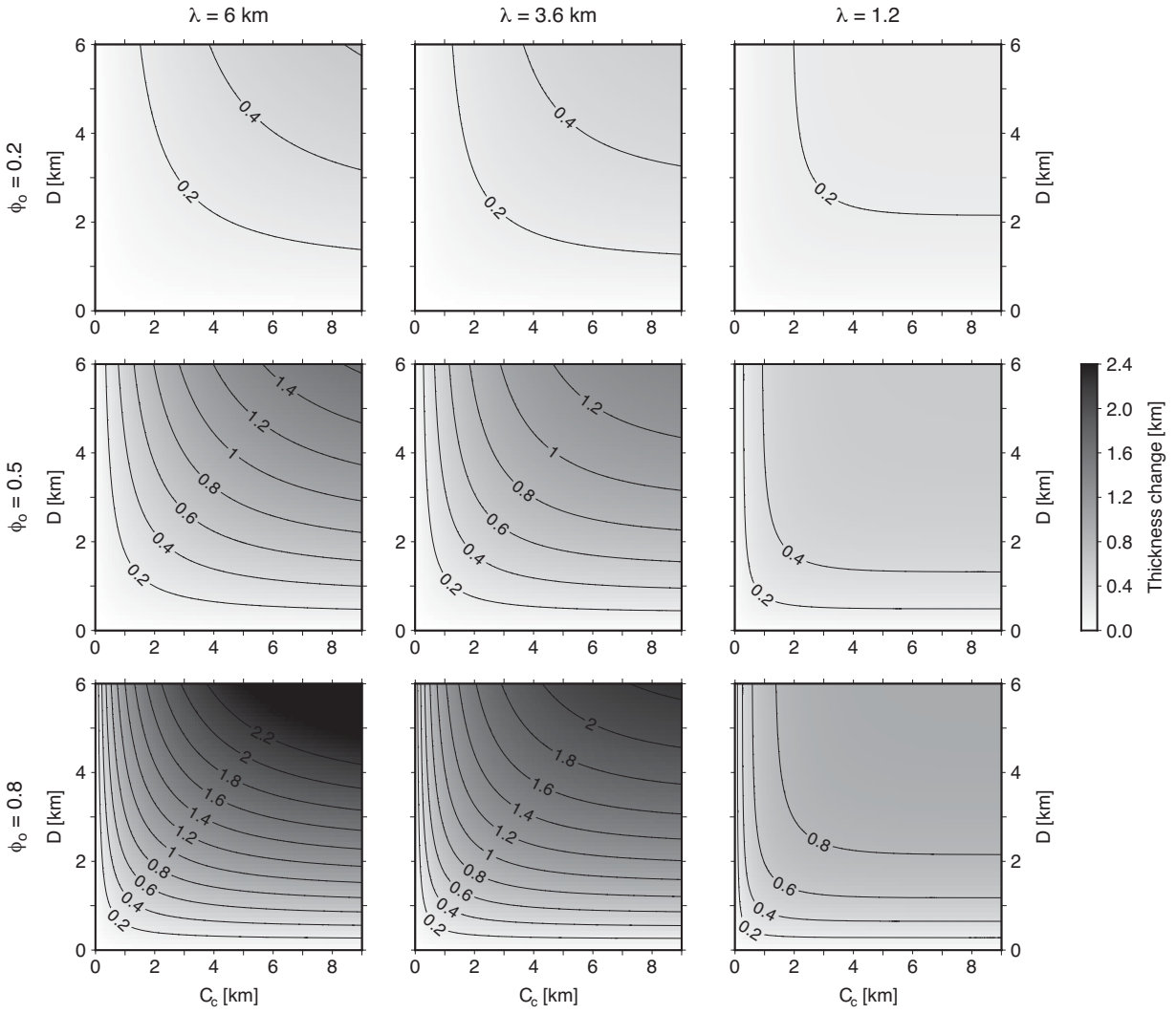

Figure 2.6: **Compaction correction parameter space.** Panels show thickness change between a compacted and decompacted sedimentary rock column as a function of thickness of underlying rock, C_c, and denudation of overlying rock, D, for minimum, mean and maximum values of initial porosity, $\phi_\circ$, and compaction wavelength, λ. Range of $\phi_\circ$ and λ represents extremal values for carbonate and siliciclastic rocks (*Sclater and Christie*, 1980; *Goldhammer*, 1997).

(C_{c_1} = 1.4 km and C_{c_2} = 2.7 km, respectively; Figure 2.7; *Hintze and Kowallis*, 2009). Existence of a regional Lower Cretaceous unconformity throughout the Western Interior Basin suggests Early and Mid-Mesozoic rocks of the western Cordillera were compacted and partly eroded during Sevier orogenesis (e.g., *Bjerrum and Dorsey*, 1995; *Heller and Paola*, 1989). I therefore initially assume that they were not compacted by deposition of Cretaceous to Recent stratigraphy. Instead, I start by assuming that only Cretaceous sedimentary rock was affected by compaction, i.e. C_c = 1.4 km. Thickness of denuded rock, D, can be tentatively estimated from preserved thicknesses of sedimentary rock in adjacent non-eroded sections or neighbouring basins of similar stratigraphy. This correction ought to be applied on a case-by-case basis because lateral changes in facies or structural variations

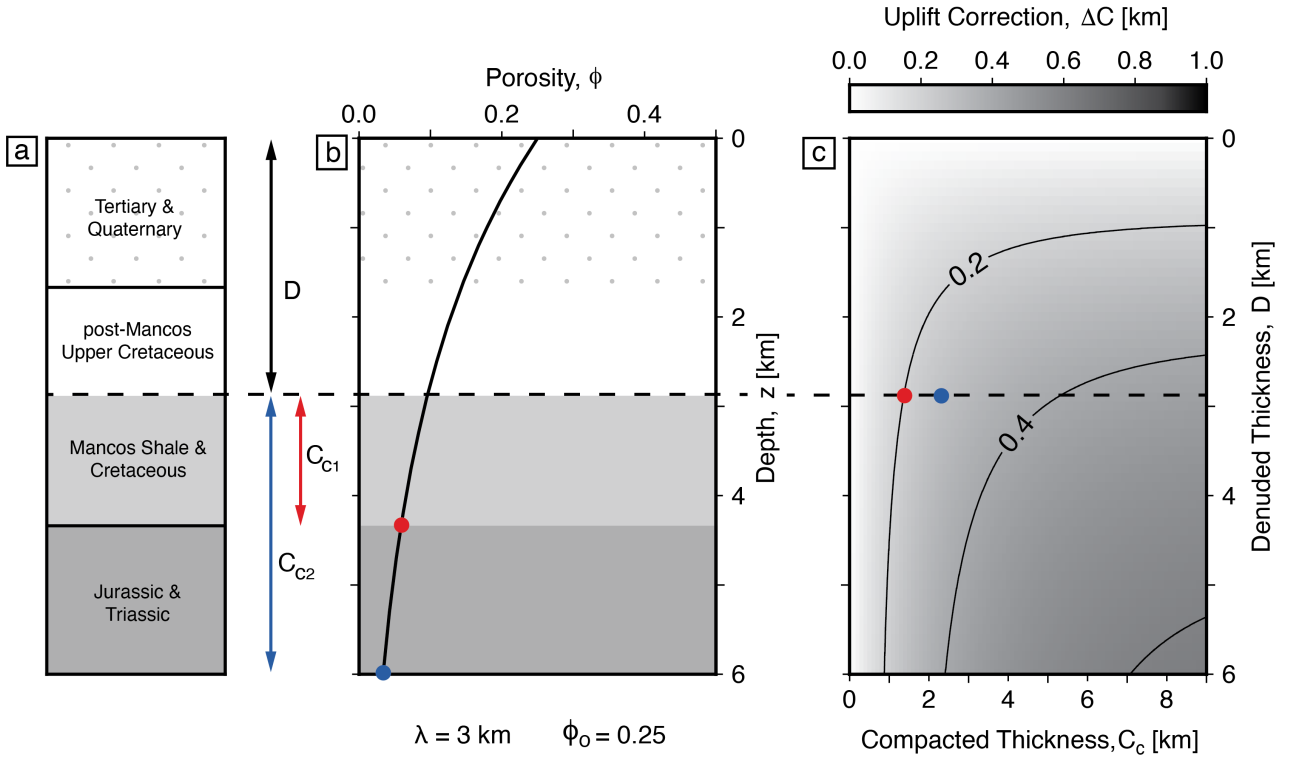

Figure 2.7: **Example compaction correction.** Panels show calculated elevation change from decompacting rock beneath the sample (dashed line), C_c, and denudation of overlying rock, D. (a) Generalised stratigraphy of western North American example (see star in Figures 2.1a & 2.2). C_{c1} is thickness of Cretaceous sedimentary rock beneath Prarie Canyon Member of the Mancos Shale (C_{c1} = 1.4 km), C_{c2} is thickness of Triassic to Cretaceous rock beneath Prarie Canyon Member (C_{c2} = 2.7 km); thicknesses were estimated from composite stratigraphic logs (*Hintze and Kowallis*, 2009). (b) Black curve = porosity-depth function for the Piceance Basin calculated by fitting porosity-depth data from well logs (see Equation 4.1); initial porosity $\phi_\circ = 0.25$, compaction wavelength $\lambda = 3$ km (*Chapman et al.*, 1984). (c) Gray scale and contours show uplift correction, ΔC, following decompaction. For this example decompacting only C_{c1} yields 0.21 km of additional uplift (red circle), and 0.31 km when C_{c2} is decompacted (blue circle).

can affect thickness estimates. D ranges from $0.8-2.9$ km for this example (e.g., *Hintze and Kowallis*, 2009). Published porosity-depth data from wells in the adjacent Uinta Basin, which contain similar stratigraphy, have best-fit values of $\phi_\circ = 0.25$ and $\lambda = 3.0$ km (*Chapman et al.*, 1984). These compaction parameters, combined with the range of values of C_c and D, result in a compaction correction (additional uplift) of $0.08-0.31$ km for the example shown in Figure 2.7.

The analysis presented above shows that compaction of underlying sediments can make a significant difference. But, for simplicity, I have not applied this correction to the full database and explore compaction corrections on a case-by-case basis. I chose this approach for two reasons. First, to constrain C_c a global map of sedimentary thickness on continents would be required. Such maps exist for the oceanic realm, but not for the continents (e.g., GlobSed; Straume et al., 2019). Additionally, as

illustrated in the example above, knowledge of periods of potential overcompaction of the sedimentary pile would be required for an accurate correction. Secondly, determining D for each point in the database is a even harder task. This information is by nature difficult to constrain and not often available for specific basins or depocentres.

2.3.5 Elevation

Locations in the PBDB are typically reported with an accuracy of at least 0.01° (∼ 1 km at the equator). However, present-day elevation of each fossil assemblage is not usually provided. Instead it was extracted from digital elevation data. Elevations were extracted from the ETOPO1 digital elevation model, which has a grid spacing of one arc minute (∼ 1.85 km) and sea-level as the vertical datum (*Amante and Eakins*, 2009). Other datums, such as mean high water, and mean low water,

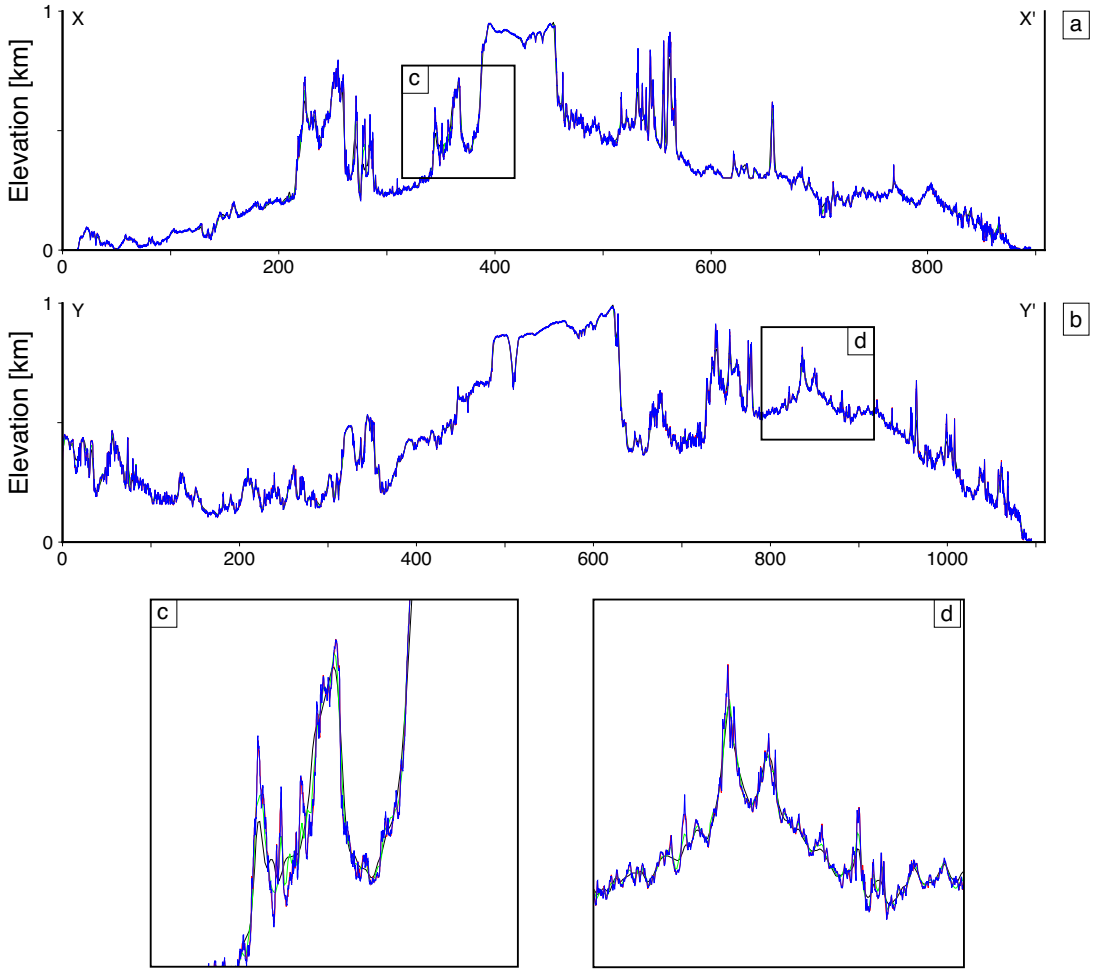

Figure 2.8: **Comparison between different resolution DEMs** for two transects, (a) and (b), within the Borborema Province, NE Brazil. Black curve = ETOPO1; Green curve = SRTM+, Red curve = SRTM 250 m, and Blue curve = SRTM30. (c) and (d) show zoom in of elevation transects for better evaluation.

typically differ by less than the vertical accuracy of ETOPO1, which is of order 10 meters. I note that ETOPO1 was generated using weighted means from the SRTM30 data set (horizontal resolution ~ 30 m) and the GLOBAL digital elevation model, which was used to fill in gaps (*Amante and Eakins*, 2009). Higher resolution digital elevation data (e.g., ASTER, TanDEM-X) could also be used to extract information about elevation. A comparison was made for the elevations along two transects crossing the Borborema Province (Figure 2.8, see Figure 2.1 for location). At the scales of interest, there is very little difference in elevation measured from ETOPO1 and other higher-resolution DEMs. For the PBDB points located in western North America and the Borborema Province, elevations from ETOPO1 differ from SRTM30 by < 60 m, which is significantly less than nearly all paleo-water depth uncertainties (see Figure 2.9). The present-day elevation of the example from western North America is 1.90 km (Figure 2.2).

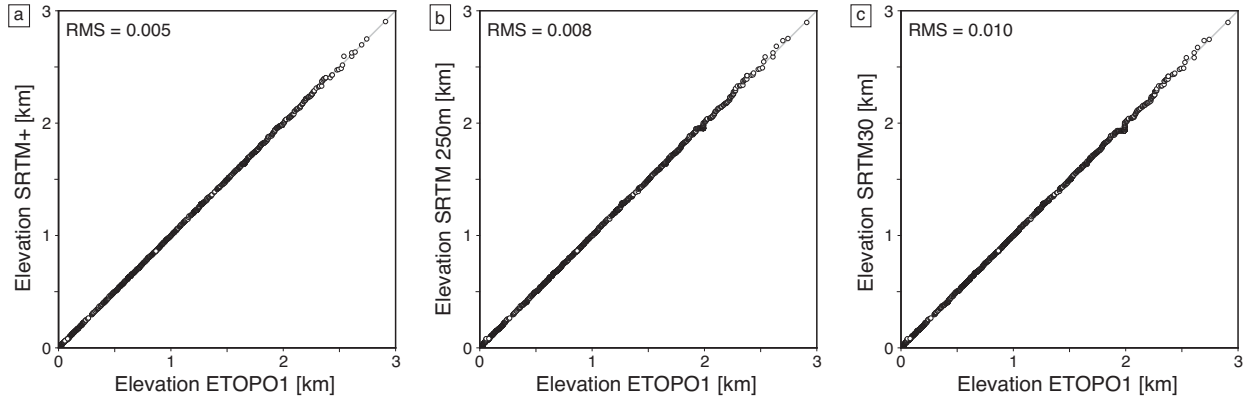

Figure 2.9: **Elevation consistency test.** Comparison of elevations from ETOPO1 and (a) SRTM+, (b) SRTM 250 m, and (c) SRTM30, for all 24,372 points within the database. Grey line = 1:1 relationship. RMS misfit is given for each comparison.

2.4 Global Patterns of Uplift

Figure 2.10 shows the inventory of global uplift measurements calculated by combining present-day elevation, paleo-water depth and sea-level (Equation 1). Compaction corrections were not included for simplicity, as such, Figure 2.10 shows minimum net uplift. The collection of uplift measurements is particularly dense along the coastlines of most continents, as well as in western North America, Europe, Japan and New Zealand. Figure 2.10b–e shows examples of cross sections in places where the density of the inventory is such that uplift at large length scales ($\sim 100 - 1000$ km) can be constrained. For example, a reasonably densely sampled transect can be constructed from northernmost North America to the southern tip of South America (Figure 2.10b). This transect includes the Yukon Plateau, Rocky

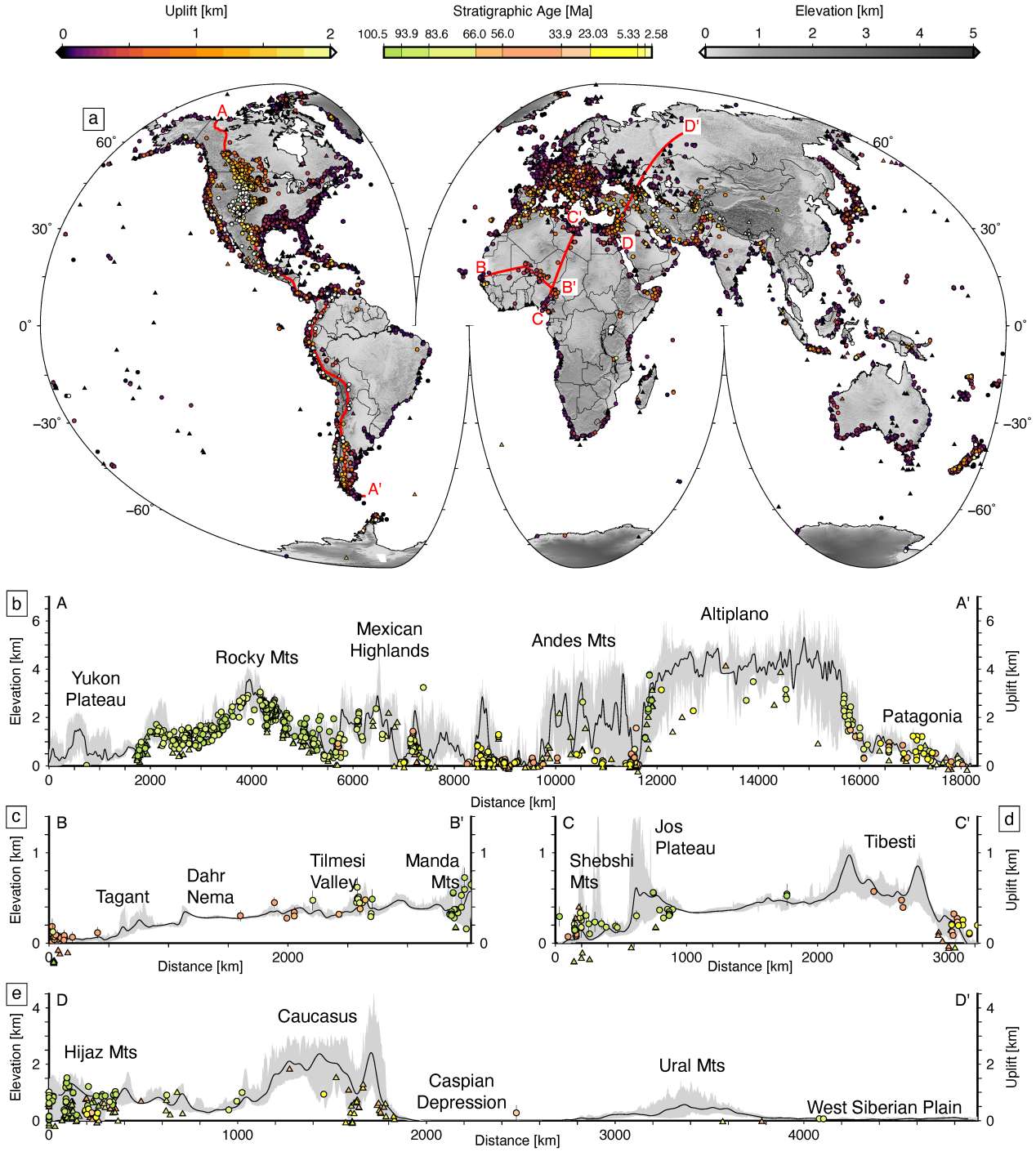

Figure 2.10: **Global measurements of uplift.** (a) Circles = global inventory of uplift measurements generated using the PBDB. Curves labelled A–A′, B–B′, C–C′ and D–D′ are locations of swaths shown in panels (b–e). (b) Circles = uplift constraints within 100 km wide swath through North, Central and Southern America; colours = mean stratigraphic age. Major provinces are labelled. Black curve = topography along centre of transect; grey polygon = extreme topography within swath. (c)/(d)/(e) = Cross sections through northwest Africa/North Africa/Middle East and Eurasia.

Mountains, Mexican Highlands, the Andes, Altiplano, and Patagonia. A prominent feature of this transect is the > 2000 km wide post-Cretaceous domal swell centred on the Colorado Plateau in western North America. Patterns of uplift in the Andes and Altiplano contain shorter wavelength (< 500 km) relatively large, kilometre-scale, changes in net uplift. Transects through the southern Appalachian Mountains, North America, indicate that the topography there has been uplifted and tilted by ∼ 300 m during the last ∼ 40 Ma. These results are a consequence of careful biostratigraphic mapping by *Kirkland* (1996), *Keller et al.* (2002), *Sulser et al.* (2010) and many others. Citations to primary literature for all points are included in the data.

The inventory contains important, albeit sparse, measurements of uplift from within continental interiors. In northwest Africa the distribution of nearshore continental, marginal marine, and open marine fossils record the existence of a Cretaceous–Paleogene trans-Saharan seaway extending from the Gulf of Guinea, across Mali and Nigeria, to the present-day Mediterranean (e.g. *Berggren*, 1974; *Tintant et al.*, 2001; *Tapanila et al.*, 2008; *Boyden*, 2011; *O'Leary et al.*, 2019). Figures 2.10c–d show ∼ 300 m of cumulative uplift across western Africa, and ∼ 600 m of post-Paleocene differential uplift of the Tibesti dome. Figure 2.10e shows 2 km of post-Oligocene uplift of the Caucasus Mountains and uplift measurements atop the Urals and the west Siberian Plain.

In eastern Australia, fossils from the shallow-marine Mackunda Formation, deposited during the final marine regression within the Eromanga basin, show a tilt of ∼ 200 m with a wavelength of ∼ 200 km. These observations complement those generated from correlation and backstripping of well data (*Gallagher and Lambeck*, 1989). Figure 2.10 contains many other examples of useful spot measurements of uplift, especially across South America and Eurasia. I examine two case studies in more detail: Western North America and the Borborema Province, Brazil.

2.4.1 Western North America

Cretaceous flooding of western North America resulted in widespread deposition and preservation of marine rock within the continental interior (Figure 2.11; e.g., *Sloss*, 1963; *Cross and Piliger*, 1978). Extensive exploration in the region has generated a well-constrained and generally accepted chronostratigraphy, as well as a large number of sedimentological and paleoenvironmental studies (*Obradovich and Cobban*, 1975; *Roberts and Kirschbaum*, 1995; *Johnson et al.*, 2002; *Gani et al.*, 2015; *Merewether and McKinney*, 2015). This well documented stratigraphy is reflected in the high density of PBDB points in Western North America.

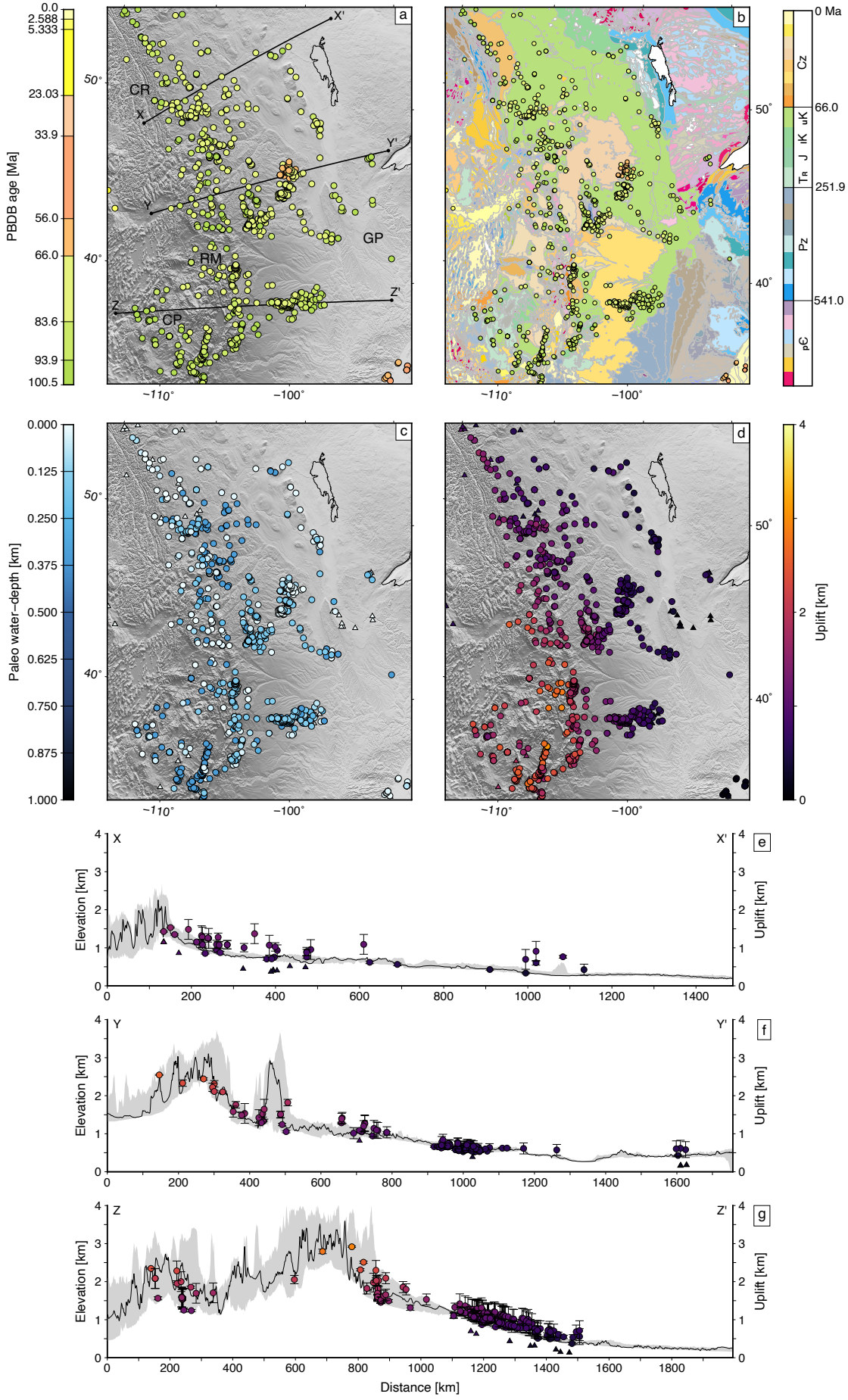
a
b
c
d
e
f
g
X
X'
Y
Y'
Z
Z'
CR
CP
GP
RM
PBDB age [Ma]
0.0
2.588
5.333
23.03
33.9
56.0
66.0
83.6
93.9
100.5
0 Ma
66.0
251.9
541.0
Cz
Mz
Pz
pC
Paleo water−depth [km]
0.000
0.125
0.250
0.375
0.500
0.625
0.750
0.875
1.000
Uplift [km]
50°
40°
−110°
−100°
Elevation [km]
Distance [km]
0
200
400
600
800
1000
1200
1400
1600
1800

Figure 2.11: **Calculated uplift of Western Interior of North America.** (a) Circles = PBDB measurements coloured by mean stratigraphic age; grey scale = hill-shaded topography (ETOPO1). CR = Canadian Rockies, GP = Great Plains, RM = Rocky Mountains, CP = Colorado Plateau. X–X′, Y–Y′, Z–Z′ = cross sections shown in panels (e–g). (b) PBDB measurements atop 1:1M geological map of North America (*Reed et al.*, 2005, see original publication for full key and unit descriptions); pC = PreCambrian, Pz = Paleozoic, Tr/J/lK/uK = Triassic/Jurassic/lower Cretaceous/upper Cretaceous, Cz = Cenozoic. (c) Mean paleobathymetry from PBDB inventory. (d) Mean cumulative uplift since time of deposition from PBDB measurements. (e–g) Cross sections X–X′, Y–Y′, Z–Z′: grey bands = topography within 100 km wide swath of central cross section (black curves); circles/triangles = mean/minimum uplift from measurements within swath; error bars = full range of paleobathymetry uncertainties.

Paleobathymetric estimates from the PBDB broadly agree with independent values. For example, they are consistent with local water-depth maxima estimated using the height of clinoforms (40 m, *Plint et al.*, 2009), planktonic to benthic foraminifera ratios (500 m, *Eicher*, 1969) and numerical simulation of oceanic circulation (100–400 m, *Ericksen and Slingerland*, 1990; *Dean et al.*, 2019). *Arthur and Sageman* (2004) correlated depositional environments, lithofacies and water depths in modern marine settings to infer maximum water depths of 200–300 m across most of the Cretaceous seaway, with local maxima of 1000 m. These values and smoothly varying paleo-water depth estimates indicate that a modern analogue is the Hudson Bay, a large, $\sim$ 1000 km-wide seaway that has an undulated bottom in most parts and a mean water depth of $\sim$ 150 m (GEBCO; *Stewart and Lockhart*, 2006).

The distribution of Cretaceous marine rocks within western North America today defines a domal swell centred on the Colorado Plateau (Figure 2.11d). Maximum uplift along the mountain belt increases to the south, from $\sim$ 1.5 km in the Northern and Canadian Rockies (Figure 2.11e), to $2 - 2.5$ km in the Middle Rockies (Figure 2.11f). The Southern Rocky Mountains and Colorado Plateau are foci of maximum post-Cretaceous net uplift ($2.5 - 3$ km; Figure 2.11g). Towards the east post-Cretaceous uplift decreases to $\sim$ 0.5 km in the Great Plains where easternmost Cretaceous marine rocks are recorded. Previous studies of tilting or epeirogenic vertical motions in this region have made use of reconstructed Cretaceous sedimentary isopachs (*Cross and Piliger*, 1978; *Sahagian*, 1987; *Mitrovica et al.*, 1989). The new PBDB measurements provide additional direct constraints on uplift, including patterns of post-Cretaceous tilting across most of western North America.

These isopach maps can be used to assess the importance of compaction of Cretaceous sediments in affecting calculated uplift (e.g., *Cross and Piliger*, 1978; *Mitrovica et al.*, 1989; *Roberts and Kirschbaum*, 1995). Reconstructed Upper Albian to Santonian isopachs indicate that up to 4 km of sedimentary

rock in foreland basins formed as a result of loading by the Sevier orogen. Foci of thick sedimentary rock are in north-central Utah, southern Wyoming and southeast Idaho. Elsewhere, for example in eastern Colorado, eastern Wyoming, central Montana and New Mexico, mapped thicknesses are less than 500 m. Campanian to Maastrichtian isopachs record a different pattern of sedimentation. The thickest isopachs ($2-3$ km) are centred on eastern Wyoming and western Colorado. Thicknesses of less than 500 m are mapped eastwards of central North Dakota, South Dakota, Nebraska and Kansas. These observations suggest that the maximum sediment thickness that could have been compacted, C_c, is ~ 6 km (in northeast Utah/southeast Wyoming), decreasing to zero towards the easternmost extent of the basin (e.g., eastern Minnesota).

Maximum denudation, D, can be approximated using the thickness of Cenozoic sedimentary rock preserved within the Laramide intermontane basins (e.g., *Hintze and Kowallis*, 2009). For example, the Uinta Basin, Utah, contains up to 5.9 km of post-Cretaceous sedimentary rock, which I regard as a conservative (maximum) estimate of the amount of material denuded from other parts of western North America. Apatite fission track analyses of Late Cretaceous sedimentary rock, from outcrops within the Rocky Mountains, provide further evidence of $\sim 4-6$ km of denudation since the deposition of Cretaceous marine rock (e.g., *Herman et al.*, 2013). By taking into account the range of possible $\phi_\circ$ and λ values the compaction correction is a maximum of $0.24-2.5$ km centred on the Southern Rocky Mountains. For easternmost points, which sit directly above basement, their compaction correction is zero (*Dyman et al.*, 1994). Assuming an average $\phi_\circ = 0.5$ and $\lambda = 3.6$ km the compaction correction would amplify the differential rock uplift between the Great Plains and Southern Rocky Mountains by ~ 1.3 km.

2.4.2 Borborema Province, northeast Brazil

The second example is from northeastern Brazil, which includes the Borborema Province and Cretaceous rift basins. This region was chosen because the broad, domal shape of the regional topography suggests mantle convective processes might be controlling the shape of the landscape. Figure 2.12 shows the spatial and temporal distribution of PBDB points, interpreted paleo-water depths and calculated uplift for the region. The broad domal swell of the region, with a diameter of $900-1000$ km and amplitude of 900 m, is illustrated in the cross-sections shown (Figure 2.12e-f). Calculated post-Aptian net uplift is > 700 m.

The key constraint on large-scale uplift of this region is the presence of late Aptian-Cenomanian

shallow marine deposits of the Romulado Formation at $700-900$ m elevation within the Araripe basin (Figure 2.12a). A fossil assemblage from this deposit is recorded in the PBDB and geologic mapping shows that this unit crops out as a thin band close to the top of the Araripe Plateau (Figure 2.12a). The Romulado Formation, which is part of the Santana Group, forms a $3-5$ m thick, shallowly dipping, black shale that is well known for excellent fossil preservation (e.g., *Martill*, 1988). Marine microfossils recovered in the well 2-AP-1-CE (dinoflagellate cysts, ostracodes and foraminifera), and a fossil-bearing layer towards the top of the formation containing Cretaceous gastropods, bivalves and echinoderms provides evidence of lagoonal and estuarine environments during a Cretaceous marine transgression (*Arai and Coimbra*, 1990; *Coimbra et al.*, 2002; *Prado et al.*, 2016; *Pereira et al.*, 2016). Sedimentological evidence for marine depositional environments, including tide-dominated coastal facies and storm-dominated shelf sedimentation, further attests to the marine origin of the Romulado Formation (*Custódio et al.*, 2017). Absence of marine sediments in the Lower Cretaceous rift basins located in between the Araripe and Potiguar basins (e.g., Rio do Peixe, Icó, Lima Campos, Iguatu and Lavras da Mangabeira basins) suggests that this portion of the continental interior might not have been inundated by marine waters in the Cretaceous Period (*Arai*, 2009). Paleoflow measurements of fluvial deposits below and above the Santana Formation in the Araripe and Tucano-Jatobá basins, the Marizal and Exu Formation, respectively, show a change from the southeast to west-southwest directions, indicating a redirection of regional drainage towards the Parnaíba Basin likely caused by regional uplift and tilting (*Assine*, 1994; *Freitas et al.*, 2017). These data suggest incipient uplift soon after the deposition of the marine units.

Aptian to Cenomanian shallow marine fossil-bearing outcrops occur at lower elevations in the onshore portions of the Atlantic rift basins (Potiguar, Pernambuco-Paraíba, Sergipe-Alagoas). Within the Potiguar Basin, shallow marine sedimentation in lagoonal, estuarine and reefal environments is recorded by the deposition of the Jandaíra Formation ($92-91$ Ma), which crops out extensively throughout the onshore portion of the basin (*Pessoa Neto et al.*, 2007; *Garcia et al.*, 2014). Additional regional paleobathymetric constraints are provided by marine stratigraphy to the west. Strontium isotope ratios, organic biomarkers and fossil assemblages indicate that the Albian Codó Formation of the Parnaíba Basin was deposited under marine conditions (*Rodrigues*, 1995; *Antonioli et al.*, 1999, Figure 2.12a).

Evidence of Cenozoic vertical motions along the modern coastal margins of this region comes from the Pirabas and Barreiras Formations (*Rossetti et al.*, 2013, Figure 2.12a, yellow polygons). The Pirabas Formation is a fossil-rich marine carbonate-siliciclastic deposit which crops out along Brazil's

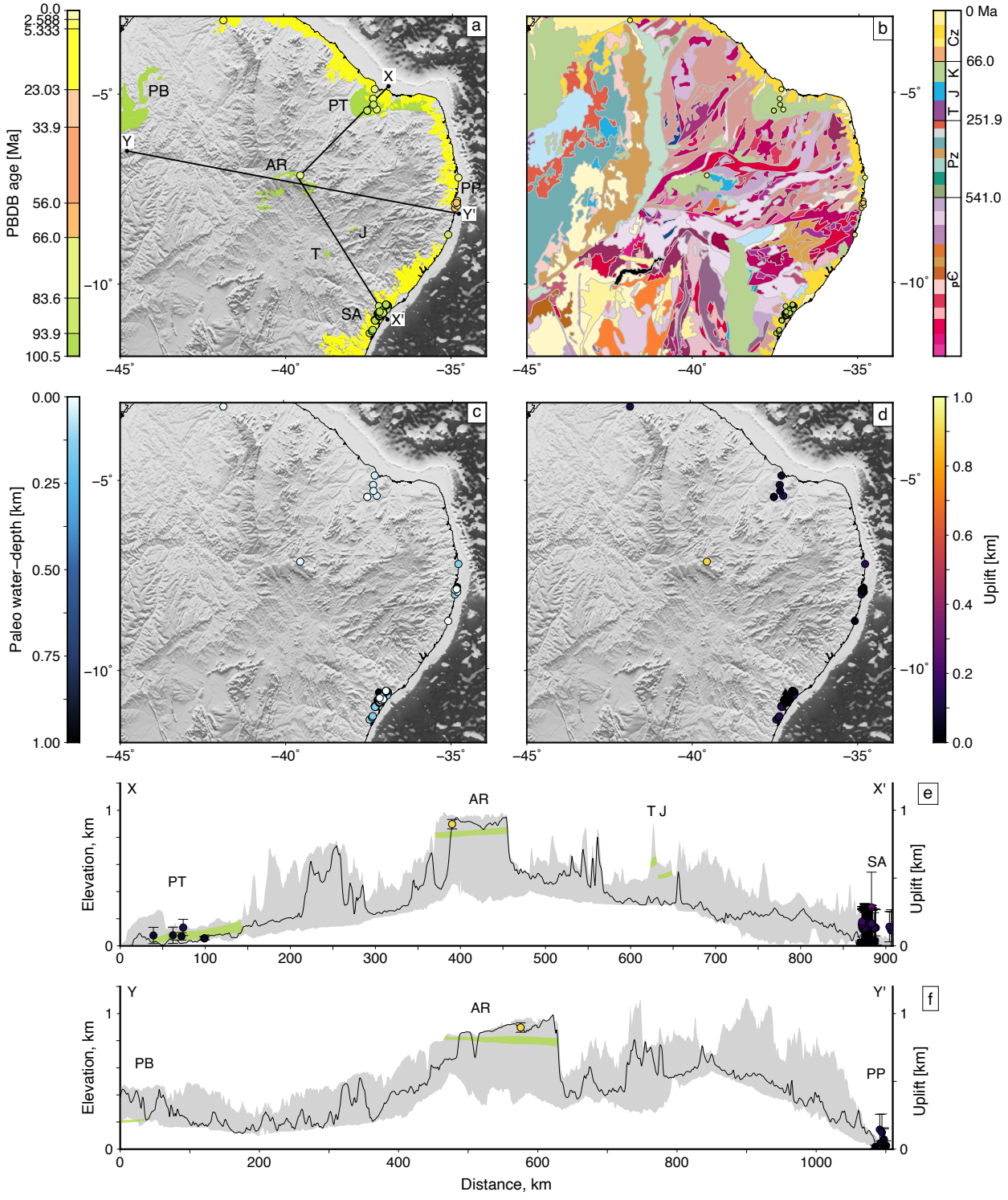

Figure 2.12: **Uplift of the Borborema Plateau, NE Brazil.** (a) PBDB measurements coloured by mean stratigraphic age atop hill-shaded topography (ETOPO1); AR = Araripe Plateau, PT = Potiguar, PP = Pernambuco-Paraíba, SA = Sergipe-Alagoas, T = Tucano, J = Jatobá, PB = Parnaíba basins. Green polygons show location of outcropping marine Santana Formation within the Araripe and Tucano-Jatobá basins (*Custódio et al.*, 2017). Yellow polygons = Miocene aged marine Pirabas and Barreiras Formations (*Rossetti et al.*, 2013). Cross sections X–X′ and Y–Y′ are shown in panels (e–f). (b) 1:5M geological map (*Gómez et al.*, 2019). (c–d) Paleobathymetry and mean post-deposition uplift from PBDB measurements. (e–f) Cross sections X–X′ and Y–Y′: Topography from ETOPO1 along cross sections (black curves) and within 100 km wide swaths (grey band); coloured circles with error bars = measurements of mean uplift and paleobathymetric uncertainties within the swaths. Green bands show elevation of (Cretaceous, marine) Santana, Codó and Jandaíra Formations projected onto cross section.

equatorial margin. Foraminifera and pollen biostratigraphy date it as late Oligocene-early Miocene in age. Sedimentological and paleontological evidence suggests the unit was deposited in a shallow inner shelf, lagoonal, shoreface, foreshore and marginal marine environment. The Barreiras Formation overlies the Pirabas Formation, and is predominantly a siliciclastic deposit that is exposed in a $\sim$ 100 km-wide band along the northeastern coast of Brazil. Mostly afossiliferous, chronostratigraphic constraints based on pollen and (U-Th)/He-dated overlying laterites constrain the age as early-middle Miocene, with an upper age limit of 16.45 Ma (*Rossetti et al.*, 2013). Although previously interpreted as a continental fluvial-alluvial deposit, sedimentological evidence of widespread bidirectional flow, mud drapes, reactivation surfaces, rhythmites and ichnofossils suggests a tidally influenced estuarine paleoenvironment (e.g., *Rossetti and Santos Jr.*, 2004). The variable present-day elevation of the Pirabas and Barreiras Formations, from $\sim$ 20 m above sea level in the equatorial and southern regions up to $\sim$ 150 m in easternmost regions, indicates post-depositional upwarping of this paleo-surface since the mid-Miocene (*Rodríguez Tribaldos et al.*, 2017).

Within the Potiguar Basin, an angular unconformity of Aptian-Albian age ($\sim$ 110 Ma) suggests that only post-rift sediments were significantly compacted by Cretaceous to Recent sedimentation (*Pessoa Neto et al.*, 2007). The thickness of Cretaceous sediments (C_c) onshore is at most $\sim$ 2.2 km and post-Cretaceous deposits (D) are $\sim$ 1 km thick (*Ojeda*, 1983). If I assume that $\phi_\circ = 0.5$ and $\lambda = 3.6$ km (i.e. mean values for carbonates and clastics) the compaction correction (ΔC) is 267 m. This value is conservative as the largest thicknesses are confined to localised depressions. A similar exercise can be performed for other Atlantic rift basins. For example, the maximum value of ΔC in the Pernambuco-Paraíba Basin is 9 m (for $C_c = 397$ m, $D = 95$ m; *Barbosa et al.*, 2007), and in the Sergipe-Alagoas Basin it is 234 m (for $C_c = 1000$ m, $D = 1500$ m; *Campos Neto*, 2007; *Ojeda*, 1983). For the onshore Araripe Basin, thickness of Cretaceous stratigraphy beneath the Santana Formation is $\sim$ 500 m, and 30–350 m of post-Santana sedimentary rock caps the Araripe plateau (*Assine*, 1994, 2007). Assuming that no additional sediments were deposited above the plateau (*Peulvast and Bétard*, 2015), ΔC ranges from 4–38 m. These maximal compaction corrections are not included in Figure 2.12d for simplicity.

Additional constraints on uplift and denudation in the region include the non-fossiliferous, terrestrial siliciclastic deposits of the Serra dos Martins Formation (*Morais Neto et al.*, 2009; *Oliveira and Medeiros*, 2012), which are found atop many high mesas in the northern Borborema Plateau. Ages of detrital Apatite and Zircon within these fluvial sedimentary rocks have calculated ages that suggest sedimentary deposition cannot be older than Paleogene (*Morais Neto et al.*, 2009). These results indi-

cate that the region was sub-aerialy exposed by Paleogene times. Cenozoic basalt flows crop out atop mesas within the central and northern parts of the province, $^{39}Ar/^{40}Ar$ dating of some flows indicates that they have a minimum age of $\sim$ 25 Ma, which has been suggested to record Paleogene to Recent mantle-drive uplift (*Menezes et al.*, 2003; *Jardim de Sá et al.*, 2005). These data have been interpreted as a record of Paleogene to Recent uplift. Vitrinite reflectance data, thermal maturity analysis and overcompacted sedimentary rock from the Recôncavo-Tucano-Jatobá basins in the southeastern part of the province suggest at least 1750 m of rock has been eroded since Cretaceous times (Figure 2.12; *Magnavita et al.*, 1994).

2.4.3 Summary

Measurements of net uplift using the PBDB show that the North American western interior has experienced large-scale, domal uplift since the Late Cretaceous. The pattern of uplift is characterised by $\sim$ 2.5 km, or up to 4 km if compaction corrections are considered, of differential uplift of the Rocky Mountains with respect to the Great Plains. Additionally, along the spine of the Rocky Mountains, uplift increases from north to south, with maximum uplift within the Colorado Plateau. In the Borborema Province, the presence of low-elevation shallow marine deposits at the coast, cropping out in the onshore portions of the Potiguar, Sergipe-Alagoas and Pernambuco-Paraíba basins, and high elevation very shallow marine beds in the Araprie Plateau show evidence for large-scale domal uplift for the region since the Late Cretaceous. In both cases, mechanisms invoked to explain the uplift of these regions must be able to explain differential uplift of 700 m to 4 km of differential uplift on wavelengths of $\sim$ 1000 km.

2.5 Discussion

In the previous section, results from western North America, where the inventory is relatively dense, and the Borborema Province where recorded fossil assemblages are more sparse, were examined. In this section I explore how such uplift measurements can be used to generate useful geologic insight. Here the uplift measurements are combined with simple calibrated isostatic calculations to constrain origins of topography. To do so, I use seismological observations from the USArray experiment and a recent deployment of broadband seismometers in the Borborema province (e.g., *Luz et al.*, 2015a,b; *Buehler and Shearer*, 2016). This simple approach assumes that flexural rigidity of the lithosphere is sufficiently low such that uplift at wavelengths $\gtrsim$ 100 km is broadly isostatic. This assumption is

probably reasonable for western North America and Borborema where the relationship (admittance) between free-air gravity and topography in the frequency domain indicate elastic thicknesses, T_e, of 12 ± 2 km and 3 km, respectively (*Stephenson et al.*, 2014; *Rodríguez Tribaldos et al.*, 2017). Admittance calculated using spherical wavelets indicate similarly low ($\lesssim 20$ km) values of T_e for these regions (*Audet*, 2014). I acknowledge that other approaches can be used and suggest that the inventory could be helpful in assessing predictions from, for example, geodynamic models of mantle convection (e.g., *Flament et al.*, 2013).

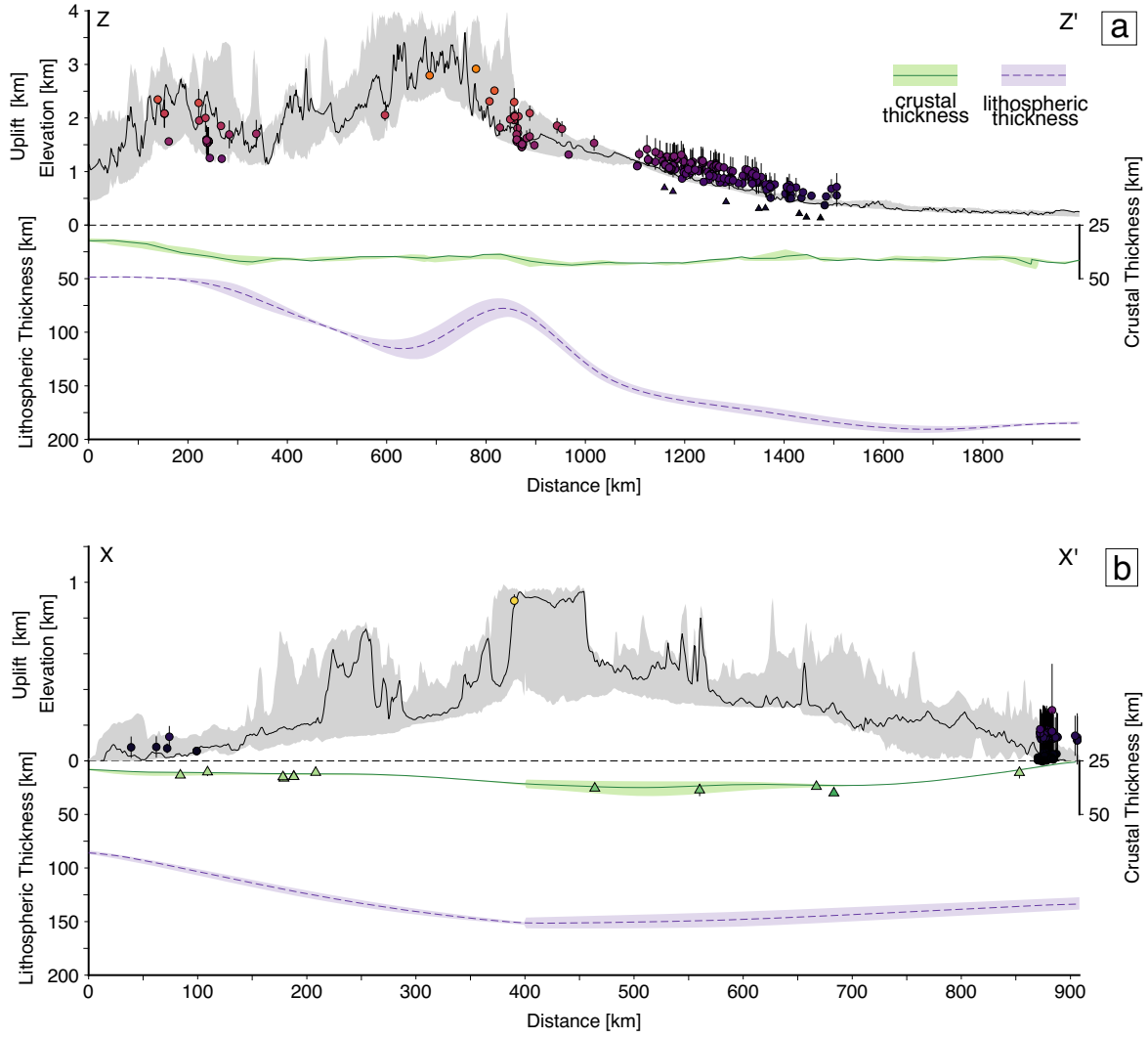

Figure 2.13: **Cross sections through uplift and geophysical measurements.** (a) Cross section through western North America (see Figure 2.11: Z–Z′; colour scale) showing crustal thickness from *Pn*-wave tomography and lithospheric thickness generated by converting a shear wave tomographic model into temperature (*Priestley and McKenzie*, 2013; *Buehler and Shearer*, 2016). (b) Cross section across Borborema province (see Figure 2.12: X–X′; colour scale) showing crustal thickness from CRUST1.0 and Moho depths from H-κ stacks of P-to-S receiver functions (triangles) and lithospheric thickness (*Laske et al.*, 2013; *Luz et al.*, 2015a).

2.5.1 Isostatic considerations

Correlations between elevation and crustal thicknesses in western North America and the Borborema province are weak (Figure 2.13; *Roberts et al.*, 2012a; *Rodríguez Tribaldos et al.*, 2017). Instead, the three primary candidates for generating support of topography (and uplift) are modification to the density and thickness of the lithosphere, or the convecting mantle. Following the approach of *McNab et al.* (2018) and *Klöcking et al.* (2018a), I explore the effects of lithospheric thinning, depletion and excess asthenospheric mantle temperature on the expected elevation of continents. I outline the governing equations below.

Calculation of isostatic elevation change

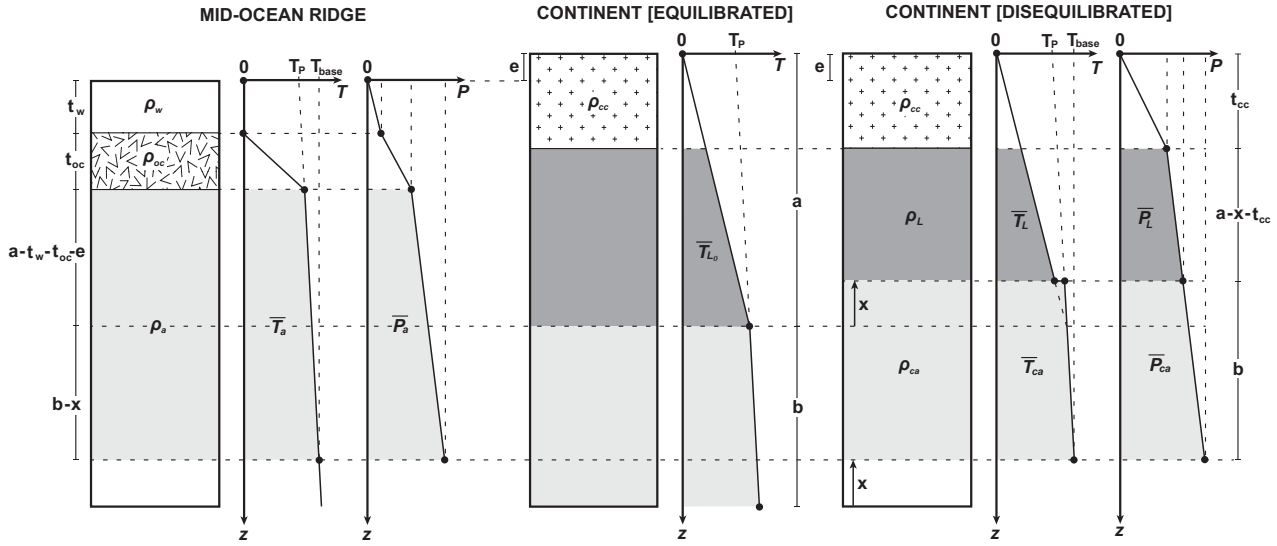

Figure 2.14: **Schematic illustrating lithospheric and asthenospheric columns used for isostatic calculations.** T, P, ρ, z refer to temperatures, pressures, densities and depths, respectively. Symbols, parameter values and units are defined in Table 2.4.

Assuming isostasy prevails (i.e. flexural effects are minimal and viscous stresses related to deeper mantle flow can be neglected), the expected elevation, e, of a column of lithospheric material and associated asthenospheric mantle with respect to the depth of a standard mid-ocean ridge is given by

$$e = t_{cc}\left(\frac{\rho_L - \rho_{cc}}{\rho_a}\right) - t_w\left(\frac{\rho_a - \rho_w}{\rho_a}\right) - t_{oc}\left(\frac{\rho_a - \rho_{oc}}{\rho_a}\right) + (a - x)\left(\frac{\rho_a - \rho_L}{\rho_a}\right) + b\left(\frac{\rho_a - \rho_{ca}}{\rho_a}\right) \quad (2.5)$$

where t_w and ρ_w are the mean depth and density of water at a mid-ocean ridge, and t_{oc} and ρ_{oc} are the mean thickness and density of oceanic crust, respectively. t_{cc} is variable thickness of continental crust (30–40 km), ρ_{cc} is density of continental crust. a is lithospheric thickness, b is thickness of astheno-

spheric mantle that contributes to uplift and x is the thickness of lithospheric mantle removed. ρ_a and ρ_{ca} are densities of asthenospheric mantle beneath mid-ocean ridge and continent respectively, ρ_L is density of lithospheric mantle. I assume that e is small compared to a. The density of asthenospheric mantle beneath a mid-ocean ridge, ρ_a, is estimated by accounting for its temperature dependence. Assuming a linear adiabatic temperature gradient and accounting for compressibility I obtain

$$\rho_a = \rho_\circ \left(1 - \alpha\overline{T_a} + \frac{\overline{P_a}}{K}\right) \tag{2.6}$$

where the average temperature of oceanic asthenosphere, $\overline{T_a}$, is given b

$$\overline{T_a} = T_{base} - \frac{1}{2}\frac{\mathrm{d}T}{\mathrm{d}z}(a - t_w - t_{oc} + b - x) \tag{2.7}$$

and the temperature at the base of the column, T_{base}, is given by

$$T_{base} = T_P + (a + b - x)\frac{\mathrm{d}T}{\mathrm{d}z}. \tag{2.8}$$

The average lithostatic pressure of oceanic asthenosphere, $\overline{P_a}$, is given by

$$\overline{P_a} = \frac{g(\rho_w t_w + \rho_{oc} t_{oc})}{1000} + \frac{1}{2}\frac{\mathrm{d}P}{\mathrm{d}z}(a - t_w - t_{oc} + b - x). \tag{2.9}$$

Instantaneous removal of the base of continental lithosphere leaves the remaining portion thermally disequilibrated. When nothing has been removed (i.e. $x = 0$), the lithosphere is assumed to be thermally equilibrated (i.e. a steady-state geotherm, $\partial^2 T/\partial z^2 = 0$). By assuming a linear geotherm from the surface ($T = 0°\mathrm{C}$) to the base of the lithosphere and by accounting for the effects of mantle depletion and compressibility, I estimate the density of the continental lithospheric mantle, ρ_l, to be

$$\rho_L = (\rho_\circ - \Delta\rho_d)\left(1 - \alpha\overline{T_L} + \frac{\overline{P_L}}{K}\right) \tag{2.10}$$

where $\Delta\rho_d$ is the density difference between normal and depleted lithospheric mantle, and the average pressure in the continental lithospheric mantle, $\overline{P_L}$, is given by

$$\overline{P_L} = \frac{g t_{cc}\rho_{cc}}{1000} + \frac{1}{2}\frac{\mathrm{d}P}{\mathrm{d}z}(a - x - t_{cc}). \tag{2.11}$$

The average temperature of continental lithospheric mantle, $\overline{T_L}$, is given by

$$\overline{T_L} = \frac{T_{L_\circ}}{2a}(a - x + t_{cc}) \tag{2.12}$$

and T_{L_0} is the temperature at the base of unthinned continental lithosphere, given by

$$T_{L_\circ} = T_P + a\left(\frac{\mathrm{d}T}{\mathrm{d}z}\right). \tag{2.13}$$

I also consider the effects of emplacing anomalously hot asthenospheric mantle of thickness b beneath continental lithosphere. For an excess temperature of ΔT, the asthenospheric mantle beneath the continent has a density of

$$\rho_{ca} = \rho_\circ\left(1 - \alpha(\overline{T_{ca}} + \Delta T) + \frac{\overline{P_{ca}}}{K}\right) \tag{2.14}$$

where the mean temperature of unheated continental asthenosphere, $\overline{T_{ca}}$, is given by

$$\overline{T_{ca}} = T_P + \left(a - x + \frac{b}{2}\right)\frac{\mathrm{d}T}{\mathrm{d}z} \tag{2.15}$$

and the average pressure of the asthenosphere, $\overline{P_{ca}}$, is given by

$$\overline{P_{ca}} = \frac{g\rho_{cc}t_{cc}}{1000} + \frac{\mathrm{d}P}{\mathrm{d}z}\left(a - x - t_{cc} + \frac{b}{2}\right). \tag{2.16}$$

Individual values used for each parameter is listed in Table 2.4.

I start by assuming lithospheric thinning is instantaneous such that the geotherm has not reached steady state. My rationale is that most of the measurements considered indicate that uplift occurred on timescales shorter than lithospheric thermal time constants (e.g., $\tau = a^2/\pi^2\kappa$; $\tau \approx 130$ Ma for $a = 200$ km, and $\tau \approx 80$ Ma for $a = 50$ km, where $\kappa = 10^{-6}$ m^2 /s). Figure 2.15a, b, and c shows how elevation, e, varies by changing ρ_L, a, and ΔT, respectively, for different crustal thicknesses, t_{cc}. Both changes in ρ_L and ΔT result in a linear increase in elevation, while thinning the lithosphere leads to a non-linear response of the elevation. These three parameters trade off against each other, and these are shown in Figure 2.15d, e, and f for $t_{cc} = 40$ km, and 2.15g, h, and i for $t_{cc} = 30$ km. It is important to note that a ~ 1 km change in crustal thickness results in a ~ 200 m change in elevation. These trade-off plots will be used to explore possible mechanisms that can generate the net uplift calculated from the PBDB.

Table 2.4: Parameters used in isostatic calculations

	Parameter	Symbol	Value	Units
Mid-ocean Ridge	Ridge depth	t_w	2.8	km
	Oceanic crust thickness	t_{oc}	7.1	km
	Water density	ρ_w	1.0	Mg m^{-3}
	Oceanic crust density	ρ_{oc}	2.86	Mg m^{-3}
	Oceanic asthenosphere density	ρ_a		Mg m^{-3}
	Oceanic asthenosphere average temperature	$\overline{T_a}$		°C
	Oceanic asthenosphere average pressure	$\overline{P_a}$		GPa
Continent	Elevation above sea-level	e		km
	Continental crust thickness	t_{cc}		km
	Original continental lithosphere thickness	a		km
	Removed lithospheric mantle thickness	x		km
	Thickness of hot asthenosphere	b	200	km
	Continental crust density	ρ_{cc}	2.75	Mg m^{-3}
	Continental lithospheric mantle density	ρ_L		Mg m^{-3}
	Lithospheric mantle depletion density	ρ_d		Mg m^{-3}
	Continental lithosphere average temperature	$\overline{T_L}$		°C
	Temperature at base of equilibrated lithosphere	$T_{L_\circ}$		°C
	Continental asthenosphere average temperature	$\overline{T_{ca}}$		°C
	Asthenospheric mantle temperature anomaly	ΔT		^{o}C
	Lithospheric mantle average pressure	$\overline{P_L}$		GPa
	Continental asthenosphere average pressure	$\overline{P_{ca}}$		GPa
General	Reference mantle density	$\rho_\circ$	3.33	Mg m^{-3}
	Mantle adiabatic temperature gradient	dT/dz	0.44	°C km^{-1}
	Mantle thermal expansion coefficient	α	3.3×10^{-5}	°C^{-1}
	Potential temperature of ambient mantle	T_P	1320	°C
	Temperature at base of column	T_{base}		°C
	Mantle pressure gradient	dP/dz	0.033	GPa km^{-1}
	Bulk Modulus	K	115.2	GPa
	Gravitational acceleration	g	9.8	m s^{-1}

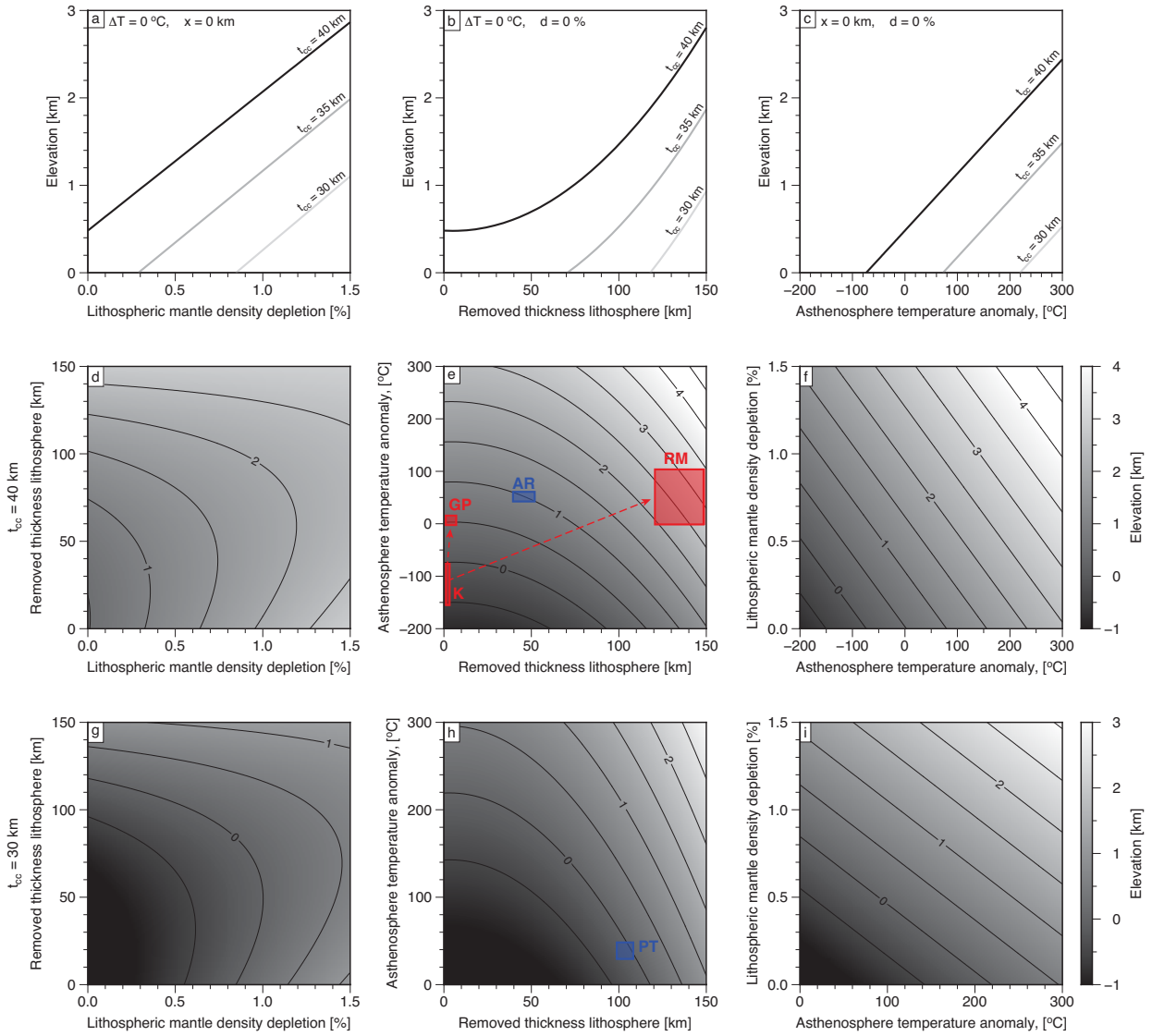

Figure 2.15: **Parameterisation of isostatic calculations.** Top row shows predicted elevation as a function of crustal thickness, t_{cc}, and (a) % depletion, d, (density) of lithospheric mantle; (b) removed thickness of lithospheric mantle, x; (c) asthenospheric temperature anomalies, ΔT. Middle row: Gray scale and contours show calculated elevations for a crustal thickness of 40 km and (d) depletion and thinning of the lithosphere, (e) lithospheric thinning and asthenospheric temperature anomalies, and (f) asthenospheric temperature anomalies and mantle depletion. (g)-(i) Predicted elevations for a crustal thickness of 30 km. Labelled boxes indicate estimates of support for Cretaceous western interior of North America (K), Great Plains (GP), Araripe Plateau (AR), Rocky Mountains (RM) and Potiguar Basin (PT).

Alternatively, it is straightforward to perform the same isostatic calculations assuming a state-state, equilbrated, geotherm (i.e. the lithospheric geotherm is thermally equilibrated as the base of the lithosphere is removed) by modifying the term for $\mathrm{d}T/\mathrm{d}z$. The most significant difference between the equilibrated and non-equilibrated geotherm assumptions is in the non-linearity of the elevation response to thinning the lithosphere, shown in Figure 2.16a and b. Figures 2.16c, d, e and f compare

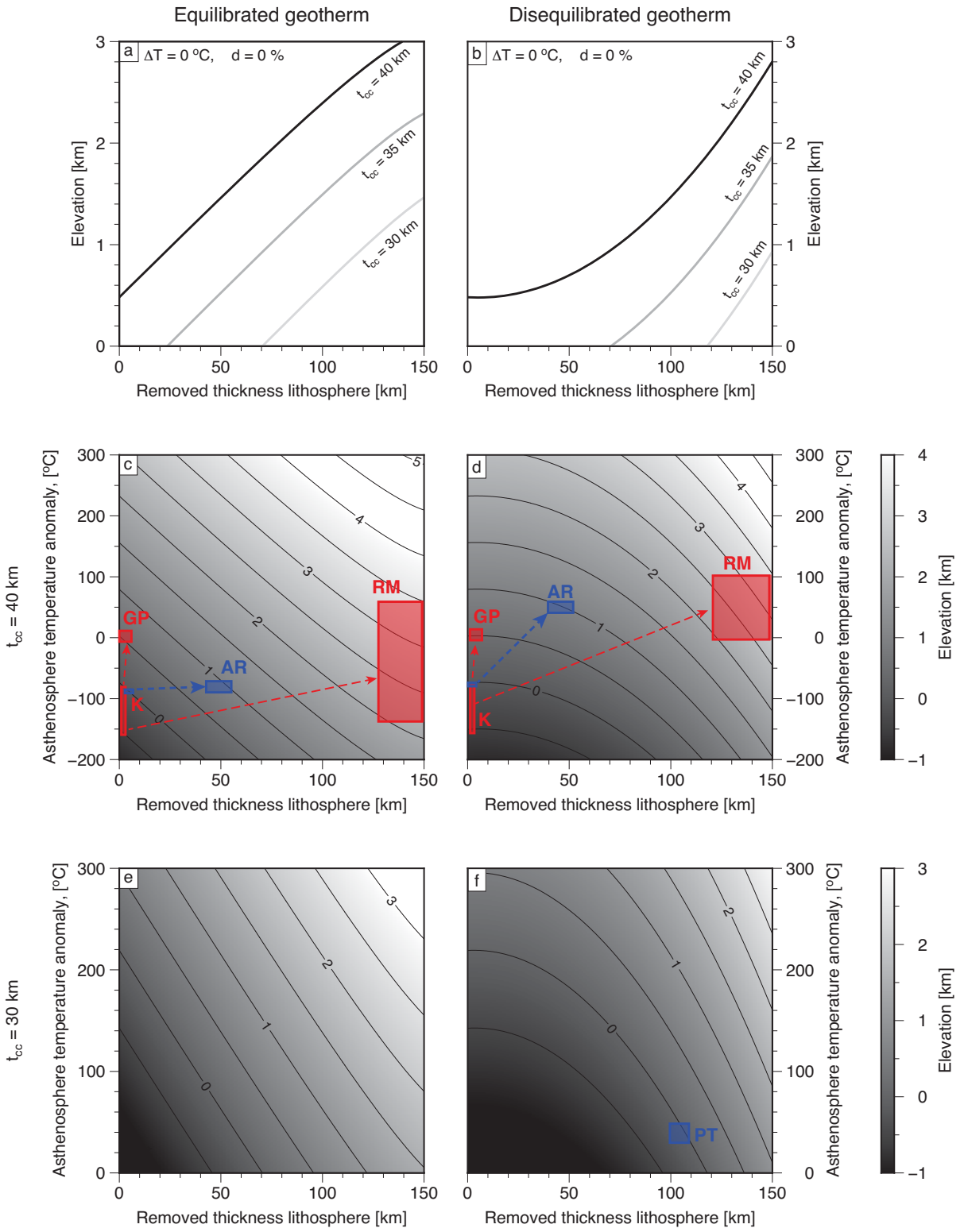

Figure 2.16: **Comparison of a steady-state (equilibrated) and a disequilibrated geotherm on the generation of uplift by lithospheric thinning**. Top row: predicted elevation as a function of removed thickness of lithosphere for a (a) steady-state and (b) disequilibrium lithospheric geotherm. Middle row: Gray scale and contours show calculated elevations for a crustal thickness of 40 km, and lithospheric thinning and asthenospheric thermal anomaly for a (c) steady-state and (d) disequilibrium geotherm. Bottom row: Predicted elevation for a crustal thickness of 30 km for a (e) steady-state and (f) disequilibrium geotherm. Labelled boxes indicate estimates of support for Cretaceous western interior of North America (K), Great Plains (GP), Araripe Plateau (AR), Rocky Mountains (RM), and Potiguar Basin (PT).

the effects of trading-off a and ΔT on the resulting elevation, assuming steady-state and disequilbrated geotherm. These figures show that thermal equilibration after following lithospheric thinning of 50 km, or lithospheric thinning with a steady-state geotherm, generates additional uplift of $\sim$ 1 km. However, as previously outlines, the long thermal time constant of the lithosphere suggests assuming a disequilbrated geotherm is appropriate to examine the geodynamic evolution of lithosphere and asthenosphere beneath western North America and eastern South America.

2.5.2 Western North America

Proposed mechanisms for uplift of the Colorado Plateau and surrounding regions include isostatic uplift from crustal thickening (e.g., *Morgan and Swanberg*, 1985; *McQuarrie and Chase*, 2000), mantle convection and shallow subduction of the Farallon slab (e.g., *Moucha et al.*, 2008b; *Liu and Gurnis*, 2010), edge-driven convection (e.g., *van Wijk et al.*, 2010), large-scale uplift by lithospheric thinning (*Roberts et al.*, 2012a; *Bailey et al.*, 2012) or a combination of such processes (e.g., *Levander et al.*, 2011). I make use of the inventory of uplift constraints and simple isostatic calculations to assess the contribution of changing lithosphere thicknesses, densities, and asthenospheric thermal anomalies.

Figure 2.17 shows free-air gravity anomalies, lithospheric thickness, shear-wavespeed velocity anomlay and crustal thickness beneath western North America. Crustal thicknesses beneath the Rocky Mountains and the Great Plains are broadly similar, ranging from 36–43 km with a mean of 40 km (Figure 2.13 and 2.17c; *Buehler and Shearer*, 2016). Conversion of shear wave tomographic models into temperature indicates that the lithosphere beneath the Great Plains (e.g., Minnesota, Iowa) is $\sim$ 200 km thick (*Priestley and McKenzie*, 2013). Solving Equation 5 using this value, a crustal thickness of 40 km and assuming that the plate rests directly upon asthenosphere that does not have excess temperature anomalies yields an elevation of 480 m. This value is consistent with the average present-day elevation of the plains (Figure 2.15e: red box labelled GP). However, the distribution of Cretaceous marine rock across the plains, and paleo-water depth assessments from the PBDB indicate that most of the region was at or below current sea level by as much as $\sim$ 100 m (Figure 2.15e). This paleogeography is well known and used as a basis to parameterise geodynamic models of drawdown, which are often related to subduction of the Farallon Slab (e.g., *Liu and Nummedal*, 2004; *Flament et al.*, 2013). If dynamic stresses and lithospheric thickness are assumed to not have changed since the Cretaceous Period, I can explore an alternative explanation where the asthenosphere directly beneath the plate was cooler than it is today. For example, a 200 km thick asthenospheric layer that has an excess temperature of -74 to -89°C yields elevations of 0 to 100 m below modern sea level. Increasing

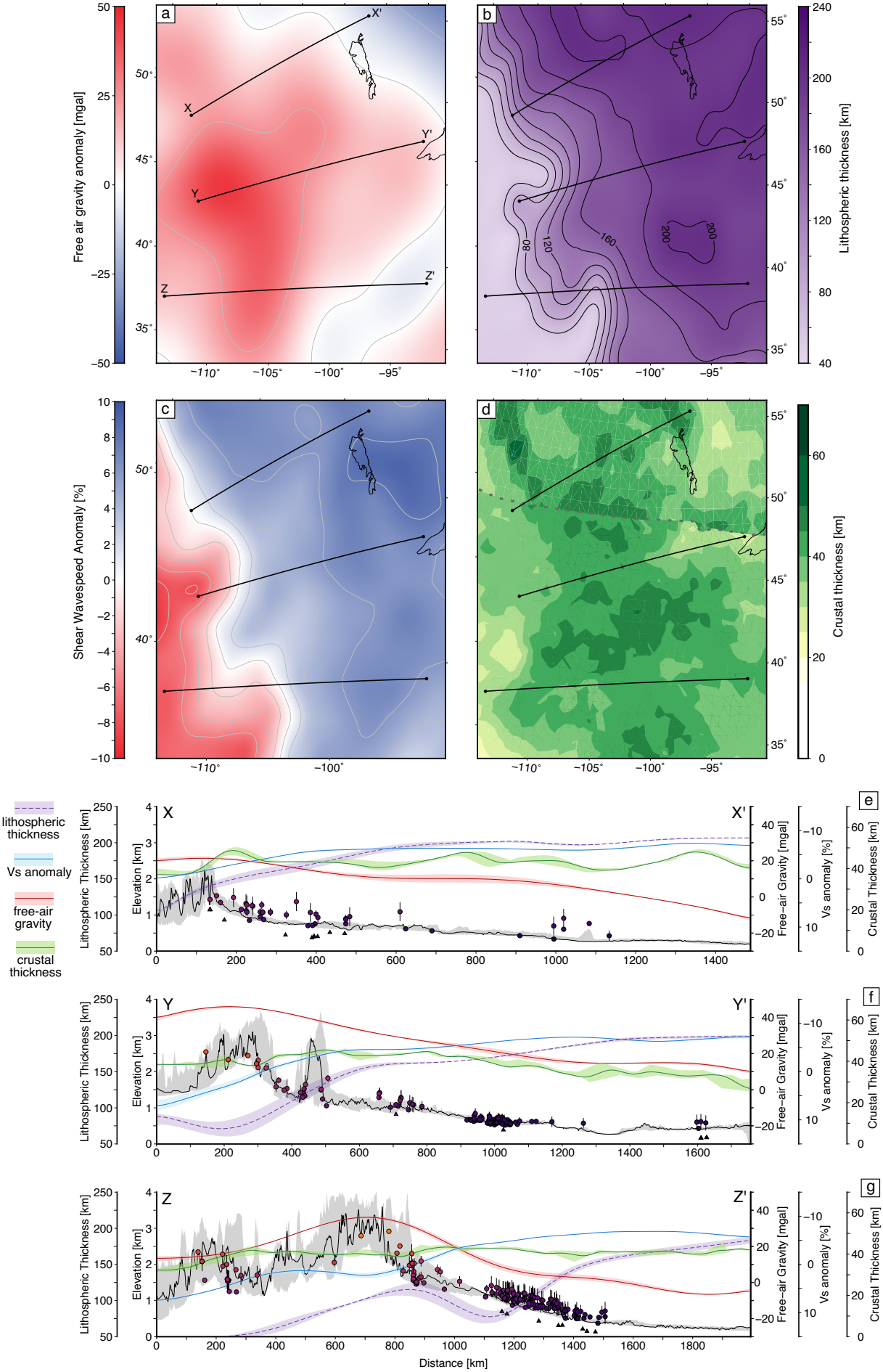
a
b
c
d
e
f
g
X
X'
Y
Y'
Z
Z'
Free air gravity anomaly [mgal]
Lithospheric thickness [km]
Shear Wavespeed Anomaly [%]
Crustal thickness [km]
lithospheric thickness
Vs anomaly
free-air gravity
crustal thickness
Lithospheric Thickness [km]
Elevation [km]
Free−air Gravity [mgal]
Vs anomaly [%]
Crustal Thickness [km]
Distance [km]

Figure 2.17: **Geophysical observations from the Western Interior of North America.** (a) Long wavelength free-air gravity (GRACE; 800 − 2500 km long pass filter; *Tapley et al.*, 2005). (b) Lithospheric thickness from CAM2016 model (*Priestley and McKenzie*, 2013). (c) Shear-wavespeed anomaly at 100 km depth (SL2013sv; *Schaeffer and Lebedev*, 2013). (d) Crustal thickness from PnUS model (south of dotted grey line *Buehler and Shearer*, 2016) and CRUST1.0 (north of dotted grey line *Laske et al.*, 2013). Black curves show locations of cross sections X–X′, Y–Y′ and Z–Z′. (e–g) Cross sections X–X′, Y–Y′ and Z–Z′ showing topography from ETOPO1 (black curve), topography within 100 km wide swath (grey band), mean uplift of points within swath (coloured circles). Mean and extrema of geophysical observations are shown along the swaths as coloured curves and bands (see key).

---

or decreasing the thickness of the layer adjusts estimated temperatures in a straightforward curvilinear way (e.g., Figure 2.15).

Causes for differential uplift between the Rocky Mountains and the Great Plains can be explored by considering the effects of lithospheric thinning and asthenospheric thermal anomalies (Figure 2.15e). I estimate the amount of lithospheric thinning beneath the Rocky Mountains by comparing its present-day thickness to thicknesses beneath the Great Plains. Figure 2.13a shows that conversion of shear wave tomography into estimates of lithospheric thicknesses indicates a difference of $\sim$ 150 km. Inverse modelling of rare earth, major and trace elements from basalts across the plateau suggests that the average potential temperature of the asthenosphere beneath western North America is currently 1340 ± 20 °C. The highest values ($\sim$ 1365 °C) are beneath the Snake River Plain, which implies excess temperatures of 0 to 45 °C (*Klöcking et al.*, 2018a). These measurements predict that the asthenosphere and lithosphere support almost all of the present-day elevation of the Southern Rocky Mountains ($\sim$ 3.1 km; red box, RM; Figure 2.15e).

Using these values and Equation 5, I suggest that Late Cretaceous-Recent uplift of the Southern Rocky Mountains can be explained by an average increase in asthenospheric temperatures of $\sim$ 200 °C and 150 km of lithospheric thinning (red arrows, Figure 2.15e). In other words, I suggest that post-Cretaceous uplift of the Rocky-Mountains-Colorado Plateaux could be the result of heating of the asthenosphere that was anomalously cool during Cretaceous times to its current anomalously warm state, and thinning of the plate beneath the region. These calculations are in agreement with the presence of colder, downwelling mantle in the Cretaceous, and subsequent emplacement of hotter mantle following lithospheric thinning (e.g., *Moucha et al.*, 2008b; *Liu and Gurnis*, 2010; *Roberts et al.*, 2012a; *Bailey et al.*, 2012). On the other hand, assuming a steady-state geotherm requires $\sim$ 100°C of heating to generate the uplift of the Great Plains and $\sim$ 150°C of heating to support highest topography in the Rocky Mountains. These results are consistent with interpretations of major

and trace element chemistry of basaltic rock from across the region, which suggests the lithosphere beneath the Rocky Mountains is relatively thin, and upper mantle temperatures only slightly above average (*Klöcking et al.*, 2018a).

2.5.3 Borborema

Suggested mechanisms for Late Cretaceous to Recent uplift of the Borborema Plateau and Araripe Basin include crustal thickening by lateral flow related to Mesozoic rifting and mafic underplating driven by a deep mantle plume (*Morais Neto et al.*, 2009), emplacement of a shallow upper mantle thermal anomaly (*Ussami et al.*, 1999), localised mantle plume (*Jardim de Sá et al.*, 1999), mafic underplating (*Oliveira and Medeiros*, 2012), basin inversion caused by plate-wide compression (*Marques et al.*, 2014), and a modest, positive, asthenospheric thermal anomaly that has thinned the overlying lithosphere (*Klöcking et al.*, 2020). Here, I explore how the uplift measured using the PBDB inventory, combined with isostatic calculations, can help shed light on the mechanism responsible for the long-wavelength uplift of the region.

Late Cretaceous shallow marine rock in the Araripe Plateau and basins along the Atlantic margin record ~ 700 m of differential uplift on a length scale of $\sim 900 - 1000$ km (Figure 2.18). Shear-wave-to-temperature conversions indicate that the lithosphere beneath the Araripe Plateau is ~ 150 km thick, and thins to less than 100 km at the coast (*Priestley and McKenzie*, 2013). In contrast, inverse modelling of magnetotelluric data has been used to suggest that the lithosphere beneath the Araripe Plateau is ~ 120 km thick, and surrounding lithosphere is as thick as ~ 200 km (*Garcia et al.*, 2019). H–κ stacking of receiver functions in the Borborema Province indicates that crustal thicknesses are variable (30–41 $\pm$ 2 km; *Luz et al.*, 2015a). They are as low as 30 km in the Potiguar and Sergipe-Alagoas Basins, 38 km on the eastern edge of the Araripe Basin and 40 km within the Borborema Plateau. *Luz et al.* (2015b) suggest that p-wave velocities, V_p, of the upper and lower crust beneath the Borborema plateau are 6.03–7.33 km s^{-1}. Conversion of these V_p values into density suggests crustal densities of 2.73–2.91 Mg m^{-3} (*Barton*, 1986). Inserting these values into Equation 5 indicates that present-day lithospheric and crustal thicknesses (150 and 38 km, respectively) are sufficient to explain the elevation of the Araripe Plateau without recourse to excess temperature anomalies in the asthenosphere.

A remaining question is why were significant tracts of the province marine in the Cretaceous Period? By Late Aptian times rift basins had developed along the Atlantic margin of the South American plate

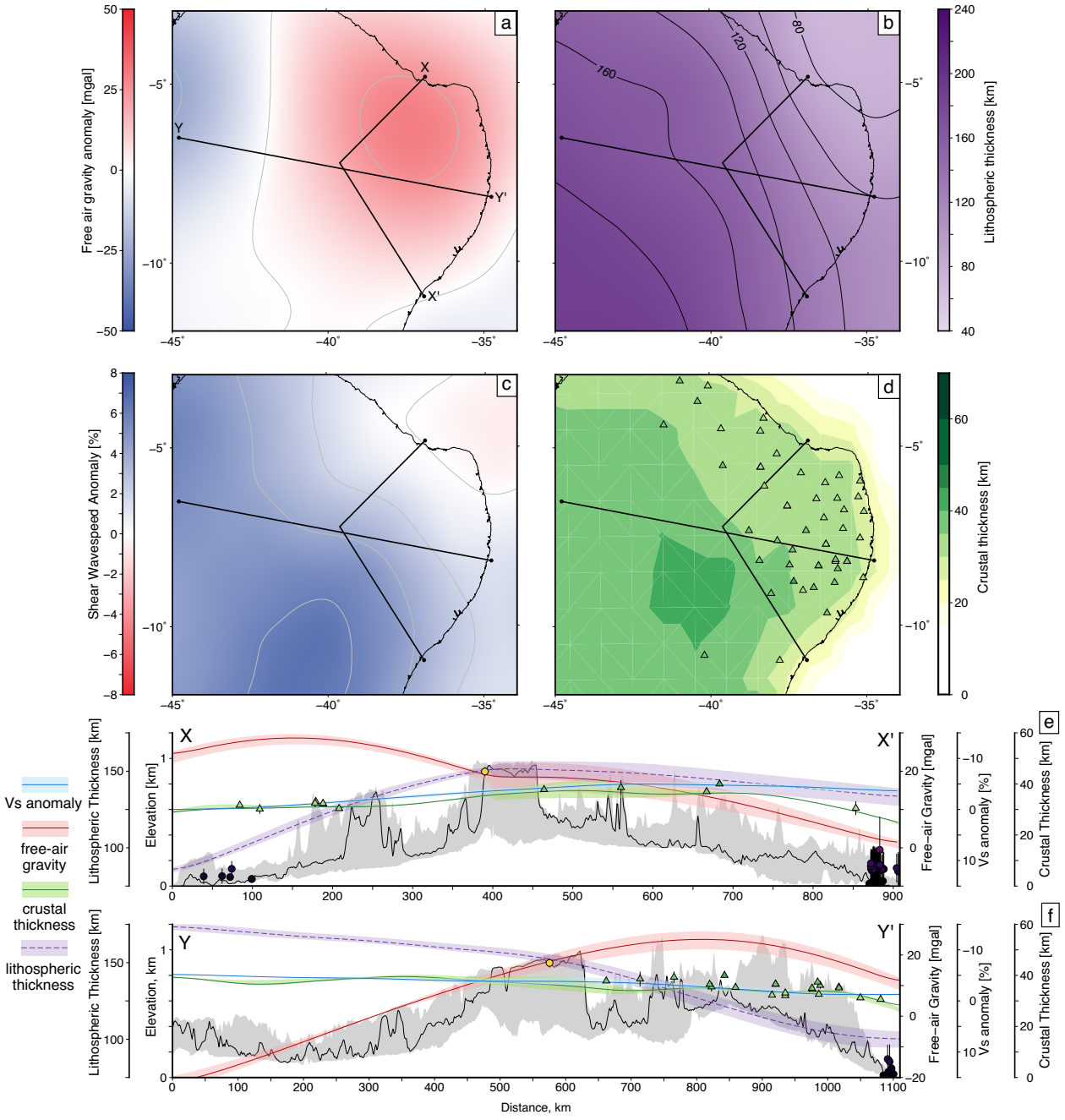

Figure 2.18: **Geophysical observations from the Borborema Province, northeast Brazil.** (a) Long wavelength free-air gravity (GRACE; 800−2500 km long pass filter; *Tapley et al.*, 2005). (b) Lithospheric thickness from CAM2016 model (*Priestley and McKenzie*, 2013). (c) Shear-wavespeed anomaly at 100 km depth (SL2013sv; *Schaeffer and Lebedev*, 2013). (d) Crustal thickness from CRUST1.0 (north of dotted grey line *Laske et al.*, 2013). Black lines show locations of cross sections X–X′ and Y–Y′. (e–f) Cross sections X–X′ and Y–Y′ showing topography from ETOPO1 (black curve), topography within 100 km wide swath (grey band), mean uplift of points within swath (coloured circles). Mean and extrema of geophysical observations are shown along the swaths as coloured curves and bands (see key).

and within the continental interior (e.g., *Machado Júnior et al.*, 1990; *de Matos*, 1992). *Morais Neto et al.* (2009) use thermal modelling of apatite fission track data to suggest two phases of exhumation of the Borborema Plateau, during Cenomanian-Turonian and Miocene times. Their results are broadly consistent with the transition from marine to fluvial depositional environments in the Araripe, Tucano and Jatobá basins, and the presence of the marine Miocene Barreiras Formation that crops out at higher elevations along the coast (Figure 2.12; *Rossetti et al.*, 2013).

I note that Late Cretaceous marine rock that is exposed near the top of the Araripe Plateau was probably deposited after rifting. Interpreted paleo-water depths of the Santana Formation are < 50 m, and the formation crops out at an elevation of 600–850 m. I tentatively suggest that one way of explaining observed vertical motions is that the asthenosphere beneath the Araripe Plateau was cooler in Cretaceous times than it is today. For example, warming of asthenosphere by 155 °C to ambient (1330 ± 15 °C) temperatures yields 995 ± 95 m of uplift (Equation 5). These results are consistent with *Klöcking et al.* (2018b, 2020) who, based on forward and inverse modelling of major, trace and rare earth element concentrations of volcanic samples, suggest a mantle potential temperature of $\sim 1320 - 1340$ °C. Alternatively, removal of ~ 100 km of lithospheric mantle beneath the plateau can generate observed uplift. For the steady-state scenario, it would require the present-day asthenosphere to have a ~ 90°C negative thermal anomaly and thinning would be sufficient to explain the present-day elevations.

2.5.4 Summary

In this study, I have generated an inventory of 24,372 measurements of Cretaceous to Recent net uplift. The inventory includes measurements in all continents and many ocean islands. The measurements were generated by combining records of Cretaceous to Recent marine rock in the Paleobiology Database (PBDB) with estimates of elevation, paleobathymetry, compaction, and global sea-level change. In some places the inventory is sufficiently dense that wavelengths and amplitudes of regional uplift can be constrained (e.g., western North America, Figure 2.19a,b). In other places sparse measurements provide useful bounds on topographic evolution (e.g., Borborema province, Brazil, , Figure 2.19d,e). Less than 1% of the records in the PBDB required manual modification to correct erroneously located samples. A larger effort was required to check the quality of paleo-water depth and paleoenvironment records. I combined points from western North America and the Borborema province with seismological observations and simple isostatic calculations to investigate the origins of topography. In these regions post-Cretaceous net uplift has amplitudes up to ~ 1 km at wavelengths of $100 - 1000$ km,

and can be explained by a balance of lithospheric thinning and heating up of the upper mantle from relatively cooler temperatures.

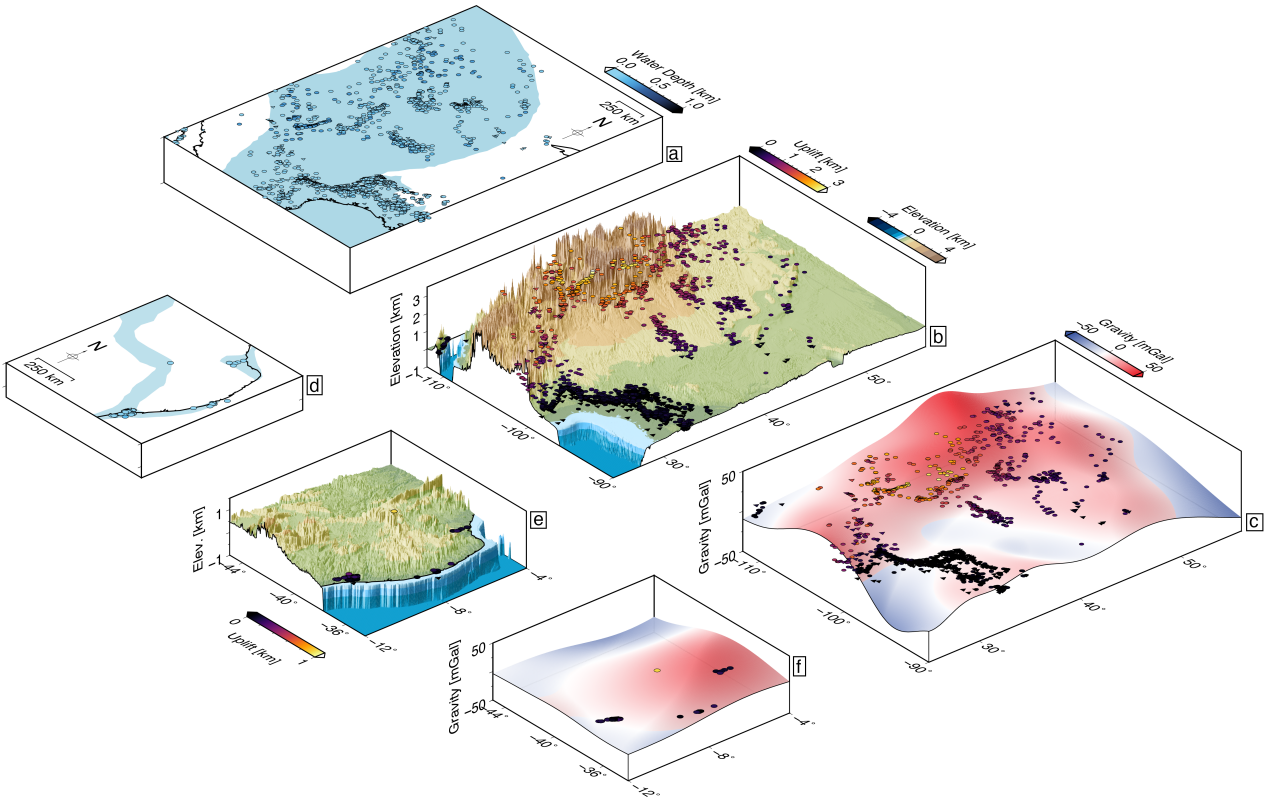

Figure 2.19: **Schematic paleogeographies and uplift patterns from PBDB measurements.** (a) Cretaceous paleogeography of western North America. Coloured circles = paleobathymetry from PBDB measurements; blue polygon = Turonian (∼ 98 Ma) seaway (*Heine et al.*, 2015). (b) Measured uplift (coloured circles) atop modern topography (ETOPO1). (c) Uplift (coloured circles) atop long-wavelength free-air gravity (GRACE). (d–f) Paleogeography, uplift and sub-plate support of Borborema province, NW Brazil. Blue polygons in panel (a) indicate late Albian (∼ 100.5 Ma) paleocoastline (*Arai*, 2009).

2.5.5 Remarks on limitations and further work

There are two main shortcomings in this study. The first is that although these measurements provide robust constraints on the net uplift experienced by the region, they cannot provide information on the temporal variation of uplift rates, or whether the region underwent periods of subsidence. There is a suite of additional uplift and denudation constraints that can be combined with these observations to understand the evolution of North American topography, which I discuss in Chapter 3. For example, observations including stable isotopes, palynology, radiometrically dated incision, thermochronology and additional stratigraphic observations could be brought in to better constrain the surface evolution of the region (e.g., *Dickinson et al.*, 1988; *Gregory and Chase*, 1992; *Flowers et al.*, 2008; *Karlstrom et al.*, 2008; *Chamberlain et al.*, 2012; *Heller et al.*, 2013). An additional approach that could be used

to fill in the gaps between spot measurements of post-Cretaceous uplift is a continent-wide inversion of drainage patterns. The inverse methodology uses families of drainage networks to recover smooth spatio-temporal uplift rate histories using a calibrated stream power erosional model (e.g., *Roberts et al.*, 2012a), a technique which I explore in Chapter 3. Second, although the inventory of uplift measurements is reasonably dense in some places, there are clearly large gaps especially in continental interiors, most notably in Africa, central South America, northeastern Eurasia, and central Australia. These gaps represent a lack of marine deposition in some places, but in others it is where the inventory is not yet exhaustive.

An obvious way to improve the inventory is inclusion of more documented marine rock. Another is addition of uplift and subsidence estimates generated using alternative approaches, for example, isotopic altimetry. I feel it is important to make a distinction between such estimates and the more direct, typically less equivocal, constraints provided by uplifted marine rock. A general challenge is designing sensible schemes to interpolate between spot measurements of uplift, subsidence and denudation. Attempts to do so have included interpolation of interpreted paleoenvironments and tectonic histories provided by geological observations (e.g., *Sahagian*, 1987; *Scotese and Golonka*, 1992; *Carena et al.*, 2019; *Markwick*, 2019). For the Cenozoic Era, a useful approach is to make use of inverse modelling of drainage patterns. This approach provides a quantitative means for filling in spatio-temporal gaps between spot measurements of uplift and denudation, and is testable using inventories of uplift such as those generated in this study. The next chapter focuses on developing and analysing such inverse techniques to understand the history of sub-plate support in North America, where the inventory of net uplift is dense.

Chapter 3

The Ups and Downs of a Continent - Evolution of the North American Landscape

The material in this chapter has been published as

Fernandes, V.M., Roberts, G.G., White, N.J., and Whittaker, A.C. (2019). Continental-Scale Landscape Evolution: A History of North American Topography, *Journal of Geophysical Research: Earth Surface*, *124*, 2689–2722, doi:10.1029/2018JF004979.

Copyright 2019, American Geophysical Union.

3.1 Chapter Overview

The generation and evolution of continental topography are fundamental geologic and geomorphic concerns. In particular, the history of landscape development might contain useful information about the spatio-temporal evolution of deep Earth processes, such as mantle convection. A significant challenge is to generate observations and theoretical predictions of sufficient fidelity to enable landscape evolution to be constrained at scales of interest. Here, I combine substantial inventories of stratigraphic and geomorphic observations with inverse and forward modelling approaches to determine how the North American landscape evolved. First, the biostratigraphic inventory developed in Chapter 2 is augmented by stratigraphic markers and used to estimate post-depositional regional uplift.

Present-day elevations of these deposits demonstrate that > 2 km of long wavelength surface uplift centred on the Colorado-Rocky-Mountain Plateaux occurred in Cenozoic times. Secondly, to bridge the gaps between these measurements, an inverse modelling scheme is used to calculate the smoothest spatio-temporal pattern of rock uplift rate that yields the smallest misfit between 4161 observed and calculated longitudinal river profiles. Results suggest that Cenozoic regional uplift occurred in a series of stages, in agreement with independent stratigraphic observations. Finally, a landscape evolution model driven by this calculated rock uplift history is used to determine drainage patterns, denudation and sedimentary flux from Late Cretaceous times until the present day. These patterns are broadly consistent with stratigraphic and thermochronologic observations. I conclude that a calibrated inverse modelling strategy can be used to reliably extract the temporal and spatial evolution of the North American landscape at geodynamically useful scales.

3.2 Introduction

Topography is the result of complex interactions between the solid Earth and surface processes that operate on multiple spatial and temporal scales (e.g., *Anderson and Anderson*, 2010; *Roberts et al.*, 2019). Consequently, surface uplift and subsidence histories have been combined with magmatic and tomographic information to estimate temperatures, wavelengths and timescales of mantle convection (e.g., *Gurnis et al.*, 2000; *van Wijk et al.*, 2010; *Salles et al.*, 2017; *Roberts et al.*, 2018; *Lodhia et al.*, 2018). The results of these studies imply that mantle processes play a significant role in driving the erosional history of a landscape. Unfortunately, existing inventories of uplift or denudation measurements are sparse, which makes it difficult to determine histories of geodynamical processes (e.g., sub-plate support) at appropriate scales. In Chapter 2, I showed how an existing paleobiology database can be explored to generate a global inventory or rock uplift measurements. From these data I was able to extract the timing, magnitude and wavelength of uplift on a global scale, with a focus on two case studies: Borborema Province, NE Brazil, and Western Interior of North America. Both regions display kilometre-scale Late Cretaceous to Recent uplift on wavelengths of 1000–2000 km. Using isostatic calculations I showed that sub-plate processes, specifically the thinning of lithospheric mantle and emplacement of asthenospheric thermal anomalies, can provide explanations for generating the observed uplift patterns.

Although measurements of continental uplift provide robust constraints on continental uplift histories, they contain little information about the temporal and spatial variability of uplift. Vast expanses

of continental interiors do not contain Cretaceous or younger marine rock, either due removal of stratigraphy by erosion or a lack of deposition. Further, these measurements are temporally limited, in that they do not contain information about how uplift rate might have changed over time. In this chapter I explore how the PBDB-derived uplift measurements for the North American continent, shown in Chapter 2 can be combined with thermochronometric and stratigraphic information to constrain continental-scale surface uplift histories on time scales of O(1–100) Ma. I match insights from this approach with geomorphic inverse modelling to reconstruct a Cretaceous to Recent uplift history of North America, where sub-plate processes appear to have played an important role in generating and maintaining long-wavelength topography. Finally, I explore how calibrated rock uplift histories can be used to parameterise three-dimensional forward models of landscape evolution, which make predictions about continental denudation, drainage routing and sedimentary flux that can be assessed using independent geologic observations.

Particular attention is paid to four regions with elevated topography: the Colorado-Columbia-Rocky Mountains Plateaux, the Appalachian mountain belt, the Yukon plateau, and the Mexican highlands. Spot measurements of rock and surface uplift (e.g., uplifted marine stratigraphy, stable isotopes, paleoflora, structural geology), denudation (e.g., low temperature thermochronometry, fluvial incision dating) and the geochemistry of basaltic magmatism suggest that a broad region encompassing the Colorado-Rocky Mountain Plateaux experienced multi-staged Cenozoic uplift and denudation generated, at least in part, by time-dependent thermal anomalies within the upper mantle (e.g., *Sahagian*, 1987; *Flowers et al.*, 2008; *Karlstrom et al.*, 2008; *Huntington et al.*, 2010; *Mix et al.*, 2011; *Chamberlain et al.*, 2012). Punctuated delivery of clastic sediments into the Gulf of Mexico corroborate these observations (*Galloway et al.*, 2011). There is also evidence for youthful regional uplift elsewhere. For example, uplifted Pliocene marine sedimentary rocks that crop out along the eastern seaboard and sedimentation rates within the Baltimore Canyon Trough imply that significant topography of the Appalachian mountains may have been generated during the last 20 million years (e.g., *Poag and Sevon*, 1989; *Rowley*, 2013). In the northern cratonic interior, thermochronometric observations and scattered outliers of Cretaceous marine sedimentary rock suggest several hundred meters of post-Cretaceous uplift and denudation occurred (e.g., *Nassichuk and McIntyre*, 1995; *Ault et al.*, 2013). Widespread magmatism, uplifted marine terraces and incised drainage patterns suggest that Mexico also experienced long wavelength Cenozoic uplift (e.g., *Stephenson et al.*, 2014). Nevertheless, the timing and mechanism for generating these patterns of regional uplift remain uncertain.

3.2.1 A Role for Large-Scale Crustal and Lithospheric Thickening?

Some models explain kilometre-scale changes in continental elevation by invoking crustal thickening by, for example, Early Cenozoic crustal flow (e.g., *McQuarrie and Chase*, 2000). These models have largely fallen out of favour since they are difficult to reconcile with present-day crustal thicknesses estimated from seismic wide-angle surveys, from receiver function analyses and from shear wave dispersion modelling (e.g., *Levander and Miller*, 2012; *Becker et al.*, 2014; *Shen and Ritzwoller*, 2016).

Isostatic calculations can be used to estimate the crustal (and lithospheric) thickening factor required to generate the observed 1.5 km of relief (Figure 3.1a; *Klöcking et al.*, 2018a)). A reference column of

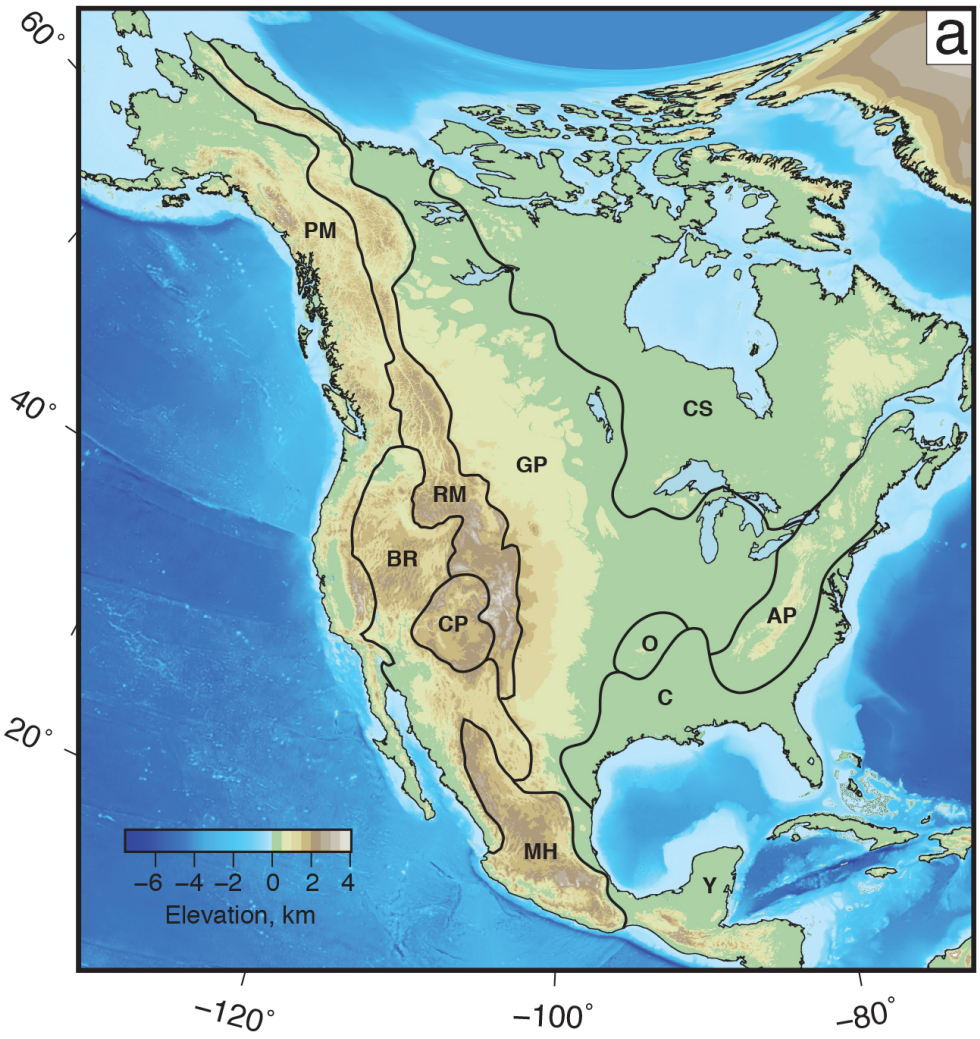

Figure 3.1: **Topography and physiographic provinces of North America** (a) Topographic map based upon ETOPO1 database. Physiographic provinces are named using nomenclature of *Fenneman* (1928). PM = Pacific margin; RM = Rocky Mountains; BR = Basin and Range; CP = Colorado Plateau; GP = Great Plains; CS = Canadian Shield; O = Ozark-Ouachita Plateau; AP = Appalachian mountains; C = Gulf and Atlantic Coastal Plains; MH = Mexican Highlands. Albers Equal Area projection.

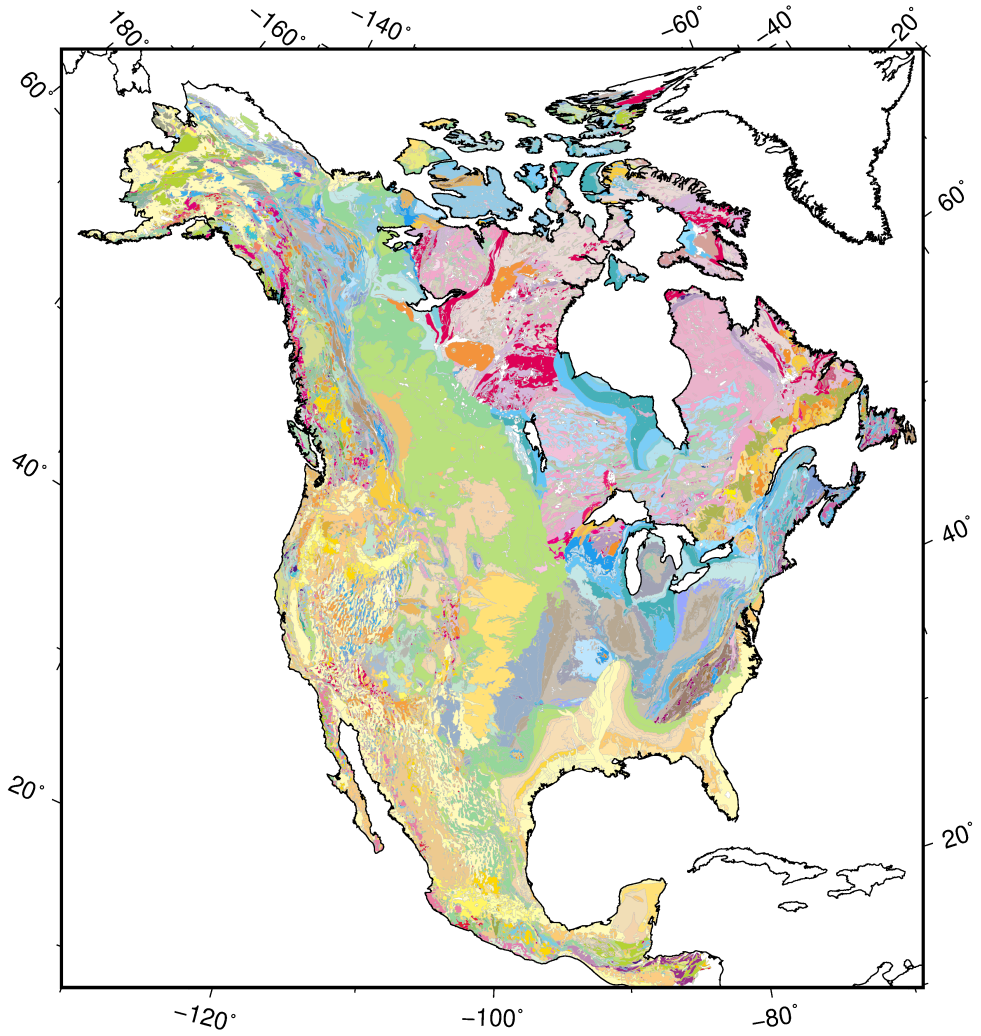

Figure 3.2: **Geological map of North America** from USGS (a). (b) Colour scale following original publication.

continental lithosphere is shortened uniformly by thickening factor, f, to estimate value of f required to generate regional uplift, U, where

$$U = \frac{a\left[(\rho_m - \rho_c)\frac{t_c}{a}\left(1 - \frac{\alpha T_1}{2}\frac{t_c}{a}\right) - \frac{\alpha T_1}{2}\rho_m\right]}{\rho_m(1 - \alpha T_1)}(f - 1). \tag{3.1}$$

Respective densities of mantle and crustal rocks are $\rho_m = 3.33$ and $\rho_c = 2.8$ Mg m^{-3} at standard temperature and pressure, thermal expansion coefficient is $\alpha = 3.28 \times 10^{-5}$ K^{-1}, and temperature at the base of the plate is $T_1 = 1333$°C. I assume a linear geothermal gradient and initial crust and lithospheric thicknesses of $t_c = 30$ km and $a = 125$ km, which are appropriate for a reference lithospheric column with zero elevation (i.e. $U = 0$). Substitution of the values of these parameters yields $U = 2.1(f - 1)$. To produce 1.5 km of relief difference between Colorado Plateau and Great

Plains (e.g., Figure 3.1a) by lithospheric thickening alone, requires crust and lithosphere beneath Colorado Plateau to be $f = 1.7$ times thicker than that beneath Great Plains.

However, empirical parameterisation of shear wave tomographic models suggests that the lithospheric thickness beneath the Great Plains is approximately double that of the Colorado Plateau (e.g., *Priestley and McKenzie*, 2006; *Shen and Ritzwoller*, 2016). The striking similarity of crustal thicknesses beneath the Colorado-Columbia-Rocky Mountains Plateaux and beneath the Great Plains (35–45 km) is consistent with the view that orogenesis played an insignificant role in generating and maintaining the regional elevation of western North America since Late Cretaceous times (*Spencer*, 1996; *Wilson et al.*, 2005). The observed velocity structure of the crust indicates that differences in crustal and sedimentary densities alone are insufficient to account for these dramatic changes in topographic relief (2; *Roberts et al.*, 2012a; *Klöcking et al.*, 2018a; *Levandowski et al.*, 2018).

3.2.2 Epeirogeny and the Role of Dynamic Support

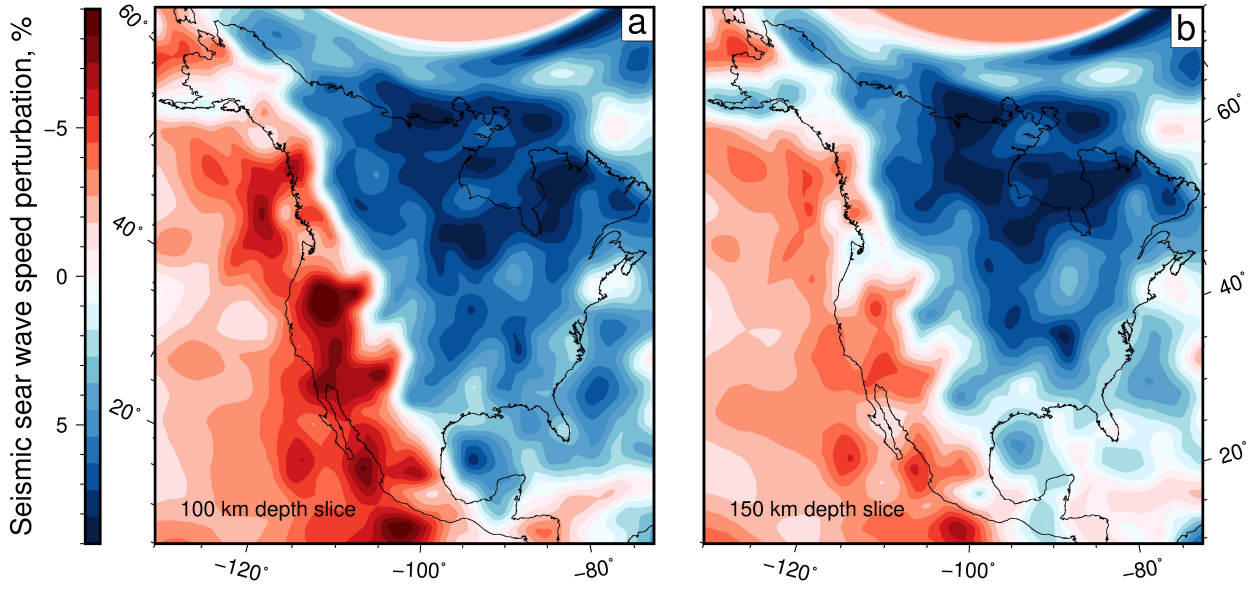

Figure 3.3: **Shear wavespeed anomalies beneath North America** (a) at depth of 100 km and (b) 125 km (*Schaeffer and Lebedev*, 2013).

More popular models invoke the development of positive and negative mantle buoyancy anomalies generated by hot upwellings and subducting slabs to generate vertical motions (e.g., *Thompson and Zoback*, 1979; *Humphreys*, 1995; *Spencer*, 1996; *Liu and Gurnis*, 2010; *Karlstrom et al.*, 2012). The admittance, Z, between long-wavelength ($\gtrsim$ 800–2500 km) free-air gravity anomalies and topography for western North America show it has an elastic thickness of 12 ± 3 km, which implies that sub-plate buoyancy anomalies ought to measurably deflect the Earth's surface (*McKenzie*, 2003). At the longest

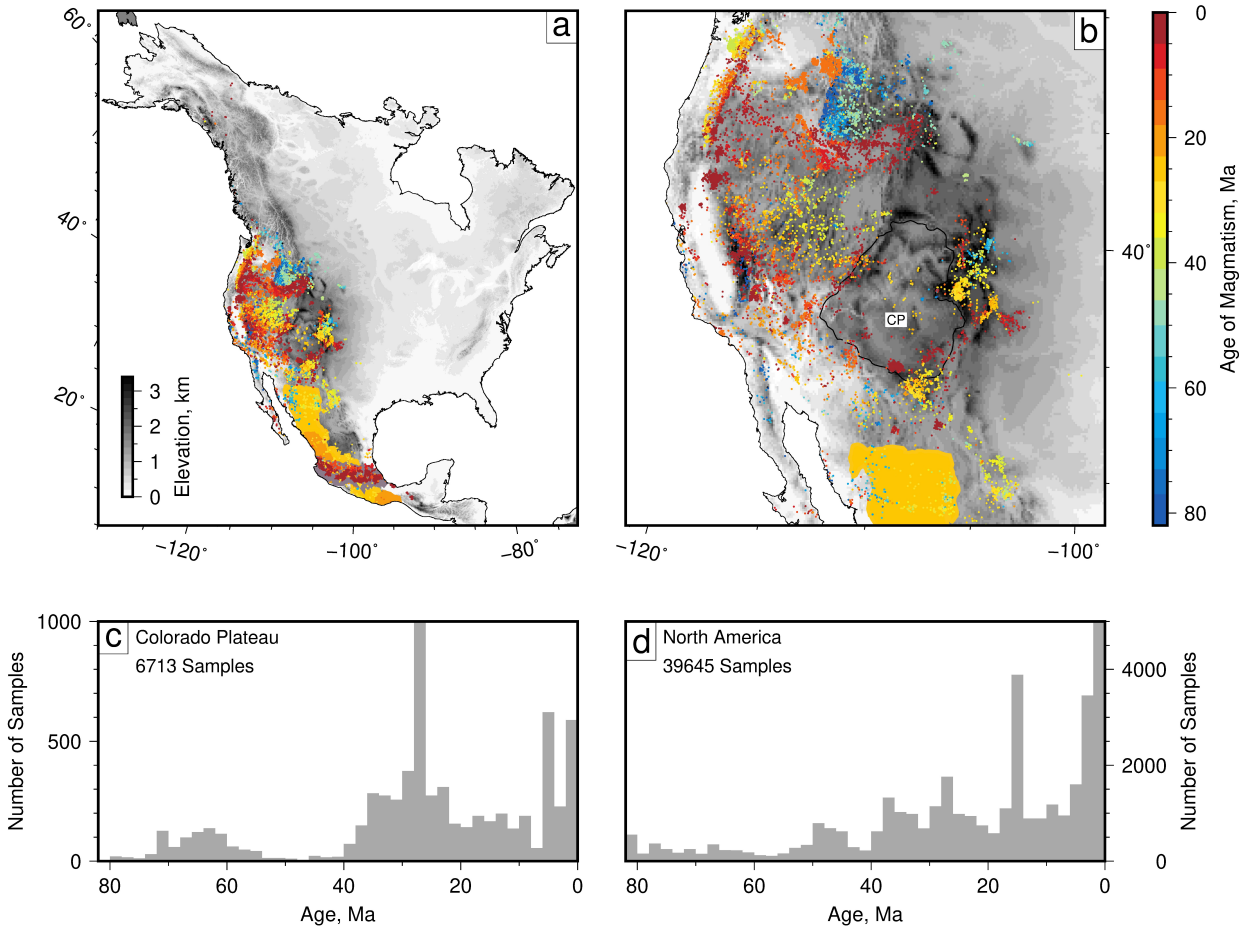

Figure 3.4: **Distribution of Cretaceous to Recent magmatism** (a) North American Cenozoic magmatism from NAVDAT database (*Ferrari et al.*, 2012, ; `www.navdat.org`). Gray shading = present-day topography from ETOPO1 database; orange/yellow polygons = Oligocene/Miocene ignimbrites (*Ferrari et al.*, 1999; *Chapin et al.*, 2004). (b) Western North American magmatism centred on Colorado Plateau, which is outlined by black polygon labelled CP.

wavelengths, $Z = 23 \pm 5$ mGal/km, which suggests that the topographies of western North America, the Yukon, Central Mexico and the Appalachian mountains are at least partially supported by sub-plate processes (e.g., Figure 3.1b, *Roberts et al.*, 2012a; *Stephenson et al.*, 2014). These locations of inferred sub-plate support are corroborated by seismic tomographic imaging, which shows that the upper mantle beneath these parts of North America is anomalously slow and juxtaposed against a central region with thick (> 150 km) lithosphere (e.g., Figure 3.3; *Priestley and McKenzie*, 2006; *Ritsema et al.*, 2011; *French et al.*, 2013; *Rowley*, 2013; *Schaeffer and Lebedev*, 2013; *Molnar et al.*, 2015). Basaltic magmatism coincides with many of these low velocity zones (e.g., Figures 3.3 and 3.4). Beneath western North America, an overall increase in melt volume at 40 Ma, as well as an abrupt change from lithospheric to asthenospheric signatures at 5 Ma, point towards the emplacement of anomalously hot material during the last 70 Ma (e.g., Figure 3.4; *Fitton et al.*, 1991; *Roy et al.*, 2009;

Klöcking et al., 2018a). Drainage patterns of the four most prominent topographic swells (e.g., Yukon, western North America, Mexico, Appalachians) are broadly radial, which suggests domal support of the present-day landscape (Figure 3.1b).

A burgeoning number of geodynamic models have been used to predict mantle flow patterns beneath the continent with a view to constraining the history of dynamic topography (e.g., *Mitrovica et al.*, 1989; *Lithgow-Bertelloni and Gurnis*, 1997; *Liu et al.*, 2008; *Spasojević and Gurnis*, 2012; *Dávila and Lithgow-Bertelloni*, 2015). These models estimate that transient dynamic topography has amplitudes of up to ±2 km and wavelengths of hundreds to thousands of kilometres (see e.g., *Flament et al.*, 2015). They have been used to account for the aerial extent of the Western Interior Seaway as well as for Mesozoic–Cenozoic uplift, subsidence and magmatic patterns (e.g., *Rowley*, 2013; *Flament et al.*, 2015; *Liu*, 2015; *Heller and Liu*, 2016). There is considerable debate about how best to parameterise and test these models and it is notable that most of them fail to match the power spectral characteristics of a global database of oceanic residual depth measurements (*Hoggard et al.*, 2016). Thus, reliable histories of continental-scale vertical motions of the lithosphere are important constraints for this rapidly evolving field.

The primary aim of this chapter is to develop a testable history of uplift and denudation for the North American continent. First, I review published estimates of rock and surface uplift and denudation used to constrain North American topographic growth since Campanian times. I then fill in some of the gaps and omissions by exploiting regional uplift measurements obtained from stratigraphic and biostratigraphic inventories, which includes the uplift measurements from Chapter 2. Next, I generate a continent-wide history of regional rock uplift by inverting an inventory of 4161 river profiles. The calculated rock uplift history is tested using independent stratigraphic data. Finally, I use this uplift rate history to carry out continental-scale landscape simulations whose predictions are tested using a combination of legacy thermochronometric and detrital zircon measurements.

3.3 North American Landscape Evolution: Existing Constraints

3.3.1 Birth of the Western Interior Seaway

The chronology of deformed igneous rocks, metamorphic time-temperature paths, low temperature thermochronology and biostratigraphic ages of deformed and overlapping sedimentary rocks testify to the existence of an orogenic belt has spanned the length of the North American continent since

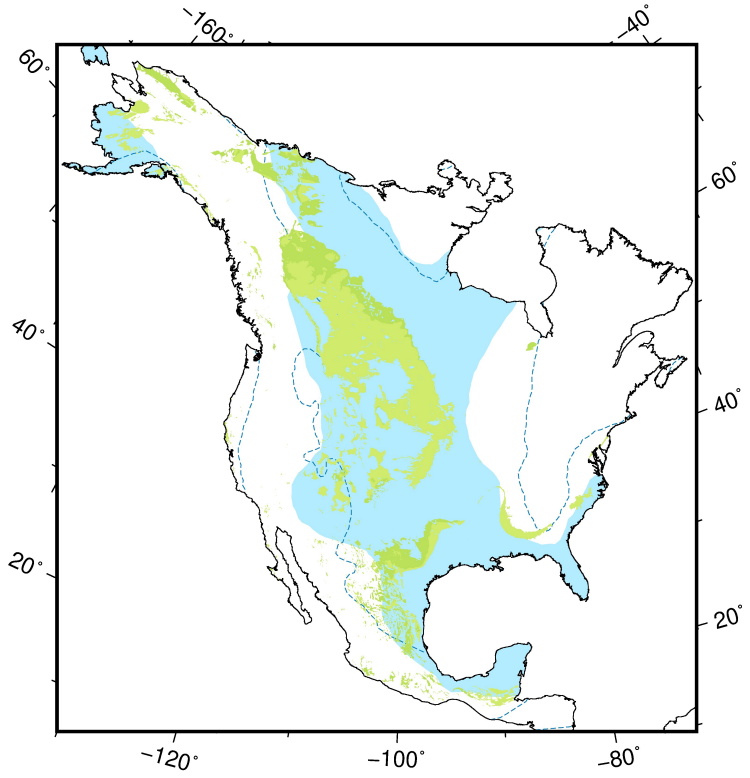

Figure 3.5: **Western Interior Seaway and Cretaceous outcrop** Solid blue polygons/dashed lines = maximum flooding extent of Cretaceous (i.e. Late Maastrichtian) interior seaway (*Smith et al.*, 1994; *Kauffman and Caldwell*, 1993). Dark/light green polygons = outcropping Lower/Upper Cretaceous rocks (*Reed et al.*, 2005).

Late Jurassic times (see, e.g. *DeCelles*, 2004). Shortening along a $\sim$ 200 km wide and $\sim$ 2000 km long structural belt that is oriented north-south manifests the Sevier orogen (*Gans and Miller*, 1983; *Wernicke*, 1992). Marine sedimentary rocks deposited within the adjacent Western Interior Seaway provide a useful datum against which Cenozoic uplift can be gauged (Figure 3.5; e.g. *Ziegler et al.*, 1985; *Sahagian*, 1987). Field mapping, seismic data and borehole penetrations imply that up to 4 km of Late Jurassic to Late Cretaceous marine sedimentary rocks were deposited within the Western Interior basin, indicating that continental flooding was widespread (e.g., Niobrara Formation, Mancos Shale; *Cross*, 1986; *DeCelles*, 1994; *Smith et al.*, 1994; *Setterholm*, 1994; *Nassichuk and McIntyre*, 1995; *Roberts and Kirschbaum*, 1995). These rocks have extensively documented ammonite biozones and known chronostratigraphy (e.g. *Jeletzky*, 1971; *Obradovich and Cobban*, 1975; *Kauffman and Caldwell*, 1993). Sedimentary isopachs and backstripped subsidence curves show that between $\sim$ 92 and 82 Ma the Western Interior basin was narrow and that subsidence patterns are consistent with the growth of foreland basins generated by loading associated with the Sevier orogeny (*Cross and Piliger*, 1978; *Cross*, 1986; *Roberts and Kirschbaum*, 1995; *Pang and Nummedal*, 1995; *Heller and Liu*, 2016).

In contrast, subsidence between ∼ 80 and 67 Ma occurred over a broader region centred on Colorado and Wyoming. Loading by the Sevier belt or changes in sea level cannot easily account for either the lateral extent or amplitude of observed subsidence (*Bond*, 1976; *Pang and Nummedal*, 1995; *Liu and Nummedal*, 2004). A range of geodynamic models have been proposed to explain these subsidence patterns by invoking kilometre-scale Cretaceous dynamic drawdown of large parts of the continent (*Mitrovica et al.*, 1989; *Gurnis*, 1993; *Liu et al.*, 2008).

3.3.2 Regression of Western Interior Seaway

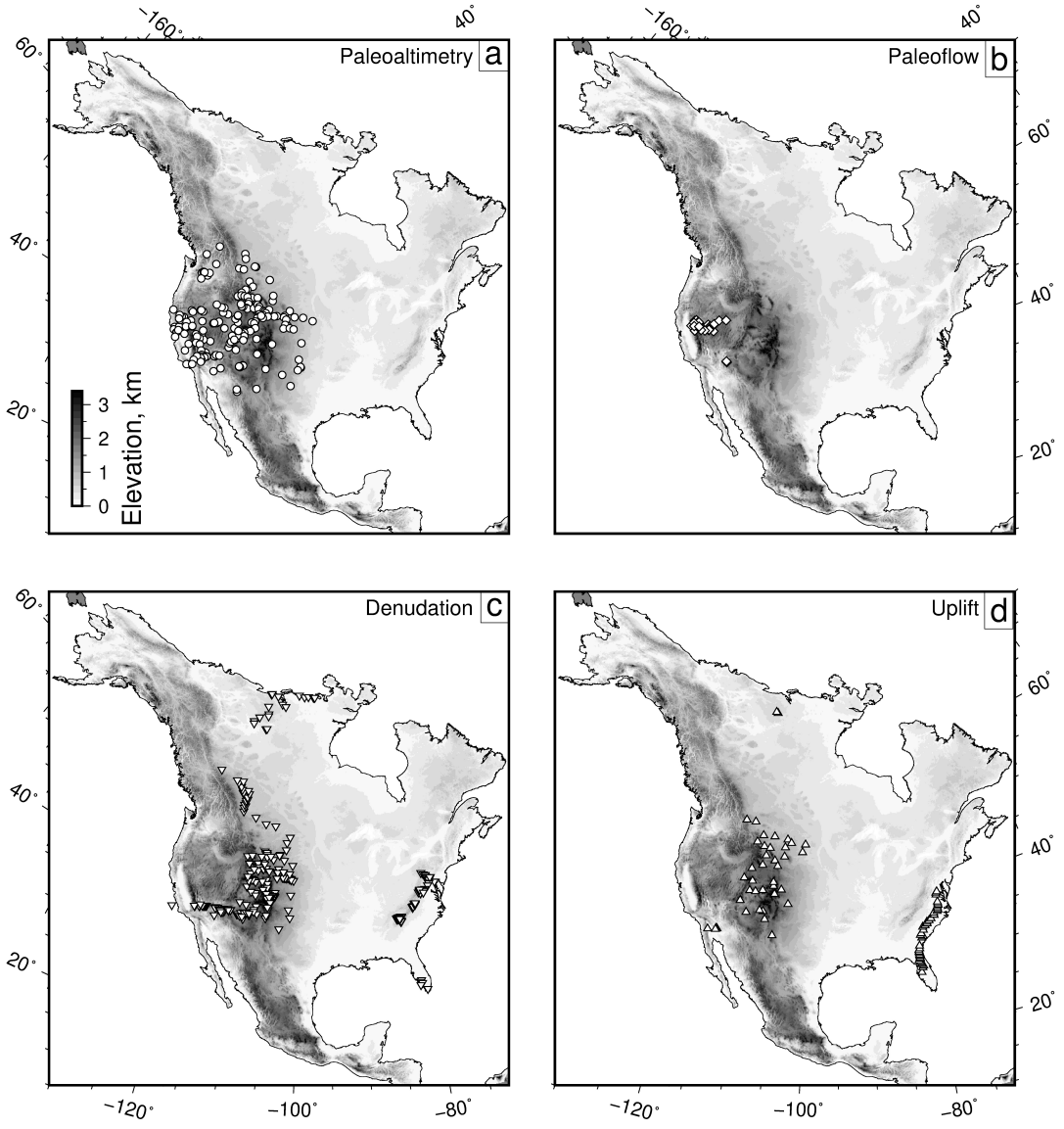

Figure 3.6: **Constraints on Landscape Evolution** Distribution of (a) paleoaltimetry, (b) paleoflow, (c) denudation and (d) uplift measurements since Late Cretaceous times (see e.g., *Dickinson and Snyder*, 1978; *Cassel et al.*, 2009; *Chamberlain et al.*, 2012; *Rowley*, 2013, and others cited in text).

By ∼ 70 Ma, when peak metamorphism was reached within the main fold belt, eastward migration

of thrust faulting resulted in an increasing partitioning of the Western Interior basin into smaller basins flanked by basement-cored uplifts (*Cross*, 1986; *Dickinson et al.*, 1988; *Stone*, 1993; *DeCelles*, 2004). This 'Laramide' structural style developed over a wide region east of the Sevier belt (*Dickinson and Snyder*, 1978; *DeCelles*, 2004). Despite the structural relief across these thrusts, intra-basinal deformation is insufficient to denude existing sedimentary deposits or to halt accumulation of Late Cretaceous marine sequences and associated deltaic facies (e.g. *Dickinson et al.*, 1988). At the same time, a Late Cretaceous to Early Paleocene transition from marine deposition (e.g., Pierre shale, Lewis shale) to deltaic (e.g., Fox Hills sandstone) to terrestrial deposition (e.g., Lance formation) facies occurred diachronously across North America (*Dickinson et al.*, 1988; *Lillegraven and Ostresh*, 1988; *Setterholm*, 1994; *Heller and Liu*, 2016). Paleoflow directions of conglomerates from the Laramide intramontane foreland basins (e.g., Paleocene Ohio Creek Conglomerate, Colorado; Maastrichtian-Paleocene Ojo Alamo Sandstone, New Mexico) indicate that a regional eastward tilt probably existed at $\sim$ 70–60 Ma (*Heller et al.*, 2013). Late Paleocene to Early Eocene terrestrial, synorogenic conglomerates deposited within the Middle Rocky Mountains record active thrust faulting and erosion (*Fan and Carrapa*, 2014). These combined observations show that during Late Mesozoic to Early Cenozoic times the Western Interior Seaway retreated and substantial parts of western North America were uplifted (*Dickinson et al.*, 1988; *Roberts and Kirschbaum*, 1995). The resultant facies change caused by retreat of this seaway has been linked with variable sedimentary flux, changing styles of subduction, hydration of the lower crust, and dynamic support (e.g. *Kauffman and Caldwell*, 1993; *Humphreys et al.*, 2003; *Dávila and Lithgow-Bertelloni*, 2015; *Levandowski et al.*, 2018)). During this period, minor tectonic shortening occurred across the Colorado Plateau (*Spencer*, 1996).

3.3.3 Post-Cretaceous Events

Thermochronometric and incision rate histories suggest that Cenozoic denudation of the Colorado and Rocky Mountains plateaus occurred in several stages (e.g. *Flowers et al.*, 2008; *Karlstrom et al.*, 2017; *Winn et al.*, 2017). Staged Cenozoic uplift and denudation of North America is consistent with the history of sedimentary deposition observed along the northern and western margin of the Gulf of Mexico (*Galloway et al.*, 2000; *Stephenson et al.*, 2014). *Feng et al.* (1994), *Peel et al.* (1995) and *Galloway* (2008) showed that that Mesozoic strata in the Gulf of Mexico are relatively uniform in thickness, while Cenozoic sedimentary strata increase in thickness towards the west. The highest rates of sedimentary flux occurred during Paleocene ($\sim$ 65 Ma), Oligo-Miocene ($\sim$ 40–15 Ma) and Plio-Pleistocene ($\sim$ 5–0 Ma Ma) times (Figure 3.7 *Galloway et al.*, 2011). Timing of these depo-

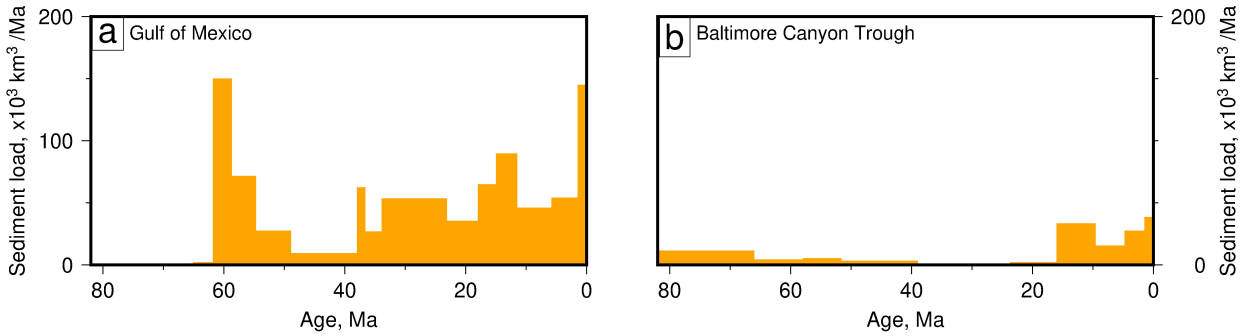

Figure 3.7: **North American solid sedimentary flux** (a) to the Gulf of Mexico determined from seismic reflection surveys and well-log information by *Galloway et al.* (2011). (b) Uncorrected sedimentary flux for New Jersey margin determined from seismic reflection surveys and well-log information by *Poag and Sevon* (1989).

sitional phases is broadly coeval with the history of uplift estimated from clumped isotopes (Δ_{47}) and with other paleoaltimetric proxies, which imply that the Colorado Plateau had an elevation of 1–2 km between Cretaceous and Oligocene times (e.g., *Gregory and Chase*, 1992; *Wolfe et al.*, 1998;

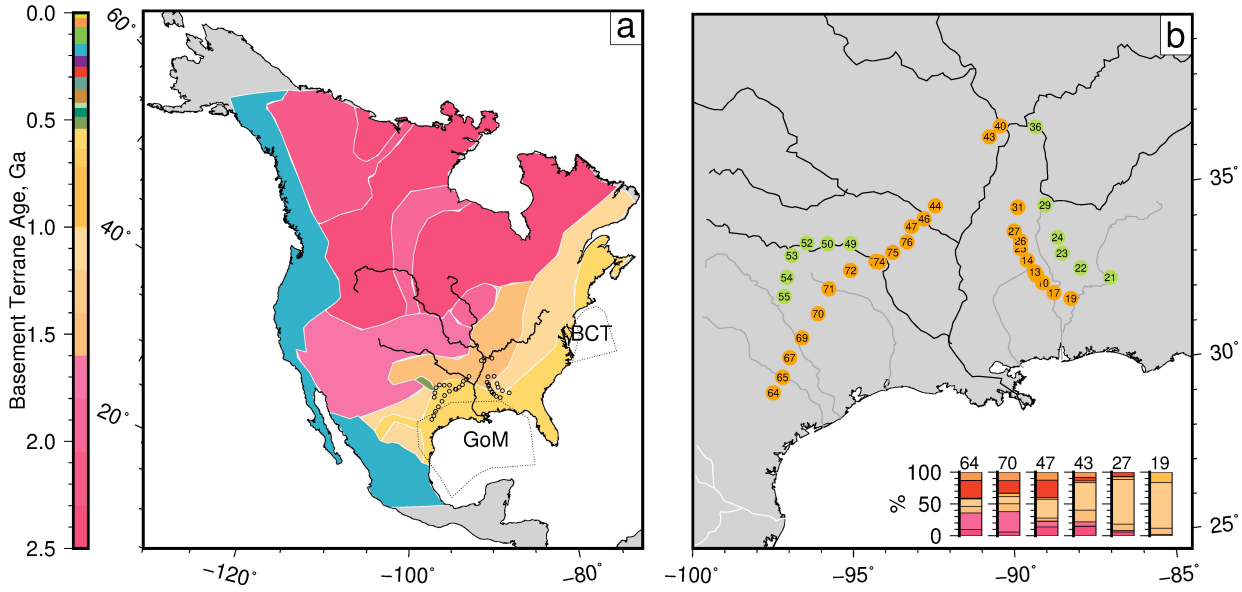

Figure 3.8: **Sediment provenance for Gulf of Mexico drainage** (a) Basement terranes coloured by age (after *Blum and Pecha*, 2014). Solid black lines = portion of present-day Mississippi drainage; circles = Cenomanian and Paleogene fluvial sandstones (*Blum et al.*, 2017). Dotted polygons labelled GoM/BCT = Cenozoic clastic sedimentary deposition within Gulf of Mexico/Baltimore Canyon Trough (*Poag and Sevon*, 1989; *Galloway et al.*, 2011). (b) Detrital zircons and drainage patterns along northern fringe of Gulf of Mexico. Black/grey/white lines = Mississippi/Texan/Mexican rivers; labelled circles = subset of detrital zircon samples extracted from Cenomanian (green) or Paleocene-Eocene (orange) fluvial deposits. Inset with labelled bars = cumulative percentages of detrital zircon populations at locations that correspond to annotated circles on map. Coloured circles = zircon ages (*Blum et al.*, 2017).

Huntington et al., 2010). *Galloway et al.* (2011), *Blum and Pecha* (2014) and *Blum et al.* (2017) argue that large-scale drainage of the Cordilleran highlands toward the Gulf of Mexico existed by at least Late Paleocene times and that drainage catchments probably extended up to the western flank of the Appalachian mountains. Further west, *Cather et al.* (2008) identified a major denudation event within the Colorado Plateau between the deposition of the Chuska Erg (35–27 Ma) and the Bidahochi Formation ($\sim$ 16 Ma).

Geologic mapping and regional palinspastic reconstructions suggest that the final stages of terrane accretion in Western Canada and Alaska occurred between $\sim$ 50 and 40 Ma and in the Pacific Northwest after $\sim$ 30 Ma, establishing the present-day tectonic configuration of the northwest Cordillera (*Johnston*, 2001; *Dickinson*, 2004). Oxygen isotope paleoaltimetry has been used to suggest that a kilometre-scale 'Nevadaplano' plateau was present in British Columbia by $\sim$ 50 Ma and that it migrated south toward Nevada by $\sim$ 30 Ma (*Chamberlain et al.*, 2012). The presence of an elevated, but low relief, plateau is corroborated by reconstruction of deeply incised, west-flowing paleo-valleys across the present-day crest of the Sierra Nevada (*Best et al.*, 2009; *Cassel et al.*, 2009; *Henry et al.*, 2012). Cross-cutting relationships of extrusive magmatism and ignimbritic flows, thermochronology together with wide-spread deposition of syn-tectonic basin fill suggest that regional compressive stress gave way to extension stress. The Basin and Range province started to extend at $\sim$ 30 Ma and experienced rapid Miocene ($\sim$ 20–15 Ma) stretching and subsidence, coeval with eruption of the Columbia River basalts (*Zoback et al.*, 1981; *Cassel et al.*, 2009; *Colgan and Henry*, 2009; *Chamberlain et al.*, 2012).

The history and chemistry of extrusive western North American magmatism suggest that Cenozoic uplift is related to decompression melting of anomalously warm asthenosphere (Figure 3.4; *Snyder et al.*, 1976; *Fitton et al.*, 1991; *Roy et al.*, 2009; *Ferrari et al.*, 2012). The NAVDAT database contains 6713 samples of extrusive volcanic rocks from the Colorado Plateau and surrounding regions that suggest a trimodal magmatic history, with peaks at $\sim$ 70–55 Ma, 40–20 Ma and 6–0 Ma (Figure 3.4c). Spatio-temporal patterns of magmatism record a westward migration, culminating in a maximum aerial extent during Oligocene times (*Chapin et al.*, 2004). These phases of magmatism are broadly coeval with pulses of sedimentary flux within the Gulf of Mexico between $\sim$ 60–50 Ma, 37–11 Ma and 2–0 Ma (Figure 3.7; *Galloway et al.*, 2011). Recent correlation of basalt geochemistry with shear wave velocities suggests that magmatism and uplift of western North America is generated by a thermal anomaly which sits beneath thin lithosphere (Chapter 2; *Klöcking et al.*, 2018a).

Mexican topography is characterised by an Altiplano-style physiography so that the 1–3 km high

Sierra Madre Occidental, the Mexican Altiplano, the Trans-Mexican Volcanic Belt and the Sierra Madre del Sur together form a broad, elevated region (Figure 3.1a). Reconstruction of an ignimbrite-capped plateau records up to 2 km of incision of the western highlands since 26 Ma (*Montgomery and López-Blanco*, 2003). The southern portion of this region has peaks that are higher than 5 km. Oligocene ignimbrite flare-ups occurred throughout the Sierra del Sur, and migrated southward during Miocene times with a decreasing lithospheric signature (Figure 3.4a, b; *Márquez et al.*, 1999; *Ferrari et al.*, 1999, 2002, 2007). Thermal modelling of heatflow measurements suggests that anomalously hot mantle sits beneath the lithospheric plate (*Ferrari et al.*, 2012).

The cratonic interior of North America, including the Canadian Shield, has a modest average elevation ($\lesssim$ 0.5 km; Figure 3.1a). Backstripping of sedimentary rocks recorded in boreholes shows that it has experienced slow ($\sim$ 0.01–0.001 mm a^{-1}) Paleozoic subsidence (*Armitage and Allen*, 2010). Nonetheless, portions of the Canadian Rockies and of the craton show evidence of youthful uplift. Kimberlites of the Lac de Gras field in central Slave craton that are $\sim$ 75–45 Ma crop out at 550–600 m elevation. Significantly, these deposits contain xenoliths of marine and terrestrial sedimentary rocks of Albian ($\sim$ 113–100 Ma) and Eocene ($\sim$ 56–45 Ma) ages, respectively. The present-day absence of cratonic Phanerozoic sedimentary cover suggests that moderate ($\geqslant$ 300 m) uplift and denudation occurred prior to, and after, magmatic emplacement (*Nassichuk and McIntyre*, 1995; *Heaman et al.*, 2004; *Ault et al.*, 2013). Variations in coal rank from the Upper Cretaceous Plains of Alberta suggest that between 1.1–1.9 km of overburden was removed from the Western Canada basin within the last $\sim$ 60 Ma (*Nurkowski*, 1984; *Bustin*, 1991). These observations are in agreement with modelling of (U-Th)/He in Apatite (A-He) from the Slave craton, which indicate that regions surrounding the cratonic core of North America experienced diachronous post-Cretaceous uplift and exhumation with wavelengths of tens to thousands of kilometres (*Flowers et al.*, 2012; *Ault et al.*, 2013).

The origin of kilometre-scale Appalachian topography remains enigmatic. After the end of rifting at $\sim$ 175 Ma, the eastern seaboard constituted a passive margin (e.g. *Klitgord et al.*, 1988). Long-term slow exhumation rates (20 m Ma^{-1} for $>$ 80 Ma) inferred from AFT measurements are comparable to rates of fluvial erosion estimated using cosmogenic dating. These measurements have been interpreted as evidence for slow and steady decay of an old orogen (cf. *Pavich et al.*, 1985; *Boettcher and Milliken*, 1994; *Matmon et al.*, 2003; *Naeser et al.*, 2004; *Portenga et al.*, 2013). In contrast, A-He thermochronometry suggests that kilometre-scale Late Cretaceous denudation of the southern and northern Appalachians has occurred (*McKeon et al.*, 2014; *Amidon et al.*, 2016). Topographic relief

of the crests of the Appalachian mountains has no obvious relationship to the underlying geologic terranes, which implies that prior tectonic shortening may not be the primary geomorphic control (*McKeon et al.*, 2014).

3.3.4 Neogene Uplift and Denudation

A range of observations suggest that the Appalachian Mountains experienced Neogene uplift and denudation. Elevation of the warped Orangeburg-Chippenham-Thornburg escarpments and of other reconstructed Cenozoic paleoshorelines record tens of meters of Pliocene to Recent uplift (*Spasojević and Gurnis*, 2012; *Rowley*, 2013; *Rovere et al.*, 2014). The shapes of longitudinal river profiles from the southern and central Appalachian Mountains are convex upward, which suggests that this landscape is in disequilibrium (*Gallen et al.*, 2013; *Miller et al.*, 2013; *Prince and Spotila*, 2013; *Gallen*, 2018). Significantly, the Cenozoic stratigraphic record from the adjacent Atlantic shelf shows major pulses of Cretaceous and Miocene sedimentary flux (*Poag and Sevon*, 1989; *Pazzaglia and Brandon*, 1996). Sedimentary flux estimates are incompatible with slow and steady erosion of the Appalachian Mountains. Thermal modelling of A-He observations show increased Miocene exhumation of this region which correlates with increased sedimentary flux (*McKeon et al.*, 2014). As *Taylor and Fitzgerald* (2011) and *McKeon et al.* (2014) point out, the lack of post-Cretaceous AFT or A-He ages at other sites does not necessarily preclude Miocene uplift but it does imply that the magnitude of this denudation is small ($\lesssim 1$ km). In Florida, coarse siliciclastic rocks with a Southern Appalachian provenance overlie Late Miocene carbonate platforms, an observation which is consistent with post-Miocene denudation (*Missimer and Maliva*, 2017). Detrital zircon analyses from the Atlantic Coastal Plain suggest that the recent erosion in the Appalachian Mountains is related to westward migration of eastern drainage divides (*Naeser et al.*, 2016). These combined observations indicate that Appalachian physiography is not solely a result of erosional decay of a Paleozoic mountain chain (cf. *Baldwin et al.*, 2003).

Youthful uplift of the northern Appalachian Mountains and of Newfoundland has also occurred. A combination of AFT modelling and $^{40}Ar/^{39}Ar$ ages from Mount Washington in New Hampshire indicates an increased exhumation rate after 60 Ma (*Roden-Tice et al.*, 2012; *Amidon et al.*, 2016). Along the continental margin of Labrador, calibrated seismic profiles show that Mesozoic strata dip seaward and are truncated by Late Oligocene and younger strata, which are consistent with phases of regional uplift (*Dickie et al.*, 2011). A regional Miocene unconformity has also been documented in offshore seismic data (*Ainsworth et al.*, 2014). Subsidence curves and vitrinite reflectance measurements from the Hopedate E-33 well offshore Labrador show that pre-Pliocene strata have been more deeply buried

by as much as 750 m prior to removal of Miocene strata (*Japsen et al.*, 2016). Earthquake tomographic modelling has identified a region of slow velocity, which has a diameter of $\sim$ 400 km and is known as the Northern Appalachian Anomaly (*Menke et al.*, 2016). This anomaly occurs within the asthenosphere beneath southern New England and, if it is of thermal origin, it may play a role in generating youthful uplift.

In western North America, sedimentary deposits of the Ogallala Group are exposed in the Great Plains and suggest that the eastern margin of the Colorado Plateau was regionally tilted during Miocene times (*McMillan et al.*, 2002). Stratigraphic constraints on the timing of regional tilting places this differential uplift between $\sim$ 6 and 3.7 Ma (*Duller et al.*, 2012). Evidence for younger (i.e. post-8 Ma) regional uplift and surface tilting is corroborated by differential incision of the Rocky Mountains and by a reconstructed low relief surface generated by post-Laramide basin fill, which reached as far east as the Great Plains (*McKenna and Love*, 1972; *McMillan et al.*, 2002). Incision histories of $^{40}Ar/^{39}Ar$-dated basaltic flows within the Colorado, Columbia and Rio Grande catchments help to constrain long-term landscape development (e.g. *Wakabayashi and Sawyer*, 2001; *Karlstrom et al.*, 2008, 2017). These catchments have been incised by tens to hundreds of meters during Neogene times (e.g. *Karlstrom et al.*, 2012; *Nereson et al.*, 2013; *Channer et al.*, 2015; *Repasch et al.*, 2017). $^{40}Ar/^{39}Ar$ dating and magnetostratigraphy of tephra deposits within the oldest marine deposits of the Gulf of California suggests that rifting of the Gulf of California initiated by $\sim$ 7 Ma. Present-day elevations ($>$ 300 m) of the shallow marine Upper Bouse formation implies that uplift of the lower reaches of the Colorado river occurred after $\sim$ 4.8 Ma (*Dorsey et al.*, 2018). Quaternary marine terraces along south-western and eastern coast of Mexico are elevated by several tens of meters above sea level, an observation that is interpreted as a consequence of uplift at rates of up to 3 m ka^{-1} (*Self*, 1977; *Ramirez-Herrera et al.*, 2011).

3.4 Stratigraphic Constraints on Uplift

Elevation of dated marine sedimentary strata is probably the least contentious and most robust constraint on the history of continental uplift. In North America, the distribution of Cretaceous marine rocks provides excellent evidence for kilometre-scale uplift of the Colorado-Columbia-Rocky Mountains Plateaux since $\sim$ 80 Ma (e.g., *Ziegler et al.*, 1985; *Sahagian*, 1987; *Roberts and Kirschbaum*, 1995). In the previous chapter, I made used of the PBDB to produce spot measurements of uplift. Similarly, the youngest outcropping marine to terrestrial sedimentary sequences, which mark the latest regres-

sive transitions, provide also provide key datum against which uplift can be measured. Stratigraphic constraints on the timing of uplift initiation were compiled using the methodology of *Dickinson et al.* (1988), which identifies the last (i.e. youngest) marine to non-marine transitions in the sedimentary record. Central to this methodology is the accurate identification of the age and facies of depositional sequences in a stratigraphic framework that is consistent across the region of interest. The steps to generating a stratigraphic database are as follows.

3.4.1 Regressive stratigraphic sequences

First, a working chronostratigraphic framework was established for the region by adapting published time-scales for the Late Cretaceous of the U.S. Western Interior (Figure 3.9 *Obradovich and Cobban*, 1975; *Cobban et al.*, 2006; *Merewether et al.*, 2011; *Merewether and McKinney*, 2015; *Lynds and Slattery*, 2017). These time-scales were compiled based on extensive fieldwork and fossil analysis by the authors and others. Biostratigraphic ages are based on Molluscan (ammonite) and Inoceramid (bivalve) fossil occurrences, and fossil zones given by the last occurrence of the biostratigraphic marker. Fossil zones are tied to the *Gradstein et al.* (2012) timescale by $^{40}Ar/^{39}Ar$ and $^{40}Ar/^{40}K$ radiometric dating of ashfall and bentonite beds.

Second, regressive stratigraphic sequences were identified from published facies interpretations (e.g., *Roberts and Kirschbaum*, 1995; *Johnson et al.*, 2002; *Gani et al.*, 2015). The approximate location of each stratigraphic column is shown with the corresponding letter on the map (Figure 3.10). References used to determine formation names, ages and depositional environments are listed in Table 3.1 and generalised stratigraphic columns are shown on Figure 3.11. Particular care was taken to identify the lateral and temporal variability of marine to terrestrial transitions, such as, for example, those observed for depositional sequences within the Star Point Sandstone, Blackhawk, Castlegate, and Sego Sandstone Formations (e.g., *Gani et al.*, 2015).

Figure 3.9: **Chronostratigraphic framework of Western Interior of the United States [following page].** Molluscan (ammonite) fossil zones were determined by the last occurrence of the biostratigraphic marker. The numbered zones include several other fossils, such as inoceramids (bivalves). Biostratigraphic ages are tied to the *Gradstein et al.* (2012) time scale by $^{40}Ar/^{39}Ar$ and $^{40}Ar/^{40}K$ radiometric dating of ashfall beds within the fossil zones (after *Merewether et al.*, 2011; *Lynds and Slattery*, 2017, and references therein).

SERIES	Stages	Substages	Western Interior ammonite age spans and radiometric ages [Ma]		Informal zone nos.	Western Interior inoceramid age spans
UPPER CRETACEOUS	Maastrichtian	Upper	K-T boundary	66.02 ± 0.08		
			"Triceratops zone"			
			Hoploscaphites nebrascensis	~68.0	78	
			Hoploscaphites nicolletii	~68.5	77	
			Hoploscaphites birkelundae	~69.4	76	
		Lower	Baculites clinolobatus	70.08 ± 0.37	75	"Inoceramus" balchii
			Baculites grandis	70.66 ± 0.66	74	Trochoceramus" radiosus
			Baculites baculus	~71.5	73	"Inoceramus" incurvus
						Endocostea typica
	Campanian	Upper	Baculites eliasi	72.50 ± 0.31	72	"Inoceramus" redbirdensis
			Baculites jenseni	~73.0	71	"Inoceramus" oblongus
			Baculites reesidei	73.41 ± 0.47	70	
			Baculites cuneatus	~73.7	69	"Inoceramus" altus
			Baculites compressus	74.05 ± 0.39	68	
			Didymoceras cheyennense	74.74 ± 0.23	67	
			Exiteloceras jenneyi	74.85 ± 0.45	66	Sphaeroceramus pertenuiformis
			Didymoceras stevensoni		65	
			Didymoceras nebrascense	75.95 ± 0.41	64	"Inoceramus" tenuilineatus
		Middle	Baculites scotti	76.62 ± 0.51	63	
			Baculites reduncus		62	
			Baculites gregoryensis		61	
			Baculites perplexus	~78.7	60	Cataceramus subcompressus
			Baculites sp. (smooth)	~79.3	59	
			Baculites asperiformis		58	
			Baculites maclearni	80.10 ± 0.61	57	"Inoceramus"azerbaydjanensis
			Baculites obtusus	80.62 ± 0.40	56	
		Lower	Baculites sp. (weak flank ribs)	~80.8	55	
			Baculites sp. (smooth)		54	Cataceramus balticus
			Scaphites hippocrepis III	~81.5	53	
			Scaphites hippocrepis II	81.84 ± 0.22	52	
			Scaphites hippocrepis I	82.29 ± 0.34	51	
			Scaphites leei III	~83.0	50	Sphenoceramus lundbreckensis
	Santonian	Upper	Desmoscaphites bassleri	83.75 ± 0.11	49	
			Desmoscaphites erdmanni	84.55 ± 0.24	48	
			Clioscaphites choteauensis	~84.8	47	Cordiceramus muelleri
		Middle	Clioscaphites vermiformis	~85.5	46	Cordiceramus bueltenensis
						Cordiceramus cordiformis
		Lower	Clioscaphites saxitonianus	85.84 ± 0.37	45	Cladoceramus undulatoplicatus
	Coniacian	Upper	Scaphites depressus	87.13 ± 0.19	44	Magadiceramus crenelatus
						Magadiceramus subquadratus
		Middle	Scaphites ventricosus		43	Volviceramus involutus
					42	Volviceramus koeneni
		Lower	Scaphites preventricosus	89.32 ± 0.34		"Inoceramus" gibbosus
					41	Cremnoceramus crassus crassus
						Cremnoceramus crassus inconstans
					40	Cremnoceramus walt. hannovrensis
					39	Cremnoceramus deformis erectus

UPPER CRETACEOUS	Turonian	Upper	Scaphites mariasensis	89.87 ± 0.18	38	Cremnoceramus walt. waltersdorfensis
			Prionocyclus germari		37	Mytiloides scupini
			Scaphites nigricollensis	~90.2	36	Mytiloides incertus
			Scaphites whitfieldi		35	Inoceramus dakotensis
					34	Inoceramus perplexus
		Middle	Scaphites ferronensis	~90.8	33	
			Scaphites warreni		32	Inoceramus dimidius
			Prionocyclus macombi	91.24 ± 0.23	31	Inoceramus aff. dimidius
			Prionocyclus hyatti	92.46 ± 0.58	30	Inoceramus howelli
			Collignoniceras praecox		29	
			Collignoniceras woollgari	~92.5	28	Mytiloides hercynicus Mytiloides subhercynicus
		Lower	Mammites nodosoides		27	Mytiloides mytiloides
			Vascoceras birchbyi	93.48 ± 0.58	26	Mytiloides kossmati
			Pseudaspidoceras flexuosum	93.19 ± 0.42	25	
			Watinoceras devonense	93.79 ± 0.26	24	Mytiloides puebloensis
	Cenomanian	Upper	Nigericeras scotti		23	Mytiloides hattini
			Neocardioceras juddii	94.10 ± 0.27	22	Inoceramus pictus
			Burroceras clydense	94.20 ± 0.28	21	
			Euomphaloceras septemseriatum	94.43 ± 0.29	20	
			Vascoceras diartianum		19	
			Dunveganoceras conditum		18	Inoceramus ginterensis
			Dunveganoceras albertense	~95.0	17	
			Dunveganoceras problematicum		16	
			Dunveganoceras pondi	95.32 ± 0.61	15	Inoceramus prefragilis
		Middle	Plesiacanthoceras wyomingense	95.53 ± 0.25	14	
			Acanthoceras amphibolum		13	Inoceramus rutherfordi
			Acanthoceras bellense	~95.8	12	Inoceramus arvanus
			Plesiacanthoceras muldoonense		11	Inoceramus macconnelii
			Acanthoceras granerosense		10	
			Conlinoceras tarrantense	96.12 ± 0.31	9	
		Lower	Unzoned	96.56 ± 0.45	8 7 6	
			Neogastroplites maclearni	~97.5	5	Gnesioceramus mowriensis
			Neogastroplites americanus		4	
			Neogastroplites muelleri	~98.5	3	
			Neogastroplites cornutus		2	
			Neogastroplites haasi	99.26 ± 0.70	1	Inoceramus maclearni
				100.5 ± 0.4		

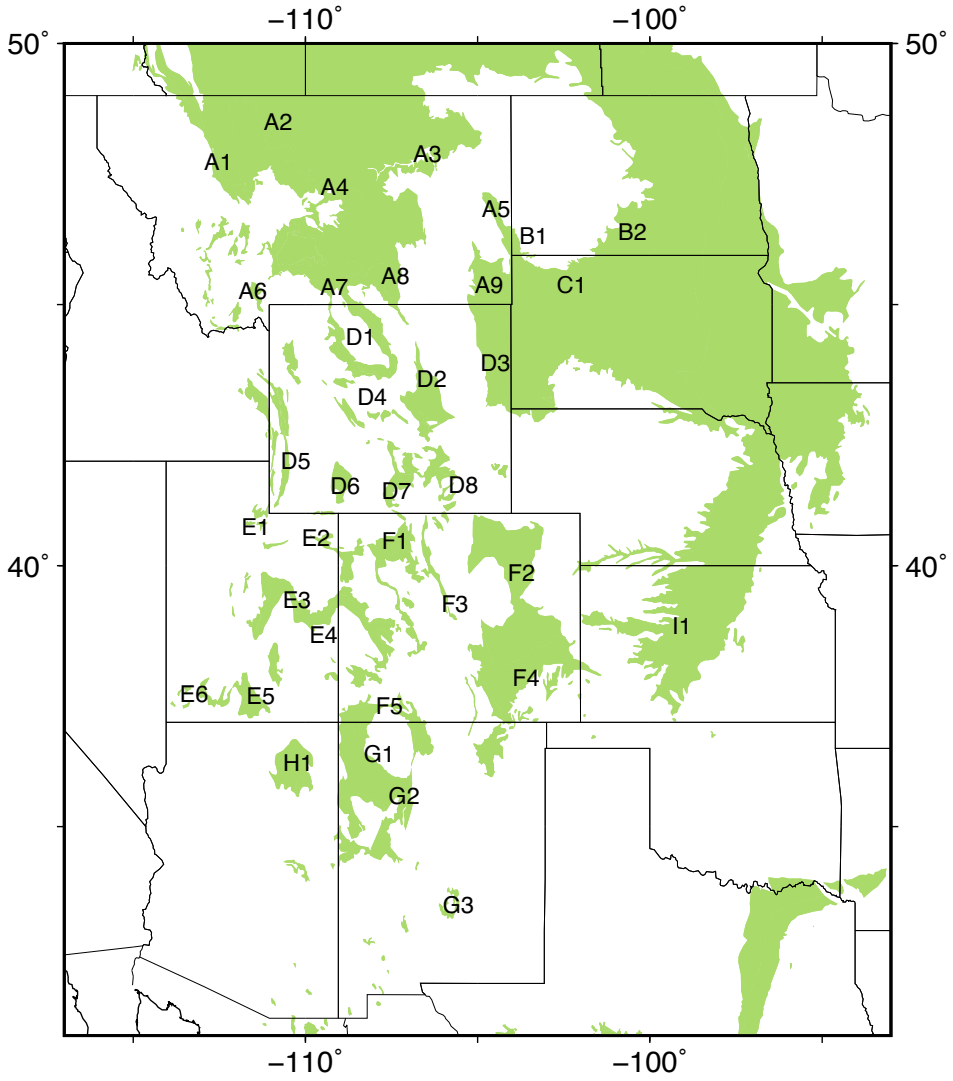

Figure 3.10: **Location of reference stratigraphic columns** containing sedimentary records of marine to terrestrial transitions (numbered letters). Green polygons = location of Cretaceous outcrop.

Figure 3.11: **Stratigraphic columns showing marine to terrestrial transitions recorded in the Cretaceous basins [following page]** of the North American western interior. The approximate location of each stratigraphic column is shown with the corresponding letter on the map (Figure 3.10). References used to determine formation ages and depositional environments for each column are listed in Table 3.1. Stratigraphic nomenclature across the U.S. Western Interior can be inconsistent, especially near the borders with surrounding states. The nomenclature used in this chart is from *Love et al.* (1993) in locations where multiple terminologies are used. Blue = offshore depositional environment (generalised); Yellow = Nearshore to transitional marine depositional environments (generalised); Brown = Terrestrial environment; Vertical lines = missing section/unconformity. fm = formation; mb = member; sst = sandstone. Triangles = last occurrence of age-diagnostic fossil and associated zone. Chronostratigraphic ages from Figure 3.9.

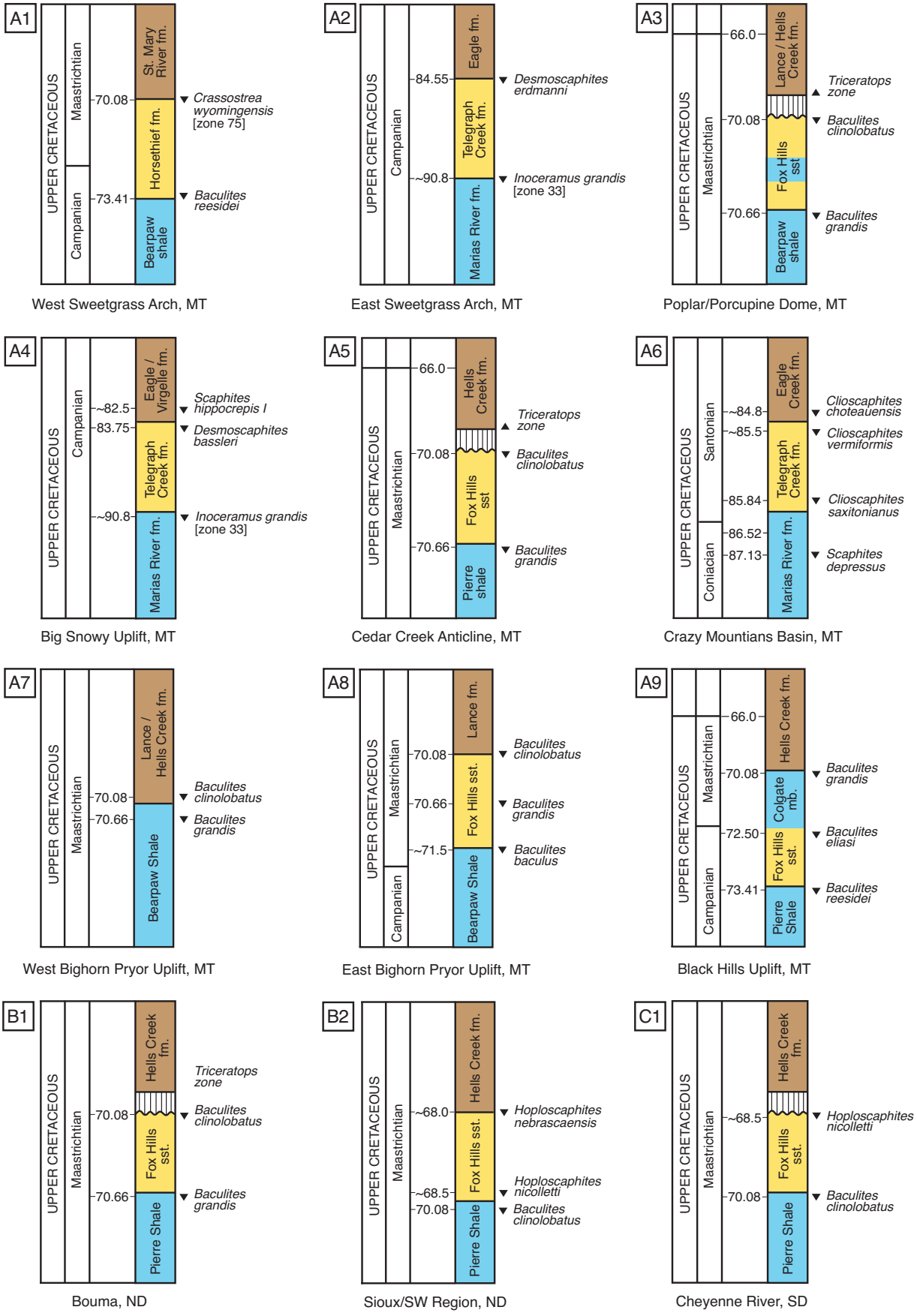
A1
UPPER CRETACEOUS
Maastrichtian
Campanian
70.08
73.41
St. Mary River fm.
Horsethief fm.
Bearpaw shale
Crassostrea wyomingensis [zone 75]
Baculites reesidei
West Sweetgrass Arch, MT
A2
UPPER CRETACEOUS
Campanian
84.55
~90.8
Eagle fm.
Telegraph Creek fm.
Marias River fm.
Desmoscaphites erdmanni
Inoceramus grandis [zone 33]
East Sweetgrass Arch, MT
A3
UPPER CRETACEOUS
Maastrichtian
66.0
70.08
70.66
Lance / Hells Creek fm.
Fox Hills sst
Bearpaw shale
Triceratops zone
Baculites clinolobatus
Baculites grandis
Poplar/Porcupine Dome, MT
A4
UPPER CRETACEOUS
Campanian
~82.5
83.75
~90.8
Eagle / Virgelle fm.
Telegraph Creek fm.
Marias River fm.
Scaphites hippocrepis I
Desmoscaphites bassleri
Inoceramus grandis [zone 33]
Big Snowy Uplift, MT
A5
UPPER CRETACEOUS
Maastrichtian
66.0
70.08
70.66
Hells Creek fm.
Fox Hills sst
Pierre shale
Triceratops zone
Baculites clinolobatus
Baculites grandis
Cedar Creek Anticline, MT
A6
UPPER CRETACEOUS
Santonian
Coniacian
~84.8
~85.5
85.84
86.52
87.13
Eagle Creek fm.
Telegraph Creek fm.
Marias River fm.
Clioscaphites choteauensis
Clioscaphites vermiformis
Clioscaphites saxitonianus
Scaphites depressus
Crazy Mountians Basin, MT
A7
UPPER CRETACEOUS
Maastrichtian
70.08
70.66
Lance / Hells Creek fm.
Beanpaw Shale
Baculites clinolobatus
Baculites grandis
West Bighorn Pryor Uplift, MT
A8
UPPER CRETACEOUS
Maastrichtian
Campanian
70.08
70.66
~71.5
Lance fm.
Fox Hills sst.
Bearpaw Shale
Baculites clinolobatus
Baculites grandis
Baculites baculus
East Bighorn Pryor Uplift, MT
A9
UPPER CRETACEOUS
Maastrichtian
Campanian
66.0
70.08
72.50
73.41
Hells Creek fm.
Colgate mb.
Fox Hills sst.
Pierre Shale
Baculites grandis
Baculites eliasi
Baculites reesidei
Black Hills Uplift, MT
B1
UPPER CRETACEOUS
Maastrichtian
70.08
70.66
Hells Creek fm.
Fox Hills sst.
Pierre Shale
Triceratops zone
Baculites clinolobatus
Baculites grandis
Bouma, ND
B2
UPPER CRETACEOUS
Maastrichtian
~68.0
~68.5
70.08
Hells Creek fm.
Fox Hills sst.
Pierre Shale
Hoploscaphites nebrascaensis
Hoploscaphites nicolletti
Baculites clinolobatus
Sioux/SW Region, ND
C1
UPPER CRETACEOUS
Maastrichtian
~68.5
70.08
Hells Creek fm.
Fox Hills sst.
Pierre Shale
Hoploscaphites nicolletti
Baculites clinolobatus
Cheyenne River, SD

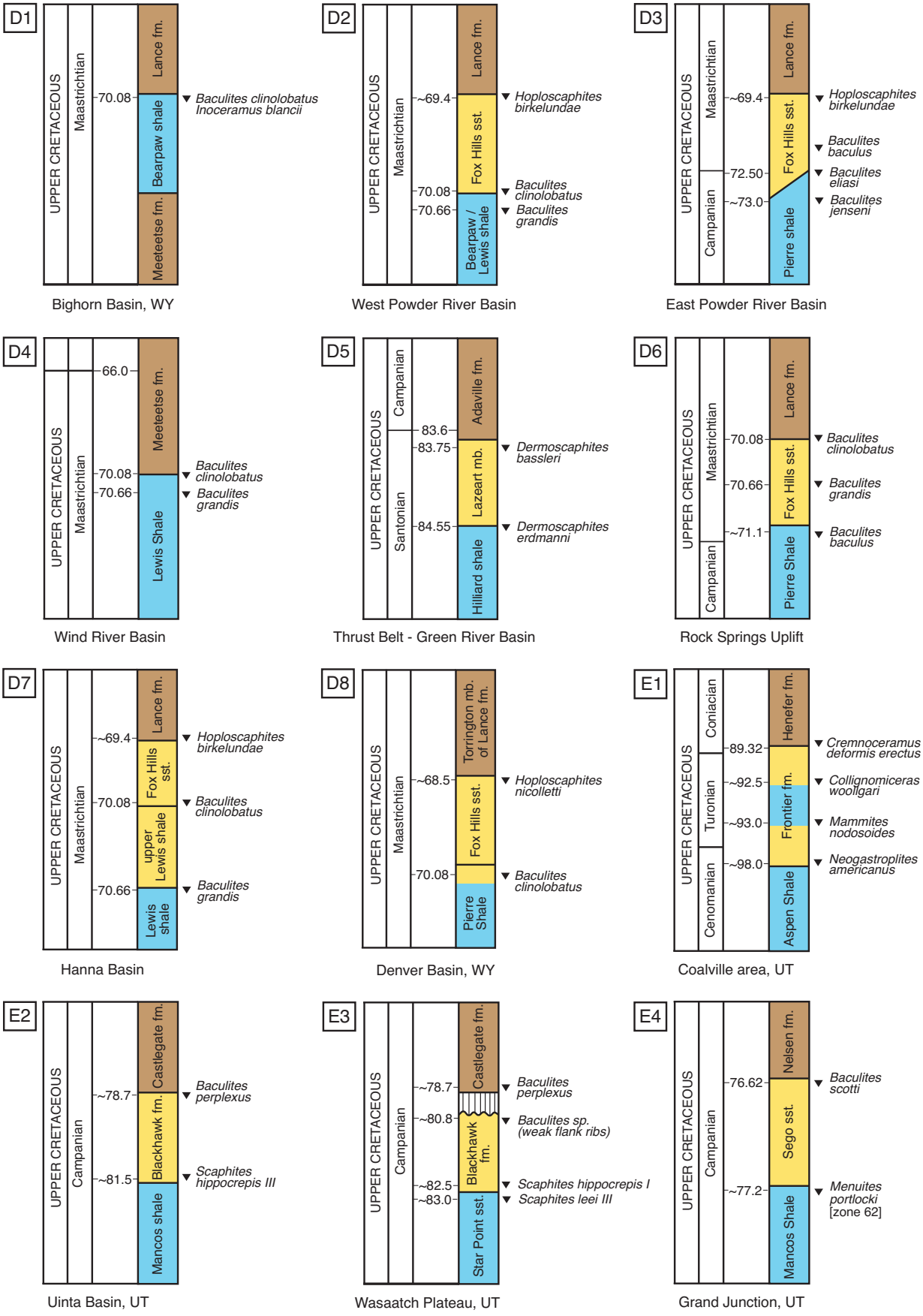
D1
UPPER CRETACEOUS
Maastrichtian
70.08
Lance fm.
Bearpaw shale
Meeteetse fm.
Baculites clinolobatus
Inoceramus blancii
Bighorn Basin, WY
D2
UPPER CRETACEOUS
Maastrichtian
~69.4
70.08
70.66
Lance fm.
Fox Hills sst.
Bearpaw / Lewis shale
Hoploscaphites birkelundae
Baculites clinolobatus
Baculites grandis
West Powder River Basin
D3
UPPER CRETACEOUS
Maastrichtian
Campanian
~69.4
72.50
~73.0
Lance fm.
Fox Hills sst.
Pierre shale
Hoploscaphites birkelundae
Baculites baculus
Baculites eliasi
Baculites jenseni
East Powder River Basin
D4
UPPER CRETACEOUS
Maastrichtian
66.0
70.08
70.66
Meeteetse fm.
Lewis Shale
Baculites clinolobatus
Baculites grandis
Wind River Basin
D5
UPPER CRETACEOUS
Campanian
Santonian
83.6
83.75
84.55
Adaville fm.
Lazeart mb.
Hilliard shale
Dermoscaphites bassleri
Dermoscaphites erdmanni
Thrust Belt - Green River Basin
D6
UPPER CRETACEOUS
Maastrichtian
Campanian
70.08
70.66
~71.1
Lance fm.
Fox Hills sst.
Pierre Shale
Baculites clinolobatus
Baculites grandis
Baculites baculus
Rock Springs Uplift
D7
UPPER CRETACEOUS
Maastrichtian
~69.4
70.08
70.66
Lance fm.
Fox Hills sst.
upper Lewis shale
Lewis shale
Hoploscaphites birkelundae
Baculites clinolobatus
Baculites grandis
Hanna Basin
D8
UPPER CRETACEOUS
Maastrichtian
~68.5
70.08
Torrington mb. of Lance fm.
Fox Hills sst.
Pierre Shale
Hoploscaphites nicolletti
Baculites clinolobatus
Denver Basin, WY
E1
UPPER CRETACEOUS
Coniacian
Turonian
Cenomanian
89.32
~92.5
~93.0
~98.0
Henefer fm.
Frontier fm.
Aspen Shale
Cremnoceramus deformis erectus
Collignomiceras woollgari
Mammites nodosoides
Neogastroplites americanus
Coalville area, UT
E2
UPPER CRETACEOUS
Campanian
~78.7
~81.5
Castlegate fm.
Blackhawk fm.
Mancos shale
Baculites perplexus
Scaphites hippocrepis III
Uinta Basin, UT
E3
UPPER CRETACEOUS
Campanian
~78.7
~80.8
~82.5
~83.0
Castlegate fm.
Blackhawk fm.
Star Point sst.
Baculites perplexus
Baculites sp. (weak flank ribs)
Scaphites hippocrepis I
Scaphites leei III
Wasaatch Plateau, UT
E4
UPPER CRETACEOUS
Campanian
76.62
~77.2
Nelsen fm.
Sego sst.
Mancos Shale
Baculites scotti
Menuites portlocki [zone 62]
Grand Junction, UT

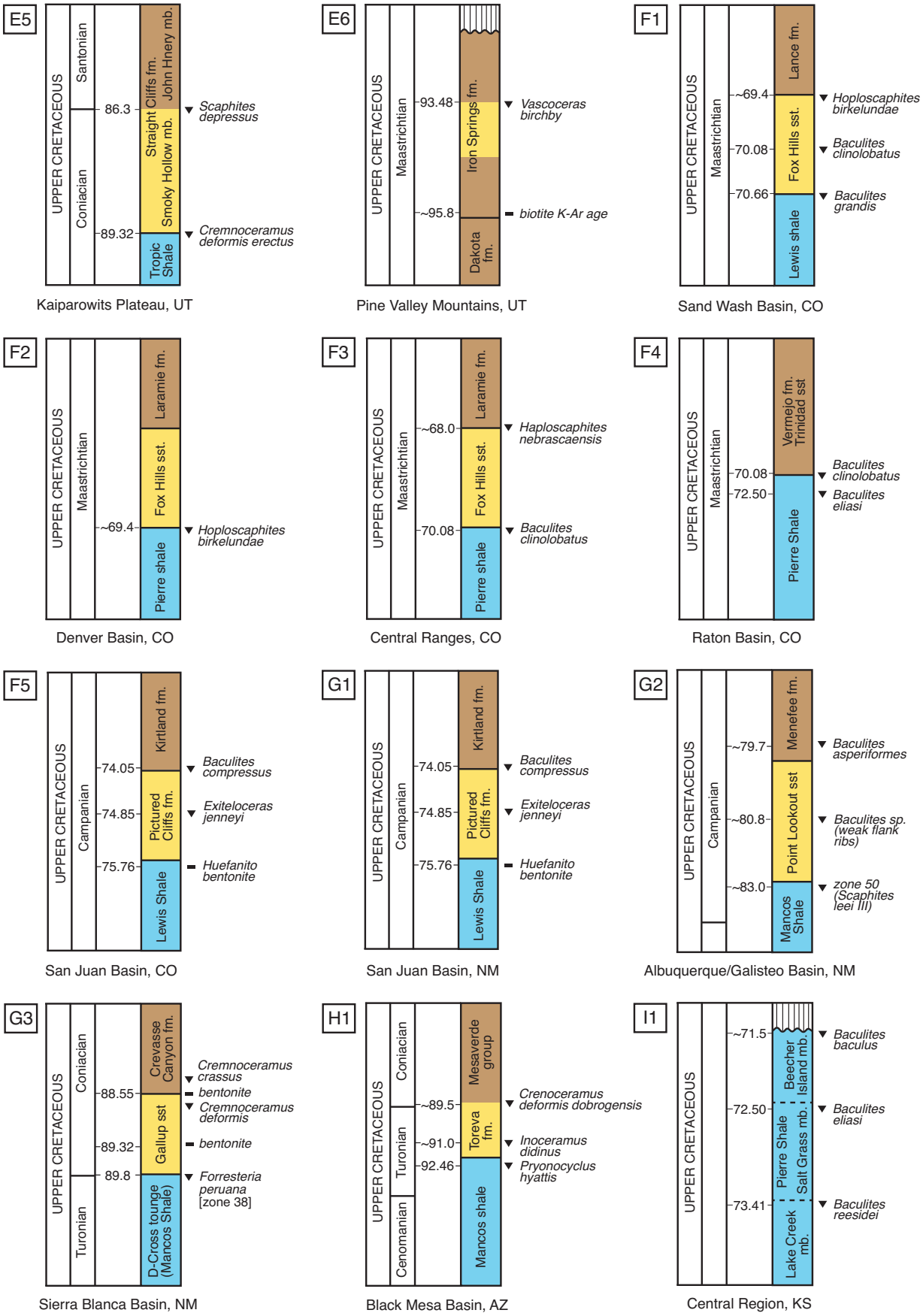
E5
UPPER CRETACEOUS
Santonian
Coniacian
86.3
89.32
Straight Cliffs fm.
John Hnery mb.
Smoky Hollow mb.
Tropic Shale
Scaphites depressus
Cremnoceramus deformis erectus
Kaiparowits Plateau, UT
E6
UPPER CRETACEOUS
Maastrichtian
93.48
~95.8
Iron Springs fm.
Dakota fm.
Vascoceras birchby
biotite K-Ar age
Pine Valley Mountains, UT
F1
UPPER CRETACEOUS
Maastrichtian
~69.4
70.08
70.66
Lance fm.
Fox Hills sst.
Lewis shale
Hoploscaphites birkelundae
Baculites clinolobatus
Baculites grandis
Sand Wash Basin, CO
F2
UPPER CRETACEOUS
Maastrichtian
~69.4
Laramie fm.
Fox Hills sst.
Pierre shale
Hoploscaphites birkelundae
Denver Basin, CO
F3
UPPER CRETACEOUS
Maastrichtian
~68.0
70.08
Laramie fm.
Fox Hills sst.
Pierre shale
Haploscaphites nebrascaensis
Baculites clinolobatus
Central Ranges, CO
F4
UPPER CRETACEOUS
Maastrichtian
70.08
72.50
Vermejo fm.
Trinidad sst
Pierre Shale
Baculites clinolobatus
Baculites eliasi
Raton Basin, CO
F5
UPPER CRETACEOUS
Campanian
74.05
74.85
75.76
Kirtland fm.
Pictured Cliffs fm.
Lewis Shale
Baculites compressus
Exiteloceras jenneyi
Huefanito bentonite
San Juan Basin, CO
G1
UPPER CRETACEOUS
Campanian
74.05
74.85
75.76
Kirtland fm.
Pictured Cliffs fm.
Lewis Shale
Baculites compressus
Exiteloceras jenneyi
Huefanito bentonite
San Juan Basin, NM
G2
UPPER CRETACEOUS
Campanian
~79.7
~80.8
~83.0
Menefee fm.
Point Lookout sst
Mancos Shale
Baculites asperiformes
Baculites sp. (weak flank ribs)
zone 50 (Scaphites leei III)
Albuquerque/Galisteo Basin, NM
G3
UPPER CRETACEOUS
Coniacian
Turonian
88.55
89.32
89.8
Crevasse Canyon fm.
Gallup sst
D-Cross tounge (Mancos Shale)
Cremnoceramus crassus
bentonite
Cremnoceramus deformis
bentonite
Forresteria peruana [zone 38]
Sierra Blanca Basin, NM
H1
UPPER CRETACEOUS
Coniacian
Turonian
Cenomanian
~89.5
~91.0
92.46
Mesaverde group
Toreva fm.
Mancos shale
Crenoceramus deformis dobrogensis
Inoceramus didinus
Pryonocyclus hyattis
Black Mesa Basin, AZ
I1
UPPER CRETACEOUS
~71.5
72.50
73.41
Beecher Island mb.
Pierre Shale
Salt Grass mb.
Lake Creek mb.
Baculites baculus
Baculites eliasi
Baculites reesidei
Central Region, KS

Table 3.1: References for generalised stratigraphic columns

Reference	Column Number
Cobban et al. (2006)	A2, A4, A8
Eaton et al. (1997)	E6
Gill et al. (1972)	I1
Hettinger and Roberts (2005)	F1
Hook et al. (2012)	G3
Johnson et al. (2002)	A3, A5, B1,B2, C1
Johnson (2003)	E2
Landman and Cobban (2003)	F3
Lynds and Slattery (2017)	A7, D1, D2, D3, D4, D5, D6, D7, D8, F1
McLaurin and Steel (2000)	E3
Merewether et al. (2011)	A9, F4
Merewether and McKinney (2015)	A1, A6, E4, E5, F5, G1, G2, H1

The stratigraphic nomenclature of correlative formations across the U.S. Western Interior is variable, such that units of the same age and depositional facies might have distinct names in individual basins. For that reason, generalised stratigraphic columns were defined for each basin. Where multiple terminologies are used, I have adopted formation names of *Love et al.* (1993). For a given stratigraphic column, maximum age of the marine to non-marine transition was assigned as the top of the offshore unit (blue), and minimum as the top of the nearshore/transitional marine unit (yellow). For example, in column B2 (Sioux Region, North Dakota) the maximum age was assigned to the *Hoploscaphites nebrascaensis* zone ($\sim$ 68.0 Ma) and the top to the *Baculites clinolobatus* zone (70.8 Ma). Where the transition is marked by an unconformity (e.g., column A5 - Cedar Creek Anticline, Montana) or an abrupt transition from offshore to terrestrial facies (e.g., column D1 - Bighorn Basin, Wyoming), the age is assigned based on the youngest marine age.

Finally, the locations were these marine to non-marine transitions occur at the surface were determined from state geologic maps (`https://ngmdb.usgs.gov`; references for individual state maps shown in Table 3.2). Rocks of the U.S. Western Interior are well exposed as surface outcrops, therefore mapped geologic units provide a good guide to the location of formation contacts. For each region, the location of the transition between marine and non-marine was defined as the contact between the nearshore/transitional marine units and terrestrial units (yellow and brown, respectively, on Figure 3.11). Contacts were then extracted from geo-referenced Geological Maps using ArcGIS.

Table 3.2: References for state-wide geological maps

	Map	Reference
A	Montana	*Vuke et al.* (2007)
B	North Dakota	*Clayton et al.* (1980)
C	South Dakota	*Martin et al.* (2004)
D	Wyoming	*Love and Christiansen* (1985)
E	Utah	*Hintze* (1980)
F	Colorado	*Tweto* (1979)
G	New Mexico	*Scholle* (2003)
H	Arizona	*Richard et al.* (2000)
I	Kansas	*Kansas Geological Survey* (2008)

Net uplift at these spot locations was determined using the methodology outlined in Chapter 2. The paleobathymetric range for each regressive sequence was set at 0 ± 10 m. The error was included to account for environmental variability within the nearshore/transitional marine units. Together, the regressive sequences and PBDB points comprise 4972 individual spot measurements of net uplift. Elevation of each sample was extracted from the Advanced Space-borne Thermal Emission and Reflection Radiometer (ASTER) global digital elevation model which has vertical and horizontal resolutions of ~ 20 m and ~ 75 m, respectively (*Tachikawa et al.*, 2011).

3.4.2 Net Uplift of North America

Paleo-water depth and net uplift calculated from the PBDB and stratigraphic constraints are shown in Figure 3.12. In Figure 3.13, cross sections 3.13c–e compare present-day elevations of biostratigraphic and stratigraphic constraints with a 100 km wide topographic swath along three key transects. In each case, the spatial distribution of samples reveals a broad swell which matches the topography. Net calculated uplift, shown in Figure 3.12, is greater than present-day elevation. Samples used in this study indicate that water depth of the Late Cretaceous Western Interior Seaway was ≤ 300 m (Figure 3.12a; *Arthur and Sageman*, 2004). These shallow values imply that the present-day elevation of each sample is broadly representative of its net uplift. As previously shown in Chapter 2, the compiled results show that since 80–65 Ma, a region encompassing the Colorado Plateau, Southern Rocky Mountains and swathes of the Great Plains have been uplifted to form a broad swell that has a wavelength of ~ 1500 km (Figure 3.12b, Figures 3.13c and e). Uplift reaches a maximum of ~ 3 km in the Colorado Plateau and Southern Rocky Mountains, decreasing smoothly to ~ 500 m at the eastern

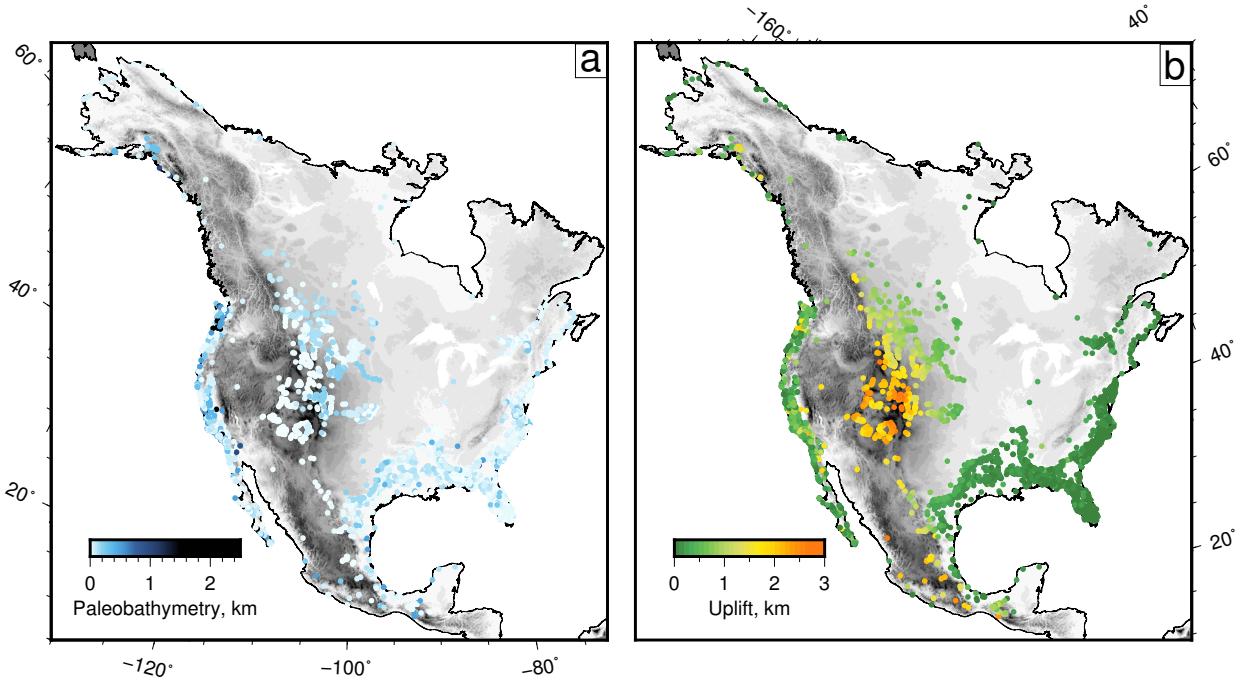

Figure 3.12: **Paleobathymetry and net uplift** from stratigraphic and biostratigraphic PBDB constraints (a) Blue circles = paleo-water depths (see scale bar). (b) Coloured circles = net uplift determined from marine to terrestrial transitions recorded by stratigraphic record and fossil assemblages.

edge of the Great Plains (e.g., Figure 3.12, Chapter 2).

The age constraint for initiation of uplift is in general agreement with the proposed start of the Laramide orogeny (*Dickinson et al.*, 1988). Superimposed on this broad swell are shorter wavelength (< 100 km) variations in elevation of up to 1 km, which probably reflect uplift caused by horizontal

Figure 3.13: **Stratigraphic and biostratigraphic constraints** (following page). (a) Coloured circles show location and age of marine fossil assemblages from the PBDB as well as youngest marine to non-marine stratigraphic transitions. Black lines = locations of vertical cross sections shown in panels c–e; white circles = locations of stratigraphic columns shown in panels f–h, i–k and l–n. (b) Extent of Late Cretaceous seaway interpreted from PBDB. Solid blue polygons/dashed lines = maximum flooding extent of Cretaceous (i.e. Late Maastrichtian) interior seaway (*Smith et al.*, 1994; *Kauffman and Caldwell*, 1993). Dark/light green polygons = outcropping Lower/Upper Cretaceous rocks (*Reed et al.*, 2005). (c–e) Topographic and stratigraphic cross sections (see panel a for location); black line with grey band = topography ± maximum and minimum elevation within 100 km swath; labelled arrows = location of stratigraphic columns shown in adjacent panels; coloured circles = biostratigraphically dated marine rock coloured according to age (see scale bar); light blue band = free-air gravity anomaly ± maximum and minimum within 100 km swath from GRACE database (Figure3.1). SG = San Gabriel Mountains, RM = Rocky Mountains, GP = Great Plains, MH = Mexican Highlands, TX = Texas, A = Appalachian Highlands, PC = Pacific Coast Ranges, CP = Colorado Plateau. (f–n) Generalised stratigraphic sections with youngest marine regression or outcropping marine strata (arrow); blue boxes = shallow marine facies; yellow boxes = marginal marine/shoreface facies; brown boxes = terrestrial facies.

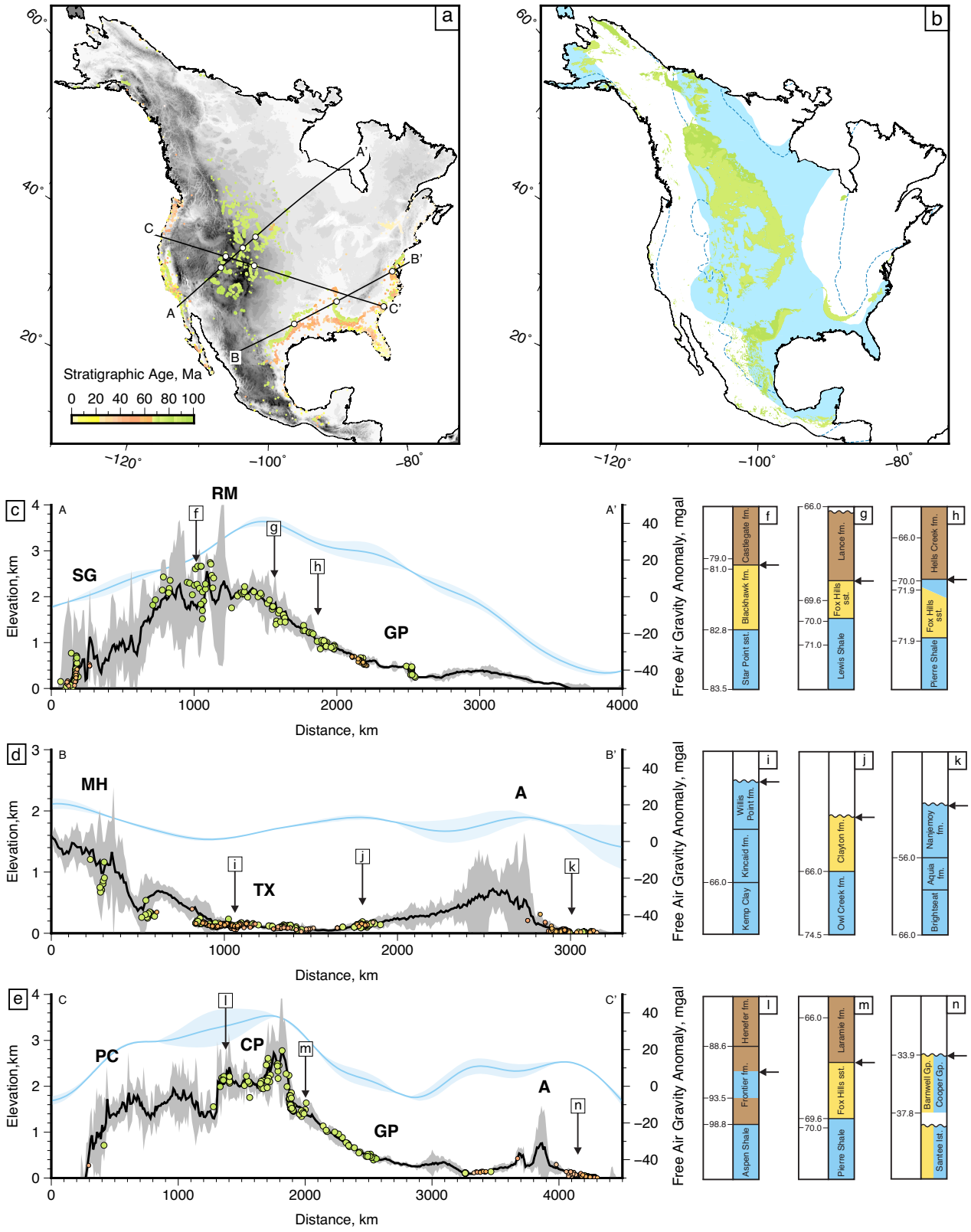
a
b
c
d
e
60°
40°
20°
−120°
−100°
−80°
A
A'
B
B'
C
C'
Stratigraphic Age, Ma
0 20 40 60 80 100
RM
SG
GP
MH
TX
A
PC
CP
Elevation,km
Distance, km
Free Air Gravity Anomaly, mgal
Castlegate fm.
Blackhawk fm.
Star Point sst.
Lance fm.
Fox Hills sst.
Lewis Shale
Hells Creek fm.
Pierre Shale
Wills Point fm.
Kincaid fm.
Kemp Clay
Clayton fm.
Owl Creek fm.
Nanjemoy fm.
Aquia fm.
Brightseat
Henefer fm.
Frontier fm.
Aspen Shale
Laramie fm.
Pierre Shale
Barnwell Gp.
Cooper Gp.
Santee lst.

shortening within the Rocky Mountains (Figure 3.13c and e; e.g. *Fan and Carrapa*, 2014). In general, however, the correlation between large-scale uplift patterns and individual Laramide structures is tenuous since in many locations there is little difference in net uplift between the Rocky Mountain front and the Great Plains (cf. *DeCelles*, 2004, ; Figure 3.12b). A similar pattern is observed for the central and southern portions of the Mexican Highlands where 1.5–2.5 km of post-Cretaceous uplift decreases smoothly toward the Gulf coast and toward the Basin and Range province. Sample density makes it difficult to distinguish smaller scale uplift patterns.

Along the Gulf and Atlantic Coastal Plains, sedimentary successions containing marine fossils were deposited on a shallow marine shelf, at the shoreface, or within a deltaic environment. In general, they record seaward progradation of the continental shelf (Figure 3.12a; *Olsson et al.*, 1988; *Gohn*, 1988; *Pazzaglia and Gardner*, 1994). Figure 3.13d shows Late Cretaceous to Eocene age samples from the Gulf Plain region at elevations of $\sim$ 200 m. Here, calculated uplift smoothly increases westward towards the Mexican Highlands where Cretaceous samples from the Rio Grande Embayment are at an elevation of 500 m. Regional tilt of the eastern Gulf Coast and Atlantic Coastal Plain samples (Figure 3.13d and e; stratigraphic columns j, k and n) is suggestive of long-wavelength ($\sim$ 1000 km) surface uplift of magnitude $\leq$ 300 m that has developed since Eocene times. Regional uplift calculated for samples along the Pacific Coastal Ranges reveals no simple large-scale pattern, which probably reflects the complex tectonic history of terrane accretion, lateral displacement, subduction and subsidence (e.g., *Awater*, 1970).

The magnitude of regional uplift across the Colorado Plateau, Mexico and the Appalachian Mountains is obviously too great to be accounted for by glacio-eustasy (cf. *Miller*, 2005). Figure 3.13c-e shows the pattern of maximum and minimum free-air gravity anomalies, which broadly mimics topographic elevation. Long wavelength ($>$ 1000 km) post-Cretaceous warping of North American topography and the co-location of gravity anomalies, slow shear wave velocity anomalies, and magmatic observations indicate that sub-plate support has played a significant role in generating and maintaining kilometre-scale Cenozoic epeirogeny of large portions of North America (Figures 3.1, 3.3 and 3.4). Despite the spatial and temporal coverage provided by the PBDB, there are extensive tracts where uplift histories are poorly understood since it is difficult to interpolate between spot measurements. A potentially fruitful approach is to exploit drainage patterns, which are ubiquitous throughout the continent.

3.5 River Profile Inversion

In principle, drainage networks should indirectly record uplift histories although this record is obscured by the erosional process (e.g. *Howard*, 1994; *Whipple and Tucker*, 1999; *Snyder et al.*, 2000; *Kirby and Whipple*, 2001; *Wobus et al.*, 2006). Significant effort has been put into developing techniques that can be used to extract information about geologic and geomorphological processes from fluvial networks. Many modelling studies have shown that the shape of a river profile is affected by changes in uplift rate, which acts to generate transient knickzones (e.g. *Howard and Kerby*, 1983; *Rosenbloom and Anderson*, 1994; *Crosby and Whipple*, 2006). It is evident that longitudinal rivers profiles from multiple catchments share common knickzones, which suggests that uplift rate can affect whole catchments (e.g. *Roberts et al.*, 2012a; *Roberts*, 2019). Here, I apply a general inverse approach that enables regional rock uplift rates as a function of time and space to be extracted from large inventories of river profiles (*Rudge et al.*, 2015). This approach has three important steps. First, continent-wide drainage patterns are extracted from a suitable digital elevation model and their veracity checked using satellite imagery. Secondly, a physically appropriate erosional model is chosen. Thirdly, the erosional constants used in this model are calibrated and the drainage inventory is inverted to determine the smoothest rock uplift rate history that minimises the misfit between observed and calculated river profiles. It is crucial that the calculated rock uplift history is carefully tested using independent geologic observations. Each of these steps is tackled in the following way.

3.5.1 Drainage Inventory

An inventory of 4161 river profiles was extracted from the ASTER GDEM database. Esri flow-routing algorithms were used to calculate overland flow, which in turn enables river profiles to be constructed. Rivers were extracted from cells with calculated upstream drainage areas larger than 4 km^2. The planform drainage network was compared to satellite imagery (e.g., Copernicus, Landsat) and it can be shown that the extracted network has high fidelity in regions away from flat topography and narrow (< 30 m wide) gorges. Figure 3.14 shows the drainage distribution for North America, which is radially distributed about four major topographic swells: the Yukon plateau (centred on 60° N and 140° W), the Colorado-Columbia-Rocky Mountains Plateaux (45° N and $-05°$ W); Mexico (20° N and 100° W); and the Appalachian mountains (35° N and 80° W).

Families of longitudinal river profiles grouped by catchment are shown in Figure 3.15. Profiles from the Colorado catchment exhibit two substantial convexities at $\sim$ 500–1000 km and at $\sim$ 1500–2500 km

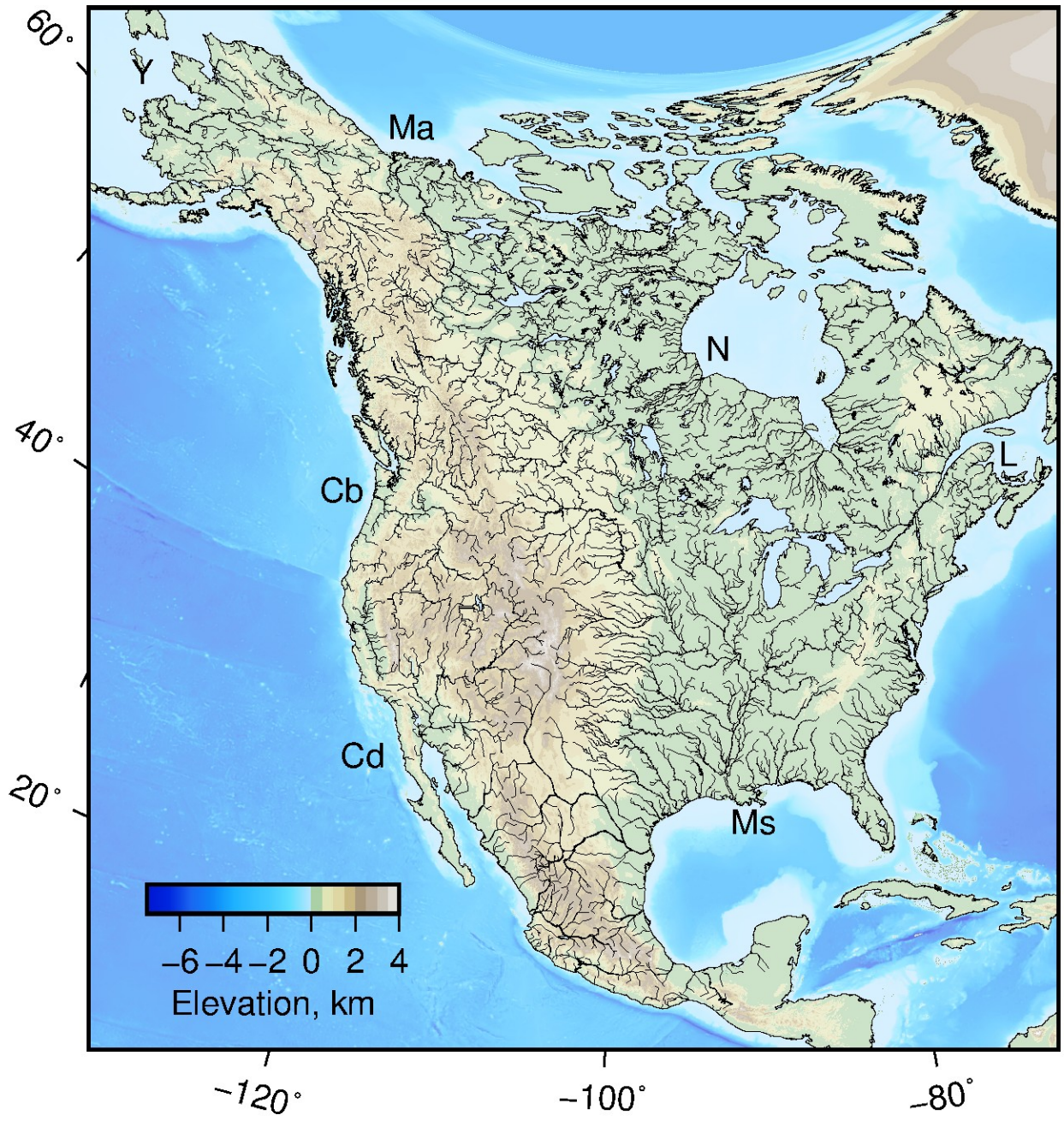

Figure 3.14: **Topography and drainage of North America.** Thin black curves = 4161 rivers extracted from ASTER GDEM database. Ms = mouth of Mississippi; L = St. Lawrence; N = Nelson; Ma = Mackenzie; Y = Yukon; Cb = Columbia; Cd = Colorado. Drainage network is draped over topography from ASTER GDEM

(Figure 3.15). River profiles from the Columbia catchment and from the upper western reaches of the Mississippi catchment also have substantial knickzones (Figure 3.15). Pronounced convexities are observed on river profiles that drain northern and eastern North America (e.g., at $\sim$ 1500–2000 km along the Nelson river). Many other North American catchments also have large convex-upward knickzones. The locations of these broad knickzones do not generally correlate with lithologic contacts,

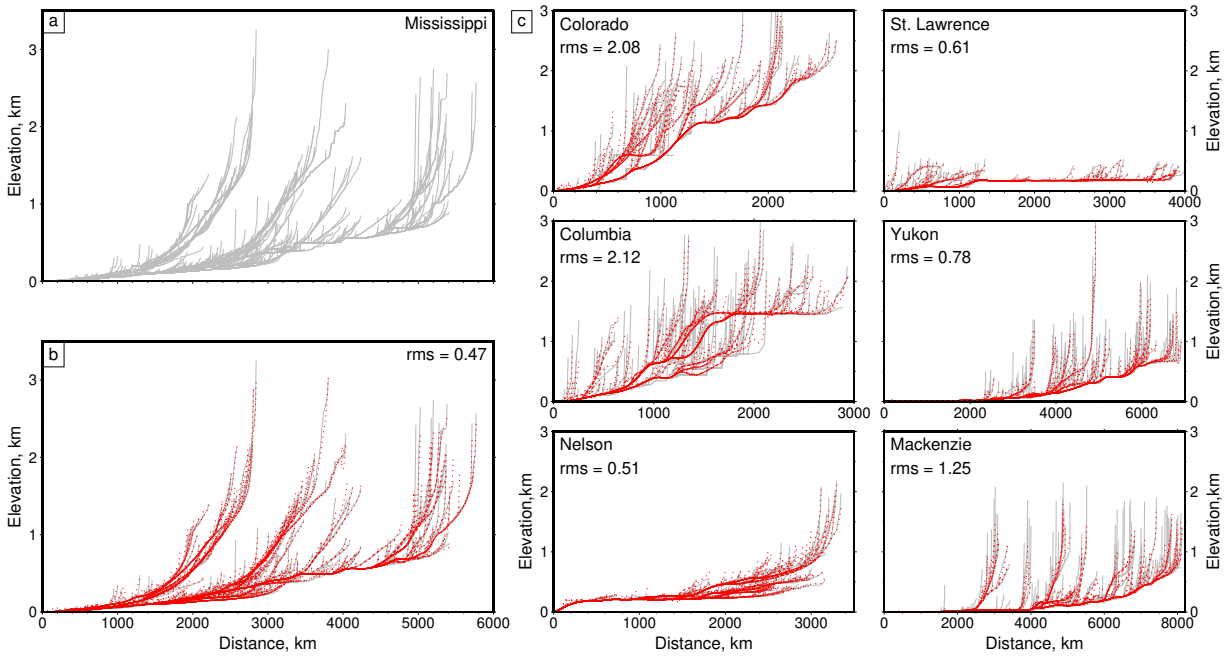

Figure 3.15: **Inverted longitudinal river profiles.** (a) Observed river profiles for Mississippi and its principal tributaries (see Figure 3.1). (b) Observed and calculated river profiles for Mississippi catchment. Red dotted lines = best-fitting theoretical river profiles calculated using uplift history shown in Figure 3.18; value of root-mean-squared (rms) misfit is shown in top right-hand corner. Spatial distribution of misfit is shown in Figure 3.17. (c) Observed and calculated river profiles from six catchments shown in Figure 3.1.

which suggests that their shapes are not related to substrate (e.g., bedrock) in a simple way (*Roberts et al.*, 2012b). Instead, the observed commonalities of long wavelength knickzones draining the four topographic swells suggests that they could have been generated by the spatial and temporal pattern of regional uplift.

3.5.2 Erosional Parameterisation

Shapes of longitudinal river profiles, $z(x)$, are controlled by the history of rock uplift rate, U, and by erosion rate, E, both of which can vary as a function of space, x, and time, t (e.g. *Gilbert*, 1877; *Davis*, 1899; *Howard*, 1994; *Whipple and Tucker*, 1999; *Sklar and Dietrich*, 1998; *Loget and Van Den Driessche*, 2009; *Anderson and Anderson*, 2010). A range of laboratory experiments and field measurements suggest that erosion rate depends upon a suite of complex processes that include the dynamics of water flow (e.g., discharge, turbulence, vorticity), strength of the substrate (e.g., bedrock), orientation of jointing and fracturing, local erosional mechanisms, sediment supply and biota (e.g. *Sklar and Dietrich*, 1998, 2001; *Brocard and Van Der Beek*, 2006; *Allen et al.*, 2013; *DiBiase et al.*, 2014; *Mackey et al.*, 2014; *Rengers and Tucker*, 2014; *Castelltort et al.*, 2015; *Brocard et al.*, 2016; *Baynes*

et al., 2018).

At continental scales, it appears that large, coherent signals become emergent and that the stream power equation provides a practicable way to model drainage evolution through time and space (e.g. *Roberts*, 2019). For example, at wavelengths > 10 km, lithology does not appear to correlate with changes in slope, with curvature or with stream power (*Roberts et al.*, 2012b; *Czarnota et al.*, 2014). These inferences are consistent with spectral analyses of river profiles, which suggest that processes operating at long wavelengths (> 100 km) dominate the shapes of river profiles (*Roberts et al.*, 2019; *Roberts*, 2019). Assumptions of erosional thresholds do not seem to be required in order to achieve a good match between observed and calculated river profiles at these long wavelengths (*Roberts et al.*, 2012a). Furthermore, changes in precipitation rate where the period is less than about 1 Ma do not significantly affect calculated river profile shapes (e.g. *Paul et al.*, 2014)). Fluvial erosion appears to be a highly integrative process such that regional uplift primarily determines profile shape. The empirical stream power equation is given by

$$\frac{\partial z(x,t)}{\partial t} = -vA(x)^m \left(\frac{\partial z(x,t)}{\partial x} \right)^n + U(x,t), \tag{3.2}$$

where upstream drainage area A varies as a function of distance, x. z is elevation above sea level, t is time and U is rock uplift rate. Values of the erosional constants v, m and n can be determined by independent calibration. Equation (2) can be solved in order to calculate U. For example, *Pritchard et al.* (2009) demonstrated that U can be extracted from river profiles by exploiting the method of characteristics. Later, *Royden and Perron* (2013) employed the same integrative approach to calculate metrics that may relate to landscape evolution. These metrics, notably τ_G and χ, are often used to gauge the time taken for erosional signals to propagate through a given landscape and to infer drainage divide migration. A challenging problem is that regional uplift signals are generally inserted into the upstream reaches of individual rivers and catchments. An obvious solution is to pose the inverse problem whereby a smoothly varying rock uplift rate history, $U(x, y, t)$, is sought. The problem can be solved by either linear or non-linear optimisation. I make the assumption that drainage area is temporally invariant, which implicitly assumes that reorganisation of planform does not significantly affect shapes of rivers at the scales of interest (*Paul et al.*, 2014; *Rudge et al.*, 2015). Significantly, no *a priori* assumptions about the spatial and temporal distribution of uplift signals are made. An inverse approach provides a pragmatic and testable way to calculate rock uplift rate histories at scales appropriate for investigating histories of sub-plate support.

3.5.3 Inverse Modelling

The inverse scheme proposed by *Pritchard et al.* (2009) was generalised to incorporate 'erosional diffusivity' and spatio-temporal changes in uplift rate histories by exploiting quasi-linear optimisation methodologies (*Roberts and White*, 2010; *Roberts et al.*, 2012a). A significant benefit of non-linear inverse modelling is that it is possible to investigate the importance of erosional parameters whose values are much debated (*Lague*, 2014). For example, a suite of inverse models shows that residual misfit is minimised when the slope exponent, n, equals 1 (*Paul et al.*, 2014). This result means that a simplified erosional model can be used to develop a linearised inverse model using a Bayesian approach in which *a posteriori* probability distributions (e.g., prior guesses at approximate rock uplift histories) are defined and, alternatively, a damped linear least squares approach that has a null starting set (*Fox et al.*, 2014; *Goren et al.*, 2014; *Rudge et al.*, 2015). Other schemes have also been proposed (e.g. *Campforts and Grovers*, 2015; *Glotzbach*, 2015).

Rudge et al. (2015) show that smooth spatio-temporal rock uplift histories can be obtained by linear inverse modelling without recourse to prior information. By solving the simplified stream power equation using the method of characteristics, the landscape response time, τ_G, can be expressed as

$$\tau_G - t = \int_0^{x(t)} \frac{\mathrm{d}x}{vA^m}. \tag{3.3}$$

Elevation is given by

$$z^* = \int_0^{\tau_G} U(x(t), t)\mathrm{d}t, \tag{3.4}$$

(*Luke*, 1972; *Weissel and Seidl*, 1998). The resultant set of linear equations that relate elevation to rock uplift and erosion is rewritten in matrix form as

$$\mathbf{z} = \mathrm{M}\mathbf{U}. \tag{3.5}$$

Families of river profiles are inverted by minimising

$$|\mathrm{M}\mathbf{U} - \mathbf{z}|^2 + \lambda_S^2|\mathrm{S}\mathbf{U}|^2 + \lambda_T^2|\mathrm{T}\mathbf{U}|^2. \tag{3.6}$$

where S and T are the spatial and temporal smoothing matrices, respectively (*Rudge et al.*, 2015). U is permitted to vary subject to a non-negativity constraint, $\mathbf{U} \geq 0$, since river profile elevations constitute

positive measurements. Uplift rate is allowed to vary as a function of time at vertices arranged in a triangular grid with a spacing of 125 km. The starting set is the null set and no assumption is made about pre-existing North American paleotopography. Uplift along river profiles is linearly interpolated from this spatio-temporal grid. It is important to note that the model cannot resolve uplift rate at times that are greater than the largest value of τ_G. Following *Parker* (1994)'s protocol, the spatial and temporal smoothing coefficients, λ_S and λ_T, are systematically varied to identify the smoothest model that yields the best fit between observed and calculated river profiles (Figure 3.16a). Here, I used $\lambda_S = 0.5$ and $\lambda_T = 0$ and the effective temporal resolution is 5.7 Ma. I explore the effect of using different values of λ_S in Section 3.5.4.

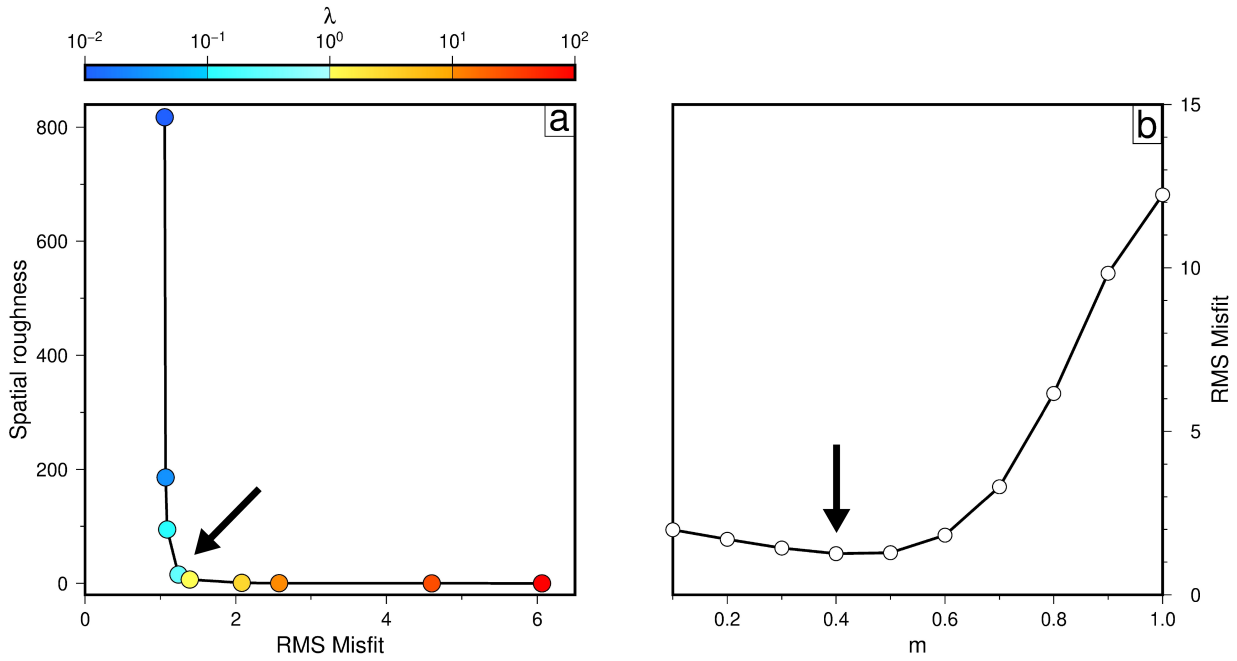

Figure 3.16: **Inverse model parameterisation** (a) Data misfit plotted as function of model smoothness for suite of inverse models with different values of smoothing parameter, λ_S (see Figure 3.18a for configuration of inverse model). Black arrow = locus of smoothest, best-fitting model where $\lambda_S = 0.5$. (b) Residual misfit plotted as function of erosional parameter m. Black arrow = locus of weak global minimum at $m \approx 0.4$.

One way to constrain the value of m is to calculate residual misfit from a suite of inverse models for which m is systematically varied. In each case, it is important to ensure that the same number of free parameters is used. In essence, this approach exploits the spatial geometry of drainage networks (i.e. $A(x)$ and $z(x)$) to constrain m. Crucially, rock uplift is allowed to vary spatially and temporally, which means signals can be inserted at any position along different river profiles, and I do not assume river profiles are in steady state (i.e. $\partial z/\partial t = 0$). Indeed, I caution against the use of methodologies which assume steady state, which exploit the derivative of river profiles, or which prescribe an a

priori uplift history (e.g., χ-analysis). In general, all three of these assumptions yield unstable and misleading results. Figure 3.16b shows that North American river profiles are consistent with an optimal value of $m = 0.4$, although the range $0.2 \leq m \leq 0.5$ has sufficiently small residual misfits to be deemed acceptable. The value of v, which trades off against m, was calibrated using the history of incision recorded by eroded lava dams within the Grand Canyon (*Karlstrom et al.*, 2008). The mean incision rate is 111 ± 7 m Myr^{-1}. By combining this rate with local slope and area measurements *Roberts et al.* (2012a) showed the relationship between erosional parameters v and m is $v = 4.16 \times 10^4 \times (2.78 \times 10^{-12})^m$. For $m = 0.4$, v has a value of 0.99 ± 0.062 m$^{0.2}$ Myr^{-1}. I explore the impact of changing v by plus or minus one order of magnitude in Section 3.5.4.

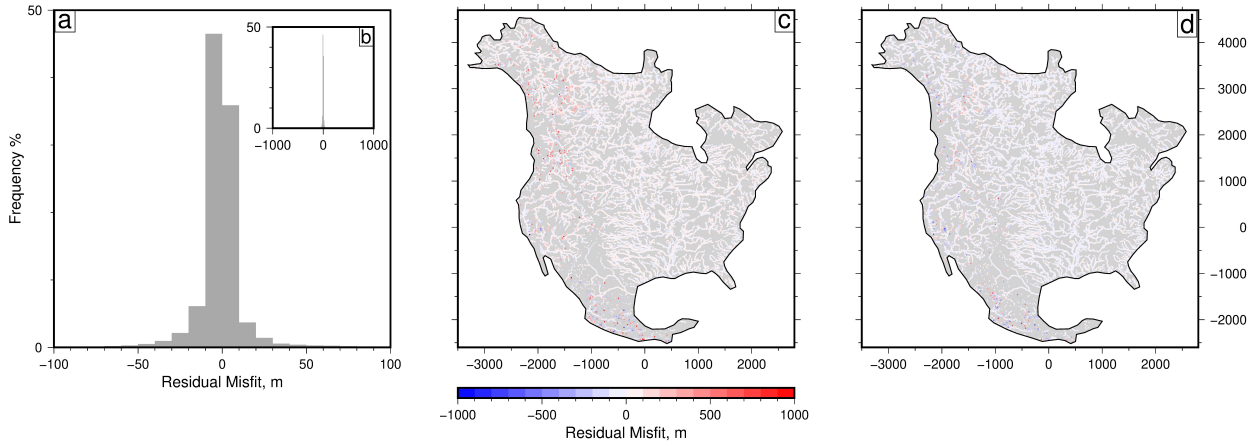

Figure 3.17: **Residual misfit.** (a) Histogram of residual misfit between observed and predicted river profiles. (b) Inset showing full frequency distribution of residuals. (c) Residual positive misfit map between observed and calculated river profiles. (d) Residual negative misfit map.

The optimal fit between observed and calculated river profiles shown in Figure 3.15 is obtained for the cumulative rock uplift history shown in Figure 3.18. The root-mean-squared (rms) misfit is given by

$$\left[\frac{1}{N}\sum_{i=1}^{N}\left(\frac{z_i^o - z_i^c}{\sigma}\right)^2\right]^{1/2}, \tag{3.7}$$

where N = number of data values, z^o and z^c are observed and calculated river elevations, respectively. Distribution of residual misfit, both positive and negative, is shown in Figure 3.17. Elevation variance was set as a constant value of $\sigma = 20$ m, based upon the reported resolution of the ASTER database (*Tachikawa et al.*, 2011). I emphasise that alternative objective functions can be used to measure the goodness of fit between observed and calculated river profiles without significantly affecting the principal results. I chose a standard approach to calculating misfit (i.e. root-mean-squared misfit). This approach has the benefit of being transparent and readily relatable to the observed and theoretical

rivers profiles (Figure 3.15). Finally, I note that this approach does not explicitly address the difficult problems of internal drainage or of strike-slip tectonics, which means that calculated uplift histories along the Pacific seaboard and Great Basin should be treated with caution. Drainages from these regions were not removed from the inversion, principally because it is unclear what parts of these rivers should be removed.

3.5.4 Calculated Rock Uplift History

The calculated uplift history is shown in Figure 3.18. This history yields a global residual rms misfit of 1.25 between observed and calculated river profiles. The most striking feature of this history is the Cenozoic growth of topography in western North America which can be divided into two principal uplift events. Cumulative uplift over time is shown for selected model nodes in Figure 3.20. Between $\sim$ 80 and 40 Ma, regional uplift rate is modest, rarely exceeding $\sim$ 0.02 mm/a. Between 30–20 Ma and the present day, uplift rate dramatically increases and reaches values as high as 0.1 mm/a. This calculated history predicts that the Colorado-Columbia-Rocky Mountains Plateaux was uplifted from approximately sea level (i.e. $<$ 250 m) at $\sim$ 80 Ma to an average elevation of 1.5–2.5 km at the present day. Note that the Rocky Mountains front and the Great Plains are uplifted at approximately the same time. Late Cretaceous to Recent cumulative uplift reaches 2.5–3.0 km within the southern Rocky Mountains, decreasing northward to $\sim$ 1.5 km toward the Canadian Rockies and eastward to 0.5–1.0 km toward the Great Plains. Along the southern slopes between the Rocky Mountains and the Great Plains, cumulative uplift appears to have occurred in two broadly synchronous pulses between 60–40 Ma and 20–0 Ma. Regional uplift is progressively younger and of shorter duration toward the north. The southern portion of the Great Plains becomes emergent after 20 Ma.

With the exception of the Rio Grande Embayment, calculated cumulative uplift along the Gulf Coastal Plain is $<$ 250 m. Between Georgia and the Mississippi Embayment, a rapid episode of regional uplift occurs at $\sim$ 35 Ma. Cumulative uplift of 400 m is predicted to have occurred within the last 20 Ma for the Rio Grande Embayment with fastest uplift rates between 20 and 10 Ma. Post-Cretaceous uplift of the Mexican Highlands generally exceeds 1 km. The southern and northernmost portions of these highlands were uplifted by almost 3 km and $\sim$ 2 km, respectively. Along the eastern seaboard, the results suggest that the central Appalachian mountains were uplifted by $\sim$ 1 km. The adjacent coastal plain underwent a maximum uplift of 300 m. Within cratonic North America, cumulative uplift is modest which suggests that the Canadian Shield and Interior lowlands have sat at relatively low elevation since Late Cretaceous times.

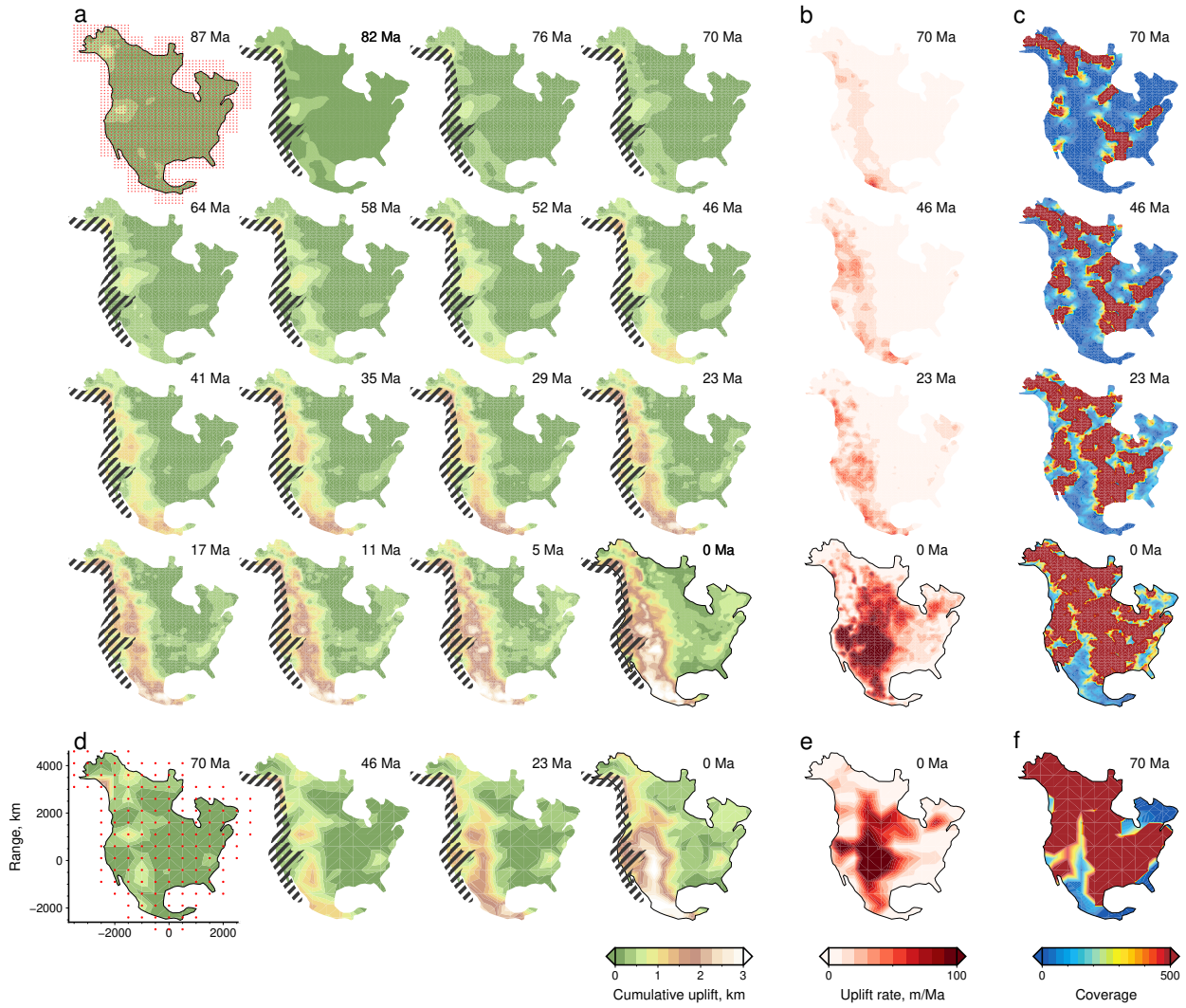

Figure 3.18: **Calculated uplift history for North America.** (a) 16 panels that show cumulative uplift history (i.e. temporally integrated uplift rate history) calculated by linear inverse modelling of 4161 river profiles (residual rms misfit = 1.25; Figure 6). Grid of red points in top left-hand panel = loci of vertices used to discretise uplift rate. Age, in millions of years, is shown for each panel. Hatched region = Great Basin and Pacific margin where internal drainage, plate accretion and strike-slip tectonics compromise assumptions that underpin inverse model. (b) Calculated uplift rate at four different times. (c) Selected panels at four different times that show model coverage (i.e. number of non-zero entries in model matrix, M, corresponding to given uplift node). Note that model coverage is highest toward present day and significantly decreases for ages > 70 Ma (see Figure 3.19). (d) Four panels showing cumulative uplift history of North America calculated using coarser mesh (residual rms misfit = 2.62). (e) and (f) Calculate uplift rates and model coverage for coarser mesh at 0 Ma.

It is important to note that at the oldest time-step, 87 Ma, the model predicts small amounts of cumulative uplift and low uplift rates for most of the North American continent. Such observation is at odds with many tectonic models of western North America in mid-Cretaceous times (e.g., *Dickinson and Snyder*, 1978; *DeCelles*, 2004). This modelled uplift history, however, a function of model coverage. Figure 3.19 shows cumulative model coverage as a function of time. τ_G defines how much

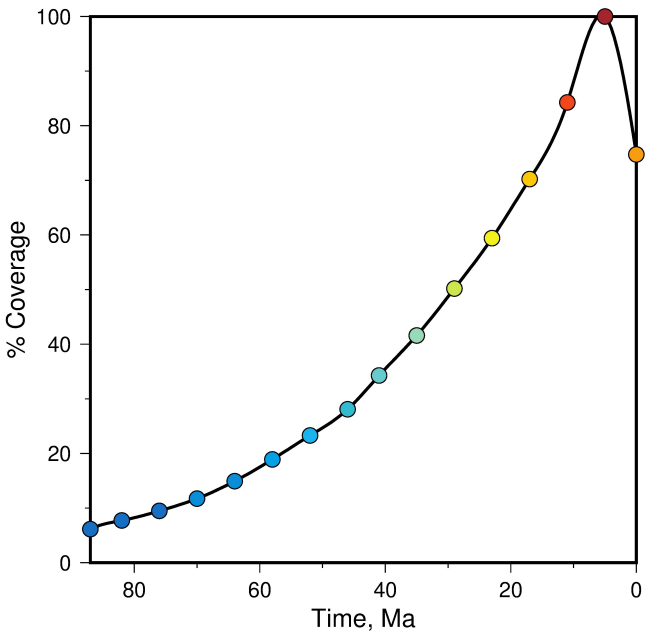

Figure 3.19: **Data coverage as a function of model time** Coverage is calculated as the percentage of total river data points with τ_G equal to or older than model age. Circles are coloured with colour scale from Figure 3.18

data is present in the model at any given time-step (see coverage maps in Figure 3.18c, which shows the spatial density of river segments with ages older than a given τ_G). Given this relationship, at the oldest ages considered by the inverse model (82 Ma), there is very little river data available to constrain calculated uplift. This lack of resolution does not imply that there was no topography in western North America at 82 Ma, simply that the model lacks the resolution to calculate uplift rates before this time.

I explored the effects of changing the spatial smoothing parameter on the resultant uplift model. Figure 3.21 and 3.22 show cumulative uplift, uplift rate and model coverage over time for $\lambda_s = 0.05$ and $\lambda_s = 5.0$, respectively. Changing the smoothing parameter alters both the spatial distribution of predicted uplift, as well as the maximum observed uplift rate at any given point in the model.

3.5.5 Independent Tests

A significant advantage of an inverse modelling approach is that the predicted regional rock uplift as a function of space and time can be tested against independent observations. Here, I have carried out this testing by comparing predicted uplift histories with those determined from the biostratigraphic (PBDB) and stratigraphic inventory presented in Chapter 2 and Section 3.4 of this Chapter. The average uplift rate at each location was estimated from the age and elevation of the biostratigraphic

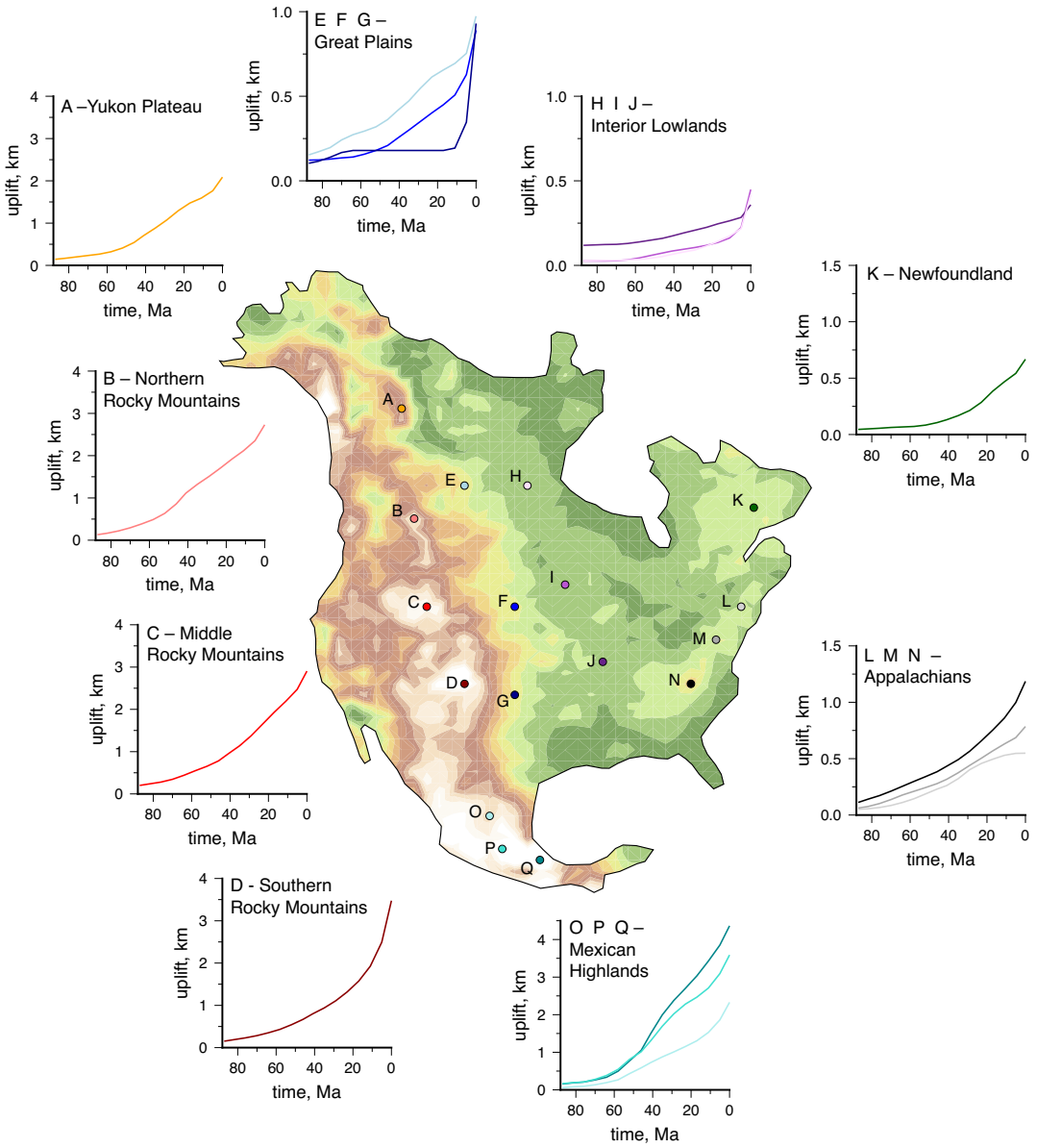

Figure 3.20: **Calculated uplift history at grid nodes**. North America map shows cumulative uplift at 0 Ma. Cumulative uplift as a function of time shown for key locations in North America, identified by letters on map. For graphs where more than one location is shown, these can be distinguished by colours.

sample. This value can be directly compared with the average predicted uplift rate, which is determined from the amount of cumulative uplift that has occurred since the time of deposition. Samples younger than 5 Ma were not used, since the temporal resolution of the calculated uplift history is of order 5–10 Ma (Figure 3.18).

Figures 3.23 and 3.24 show a comparison between observed and predicted uplift for key stratigraphic and PBDB-derived measurements, respectively. Comparison between all observed stratigraphic and biostratigraphic constraints, and predicted average uplift rate measurements are presented in Figure

3.25. The inverse model used for comparison is the preferred, calibrated and smoothest, best-fitting run, where $m = 0.4$, $v = 0.99$, and $\lambda_s = 0.5$. Analysis of the smaller stratigraphic database shows that the inverse model yields a good agreement between observed and predicted uplift rates. Figure 3.25b presents a similar set of results for the much larger PBDB inventory. Open white circles comprise observations with relatively small uncertainties that are within an order of magnitude of the central value. In these cases, observed and predicted values agree to within a factor of two. Gray circles also agree but have large observed uncertainties, principally because of relatively poorly constrained paleobathymetry. I conclude that calculated average uplift rates for most of the Colorado-Columbia-Rocky Mountains Plateaux, the Appalachians, Texas, Mexican Highlands, Yukon and the Great Plains are consistent with a combination of biostratigraphic and stratigraphic uplift measurements (Figure 3.25c and d).

There are two regions where the inverse model significantly over- or under-predicts observed uplift rates: the Pacific Coastal Ranges and the Rio Grande Embayment (Figure 3.24). It is unsurprising that a damped inverse model yields a poorer fit along the Pacific Coast, which has experienced a complex tectonic history dominated by transcurrent plate motions and regional subsidence (e.g. *Awater*, 1970; *Bartow*, 1991). Over-predicted uplift rates within the Rio Grande Embayment are more problematic.

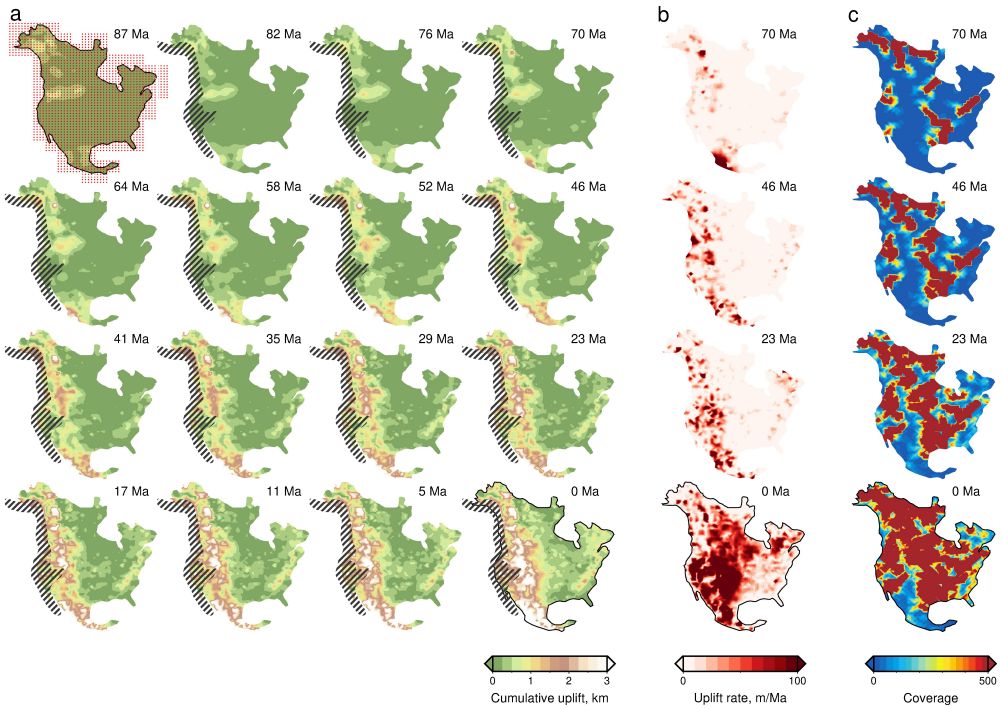

Figure 3.21: **Calculated uplift history with spatial smoothing** $\lambda_s = 0.05$. (a) 16 panels that show cumulative uplift history. (b) Calculated uplift rate at four different times. (c) Selected panels at four different times that show model coverage.

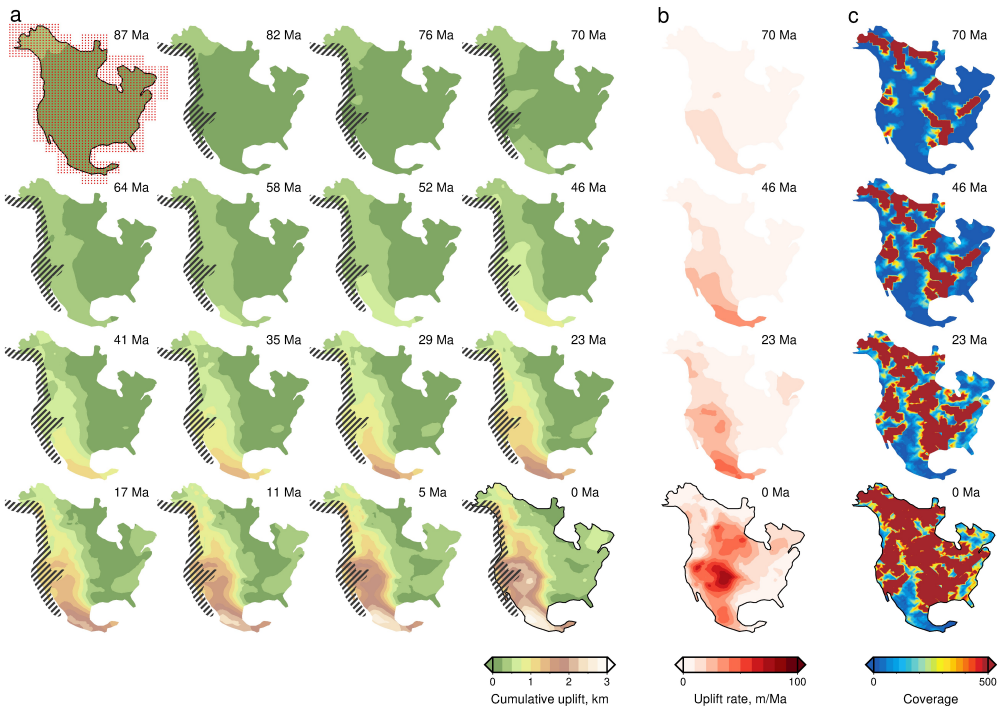

Figure 3.22: **Calculated uplift history with spatial smoothing $\lambda_s = 5$.** (a) 16 panels that show cumulative uplift history. (b) Calculated uplift rate at four different times. (c) Selected panels at four different times that show model coverage.

The biostratigraphic compilation indicates that this embayment progressively shoaled from a deep marine Upper Cretaceous environment until Late Eocene times when deposits were predominantly deltaic or estuarine (e.g., Wilcox Formation; *Galloway*, 2001; *Milliken et al.*, 2018). Since then, this

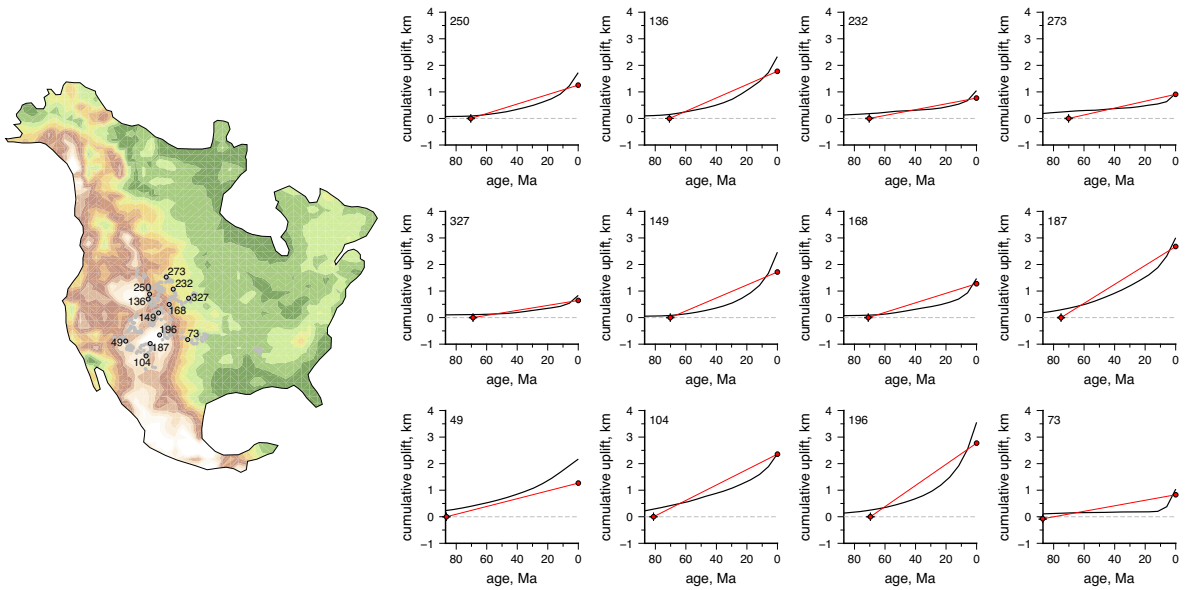

Figure 3.23: **Comparison uplift history with stratigraphic data.** Observed vs Predicted uplift from the stratigraphic sections of marine to terrestrial transitions.

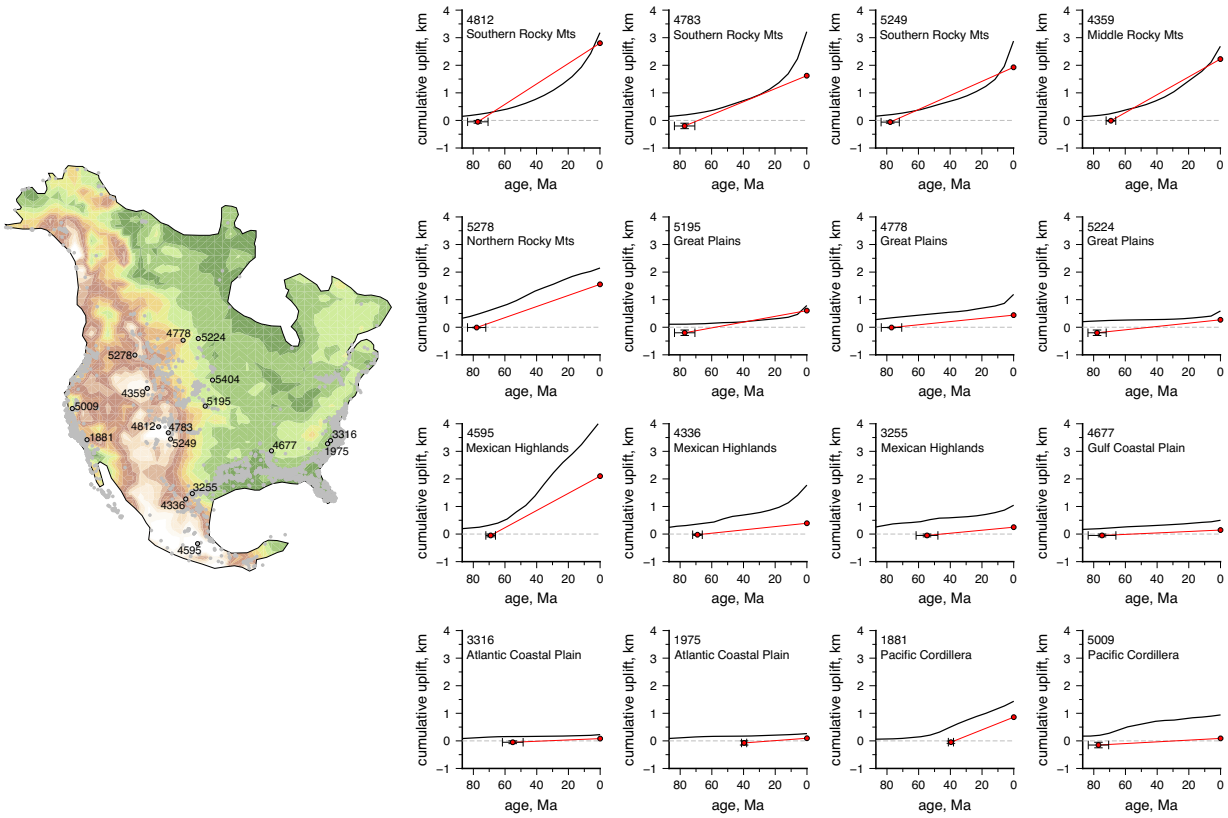

Figure 3.24: **Comparison uplift history with PBDB data.** Observed vs Predicted uplift from example points from the paleobiology database.

region probably remained close to sea level, manifest by a record of Cenozoic shoreline progradation along the Coastal Plain (*Hosman*, 1996; *Galloway*, 2001). At present, the embayment is adjacent to the uplifted Sierra Madre province. Since relatively few rivers drain this region, there is lower model coverage and thus smoothing is larger, which is a possible reason why regional uplift has been over-predicted (Figures 3.14, 3.18).

One plausible explanation for poor fit between some observed and predicted uplift rates could be that the prefactor of the stream power relationship, v, is not appropriate. To test this, I compared uplift rates derived from the bisotratigraphic and stratigraphic constraints to uplift histories where v is either decreased or increased by one order of magnitude (Figures 3.26 and 3.27, respectively). The resultant uplift histories yield calculated rates that significantly mismatch stratigraphic and biostratigraphic constraints. These tests suggest that the calibrated value of v used in this study is a reasonable one.

An assessment of model fidelity can also be made using additional independent uplift constraints (e.g., number of recorded extrusive events, clumped-isotope constraints). A two stage Cenozoic uplift

history of the Colorado Plateau is consistent with paleoaltimetric observations calculated from clumped

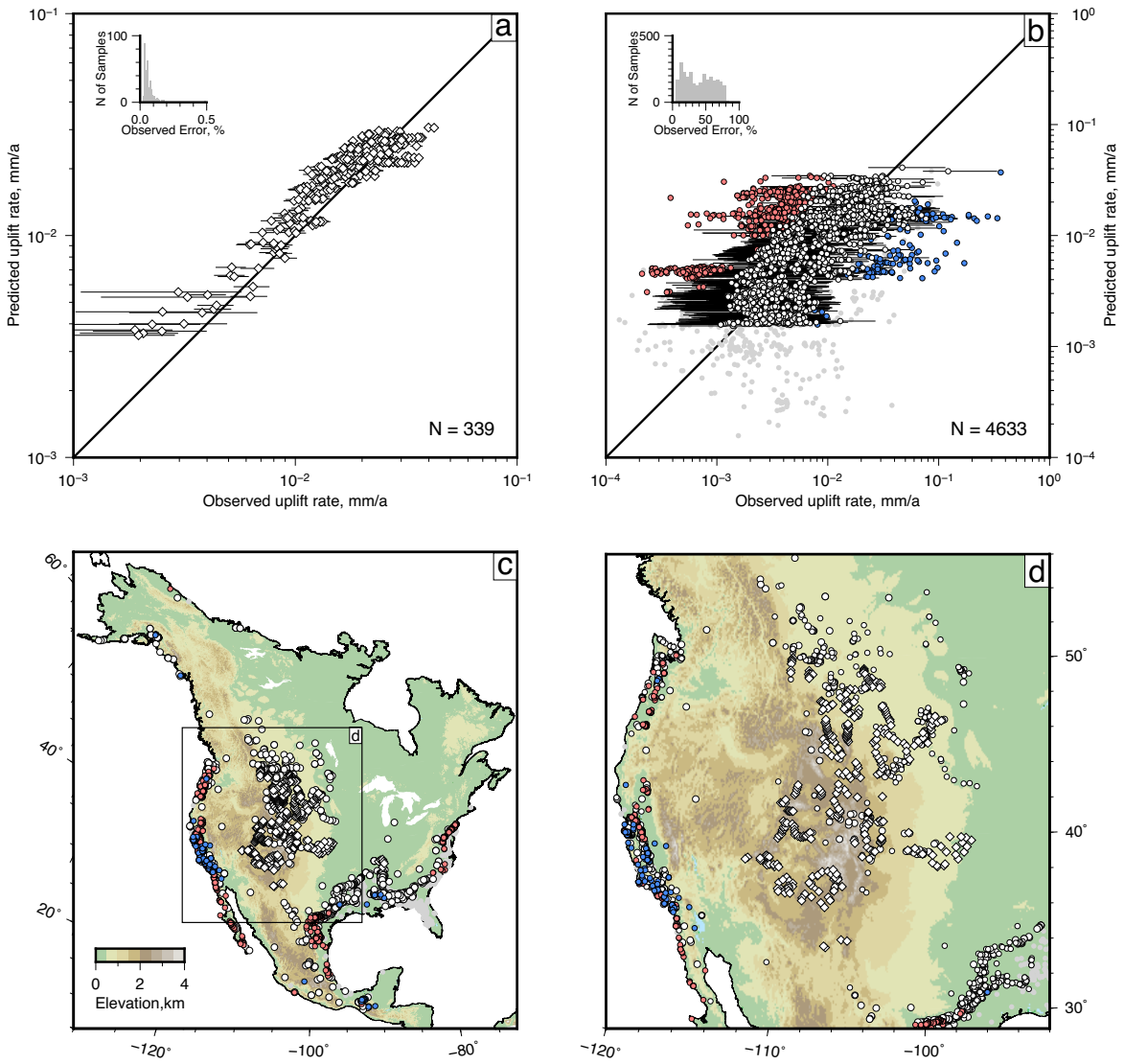

Figure 3.25: **Testing results of inverse modelling.** Comparison of time-averaged Late Cretaceous to Recent uplift from inverse model and (a) stratigraphic and (b) biostratigraphic constraints (Figures 3.13f–n and 3.13a, respectively). Inset histograms = percentage error distribution of observations. Solid black line = 1:1 relationship; white circles = inverse results that agree with stratigraphic estimates; grey points = samples with large observational uncertainties (i.e. greater than one order of magnitude) with error bars omitted for clarity; red/blue points indicate where inverse model over-/under-predicts uplift rate by more than a factor of two. (c) Spatial distribution of stratigraphic and biostratigraphic constraints coloured by accuracy of inverse model. Symbols same as for panels a and b. (d) Comparison of inverse modelling results and observations centred on Colorado Plateau (labelled box in panel c). Inverse model best matches uplift measurements across the Colorado Plateau and Rocky Mountains.

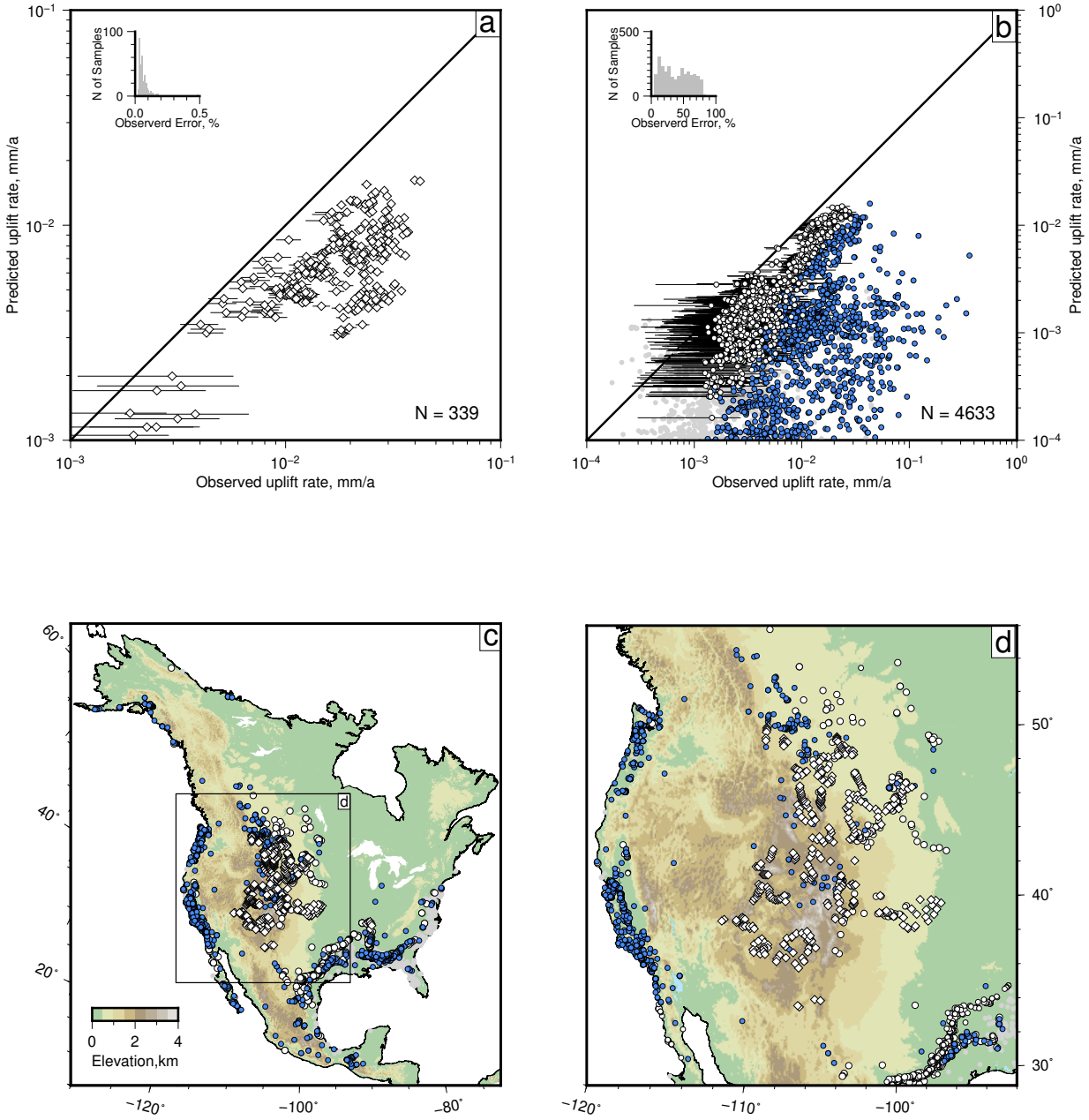

Figure 3.26: **Testing effect of reducing erosional parameter**, v, by one order of magnitude. (a) Comparison of uplift rates calculated by inverting drainage patterns and those determined from stratigraphic observations (see Figure 9 of main text for further details). Solid diagonal line = 1:1 relationship. (b) Comparison of uplift rates calculated by inverting drainage patterns and those determined from biostratigraphic inventory. Blue circles = significantly under-predicted values obtained by inverting drainage patterns. (c) Comparison of observed and calculated uplift rates as function of space. Labelled box shows panel d. Note that these results were obtained using parameterisation with unrealistically small value of v, tends to under-predict uplift rates. (d) Zoom of panel c.

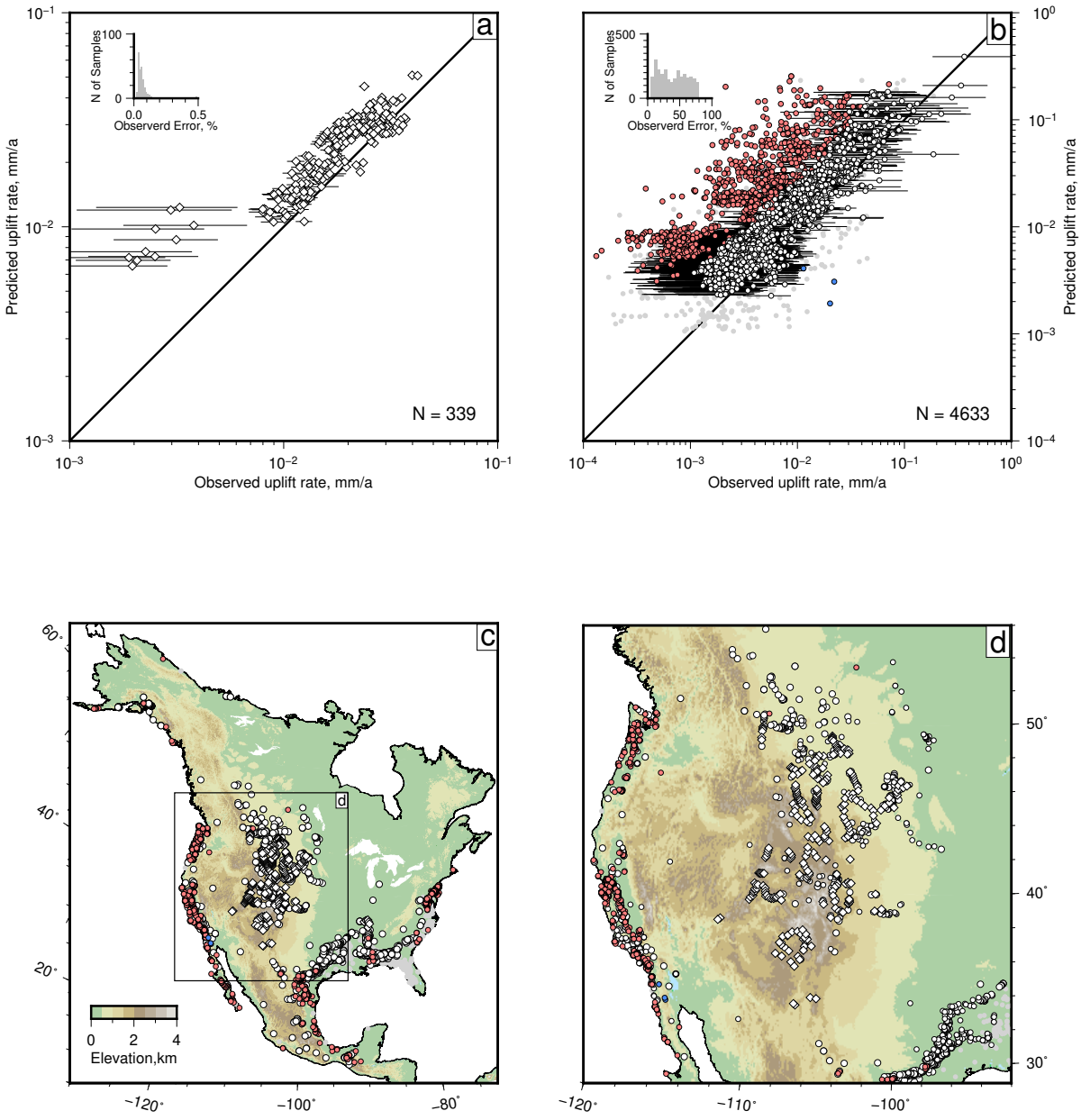

Figure 3.27: **Testing effects of increasing value of erosional parameter**, v, by one order of magnitude. (a) Comparison of uplift rates calculated by inverting drainage patterns and those determined from stratigraphic observations. Solid diagonal line = 1:1 relationship. (b) Comparison of uplift rates calculated by inverting drainage patterns and those determined from biostratigraphic inventory. Red/blue circles = significantly over/under-predicted values obtained by inverting drainage patterns. (c) Comparison of observed and calculated uplift rates as function of space. Labelled box shows panel d. (d) Zoom of panel c.

isotopic analysis (*Huntington et al.*, 2010). The distribution of extrusive magmatic events summarised in the NAVDAT database displays two broad peaks at $\sim$ 80–55 Ma and at $\sim$ 40–0 Ma (see e.g., *Chapin et al.*, 2004). In Alaska, three phases of magmatism centred at 33, 15 and 2 Ma have been recorded (Figure 3.4). Timing of peak magmatism is consistent with changes of predicted uplift rates (Figure 3.18b). In southern North America and Mexico, predicted regional uplift is consistent with the distribution of Cretaceous marine sedimentary rocks (Figure 3.13a, Figure 3.24; *Bond*, 1976; *Sahagian*, 1987). Along the Atlantic margin, Cretaceous marine sedimentary rocks also crop out which is consistent with calculated regional uplift since the age of deposition. Between 30°N and 35°N, the elevation of an emergent Pliocene marine terrace increases from 20–30 m to 60–80 m (*Rowley*, 2013; *Rovere et al.*, 2014). Calculated cumulative uplift in this region increases from $\sim$ 40 Ma with higher rates between 30 Ma and the present day (Figure 3.18b).

In summary, the inverse model yields a reasonable match to most of the stratigraphic and biostratigraphic inventories, respectively. I conclude that a continent-wide spatial and temporal uplift history calculated by inverting an inventory of 4161 river profiles generally agrees with a suite of independent constraints. These results build upon, and are consistent with, non-linear inverse modelling of a much smaller inventory of 93 river profiles (*Roberts et al.*, 2012a).

3.6 Landscape Evolution Modelling

The inverse modelling procedure described and applied in the preceding section can be further tested by forward modelling. By forcing a landscape evolution model with the rock uplift rate history calculated by inverse modelling, testable predictions about elevation, drainage patterns, denudation and sedimentary flux are made. In particular, the way in which the planform of drainage patterns evolves as it responds to regional uplift can be examined. In future, it may prove possible to directly invert continental-scale topography for uplift and denudation using a landscape evolution model (e.g., *Croissant and Braun*, 2014). At present, guided forward modelling is a pragmatic and computationally efficient approach for calculating continental-scale landscape evolution.

3.6.1 Badlands Algorithm

A modified version of the Basin and Landscape Dynamics (Badlands) model is used to calculate the spatial and temporal evolution of North American topography during the last 82 Ma together with

discharge, denudation and sedimentary flux (*Salles*, 2015). Badlands exploits an irregular triangular mesh to solve the relevant geomorphic equations. Here, this mesh was generated from user-defined vertices with a regular spacing of 10×10 km using Delauney-Voronoi triangulation (*Voronoï*, 1908; *Delaunay*, 1934). Drainage flow paths were determined using a single flow direction, steepest descent algorithm. Using a finite volume approach, the continuity of mass equation is solved to calculate sedimentary flux across cell edges. The time steps are determined in accordance with a Courant-Friedrichs-Lewy condition to ensure numerical stability. Sediment properties, such as composition, particle size and bulk density, are assumed to be spatially and temporally uniform. No differentiation between regolith and bedrock is made.

As proposed by *Salles* (2015) a diffusion coefficient, $\kappa = 10^{-20}$ m^2 Ma^{-1}, is included to ensure model stability. I purposefully ensured that the forward model was kept as simple as possible and that erosional parameters, v, m and n, have identical values to those used for inverse modelling. Fixed Dirchlet boundary conditions were employed along the edges of the box to ensure that no interference with drainage development of the continental domain occurred. The model was not permitted to deposit sediment on the continent or along its margins, sea level was assumed to be constant and precipitation rate, P, was set to unity. Finally, flexural responses to re-partitioning of surface loads, glacial erosion and ice cover were not included and no corrections to the loci of paleo-shorelines were made (cf. *Wickert*, 2016; *Salles et al.*, 2017). The governing empirical equation takes the form

$$\frac{\partial z}{\partial t} = -v(AP)^m \nabla z - \kappa \nabla^2 z + U(x, y, t), \tag{3.8}$$

where U is the rock uplift rate history that was previously obtained by inverse modelling of the drainage inventory (Figure 3.18a). Only vertical displacements are considered. Incision rates (i.e. $\partial z/\partial t - U$) are easily extracted from numerical solutions of Equation 3.8. In turn, these rates can be used to calculate cumulative denudation at spot locations by integrating incision rate with respect to time or to calculate sedimentary flux by integrating with respect to flow length in a downstream direction. The initial condition was set to 5% of the present-day topography, which was calculated by multiplying the ASTER GDEM grid by 0.05. By etching the initial condition (i.e. starting topography), the initial drainage pattern is set but is subsequently allowed to evolve as the landscape develops.

3.6.2 Calculated Landscape

Figure 3.28 shows the preferred model run, and presents elevation, discharge (i.e. drainage networks), cumulative denudation and sediment load as a function of geologic time for the last 70 Ma for a Badlands model that has a 5% initial condition. Unsurprisingly, this model predicts elevations at the present day that are similar to the ASTER GDEM topography (Figure 3.28a). In some locations, calculated elevations are lower than observed, especially within the Appalachian Highlands and Canadian Rockies, which I attribute to model smoothing. Calculated Cenozoic discharge suggests that the major continental-scale catchments (e.g., Mississippi, Colorado, Columbia, Yukon, Mackenzie) are broadly stable. For example, most of the large rivers that drain western North America into the Gulf of Mexico have similar flow patterns over the last $\sim$ 65 Ma, which is consistent with zircon provenance measurements from Cretaceous and Paleocene fluvial sandstones along the northern margin of the Gulf of Mexico (Figure 3.8; *Blum and Pecha*, 2014; *Blum et al.*, 2017).

I investigated the impact of different initial conditions on the channelisation and subsequent development of drainage planforms: a random distribution of slopes with small (i.e. meter-scale) relief, and 1%, and 10% of present-day topography. The results of these model runs are shown in Figures 3.29, 3.31 and 3.30, respectively. Similar results to those shown in Figure 3.28 have been obtained for the random slope condition and for the 1% initial condition. Drainage planforms are more entrenched for the 10% initial condition (Figure 3.30).

One concern is that the cell size used to parameterise the landscape evolution model can potentially force the drainage planform to remain fixed (*Goren et al.*, 2014). This conjecture was examined by changing the inserted rock uplift history by rotating the uplift history shown in Figure 3.18 by 90°. In these tests, the initial condition was kept as 5% of present-day topography. Results of this test are shown in Figure 3.32), which shows that calculated planforms (e.g., rivers and drainage divides) do indeed adjust and change as the landscape develops, in accordance with the pattern of forcing uplift.

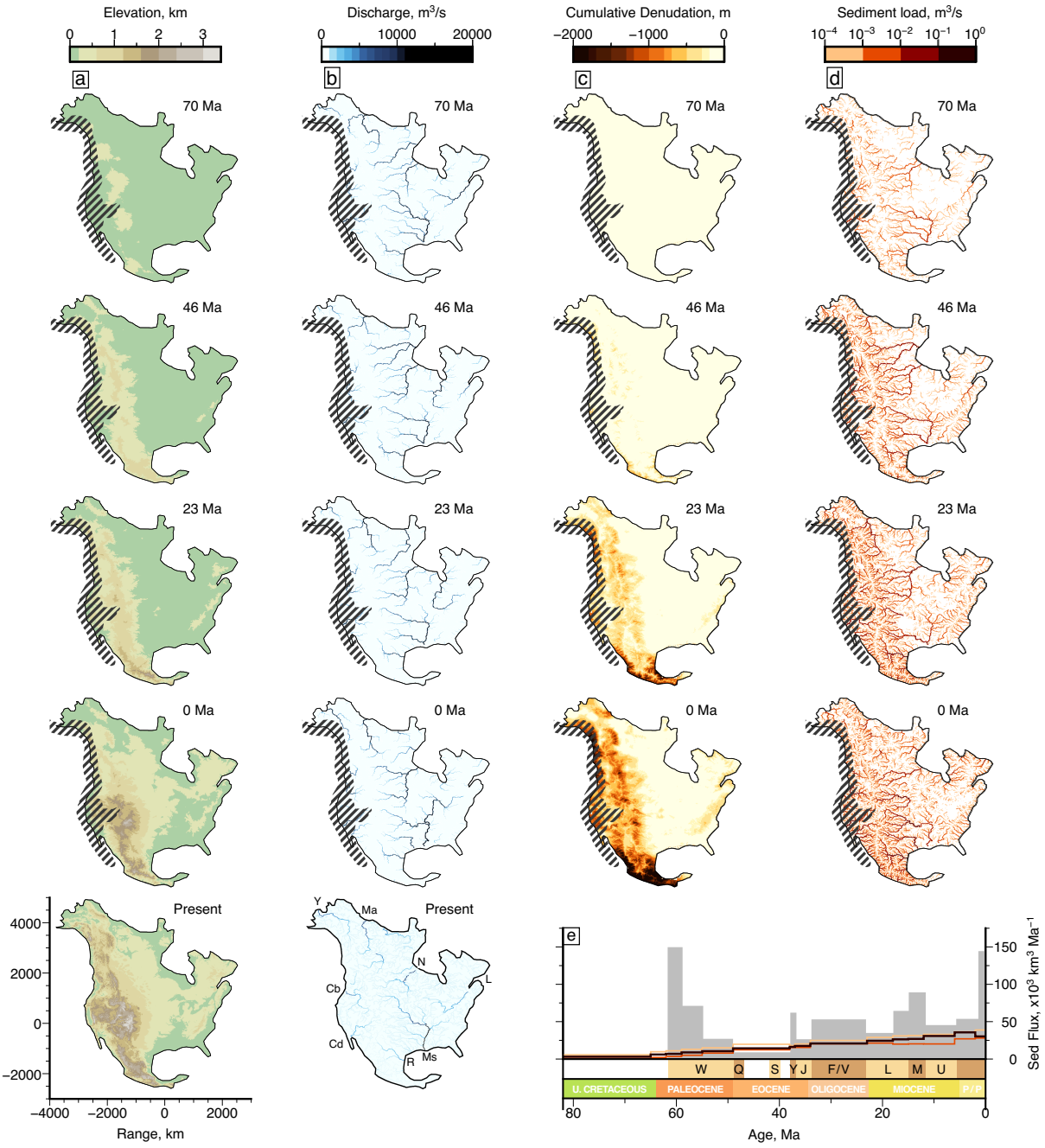

Figure 3.28: **Predicted landscape evolution.** (a) Late Mesozoic and Cenozoic topographic evolution of North America calculated using modified version of Badlands landscape evolution model (*Salles*, 2015). Model was forced using uplift history calculated by inverse modelling (Figure 3.18). Model resolution = 10 km. Hatched region = portion of model where calculated uplift history should be treated with caution. Lowest panel = present-day topography from ASTER GDEM database for comparison. (b) Calculated discharge. Bottom panel = present-day discharge calculated using Esri flow-routing algorithms and ASTER GDEM database (see Figure 3.14 for annotation). (c) Calculated cumulative denudation (i.e. $\int \partial z \mathrm{dt}/\partial \mathrm{t}$). (d) Calculated sedimentary load (i.e. $\int \partial z \mathrm{dx}/\partial \mathrm{t}$). (e) Gray histogram = observed solid sedimentary flux for Gulf of Mexico redrawn from *Galloway et al.* (2011). Orange/black/red lines = flux calculated for three different Badlands landscape evolution models parameterised using 1, 5 and 10% starting conditions (see Supporting Information). Brown/peach band shows stratigraphy: W = Wilcox; Q = Queen City; S = Sparta; Y = Yegua; J = Jackson; F/V = Frio/Vicksburg; L, M, U = Lower, Middle and Upper Miocene. Note model coverage is $< 20\%$ before 55 Ma (see Figure 8c).

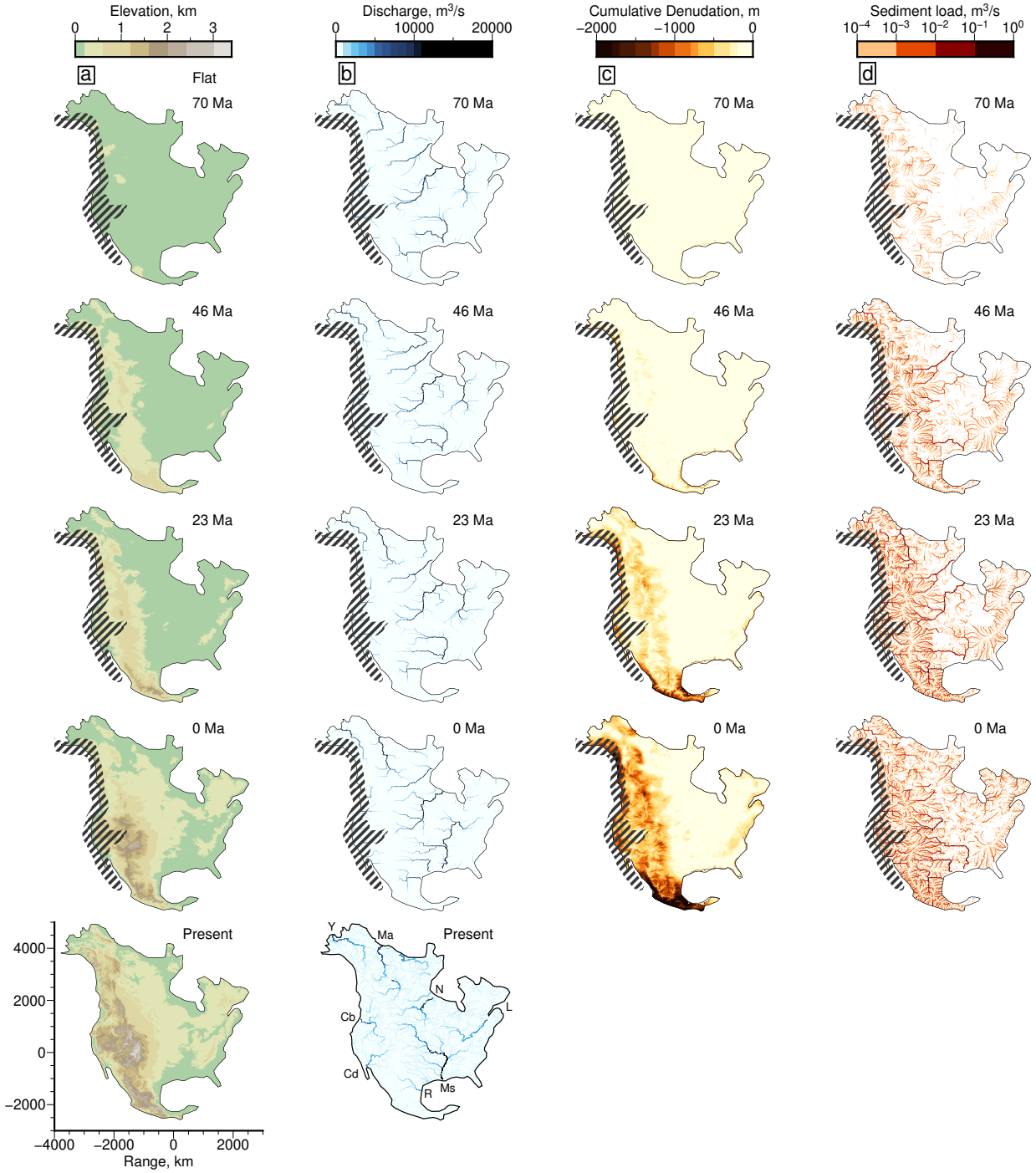

Figure 3.29: **Landscape evolution model, flat initial condition**. Testing impact of alternative starting conditions used to initiate landscape evolution model. In this example initial topography was set to zero. Note that Badlands algorithm randomizes slopes to ensure channelisation.

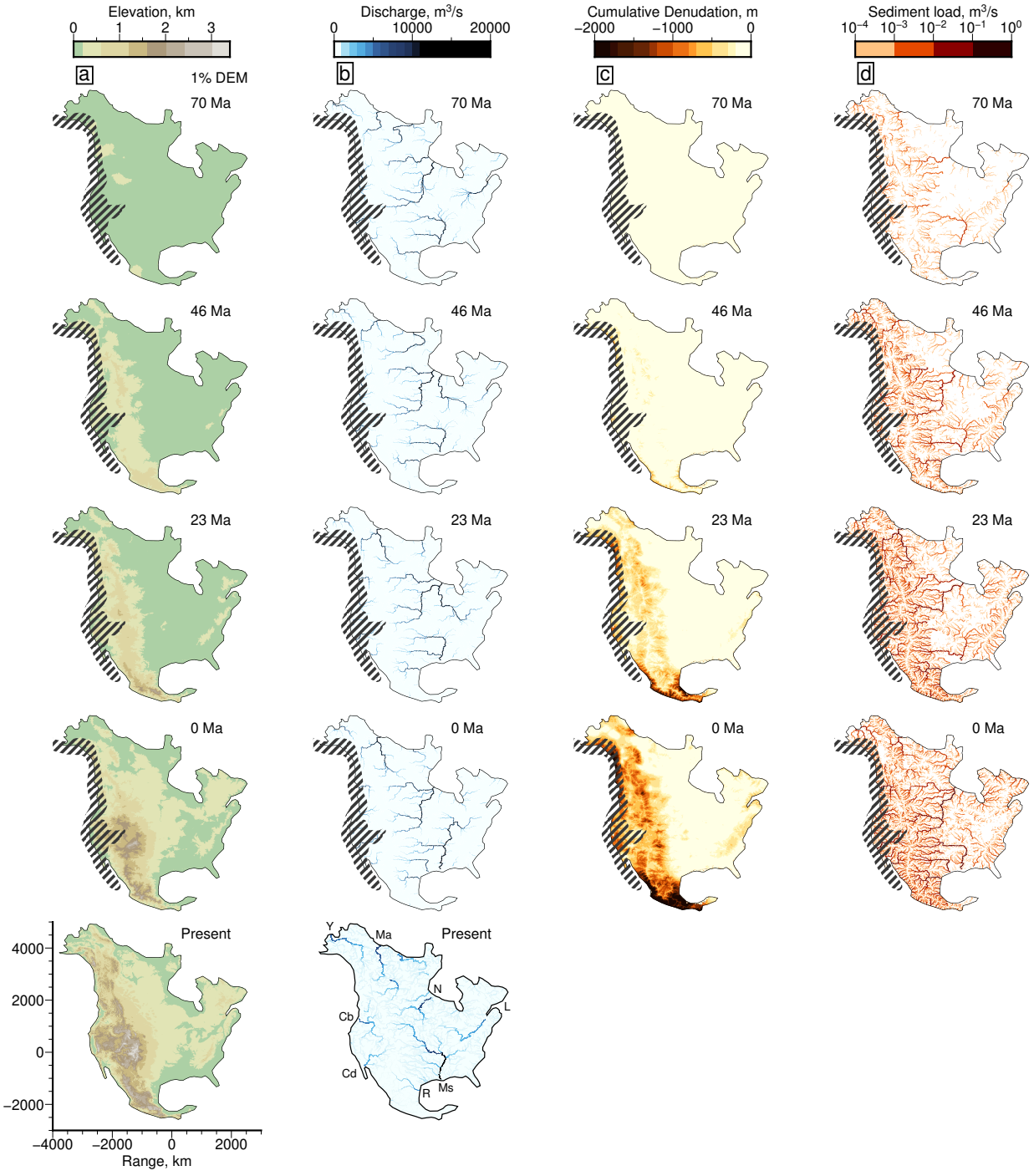

Figure 3.30: **Landscape evolution where initial topography is 1% of present-day** topography extracted from ASTER GDEM.

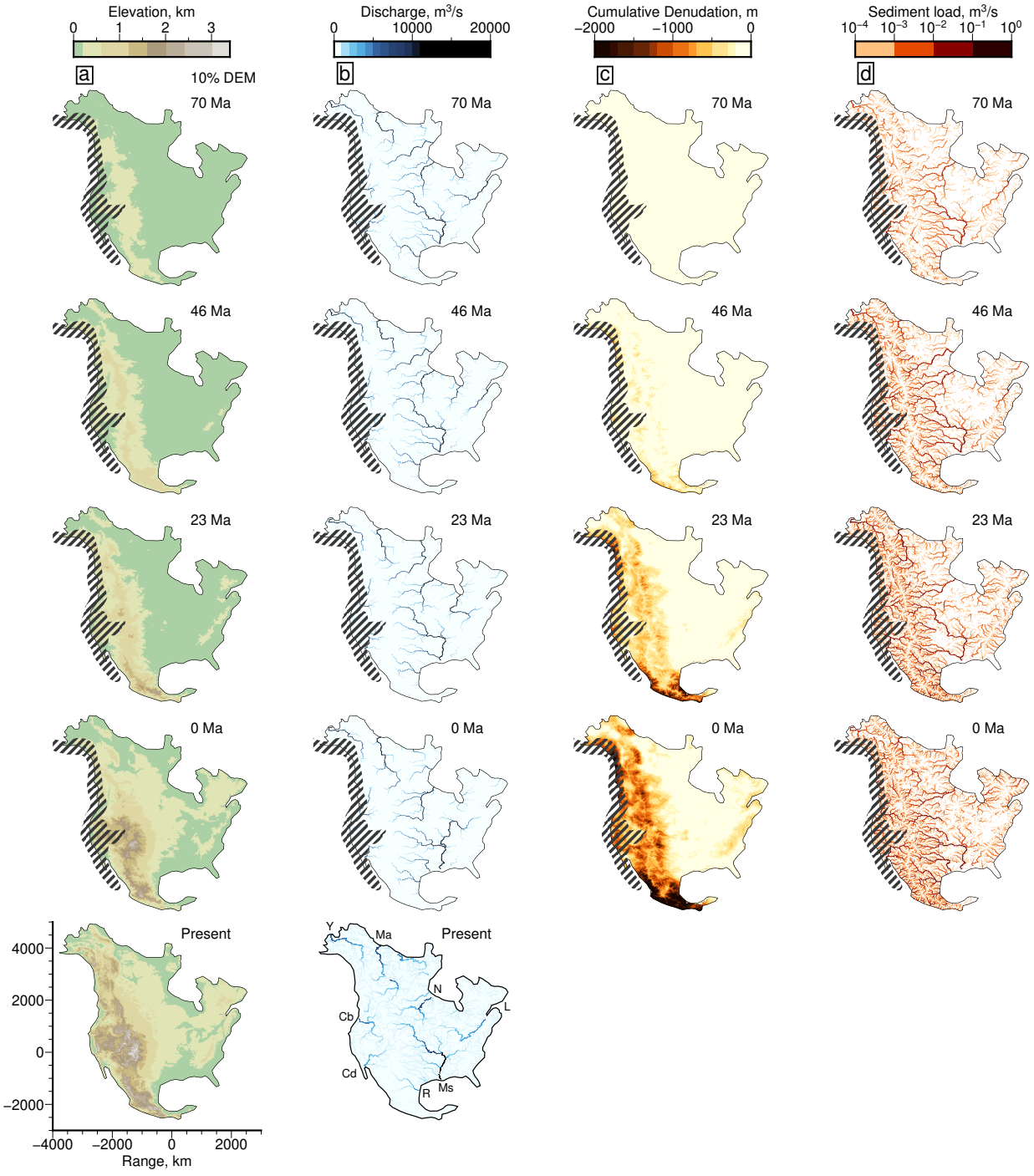

Figure 3.31: **Landscape evolution model where initial topography is 10% of present-day** topography extracted from ASTER GDEM.

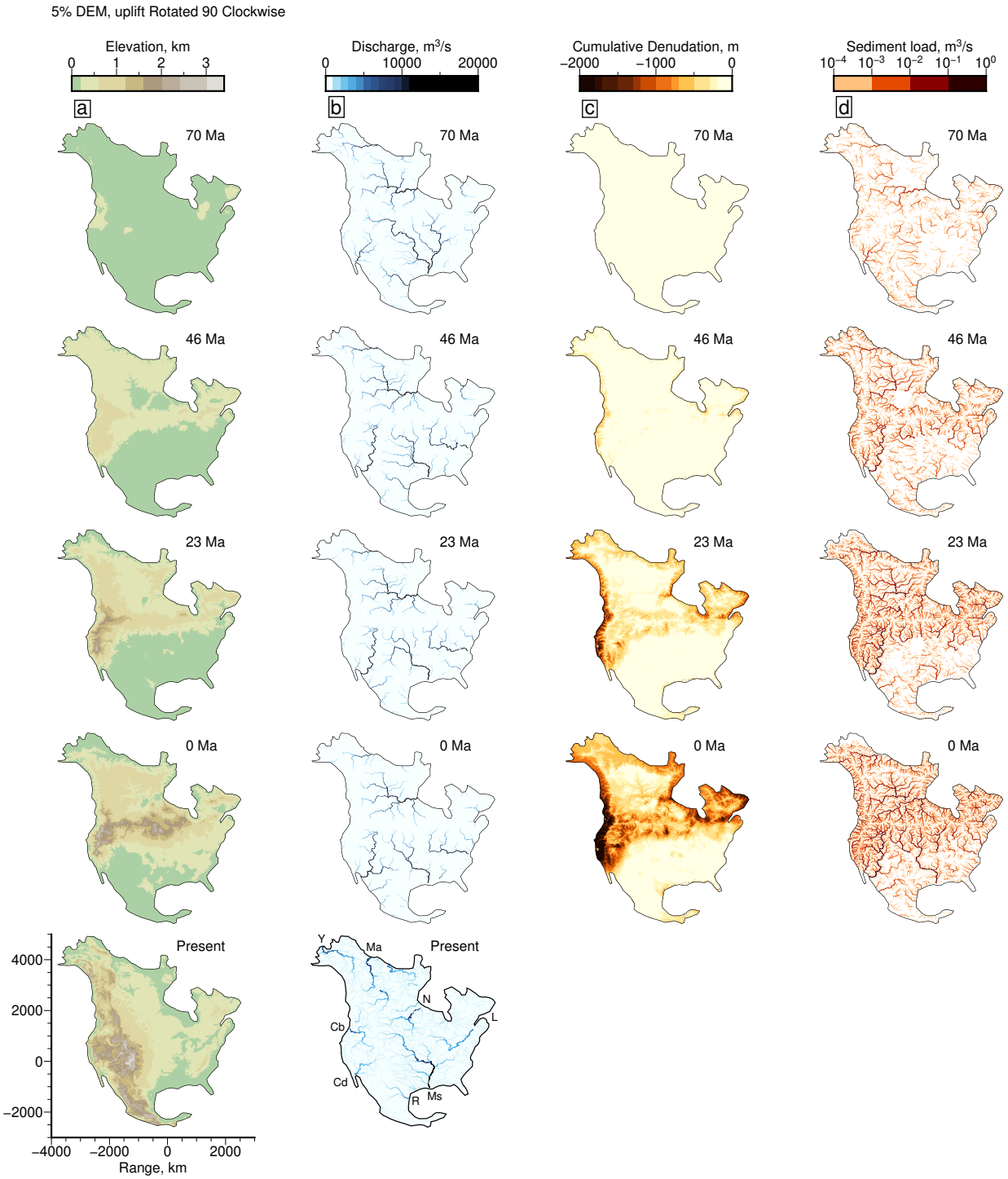

Figure 3.32: **Testing impact of alternative uplift history used to externally force landscape evolution model.** Here, uplift history calculated by inverting drainage patterns was rotated by 90° and Badlands model was rerun. This approach largely preserves length-scale and aspect ratio of inserted uplift pattern. Initial topography was set to 5% of present-day topography (i.e. initial condition was not rotated).

3.6.3 Denudational History

Thermochronometric measurements provide an additional means of estimating denudation over long time scales. In essence, these techniques record the temperature of rocks as a function of time. By relating these histories to estimates of crustal temperatures, it is possible to extract denudational histories (see e.g., *Green et al.*, 1989; *Gleadow and Brown*, 1999; *Gallagher*, 1995; *Farley*, 2002). A key result from thermochronometers is the age at which rock has cooled below the closure temperature of the individual system. The presence of cooled rock at Earth's surface today is usually interpreted as removal of overburden by denudation. Predicted denudation history was tested by exploiting the results from two well-known low-temperature thermochronometers: apatite fission track (AFT) and apatite (U-Th)/He (A-He). The principal aim is to investigate how well the landscape evolution model, which was parameterised using a smoothly varying rock uplift history, can reproduce independent estimates of exhumation. This compilation of thermochronometric results builds on previous inventories and includes 1642 AFT and 789 A-He closure ages from North America (e.g., *Sloan et al.*, 2003; *Herman et al.*, 2013, ; USGS National Geochronology Database). The spatial and temporal distribution of this compilation is presented in Figure 3.33. I have attempted to identify samples with cooling histories that have been overprinted by tectonic and/or magmatic events and manually excised them from the compilation.

Figure 3.33d and f shows there are three broad peaks evident within AFT closure age measurements: 80–60 Ma, 50–30 Ma and 30–10 Ma. The number of measurements of A-He closure ages is greatest between $\sim$ 20 Ma and the present day (Figure 3.33e). Thermobarometric modelling and rock cooling histories suggest that Cenozoic denudation rates across southern North America and Mexico were highest during the last 40 Ma (*Gray et al.*, 2001; *Montgomery and López-Blanco*, 2003; *Ferrari et al.*, 2012). One interpretation of this trimodal distribution is that North America has experienced at least three discrete kilometre-scale phases of Late Mesozoic to Recent denudation. However, I acknowledge that this database has significant spatial bias; coverage is greatest on the Colorado-Columbia-Rocky Mountains Plateaux, along parts of the Appalachian mountains, Mexican highlands, and within the Yukon region (Figure 3.33a and b). Portions of the Colorado Plateau that have a two-stage Cenozoic cooling history have been interpreted as evidence for an ancestral Colorado river. I note that alternative explanations exist (see e.g., *Flowers and Farley*, 2012; *Karlstrom et al.*, 2014). Late Cretaceous to Early Paleocene A-He and AFT ages along the Appalachian mountains suggest that $\sim$ 2 km of overburden has been removed during the last $\sim$ 60 Ma. Closure ages along the northern

Pacific Coastal Ranges are mostly younger than 50 Ma. In the north and central Rocky Mountains, closure ages are between 70 and 40 Ma, which is broadly coeval with the timing of Laramide tectonism (e.g., *Dickinson et al.*, 1988; *Peyton and Carrapa*, 2013). In the Southern Rockies and Rio Grande Rift, there are a suite of A-He and AFT closure ages < 40 Ma. *Kelley and Chapin* (1995) and *Peyton and Carrapa* (2013) related this post-Laramide cooling to burial, subsequent epeirogenic uplift and

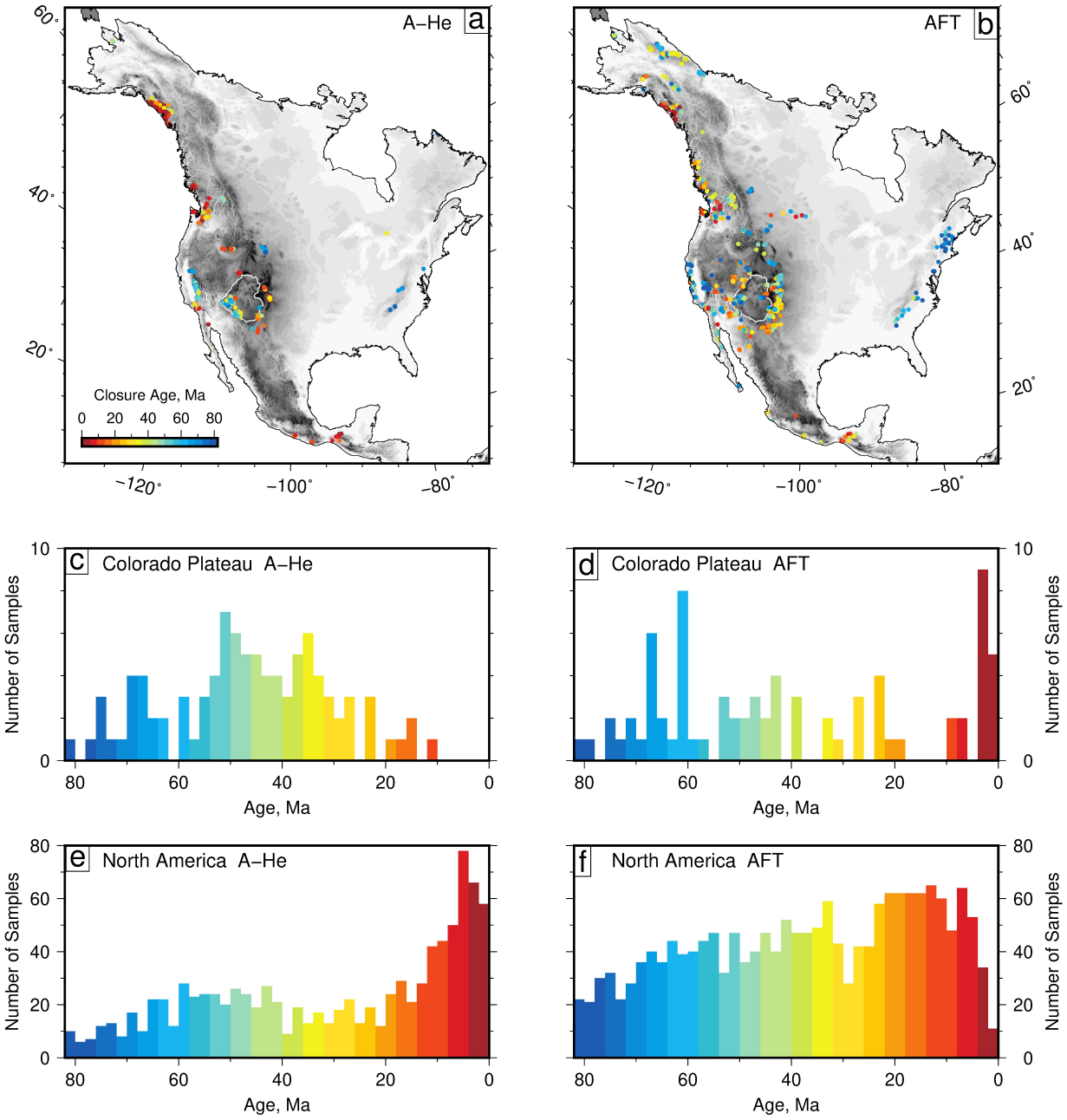

Figure 3.33: **Distribution of thermochronology data**. (a) Synthesis of independent estimates of U-Th/He (A-He) closure ages for North America. Gray shading = present-day topography calculated from ETOPO1 database; thin white line encloses Colorado Plateau. (b) Apatite Fission Track (AFT) closure ages. (c)/(d) Histograms of A-He and AFT closure ages, respectively, from Colorado Plateau. (e)/(f) Histograms of of A-He and AFT closure ages, respectively, closure ages for North America.

removal of sedimentary rocks while the Rio Grande Rift developed. *O'Sullivan and Currie* (1996) and *O'Sullivan and Lane* (1997) propose that the Yukon plateau has had a staged denudation history, with cooling phases between 60 and 40 Ma, and at $\sim$ 15 Ma.

In order to compare this compilation with predictions from the landscape evolution model, I first convert reported closure ages into average denudation rates. Temperature histories of rocks can be extracted by inverting apparent closure ages and fission track length distributions (*Ketcham*, 2005; *Gallagher*, 2012). However, it is still unclear how spatial averaging of cooling histories, exhumation rate dependence of closure temperatures, and time-dependent geothermal gradients affect these results (e.g., *Schildgen et al.*, 2009, 2018). Here, I use a simple expression that relates surface and closure temperatures, T_s and T_c, geothermal gradient, $\mathrm{d}T/\mathrm{d}z$, and closure age, a_c, in order to calculate the time-averaged denudation rate which is given by

$$\frac{\mathrm{d}z}{\mathrm{d}t} = \frac{T}{a_c(\mathrm{d}T/\mathrm{d}z)}, \tag{3.9}$$

where $T = T_c - T_s$. Measurement errors and uncertainties in the thermal properties of the crust were propagated to obtain

$$\delta_{\mathrm{d}z/\mathrm{d}t} = \left|\frac{\mathrm{d}z}{\mathrm{d}t}\right| \sqrt{\left(\frac{\delta_T}{|T|}\right)^2 + \left(\frac{\delta_{\mathrm{d}T/\mathrm{d}z}}{|\mathrm{d}T/\mathrm{d}z|}\right)^2 + \left(\frac{\delta_{a_c}}{|a_c|}\right)^2}, \qquad \delta_T = \sqrt{(\delta_{T_c})^2 + (\delta_{T_s})^2}. \tag{3.10}$$

These errors can also be gauged by using extremal values of the variables. Significant uncertainties include closure temperatures, which vary between 110 ± 10°C for AFT and $\sim 60 \pm 30$°C for A-He, although a larger range for AFT is sometimes reported (*Dodson*, 1973; *Green et al.*, 1989; *Reiners and Brandon*, 2006). Geothermal gradients can be affected by changes in basal heat flow, by the distribution of radiogenic elements, and by thermal advection. I tested a suitable range of geothermal gradients (25 ± 15°C km^{-1}), which broadly encompasses those values reported for radiogenic to weakly radiogenic crust. These values are the most significant control for crustal temperatures of unstretched lithosphere (e.g., *McKenzie et al.*, 2005). Surface temperatures are often poorly constrained and I assumed that $T_s = 15 \pm 10$°C (see e.g., *Greenwood and Wing*, 1995). I acknowledge that more complex thermo-kinetic models exist which incorporate, for example, the effects of two- and three-dimensional conductive cooling and advection of heat (e.g., *Braun*, 2002). In my view, the uncertainties in thermal structure of the crust and its time-dependent behaviour mean that simple models are justifiable in this instance. For each sample, denudation rate and associated error were calculated using Equations

3.9 and 3.10.

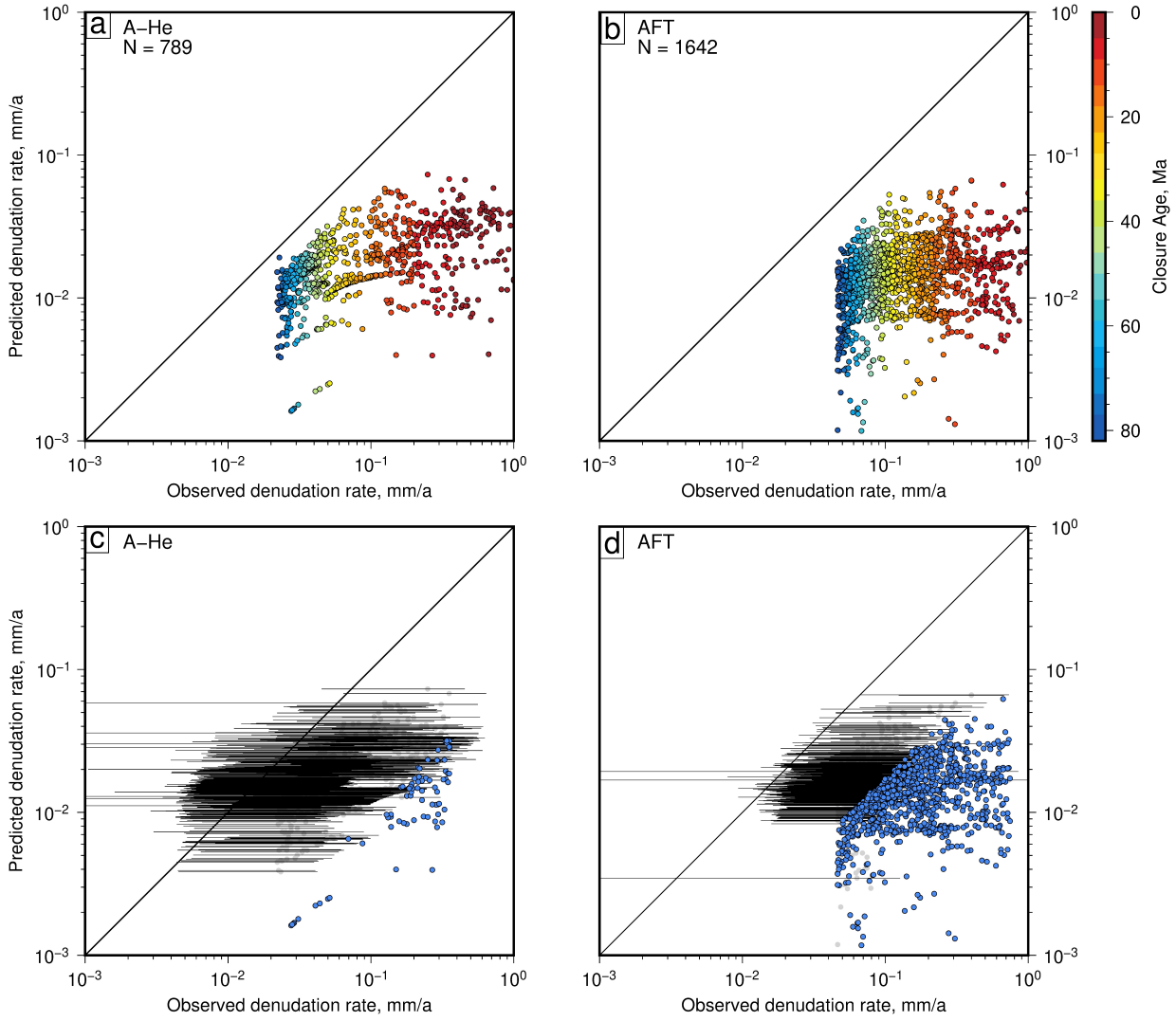

Figure 3.34: **Comparison of thermochronmetric and calculated denudation rates.** (a) Comparison of denudation rates calculated from landscape evolution model that was parameterised using results of inverse modelling (Figure 3.28c) and independent A-He closure ages (see Figure 3.33 panels a and b). Circles coloured according to closure age. Black lines = error bars for all points. (b) Comparison of calculated denudation rates and independent estimates from AFT closure ages. (c) Underpredicted data (blue circles), where calculated denudation rates are factor of two or more lower than A-He and (d) AFT estimates. Error bars have been omitted for clarity. Error bars = data with a good match between the parameterised forward model and independent estimates.

It is important to emphasise that rock uplift without concomitant denudation is difficult to detect using thermochronometric techniques. Conversely, rapid erosion can in principal produce significant denudation in the absence of surface uplift. One way to examine the cause of rock cooling and its relationship with uplift is to extract denudational estimates from parameterised landscape evolution models. Here, I use the compilation of rock cooling rates to test predicted values from my preferred model (Figure 3.28). It is important that these rates are compared at the same location and for

the timescale determined by the closure age of the thermochronometric measurement. The simple, inverse relationship between closure ages and denudation rates shown in equation 3.9 will result in an apparent increase in rates though time (e.g., *Willenbring and Jerolmack*, 2016), however is appropriate for comparison with the average denudation rates extracted from the landscape evolution model. I avoided comparing samples with closure ages younger than 5 Ma which is the limit of resolution for this landscape model. Furthermore, young AFT (or AHe) ages that are <5 Ma can be affected by thermal advection which I have ignored for simplicity (*Lisker et al.*, 2018). A comparison between observed and predicted denudation rates is presented in Figure 3.34. For clarity, uncertainties are shown for samples where my model matches thermochronometric measurements within error (plus or minus a factor of two), representing 90% of the A-He and 36% AFT samples in this inventory. Samples where denudation cannot be predicted within error are shown as blue circles. The landscape evolution model under-predicts 10% and 64% of the A-He and AFT measurements, respectively. One way to interpret these results is that A-He closure ages are more closely related to the formation of the modern landscape than AFT measurements. Rock cooling histories can be sensitive to short wavelength tectonic processes and abrupt changes of denudation rate are unlikely to be expressed in the smooth landscape evolution model presented here. Finally, fission track annealing can result in bias toward younger AFT ages, and therefore higher denudation rates, which is consistent with systematic under-prediction.

3.7 Discussion

3.7.1 Continental Epeirogeny

The stratigraphic and biostratigraphic inventories that I exploit provide excellent evidence for staged regional Cenozoic growth of North American topography, with at least 2 km of topography having been generated since Campanian times ($\sim$ 82 Ma; Figure 3.6; *Chamberlain et al.*, 2012). To further explore and constrain the history of vertical motions and sub-plate support, I solved for spatially and temporally smooth rock uplift histories by inverting a continental inventory of river profiles. This inverse model was calibrated using a small number of incision rates from the Colorado Plateau (*Karlstrom et al.*, 2008; *Roberts et al.*, 2012a). The calculated uplift history is consistent with the independent inventory of stratigraphic and biostratigraphic uplift constraints across the Colorado-Columbia-Rocky Mountains Plateaux, for large portions of the Appalachian Mountains, for Mexico and for the Gulf Coast. It is also broadly consistent with a range of other independent uplift constraints (e.g., clumped

and stable isotopes, magmatism; *Fitton et al.*, 1991; *Huntington et al.*, 2010; *Chamberlain et al.*, 2012). Calculated uplift from the Rockies to Great Plains suggests that regional tilting developed during the last $\sim$ 10 Ma, which is consistent with tilting histories recorded by the Late Miocene Ogallala Group and by the Pliocene Broadwater Formation adjacent to the North Platte river (*Duller et al.*, 2012; *Willett et al.*, 2018). The model performs poorly where there has been significant lateral tectonic

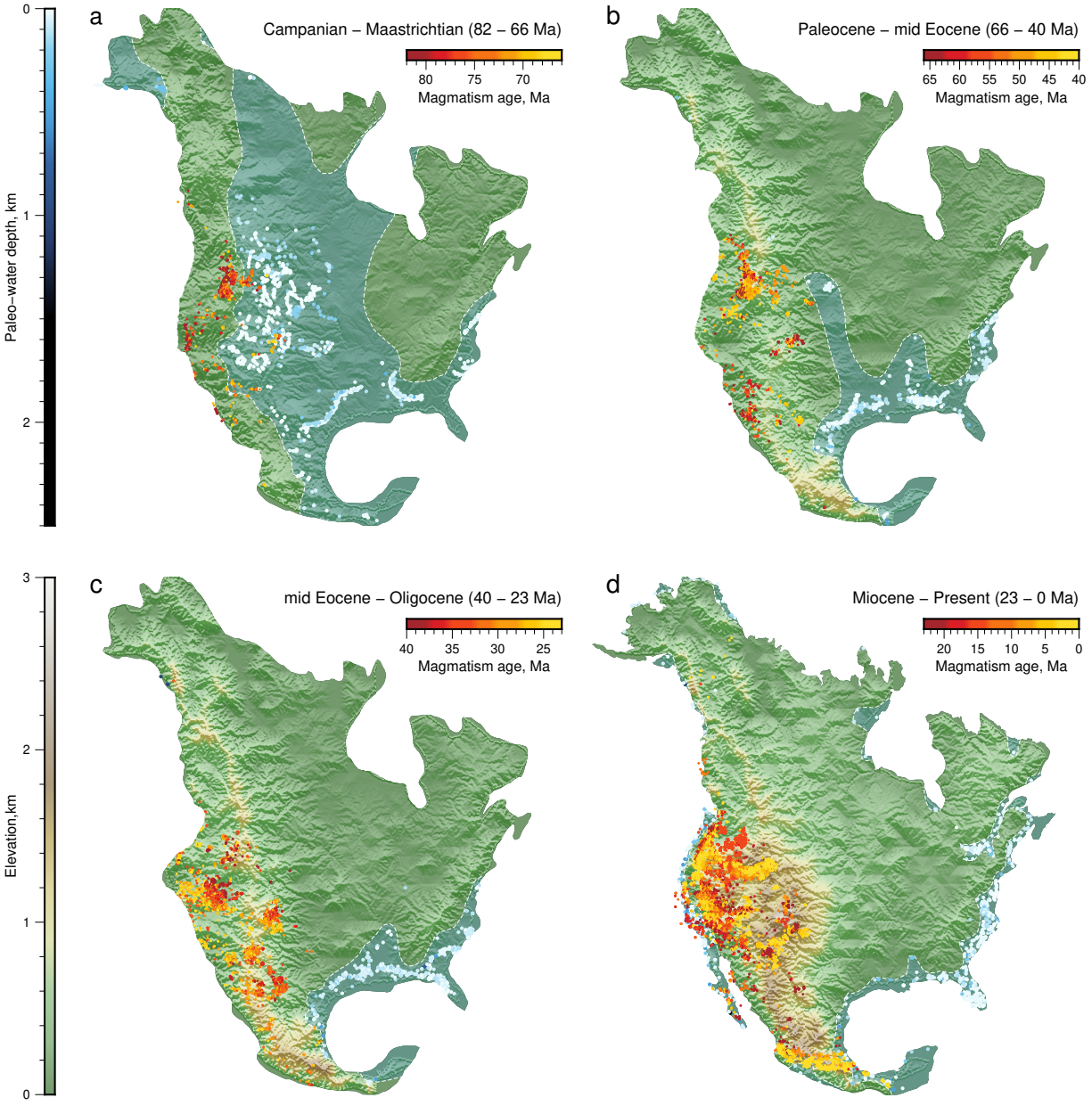

Figure 3.35: **Paleogeography model of North America.** Four panels show calculated Mesozoic to Cenozoic topographic evolution compared with coeval independent paleogeographic constraints. Red circles = magmatic record from NAVDAT database (Figure 3.4); blue circles = stratigraphic shoreline markers/marine fossils from PBDB (Figure 3.12); light blue shading = maximum flooded surface from *Smith et al.* (1994) revised with stratigraphic and biostratigraphic constraints presented here.

displacements (e.g. Pacific seaboard) or where spatially smooth uplift histories are less appropriate. Despite the simplicity of the inverse modelling scheme, there is a reasonable match between timing of uplift and location of paleo-shorelines inferred from the biostratigraphic inventory and from previous studies (Figure 3.35; *Ziegler et al.*, 1985; *Kauffman and Caldwell*, 1993; *Smith et al.*, 1994; *Roberts and Kirschbaum*, 1995).

Observed and calculated uplift rates are broadly consistent and suggest that North American topography grew in several stages. These results imply that drainage planforms tend to respond to changes in uplift rate in a predictable fashion, which can be exploited to investigate continental-scale histories of regional uplift. An important test of this approach is to compare calculated uplift and denudation with independent observations. In Figures 3.25 and 3.34, I show that a simple erosional model can yield results that provide a reasonably good match. The calibrated value of v is appropriate for extracting continental-scale uplift histories from drainage. These combined results provide additional constraints for the driving mechanisms of continental epeirogeny (Figure 3.35).

3.7.2 Consequences for Landscape Evolution

The inverse modelling strategy that I have described and applied makes a series of simplifying assumptions that warrant further discussion. With regard to the drainage evolution of North America, there are three significant concerns: simplicity of the erosional model presented here, stability of the drainage planform, and the influence of glaciation.

Erosional model

First, I have assumed a simplified version of the non-linear stream power erosional model. This model appears to be sufficiently complex to fit large inventories of river profiles with geologically meaningful uplift rate histories in that they are comparable to independent constraints (e.g., Figure 3.25). This model assumes that the values of the erosional parameters, v and m, are constant and that shockwaves are unimportant at long wavelengths (i.e. $n = 1$; Equations 3.2 & 3.8). Implicit in these assumptions is that substrate (e.g., bedrock lithology, alluvium), biota, hydrodynamic processes and changes in climate (e.g. precipitation, discharge) do not set the pace of landscape evolution at long wavelengths and timescales of tens of millions of years. More generally, poor correlations between substrate (or change in substrate) as a function of river elevation, slope, curvature or calculated stream power at wavelengths greater than a few kilometres support the suggestion that lithology may not control channel geometry at wavelengths of more than a few kilometres (*Roberts et al.*, 2012b; *Paul et al.*,

2014; *Czarnota et al.*, 2014). These observations are consistent with spectral analyses of longitudinal river profiles, which indicate that their shapes are dominated by wavelengths > 10 km, and that river profiles from adjacent catchments contain commonalities generated by regional uplift (*Roberts et al.*, 2019; *Roberts*, 2019). Nevertheless, there is a substantial body of work which demonstrates that at smaller scales these processes determine the efficacy of fluvial erosion and the geometry of river profiles (e.g., *Armitage et al.*, 2018; *Baynes et al.*, 2018; *Forte and Whipple*, 2018; *Gallen*, 2018). It is unclear how these complex, dynamic, threshold-dependent, and undoubtedly non-linear, processes scale over geologic timescales. However, at a continental scale, I propose that the long wavelength portions of landscapes are controlled by regional uplift but moderated by integrated fluvial erosion through time and space in a predictable way.

The way in which erosion scales with slope is debated. For example, the value of the slope exponent in the stream power model, n, might range between 2/3 to 5/3 or greater, and may be location, process and scale dependent (e.g., *Howard and Kerby*, 1983; *Whipple and Tucker*, 1999; *Attal et al.*, 2008; *Whittaker and Boulton*, 2012; *Lague*, 2014). If $n > 1$, then information about tectonic history may be lost from longitudinal river profiles (e.g., *Pritchard et al.*, 2009; *Royden and Perron*, 2013). However, several observations exist which suggest that the integrated history of fluvial erosion on scales of order (10^2–10^3) km and (1–10) Ma may depend linearly on slope. For instance, *Czarnota et al.* (2014) shows that there is a global minimum at $n = 1$ by minimising misfit between modelled and observed longitudinal river profiles of modern and ancient thalwegs of the Tumut river, Eastern Australia. In general, testing and validation of fluvial erosional models at long wavelengths and timescales is difficult (*Salles et al.*, 2017). Large inventories of independent constraints on surface and rock uplift can be used to evaluate the success of erosional models (see Figures 3.23, 3.24, 3.25). The simple, linear version of the stream power erosion model I use appears to provide sufficient complexity to match observed longitudinal river profiles and reproduce meaningful uplift histories. However, I acknowledge that at short timescales and length scales, more complex erosional models might be more appropriate.

Stability of the drainage planforms

A second and related issue concerns the evolution of drainage planforms (e.g., *Willett et al.*, 2014). There is much uncertainty about the longevity of drainage networks. Changing drainage planforms by divide migration or by stream capture should, with time, rearrange catchment planforms thus rendering attempts to extract information about uplift signal problematic, especially over long temporal and spatial scales. However, a small number of observations suggest that, at large scales, the assumption

of essentially fixed drainage planforms could be a reasonable one. First, laboratory sand-box experiments point to the importance of pre-existing topography in determining the fixity of drainage divides and the extent to which they can migrate under changing experimental conditions (e.g., *Lague et al.*, 2003; *Bonnet*, 2009). We note that fluvial systems have been used to infer lateral migration of drainage divides by using simple geomorphic parameters (e.g., χ). Unfortunately, use of these simple metric values require assumptions that the spatial pattern of uplift rate is fixed in space and time, which is demonstrably incorrect, especially at continental length scales (*Herman and Braun*, 2006).

Landscape evolution models suggest that drainage divide migration is not especially significant and in any case the inverse modelling presented here is robust to large excursions in values of upstream drainage area since A is taken to a fractional power. Nonetheless, I can examine how calculated uplift histories are affected by changing drainage planform by comparing our results with the history of long-term planform evolution inferred by detrital zircon studies (*Blum and Pecha*, 2014). In Figure 3.8, I summarised measurements of detrital zircon ages along the northern margin of the Gulf of Mexico. Figure 3.8a shows crustal and magmatic zircon source terranes adapted from Figure DR5 of *Blum and Pecha* (2014) where the cumulative percentage plots of Figure 3.8b were redrafted from their Figure DR6. Their observations suggest that the Paleocene drainage planform had a broadly similar distribution to that of the present day. For example, $> 50\%$ of the zircons in Paleocene samples close to the eastern tributaries were derived from the Grenville (1250–950 Ma), Mid-Continent (1500–1300 Ma) and Appalachian (750–280 Ma) terranes (e.g. sample 43). Paleocene samples located west of the Mississippi river have $> 50\%$ of zircons ages that correspond to the Yavapai-Mazatzal (1800–1600 Ma) and Western Cordillera (275–50 Ma) terranes (e.g. sample 64). These observations imply the large-scale planform of the Mississippi catchment may not have significantly changed during Cenozoic times.

Another way to estimate longevity of drainage patterns is to compare observed and predicted sedimentary flux. Sedimentary flux was calculated by integrating incision rate in a downstream direction using the landscape evolution model shown in Figure 3.28. The tectonic history of western North America complicates interpretation of sedimentary flux observations from, for example, the Los Angeles basin or Baja California (see e.g., *Dorsey et al.*, 2018). In contrast, the Gulf of Mexico appears to have acted as a stable depositional sink since Cretaceous times (*Galloway et al.*, 2000). Figure 3.28c–e compares predicted to independent estimates of flux in the Gulf of Mexico (*Galloway et al.*, 2011). Calculated cumulative denudation is highest in the regions of highest predicted uplift rates (e.g. Rocky

Mountains-Colorado Plateaux, Appalachian Mountains, Yukon, Mexican Highlands). Predicted sedimentary flux is smoother than that measured by *Galloway et al.* (2011), which is unsurprising because the landscape model was parameterised using a damped, smooth, rock uplift history. The biggest discrepancy between predicted and observed flux is at $\sim$ 60 Ma (e.g. the Wilcox Formation). I note that model coverage in the headwaters of the Mississippi catchment is low before $\sim$ 55 Ma (Figure 3.28c).

Glaciation

Finally, I have ignored the possible effects of glacial erosion and widespread continental ice cover during the last glacial maximum, partly for simplicity but mostly because it is not obvious how this issue can be addressed in a transparent way. Most of the area that was covered by ice sheets is located within the cratonic regions of northern and eastern Canada where glacial isostatic rebound continues to be a significant driver of surface uplift. Temporal resolution of the inverse model presented here is too coarse to accurately compute the effect of this glacial signal. The effect that extensive ice sheets could have upon drainage planform and their efficiency in topographic erosion relative to fluvial processes are poorly understood. For example, global compilations of erosion rates from glaciers and rivers on timescales of 10^1–10^7 years implies that glacial erosion tends to decrease by one to two orders of magnitude over glacial cycles, whereas fluvial erosion rates reveal no such dependence upon time. This observation suggests that uplift histories control rates of both fluvial and glacial erosion over millennial and longer timescales (*Koppes and Montgomery*, 2009). It remains unclear how drainage planforms were dramatically modified by the last glacial maximum (e.g., *Wickert*, 2016). Geologic constraints for the uplift and denudation history of a region covered by the Laurentide ice sheet are sparse (Figures 3.35 and 3.13). Additional testing of the results of our inverse model for this region would be insightful.

3.7.3 Geodynamic Implications

Both orogenic and epeirogenic processes can generate topography. Shortening, extension, magmatic underplating and dynamic uplift all contribute toward continental uplift and, to some extent, these phenomena can be discriminated between based upon their magnitude and wavelength (e.g., *Pazzaglia and Brandon*, 1996). Cretaceous uplift of the Rocky Mountains region was partially caused by growth of Laramide-aged structures (Figures 3.13 and 3.12). The geomorphic modelling and stratigraphic observations presented here suggest that regional uplift of western North America has dominated evo-

lution of topography. Isostatic considerations indicate that the present-day surface elevation of this extensive region is supported by density variations within and beneath the lithospheric mantle rather than by crustal thickening (e.g., *Levandowski et al.*, 2018). Rare earth element inverse modelling of < 5 Ma basaltic melts with Ocean Island Basalt affinities combined with the presence of shear wave velocity anomalies constrained by earthquake tomographic models are consistent with moderately elevated mantle potential temperatures and thin ($\sim$70 km) lithosphere beneath western North America (*Klöcking et al.*, 2018a). These observations support the notion that large-scale dynamic topography is generated and maintained by temperature anomalies within asthenospheric mantle directly beneath a thin plate. The detailed driving mechanisms that underpin observed and predicted vertical displacements have been explored by a range of numerical flow models on different temporal and spatial scales (see, e.g., *Mitrovica et al.*, 1989; *Lithgow-Bertelloni and Gurnis*, 1997; *Liu et al.*, 2008; *Moucha et al.*, 2008b; *Spasojević et al.*, 2009; *Forte et al.*, 2009; *van Wijk et al.*, 2010; *Spasojević and Gurnis*, 2012; *Rowley*, 2013; *Liu*, 2014). The results from this study could provide additional constraints for such models.

Chapter 4

Uplift, Subsidence and Evolution of the U.S. Mid-Atlantic Region

Part of the work presented in this Chapter (Section 4.3) has been published[1] as

Morris, M., Fernandes, V.M., and Roberts, G.G. (2020). Extricating dynamic topography from subsidence patterns: Examples from Eastern North America's passive margin, *Earth and Planetary Science Letters*, *530*, 115840, doi:10.1016/j.epsl.2019.115840.

4.1 Chapter overview

The two previous chapters have focused on quantifying positive vertical motions (i.e. uplift) on continents. In Chapter 2, I created a global database of uplift, and explored how these measurements can be used to examine possible causes of uplift. In Chapter 3, I used the uplift measurements generated in Chapter 2 together with additional proxies for landscape change, combined with a calibrated inverse modelling of river profiles, to generate a continental-scale uplift history of North America. This uplift history, combined with landscape evolution models, was used to make predictions of elevation, denudation, and crucially, sedimentary flux to the continental margins. In this chapter I turn my focus to the eastern margin of the North American continent, where I explore uplift, subsidence and sedimentary flux to this passive margin.

[1]My work forms the principal contribution to this publication. I supervised the preliminary data processing and analysis, which was performed by M. Morris as part of their MSci research project. I have not included results or analysis from the published article that have not been the direct result of my own work.

4.2 Introduction

The U.S. Atlantic margin, including the Appalachian Mountains and associated continental platform, has been a subject of much debate and controversy in the literature. It is generally agreed that the Appalachian Mountains have been a tectonically quiescent region since the establishment of a passive margin in the Late Jurassic (e.g. *Klitgord et al.*, 1988). Offshore sedimentary basins, formed during rifting of the North Atlantic, are generally thought to have been an effective sink for sediment shed eastward from the Appalachian Mountains and post-rift margin since Triassic-Jurassic times (*Steckler and Watts*, 1978; *Grow et al.*, 1988; *Watts and Thorne*, 1984). The largest of them, the Baltimore Canyon Trough (BCT), is a 400 km long, 18 km deep basin recording an almost complete history of continuous erosion and subsidence (*Poag and Sevon*, 1989). Onshore, geomorphological studies indicate modern rates of erosion are low ($\sim$ 20–40 m Ma^{-1}), and comparable to long-term denudation rates derived from thermochronological studies (closure ages of 80–100 Ma; *Pavich et al.*, 1985; *Boettcher and Milliken*, 1994; *Matmon et al.*, 2003; *Naeser et al.*, 2004; *Portenga et al.*, 2013; *Amidon et al.*, 2016). On the other hand, seismic and well data from offshore sedimentary basins demonstrate an order of magnitude increase in sediment accumulation rates from the Miocene to Recent (e.g. *Poag and Sevon*, 1989; *Poag and Ward*, 1993). The implication is that these changes related to increases in mechanical erosion rates, contradicting the notion of a stable passive continental margin, free from major tectonic events that could drive a change in erosion rates. One way to investigate this geological paradox is to integrate the history of subsidence and sediment accumulation offshore to measurements of uplift and denudation onshore in a self-consistent framework (e.g. *Czarnota et al.*, 2013, 2014). The Appalachians Mountain and BCT represent a suitable natural laboratory to investigate the links between the evolution of source areas and sediment sinks.

This chapter has two parts. First, I combine backstripping of wells along Eastern North America's passive margin with seismological and gravity data and simple isostatic calculations to examine the timing, amplitude and wavelength of vertical motions, which highlights the importance of subplate support in the BCT (Section 4.3). Second, I explore whether the uplift history and calibrated Landscape Evolution Model described in Chapter 3 can be used to better understand the history of denudation and sedimentary flux to the basin and the implications for the Neogene evolution of the margin (Section 4.4).

4.3 Passive Margin Subsidence and Sub-Plate Support

The stratigraphic record at passive margins can be affected by a suite of geological processes including the history of rifting and post-rift cooling, eustasy, sub-plate support and the effects of water-loading and glacial unloading (e.g., *McKenzie*, 1978; *Le Pichon and Sibuet*, 1981; *Lambeck and Chappell*, 1988; *Allen and Allen*, 2005; *Kominz et al.*, 2016; *Austermann et al.*, 2017; *Müller et al.*, 2018). One approach to circumvent the challenging task of isolating, for example, eustasy is to backstrip stratigraphy at margins with a well understood tectonic (rift and post-rift) history (e.g., *Miller et al.*, 2003; *Kominz et al.*, 1998, 2016). The eastern seaboard of North America has been used to do so because its tectonic history is, on the whole, well understood (*Watts and Ryan*, 1976; *Steckler and Watts*, 1978; *Watts and Thorne*, 1984). Biostratigraphic analyses of core and cuttings from wells along the margin combined with reflection and refraction seismology, and oceanic magnetic anomalies, show that, following late-Triassic to early-Jurassic rifting, post-rift subsidence of the margin has been governed principally by lithospheric cooling (e.g., *Steckler and Watts*, 1978; *Grow et al.*, 1988; *Steckler et al.*, 1999; *Miller*, 2005; *Miller et al.*, 2013; *Kominz et al.*, 2008, 2016; *Greene et al.*, 2017). Fitting of simple cooling models to backstripped subsidence patterns and inversion for strain rate histories indicate that the lithosphere beneath the extensively studied COST B-2 well in the Baltimore Canyon Trough stretched by a factor, $\beta \sim 2$ (e.g. *Steckler et al.*, 1999; *Flament et al.*, 2013). However, stratigraphy of the deepest (syn-rift) parts of this margin is sparsely sampled and this value is debated (see e.g. *Watts and Thorne*, 1984).

Residual subsidence, i.e., that not explained by thermal cooling of stretched lithosphere, can be interpreted as changes in accommodation space caused by eustasy. The eastern passive margin of North America has been extensively studied with the aim of documenting the history of global eustatic sea level changes (e.g., *Miller*, 2005; *Kominz et al.*, 2016). Additional mechanisms proposed to generate subsidence along this margin include a flexural response due to offshore sediment loading, plate reorganisation and epeirogeny generated by dynamic support (*Cloetingh et al.*, 1990; *Pazzaglia and Gardner*, 1994; *Vanderaveroet*, 2000; *Browning et al.*, 2006; *Kominz et al.*, 2008, 2016).

It is generally accepted that mantle convection can generate time-dependent vertical motions of the lithosphere that overlap in amplitude and timescale with estimates of eustatic (global) sea-level change (order 10–100 m, over 100 ka–100 Ma; *Hager and Richards*, 1989; *Lithgow-Bertelloni and Silver*, 1998; *Miller*, 2005; *Lovell*, 2010; *Hartley et al.*, 2011; *Rovere et al.*, 2014; *Cloetingh and Haq*, 2015; *Kominz et al.*, 2016). Stratigraphy and sub-plate shear wave velocities from the Mauritanian margin of northern

Africa and Australian's Northwest Shelf, for example, indicate that mantle convective drawdown can generate hundreds of meters of water-loaded subsidence on timescales of 1–10 Ma (*Czarnota et al.*, 2014; *Lodhia et al.*, 2018). Residual ocean age-depth measurements indicate that dynamic topography has wavelengths of hundreds to thousands of kilometres, and amplitudes of up to order 10^3 m (*Hoggard et al.*, 2017). These observations and the complex response of sea level to glacial unloading means that estimating eustasy from a single site is generally challenging (see e.g., *Austermann et al.*, 2017; *Mitrovica et al.*, 2020). Geodynamic models of mantle convection provide predictions of vertical motions at passive margins with amplitudes up to 10^3 m and wavelengths up to order 10^4 km (e.g., *Müller et al.*, 2008; *Moucha et al.*, 2008; *Spasojević et al.*, 2008; *Flament et al.*, 2013; *Steinberger et al.*, 2019). However, there is disagreement on the predicted timing, amplitude and wavelength of support, and whether sub-plate processes have generated uplift or subsidence. Given the general importance of accurately constraining sea-level change, I investigate whether a signal of sub-plate support can be isolated using stratigraphic and geophysical observations along Eastern North America's passive margin (Figure 4.1). In the first part of this chapter, the stratigraphic archive is used to examine the history of lithospheric subsidence.

4.3.1 Geophysical observations

Figure 4.1b shows free air gravity data extracted from the GRACE dataset filtered to remove wavelengths $\lesssim 800$ km, which can be used as a guide to sub-plate support (e.g., *McKenzie*, 2010; *Colli et al.*, 2016). The Baltimore Canyon Trough has negative free-air gravity anomalies of between ~ -30 to 0 mGal (*Tapley et al.*, 2005). In comparison, the Georges Bank and the Southeast Georgia Embayment, ~ 500 km north and ~ 1000 km south of the trough, respectively, have anomalies of ~ 0 to $+10$ mGal. Positive free-air anomalies are centred on the Bermuda Rise and on the Appalachian mountains (e.g. *Courtillot et al.*, 2003). If a transfer function of 30–50 mGal km^{-1}, which encompasses the range of admittance values typically assumed for oceanic and continental dynamic support, is used to convert long wavelength gravity into a prediction of sub-plate support it implies that the Baltimore Canyon Trough is drawn down by ~ 0.6–1 km today (*Crosby et al.*, 2006). Calculated drawdown does not extend to the Georges Bank or the Southeast Georgia Embayment (Figure 4.1b). These observations are broadly consistent with some geodynamic predictions of upper mantle convective drawdown (e.g. *Steinberger et al.*, 2019). Nevertheless, using single admittance values to estimate dynamic support is debated (see e.g., *Colli et al.*, 2016). Admittance methods indicate that the elastic thickness of Eastern North America's continental lithosphere is on the order of 10s of kilometres (e.g. *McKenzie*,

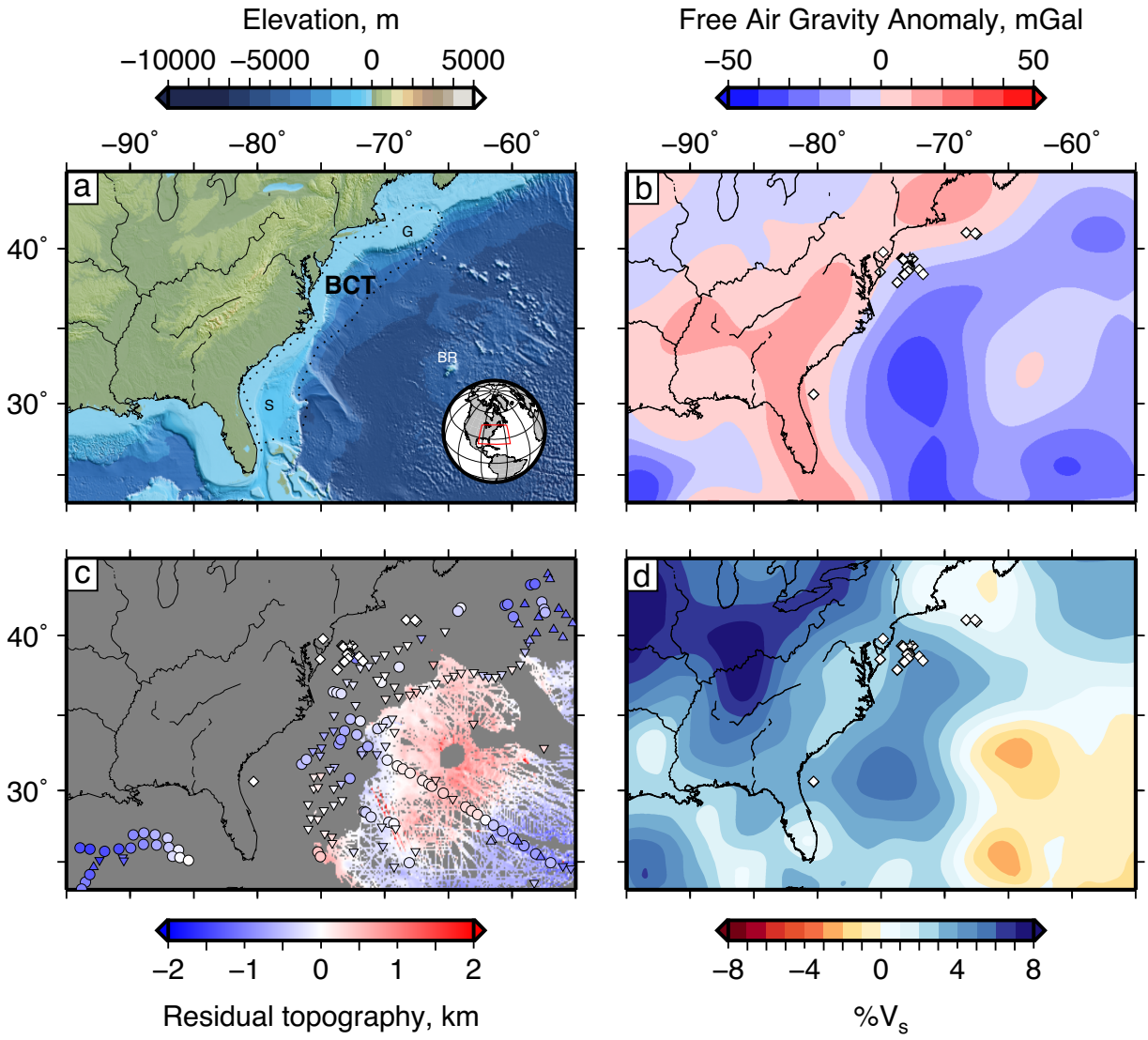

Figure 4.1: **Eastern North America and Atlantic Ocean.** (a) Topography and bathymetry of the Eastern North American passive margin (ETOPO1 dataset). Dotted line indicates extent of seismic data. G = Georges Bank, BCT = Baltimore Canyon Trough, S = Southeast Georgia Embayment, B = Bermuda Rise. (b) Free air gravity anomalies from the GRACE dataset, filtered to remove wavelengths $\lesssim$ 800 km. Diamonds = wells backstripped in this study. (c) Geoid-corrected residual ocean-age depths in 1° bins (*Hoggard et al.*, 2017). Circles represent measurements with sedimentary and crustal corrections applied. Up/down pointing triangles = lower/upper limits for which only a sedimentary correction has been applied. Filigree = residual ocean-age depth estimates from ship track data. (d) Slice through SL2013sv shear wave tomographic model at 125 km depth (*Schaeffer and Lebedev*, 2013). Note that free-air gravity anomalies and residual topography of the Baltimore Canyon Trough and its surroundings are negative, and the region sits atop fast upper mantle shear wave velocity anomalies.

2010). Recent spherical wavelet transformation of gravity and topography indicate that the elastic thickness of Eastern North America's passive margin is $\sim$ 15–40 km, which implies that sub-plate processes could be manifested at Earth's surface at wavelengths of 100s km (Figure 4.2; *Audet and Bürgmann*, 2011; *Audet*, 2014).

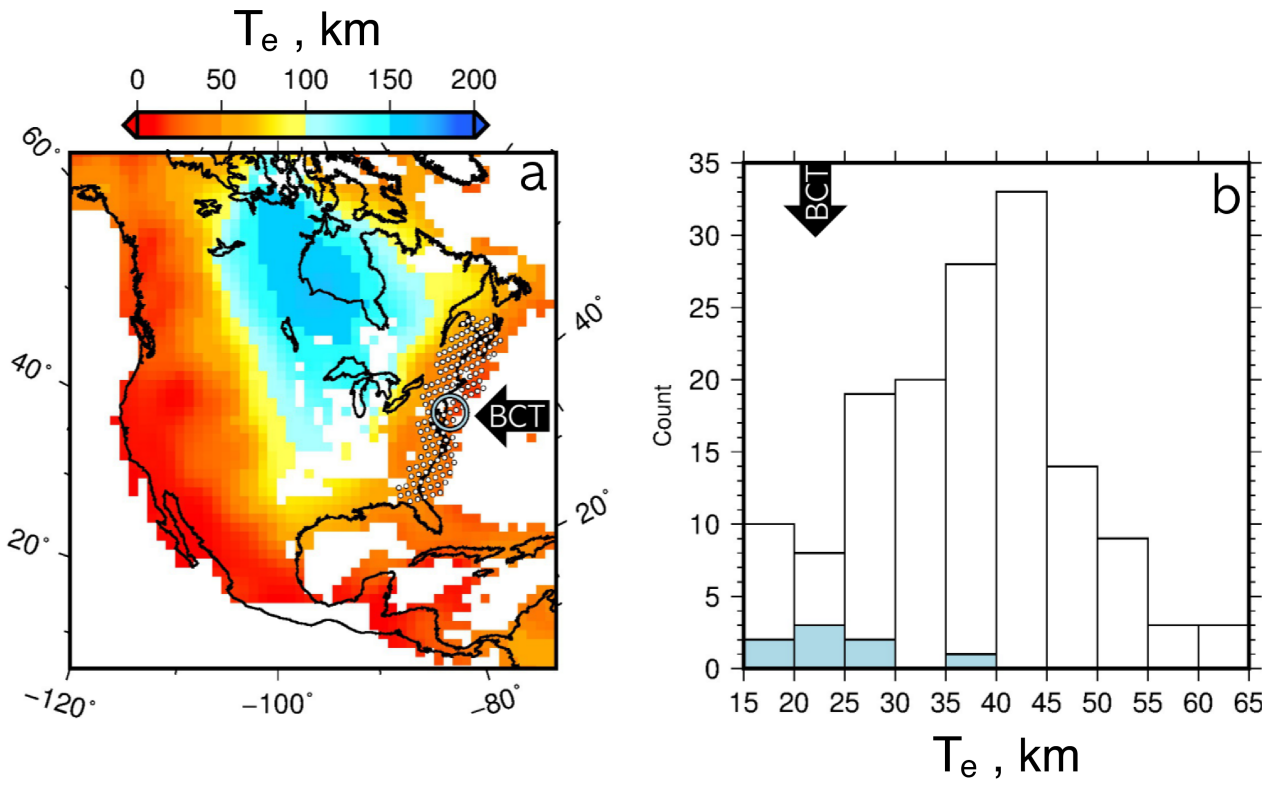

Figure 4.2: **Elastic thickness of eastern North America**. (a) Colour scale = elastic thicknesses, T_e, from *Audet* (2014)'s spherical wavelet analysis of gravity and topography. ∘ = measurements on eastern seaboard used to generate histogram shown in panel (b). Blue circle encompasses Baltimore Canyon Trough (BCT). (b) Histogram of T_e estimates from eastern seaboard (white bars) and Baltimore Canyon Trough (blue). Note T_e of ∼ 15–40 km centred on Baltimore Canyon Trough.

Residual ocean age-depth measurements can also be used to estimate present-day sub-plate support (Figure 4.1c; *Hoggard et al.*, 2017). Oceanic lithosphere close to the Baltimore Canyon Trough has a residual depth of −0.2 to −0.4 km. Highest positive residuals in this region (almost +1 km) are centred on the Bermuda Rise.

A slice through the SL2013sv shear wave tomography model at 125 km depth beneath eastern North America and the western Atlantic Ocean is shown in Figure 4.1d (*Schaeffer and Lebedev*, 2013). Upper mantle velocity anomalies appear to be a few percent faster than the AK135 global model beneath the Baltimore Canyon Trough. A suite of other recent shear wave tomographic models also shows fast upper mantle velocity anomalies beneath the New Jersey margin (e.g., *Ritsema et al.*, 2011; *Moulik and Ekstrom*, 2014; *French and Romanowicz*, 2014; *Durand et al.*, 2017). The SL2013sv model has broadly comparable velocities to the global average beneath the Southeast Georgia Embayment and the Georges Bank. A long wavelength slow velocity anomaly is centred on the Bermuda Rise. Sub-plate support calculated from gravity and residual ocean-age depths also broadly correlate with upper mantle velocity anomalies in more recent shear wave tomographic models improved by data

collected during the EarthScope Transportable Array experiment (Figure 4.1; *Clouzet et al.*, 2018). These observations combine to suggest that the Baltimore Canyon Trough sits above the margins of upper mantle that is drawing down the lithosphere. Whereas sub-plate uplift or drawdown of the Georges Bank and Southeast Georgia Embayment appears to be negligible.

A suite of geodynamic models predict dynamic drawdown of the New Jersey margin, and adjacent Appalachian Mountains, during the last $\sim$ 20 Ma. The convection model of *Spasojević et al.* (2008) predicts $\sim 500-250$ m of regional dynamic subsidence since 50 Ma, with $\sim 70-120$ m of the drawdown occurring over the last 20 Ma. *Flament et al.* (2013) models $\sim$ 750 m dynamic subsidence between 120–35 Ma, but only 30 m in the last 15 Ma. *Liu* (2014) predicts a similar history of vertical motions, with 500–700 m dynamic subsidence of Appalachians and BCT region since 60 Ma, but virtually no changes in vertical motions from 15–0 Ma. Many, but not all, geodynamic models of mantle convection predict Neogene dynamic drawdown of the eastern North American margin. For example, mantle flow simulations by *Moucha et al.* (2008) predict $\sim 50-150$ m of dynamic uplift since 30 Ma. A suite of mantle convection simulations by *Müller et al.* (2008) predict 105–385 m of dynamic subsidence of the Appalachians-BCT region, but predictions of Neogene vertical motions vary between 100 m of continuous subsidence over the last 20 Ma, and $\sim$ 40 m of uplift in the last 8 Ma.

Despite the seemingly contradictory predictions, geodynamic models tend to emphasise the importance of flow at deeper, mid-mantle, depths associated with Farallon plate subduction in driving drawdown. The models also predict patterns of uplift and subsidence on wavelengths $>$ 2000 km, meaning smaller scale sub-plate mantle processes that could generate measurable vertical motions might not be accounted for. Gravity and residual ocean age-depth data, and more recent tomographic models indicate that support of the margin might be related to upper mantle structure (e.g., Figure 4.1). In other regions, such as West Africa, Northwest Australia, and Borneo, dynamic topography appears to be governed by the thermal (buoyancy) structure of the uppermost convecting mantle (e.g., *Czarnota et al.*, 2014; *Hoggard et al.*, 2017; *McNab et al.*, 2018; *Roberts et al.*, 2018; *Lodhia et al.*, 2018).

In order to estimate the history of sub-plate drawdown of Eastern North America's passive margin, first, I calculate the subsidence histories of 27 wells from Georges Bank to the Southeast Georgia Embayment. Published backstripped subsidence histories for the BCT have previously used a single well from the basin, the COST B-2 well (e.g., *Watts and Thorne*, 1984; *Heller et al.*, 1982; *Browning et al.*, 2006). Preliminary analysis of published seismic profiles indicates a greater complexity in

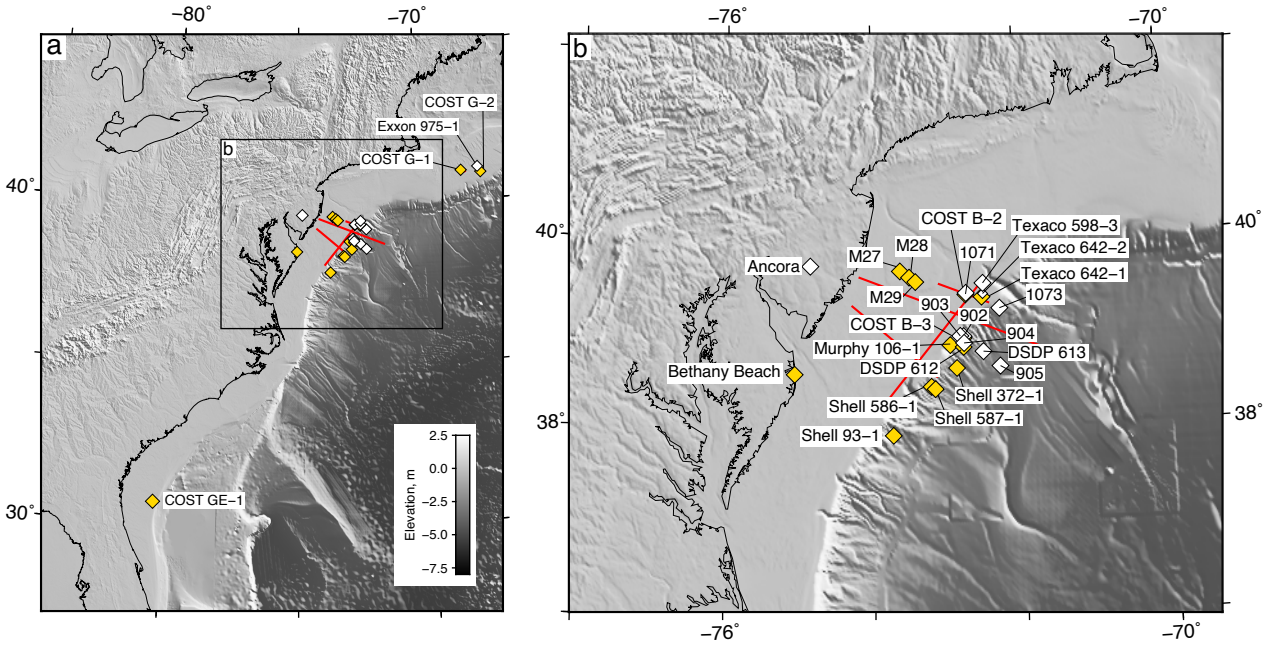

Figure 4.3: **Location of well data** on passive margin of eastern North America from Miami to Maine. Labelled gold diamonds = backstripped wells published in *Morris et al.* (2020); labelled white diamonds = additional backstripped wells; solid red lines = seismic reflection data shown in Figure 4.14.

the subsidence and sediment accumulation history of the BCT (e.g. data from *Monteverde et al.*, 2008), where a shift from prograding to aggrading clinoforms can be identified in the stratigraphic architecture. Multiple studies have indicated the region has undergone a period of increased erosion during the Middle Miocene, reflected in a regional unconformity and deeply incised canyons (e.g. *Mountain et al.*, 1996). These observations suggest the Neogene to Recent vertical motions might not be fully explained by a simple model of continuous thermal subsidence of a passive margin.

4.3.2 Data

27 wells along the Atlantic continental margin, including the COST B-2 well, were backstripped to calculate their subsidence histories (Figure 4.3). 23 of these wells are located in, or are proximal to, the Baltimore Canyon Trough. The COST G-1, COST G-2 and Exxon 957-1 wells are located on Georges Bank, and the COST GE-1 well is in the Southeast Georgia Embayment. Details of each well can be found in Table 4.1

Table 4.1: **List of wells** used in this study. Latitude and longitude are given in decimal degrees. MD = maximum depth of well below Kelly Bushing; KB = height of Kelly Bushing above sea level; WD = water depth below sea surface.

	Well Name	Latitude	Longitude	MD [m]	KB [m]	WD [m]
1	COST G-1	40.931	-68.305	4899	29.9	48.4
2	COST G-2	40.836	-67.508	6667	24.1	82.9
3	Exxon 975-1	41.007	-67.622	4452	10.4	63.7
4	COST B-2	39.375	-72.734	4890	27.4	90.8
5	COST B-3	36.917	-72.773	4822	12.8	819
6	Texaco 598-3	39.382	-72.499	4908	23.8	129.5
7	Texaco 642-1	39.348	-72.515	5428	25.0	137.2
8	Texaco 642-2	39.493	-72.494	5608	26.8	135.6
9	IODP 313 M27	39.381	-73.373	89	17.0	33.5
10	IODP 313 M28	39.339	-73.298	89	13.7	35.1
11	IODP 313 M29	39.312	-73.248	89	16.7	36.0
12	Murphy 106-1	38.850	-72.960	5610	29.9	125.6
13	DSDP 612	38.823	-72.779	675.3	32.8	1386
14	DSDP 613	38.771	-72.507	2901	10.0	2309
15	Shell 372-1	38.600	-72.871	3545	14.6	2119
16	Shell 586-1	38.406	-73.218	4877	14.6	1779
17	Shell 587-1	38.381	-73.164	4419	14.6	1965
18	Shell 93-1	37.893	-73.736	5407	14.6	1529
19	ODP 150 902	38.935	-72.773	1559	11.0	808.0
20	ODP 150 903	38.938	-72.817	1490	11.7	4441.3
21	ODP 150 904	38.863	-72.768	1711	11.2	1122.8
22	ODP 150 905	38.614	-72.284	3620	11.1	2697.9
23	ODP 174A 1071	39.382	-72.728	151	11.2	88.2
24	ODP 174A 1073	39.225	-72.276	1315	11.5	639.4
25	Bethany Beach	38.548	-75.062	448	1.4	0
26	Ancora	39.692	-74.849	356.7	31.7	0
27	COST GE-1	30.619	-80.300	4040	30.0	41.5

4.3.3 Stratigraphic framework

Basin-wide stratigraphy has been widely described in the literature over the past 35 years (e.g., *Smith et al.*, 1976; *Schlee*, 1981; *Poag and Sevon*, 1989; *Poag and Ward*, 1993; *Miller et al.*, 1998; *Pekar et al.*, 2003; *Browning et al.*, 2008; *Miller et al.*, 2017). Extensive commercial and scientific drilling of the onshore and offshore portions of the margin, which, coupled with a wealth of available seismic reflection data, has provided a comprehensive stratigraphic framework for the basin. Figure 4.4 shows a summary of the generalised basin stratigraphy based on lithologies and ages reported in the COST

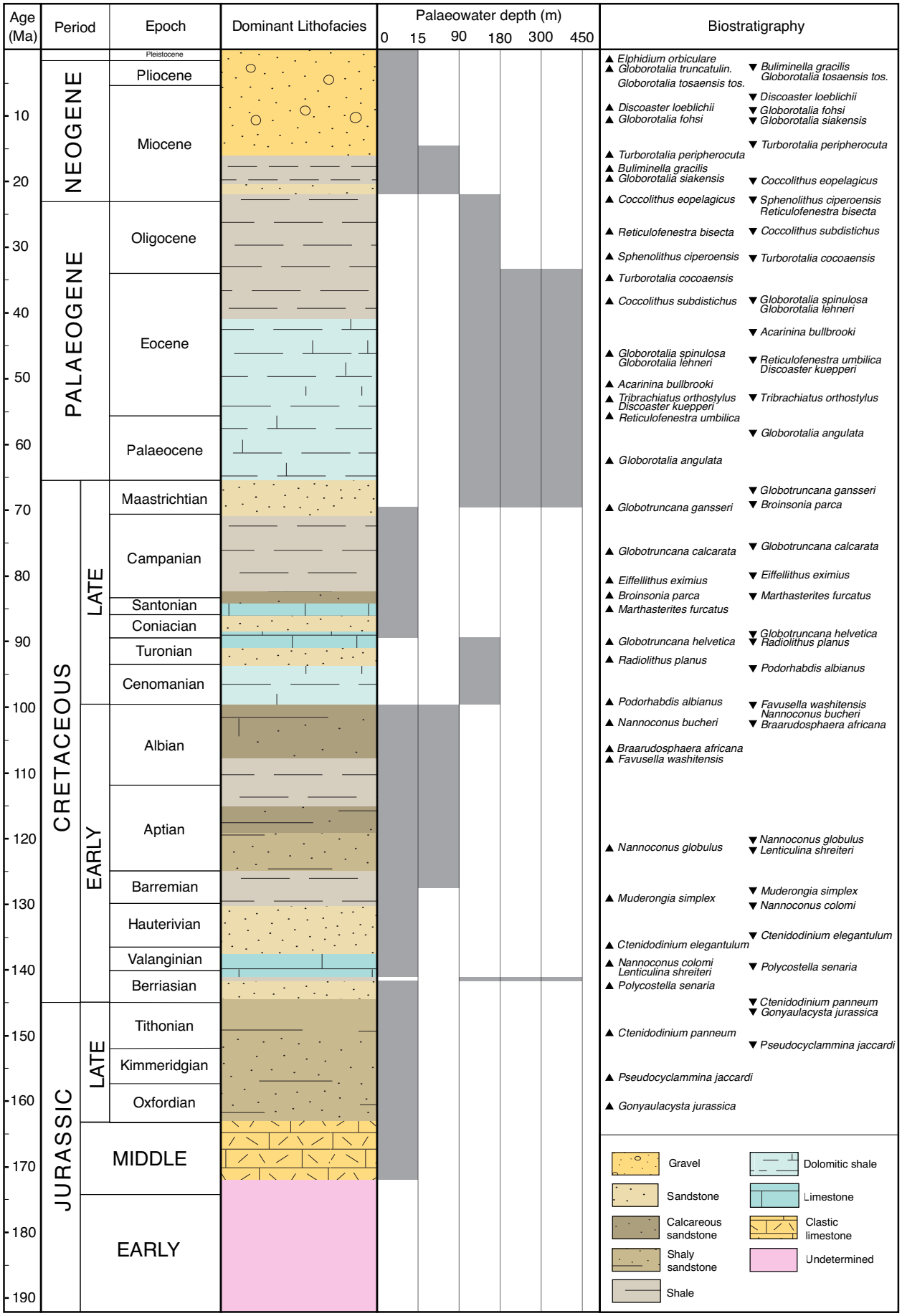
Age (Ma)
Period
Epoch
Dominant Lithofacies
Palaeowater depth (m)
0 15 90 180 300 450
Biostratigraphy
Pleistocene
NEOGENE
Pliocene
Miocene
PALAEOGENE
Oligocene
Eocene
Palaeocene
CRETACEOUS
LATE
Maastrichtian
Campanian
Santonian
Coniacian
Turonian
Cenomanian
EARLY
Albian
Aptian
Barremian
Hauterivian
Valanginian
Berriasian
JURASSIC
LATE
Tithonian
Kimmeridgian
Oxfordian
MIDDLE
EARLY
10
20
30
40
50
60
70
80
90
100
110
120
130
140
150
160
170
180
190
▲ Elphidium orbiculare
▲ Globorotalia truncatulin.
Globorotalia tosaensis tos.
▲ Discoaster loeblichii
▲ Globorotalia fohsi
▲ Turborotalia peripherocuta
▲ Buliminella gracilis
▲ Globorotalia siakensis
▲ Coccolithus eopelagicus
▲ Reticulofenestra bisecta
▲ Sphenolithus ciperoensis
▲ Turborotalia cocoaensis
▲ Coccolithus subdistichus
▲ Globorotalia spinulosa
Globorotalia lehneri
▲ Acarinina bullbrooki
▲ Tribrachiatus orthostylus
Discoaster kuepperi
▲ Reticulofenestra umbilica
▲ Globorotalia angulata
▲ Globotruncana gansseri
▲ Globotruncana calcarata
▲ Eiffellithus eximius
▲ Broinsonia parca
▲ Marthasterites furcatus
▲ Globotruncana helvetica
▲ Radiolithus planus
▲ Podorhabdis albianus
▲ Nannoconus bucheri
▲ Braarudosphaera africana
▲ Favusella washitensis
▲ Nannoconus globulus
▲ Muderongia simplex
▲ Ctenidodinium elegantulum
▲ Nannoconus colomi
Lenticulina shreiteri
▲ Polycostella senaria
▲ Ctenidodinium panneum
▲ Pseudocyclammina jaccardi
▲ Gonyaulacysta jurassica
▼ Buliminella gracilis
Globorotalia tosaensis tos.
▼ Discoaster loeblichii
▼ Globorotalia fohsi
▼ Globorotalia siakensis
▼ Turborotalia peripherocuta
▼ Coccolithus eopelagicus
▼ Sphenolithus ciperoensis
Reticulofenestra bisecta
▼ Coccolithus subdistichus
▼ Turborotalia cocoaensis
▼ Globorotalia spinulosa
Globorotalia lehneri
▼ Acarinina bullbrooki
▼ Reticulofenestra umbilica
Discoaster kuepperi
▼ Tribrachiatus orthostylus
▼ Globorotalia angulata
▼ Globotruncana gansseri
▼ Broinsonia parca
▼ Globotruncana calcarata
▼ Eiffellithus eximius
▼ Marthasterites furcatus
▼ Globotruncana helvetica
▼ Radiolithus planus
▼ Podorhabdis albianus
▼ Favusella washitensis
Nannoconus bucheri
▼ Braarudosphaera africana
▼ Nannoconus globulus
▼ Lenticulina shreiteri
▼ Muderongia simplex
▼ Nannoconus colomi
▼ Ctenidodinium elegantulum
▼ Polycostella senaria
▼ Ctenidodinium panneum
▼ Gonyaulacysta jurassica
▼ Pseudocyclammina jaccardi
Gravel
Sandstone
Calcareous sandstone
Shaly sandstone
Shale
Dolomitic shale
Limestone
Clastic limestone
Undetermined

Figure 4.4: **Chronostratigraphy of the Baltimore Canyon Trough (following page).** Lithofacies are synthesised from wells across the Baltimore Canyon Trough. Paleo-water depths were extracted from well reports, and were interpreted from benthic fauna and environmental settings; grey band = paleo-water depth uncertainty (*Smith et al.*, 1976; *Scholle*, 1977). Right panel shows first (upward pointing triangle) and last (downward pointing triangle) appearances of common and dominant species in the Baltimore Canyon Trough used to constrain age of stratigraphy.

B-2 well log, and broadly comprises a series of widespread siliciclastic and mixed carbonate sequences, bounded by erosional unconformities, that can be traced throughout the basin. I here provide a brief description of the basin stratigraphy, primarily based on the sedimentological descriptions in the analysed well reports and interpretations from *Scholle* (1977) and *Poag and Ward* (1993).

The thickest sediment succession accumulated at the margin during the rift period (Triassic-Jurassic). Non-marine Triassic clastic and evaporite deposits, preserved mainly in onshore half-graben basins (e.g. Newark-Gettysburg, Culpeper, Richmond basins) gave way to predominantly shallow marine Jurassic sedimentation. Large thicknesses of shales and sandstones accumulated in a near-shore environment, whilst limestones were deposited in outer shelf reefs. It is important to note that the oldest biostratigraphic unit drilled in the margin is Oxfordian (157–163 Ma), therefore ages of older units are less-precisely determined. Shallow marine facies continued into the Early Cretaceous. Deeper-water sequences were deposited during Cenomanian-Turonian times, before reverting back to shallow-water deposits caused by progradation of a clastic sediment wedge. A basin-wide deepening of depositional paleo-environments is observed during the Maastrichtian-Paleocene, which progressively shoaled in Neogene to Recent times due to progradation and aggradation of siliciclastic deposits. Significant regional unconformities, with time gaps estimated to range from 1–4 Ma, have been recognised between the Hauterivian and Barremian, Turonian and Coniacian, Palaeocene and Maastrichtian, late Eocene and late Oligocene, and the middle Miocene and Pliocene. The most striking of these unconformities separate the Palaeocene/Maastrichtian and late Eocene/late Oligocene where an estimated 17–18 Ma and 8 Ma, respectively, are missing.

4.3.4 Backstripping methodology

Backstripping makes use of age, depth, sediment compaction, and paleo-water depth observations from wells to estimate basement subsidence in the absence of sediment. Stratigraphy from the BCT wells was backstripped using a one-dimensional model that assumes Airy isostasy, which is probably appropriate because this stretched margin has an elastic thickness, $T_e \sim$ 15–40 km (*Watts and Ryan*, 1976; *Audet*, 2014). Age-depth relationships were determined by biostratigraphic correlation

of foraminifera, nannofossils and palynomorphs recorded in published well logs. Paleo-water depths, interpreted from benthic fauna, were extracted from individual well reports (e.g., Figure 4.4 for the COST B-2). Once age-depth relationships were obtained, the well stratigraphy was decompacted, water-loaded and corrected for paleo-water depth, in order to isolate the signal of tectonic subsidence.

To calculate the decompacted sediment thickness for each well, a porosity-depth relationship was established from available, checkshot or interval velocity data. These observations were used to determine initial porosity, $\phi_\circ$, and compaction wavelength, λ. Calculated porosity-depth curves were compared to available porosity measurements. The methodology is outlined below, and exemplified in Figure 4.5 for the COST B-2 well.

First, I sought the $\phi_\circ$ and λ values that yielded calculated time-depth pairs with the lowest residual misfit to checkshot values. Porosity as a function of depth was parameterised using *Athy* (1930)'s well-known formulation

$$\phi(z) = \phi_\circ \exp\left(-\frac{z}{\lambda}\right). \tag{4.1}$$

Velocity, v_s, as a function of porosity (and depth), which can be straightforwardly related to time-depth pairs, was calculated using *Wyllie et al.* (1956)'s approach

$$\frac{1}{v_s(z)} = \frac{\phi(z)}{v_w} + \frac{1-\phi(z)}{v_{sg}}. \tag{4.2}$$

Here, v_w represents pore fluid velocity and was assigned a value of 1.5 km s^{-1}, representative of seawater, and v_{sg} is the solid grain velocity, assigned a value of 5.5 km s^{-1} to represent a sand-clay mixture, which is appropriate for wells in the Baltimore Canyon Trough (e.g., *Scholle*, 1977; *Kominz et al.*, 2016). Porosity is not assumed to be lithology dependent, and is probably a reasonable assumption given the variability in individual lithology porosity-depth curves (*Kominz et al.*, 2016).

Two-way travel time, T, and velocity are related such that

$$\int_0^T \mathrm{d}t = 2\int_0^z \frac{\mathrm{d}z}{v_s(z)}. \tag{4.3}$$

Combining Equations 4.1 and 4.2, and substituting into Equation 4.3, yields

$$T = 2\left\{\lambda\phi_\circ\left[\frac{1}{v_{sg}} - \frac{1}{v_w}\right]\left[\exp\left(\frac{-z}{\lambda}\right) - 1\right] + \frac{z}{v_{sg}}\right\}. \tag{4.4}$$

$\phi_\circ$ and λ were systematically varied to determine the minimum misfit between observed checkshot

data and calculated time-depth curves (Figure 4.5c and d). Figures 4.6 and 4.7 show the time-depth data with best-fitting curves and trade-off between compaction parameters, respectively, for all wells where check-shot or interval velocity data were available. Where data was not available, an initial porosity of 0.6 and compaction wavelength of 2 km were assumed (*Steckler and Watts*, 1978; *Kominz et al.*, 2016).

Assuming that the total amount of solid material remains constant during compaction, the decompacted thickness of each sedimentary layer is

$$\int_{z_1}^{z_2} [1 - \phi(z)] \mathrm{d}z = \int_{z_3=0}^{z_4} [1 - \phi(z)] \mathrm{d}z, \tag{4.5}$$

where $z_2 - z_1$ and $z_4 - z_3$ are sedimentary layer thicknesses before and after compaction, respectively. Substitution with Equation 4.1 and solving the integral gives

$$z_4 = z_2 - z_1 + \phi_\circ \lambda \left[\exp\left(-\frac{z_2}{\lambda}\right) + \exp\left(-\frac{z_1}{\lambda}\right) + 1 - \exp\left(-\frac{z_4}{\lambda}\right) \right]. \tag{4.6}$$

z_4 is solved iteratively for each layer using the Newton-Raphson method, assuming an initial solution of $z_4 = z_2 - z_1$.

The resultant decompacted subsidence curves are then standardised assuming Airy isostasy and a water load, such that

$$S_w = S_s \left(\frac{\rho_a - \rho_s}{\rho_a - \rho_w} \right), \tag{4.7}$$

where S_w and S_s are water and sediment loaded subsidence, respectively. If asthenospheric density, ρ_a = 3200 kg m^{-3}, average sediment density, ρ_s = 2400 kg m^{-3}, and water density, ρ_w = 1000 kg m^{-3}, Equation 4.7 simplifies to $3S_w \approx S_s$. This methodology produces estimates of tectonic subsidence without accounting for changes in global sea level (equivalent to R1 curves in *Bond et al.*, 1989). Additional errors may arise where basin subsidence exhibits a flexural response to sediment loading (e.g., *Watts*, 1982, 1988). The flexural response was not considered here because the calculated low T_e of the margin is low (Figure 4.2 *Audet*, 2014).

Figure 4.5e shows calculated $\phi_\circ$ and λ values for the COST B-2 well compared to porosity-depth data acquired from core and cuttings (*Steckler and Watts*, 1978; *Watts and Thorne*, 1984; *Van Sickel et al.*, 2004). The porosity-depth relationship calculated from check-shot data broadly matches these independent observations and suggests that a simple calibrated parameterisation of compaction is

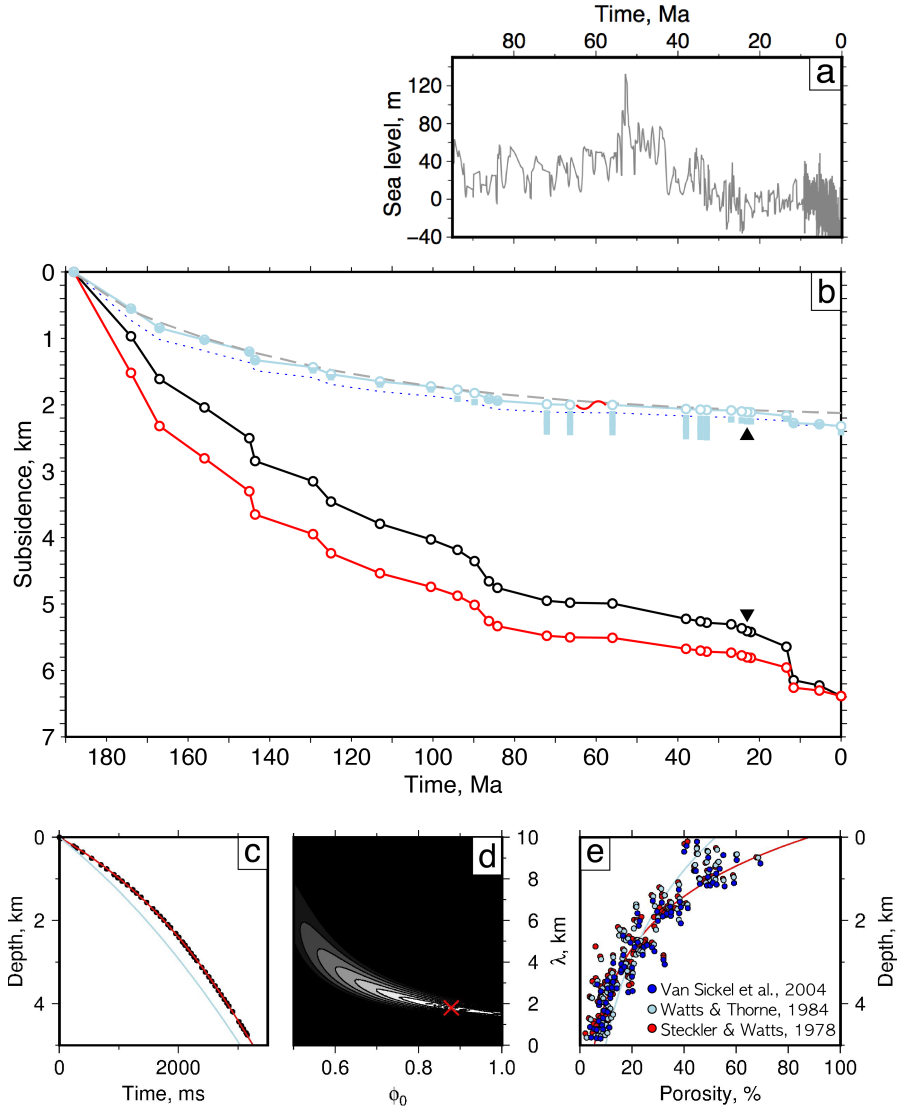

Figure 4.5: **History of New Jersey subsidence from the COST B-2 well** (a) Eustasy calculated from reduced subsidence history of COST B-2 well, New Jersey margin, from 98.4 to 9.25 Ma and oxygen isotopes from 9.25 to 0 Ma (*Miller*, 2005). (b) Subsidence at COST B-2 well from stratigraphy described in the well reports: black = backstripped burial curve; red = decompacted subsidence; dotted blue = decompacted, water-loaded subsidence. Light blue rectangles = decompacted, water-loaded subsidence, with added paleo-water depth uncertainties, obtained from well reports (see e.g., Figure 4.4). Light blue = water-loaded subsidence curve generated using *Watts and Thorne* (1984)'s compaction parameterisation (see panel e). Arrow = onset of anomalous Neogene subsidence. Dashed grey curve = best-fit thermal subsidence. (c) Black circles = time-depth measurements in the COST B-2 well from check shots; red curve = best-fitting theoretical time-depth relationship for compaction parameters indicated by red cross in panel d. Light blue curve = time-depth relationship for initial porosity, $\phi_\circ = 0.52$, and compaction wavelength, $\lambda = 3$ km (*Watts and Thorne*, 1984). (d) Colour scale = misfit between observed and calculated time-depth relationship for COST B-2 well (panel c). Parameter sweep was performed for range of $\phi_\circ$ and λ values. Red cross = best-fitting values used to generate red curve in panel c. (e) Red curve = best-fitting porosity-depth relationship calculated from check shot data. Coloured circles = measured porosities as a function of depth (*Steckler and Watts*, 1978; *Watts and Thorne*, 1984; *Van Sickel et al.*, 2004). Light blue curve = porosity as a function of depth calculated using *Watts and Thorne* (1984)'s parameterisation.

justified. Figure 4.8 shows calculated porosity-depth relationship compared to well porosity measurements for other wells, where data was available. I note that shallow wells tend to emphasise subsidence anomalies since no underlying stratigraphy is included in the decompaction procedure.

Finally, the water-loaded subsidence is corrected for the paleo-water depth of each stratigraphic unit, described in the well reports. Figure 4.4 shows a summary of paleo-water depths in the COST-B-2 well, which shows that Late Jurassic to Recent water depths have varied between upper bathyal to

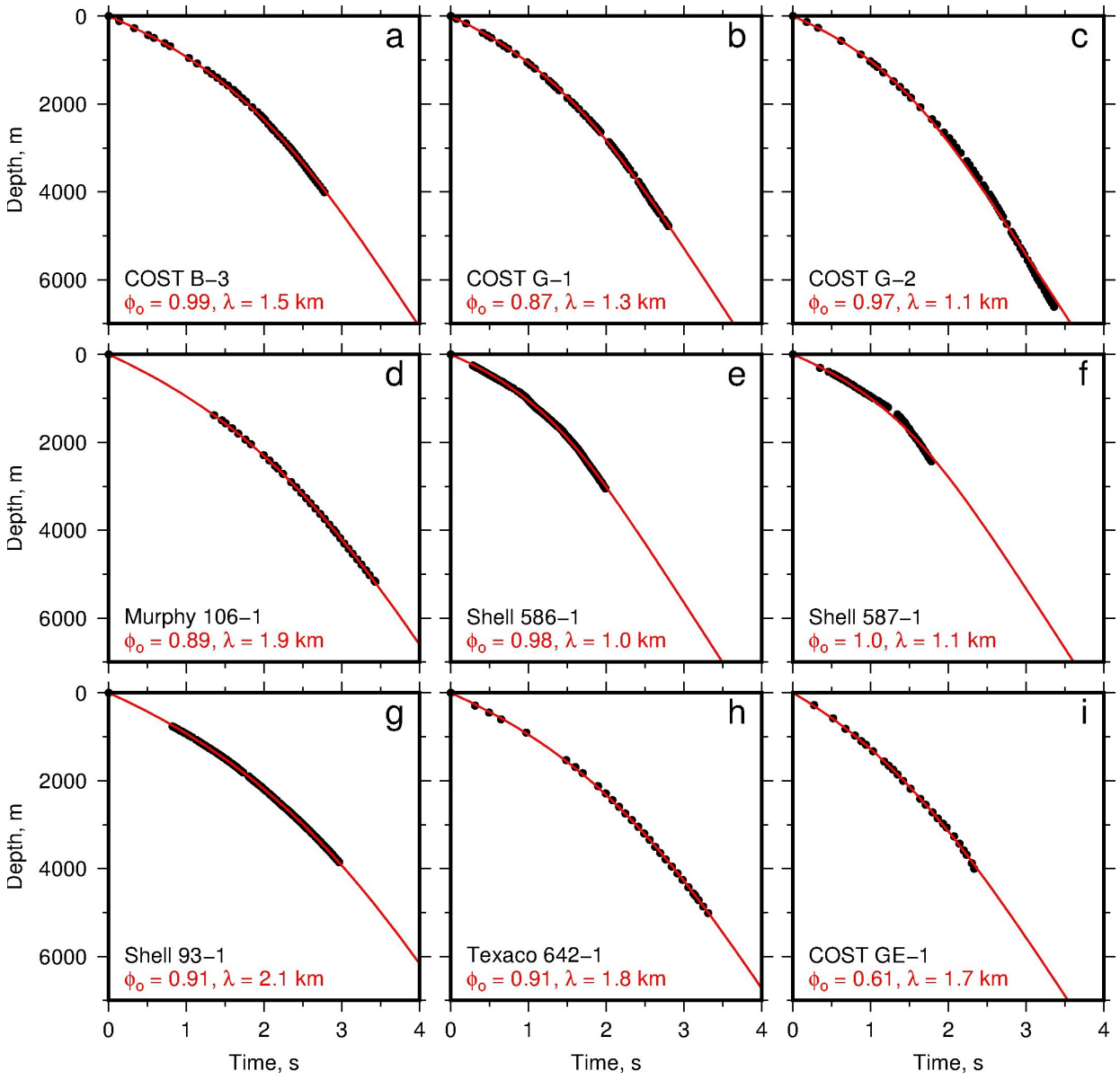

Figure 4.6: **Time-depth relationships for wells** along Eastern North America's passive margin. Black circles = time-depth data obtained from well reports, most often from integrating interval velocities. Red curves = best-fitting time-depth relationships obtained from parameter sweep of initial porosities, ϕ_o, and compaction wavelengths, λ (see Figure 4.7). Well names and best fitting compaction parameters are shown in bottom left of each panel.

neritic, which is consistent with other interpretations (e.g. *Kominz et al.*, 2016). Paleo-bathymetric estimates are laterally highly variable owing to the changing position of the shelf-edge throughout the basin's history (*Fulthorpe et al.*, 1999; *Pekar et al.*, 2000, 2003). Paleo-water depth ranges, and mean values, were individually extracted for each well.

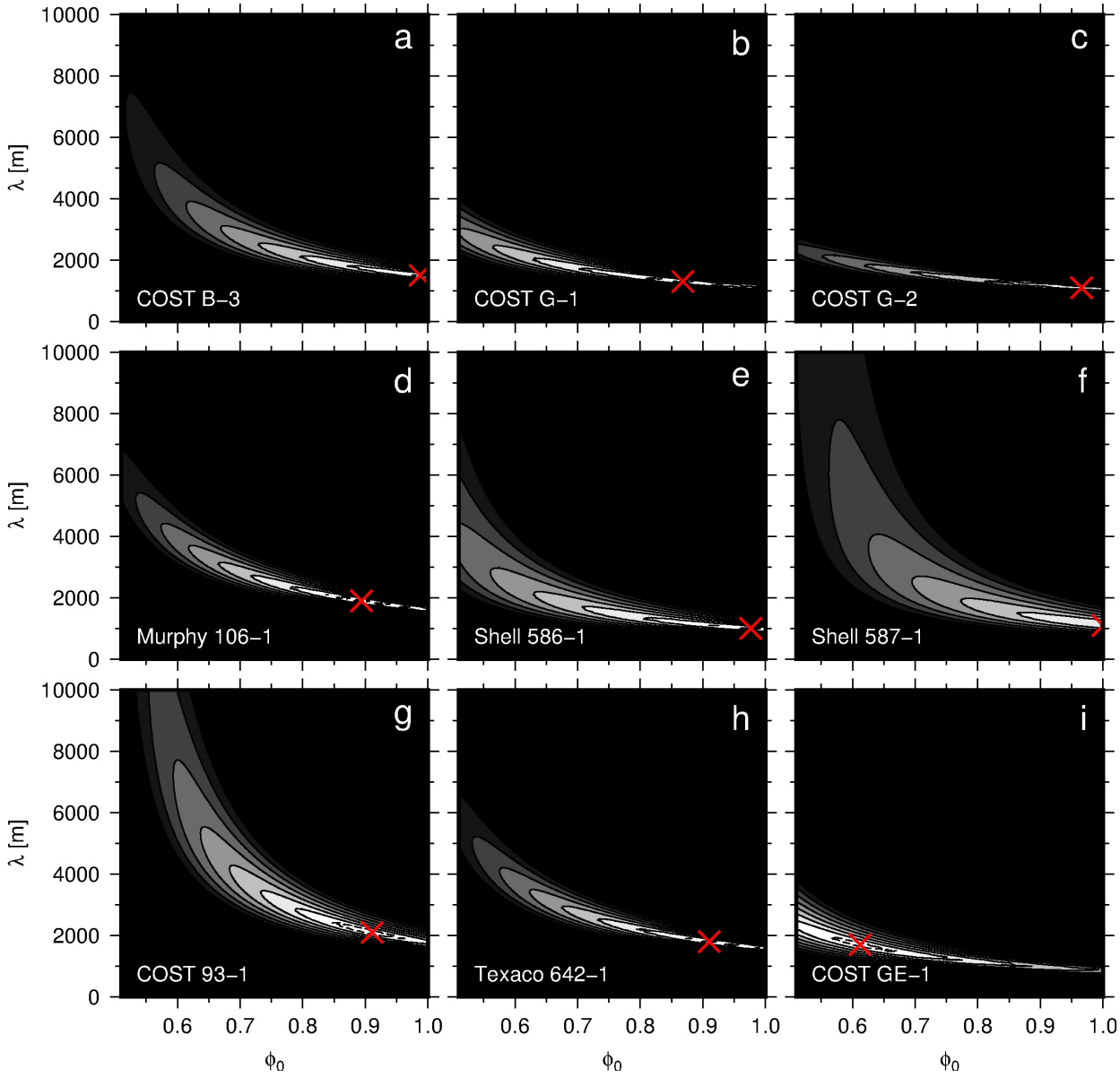

Figure 4.7: **Testing compaction parameterisation.** Colour scale = root mean squared misfit (white = low; dark = high) between observed and calculated time-depth pairs as a function of initial porosity, $\phi_\circ$, and compaction wavelength, λ (see Figure 4.6). Red crosses = global minima.

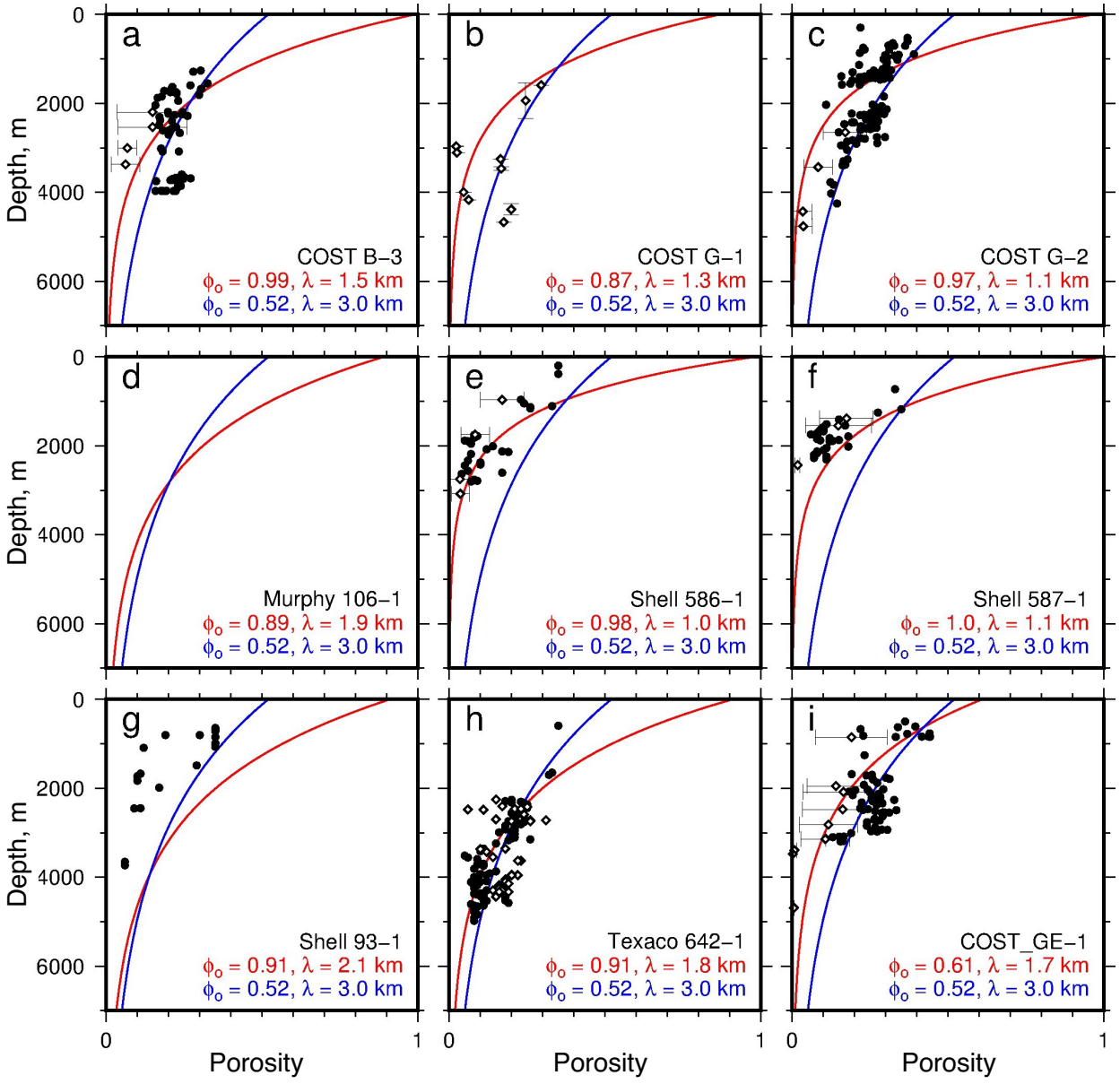

Figure 4.8: **Compaction parameterisation.** Solid circles = measured porosities described in well reports; diamonds with error bars = range of porosities recorded in well reports, typically estimated from sidewall cores. Note that porosity information was missing in the online well report for Murphy 106-1 (pg. 21). Red curves = best-fitting porosity-depth curves, $\phi = \phi_\circ \exp(-z/\lambda)$, calculated using initial porosity, $\phi_\circ$ and compaction wavelength, λ, that minimise misfit between observed and theoretical time-depth pairs (see Figures 4.6 and 4.7). Blue curves = compaction parameterisation from *Watts and Thorne* (1984), which was calculated by fitting porosity measurements from the COST B-2 well ($\phi_\circ = 0.52$, $\lambda = 3$ km).

4.3.5 Theoretical thermal subsidence

The predictability of passive margin subsidence and its relationship to strain and lithospheric cooling is well known (e.g., *McKenzie*, 1978; *White*, 1994). It forms the basis for extracting eustasy from backstripped stratigraphy (e.g. *Watts and Ryan*, 1976; *Miller*, 2005; *Kominz et al.*, 2016).

A challenging problem along this margin is that its deep structure, and therefore the timing of rifting, are poorly understood, partly because nearly all wells terminate in post-rift stratigraphy (see, e.g., *Grow et al.*, 1983; *Watts and Thorne*, 1984; *Sheridan et al.*, 1993). A guide to the time at which continental stretching (rifting) terminated is the age of oldest abutting oceanic crust. *Greene et al.* (2017) suggest that, if the source of the Blake Spur Magnetic Anomaly is oceanic crust, it may have formed at $\sim$ 168.5 Ma, which gives a basis for assuming rifting terminated before then. However, there is some debate about the age and origin of the oldest magnetic isochron offshore eastern North America (see *Greene et al.*, 2017). Seismic and geophysical data indicate that 0.5–3.7 km of sedimentary rock sits atop the rifted basement of the Baltimore Canyon Trough (e.g., *Benson and Doyle*, 1988). Diagnostic Late Triassic dinoflagellates from the deepest sampled stratigraphy in the COST G-2 well on Georges Bank correlate with the oldest sedimentary rock preserved in half-graben basins onshore (e.g. Newark Supergroup), which suggests that the earliest sediment to fill on- and offshore basins did so contemporaneously (*Cousminer*, 1983).

Onshore, the Newark supergroup comprises continental clastic and extrusive volcanic rocks preserved within asymmetric half-grabens that crop out along the coastal plain (e.g., Newark-Gettysburg, Culpeper, Richmond, Hartford and New York Bight basins; *Manspeizer*, 1988). Biostratigraphic analysis of fossil plants, pollen and spores from these sedimentary rocks indicate that these grabens are Upper Triassic aged ($\sim$ 227 Ma; *Cornet and Olsen*, 1985). Radiometrically-dated tholeiitic lavas that are interbedded within lacustrine growth strata provide additional constraints on the timing of rifting (e.g., Orange Mountain, Aspers, Watchung and Deerfield basalts). They have U-Pb and $^{40}Ar/^{39}Ar$ ages of 201 ± 1 Ma, and K-feldspar cements formed from hydrothermal fluids generated during magamtism have $^{40}Ar/^{39}Ar$ ages of 196 ± 1 Ma (*Weems and Olsen*, 1997). A complicating factor is that some of these igneous rocks show evidence of later hydrothermal alteration, which can make the calculated ages of these rocks appear younger than their true ages (*Seidemann et al.*, 1984; *Sutter*, 1988). Offshore, syn-rift sedimentary rock is separated from thick post-rift stratigraphy by a regional angular unconformity, which is observed on two-dimensional seismic profiles as a strong reflector with onlapping younger sedimentary packages (see e.g., *Grow et al.*, 1983). Palynomorphs

from the COST G-2 well indicate that this regional unconformity was generated during Lower Jurassic times (*Cousminer and Steinkraus*, 1988). These observations give a basis for assuming that rifting occurred between $\sim$ 230–170 Ma (Upper Triassic to Lower Jurassic).

Stratigraphy from the COST B-2 well has been combined with inferences about the deep structure of the margin to invert syn-rift to Recent subsidence patterns for strain rate histories, $\dot{\epsilon}(t)$, which indicate lithospheric stretching factor $\beta = \exp(\int_{\circ}^{t} \dot{\epsilon}(t)\mathrm{d}t) \sim 1.7$–$2.2$ (see, e.g., *Watts and Thorne*, 1984; *Jarvis and McKenzie*, 1980; *Grow et al.*, 1988; *White*, 1994; *Kominz et al.*, 1998; *Flament et al.*, 2013).

An alternative pragmatic approach to dealing with a poorly constrained syn-rift history is to constrain stretching factors and rifting histories by comparing root-mean-squared misfit between observed and theoretical thermal subsidence histories generated by systematically varying stretching factors and the timing of rifting. I make use of simple analytical solutions that assume instantaneous stretching and relate β, asthenospheric temperature (T), thermal expansivity (α), lithospheric density (ρ_m), and infill (e.g., water; ρ_w), time since rifting (t), and the thermal time constant of the lithosphere ($\tau = l^2/(\pi^2\kappa)$) to calculate thermal subsidence (S_t) histories

$$S_t = E_{\circ} r \left[1 - \exp\left(-\frac{t}{\tau}\right)\right], \quad \text{where} \tag{4.8}$$

$$E_{\circ} = \frac{4l\rho_m\alpha T}{\pi^2(\rho_m - \rho_w)} \quad \text{and} \quad r = \frac{\beta}{\pi}\sin\left(\frac{\pi}{\beta}\right). \tag{4.9}$$

Root mean squared was calculated such that

$$H = \sqrt{\frac{1}{N}\sum_{i=1}^{N}\left(\frac{s_i^{\circ} - s_i^{c}}{\sigma_i}\right)^2}, \tag{4.10}$$

where N is the number of subsidence measurements, s_i° and s_i^{c} are observed and theoretical subsidence and σ_i is paleo-water depth uncertainty. I set lithospheric thickness, $l = 125$ km, thermal diffusivity, $\kappa = 10^{-6}$ m^2 s^{-1}, $\rho_m = 3300$ kg m^{-3}, $\alpha = 3.28\times10^{-5}$ /°K, and $T = 1330$°C. Stretch factor, $1 \leq \beta \leq 5$, and timing of rifting, $t_{\circ}$, are systematically varied between 250–170 Ma to calculate the best-fitting values for the COST B-2 well. Best-fitting thermal subsidence histories are shown in Figure 4.9. Stretching factors and the timing of rifting tradeoff such that $2 \leq \beta \leq 5$ and $170 \leq t_{\circ} \leq 200$ Ma yield low misfits. These values overlap results from inverting subsidence patterns, probably because the duration of rifting was short (i.e. $\sim$ 15–25 Ma; *Jarvis and McKenzie*, 1980; *Flament et al.*, 2013).

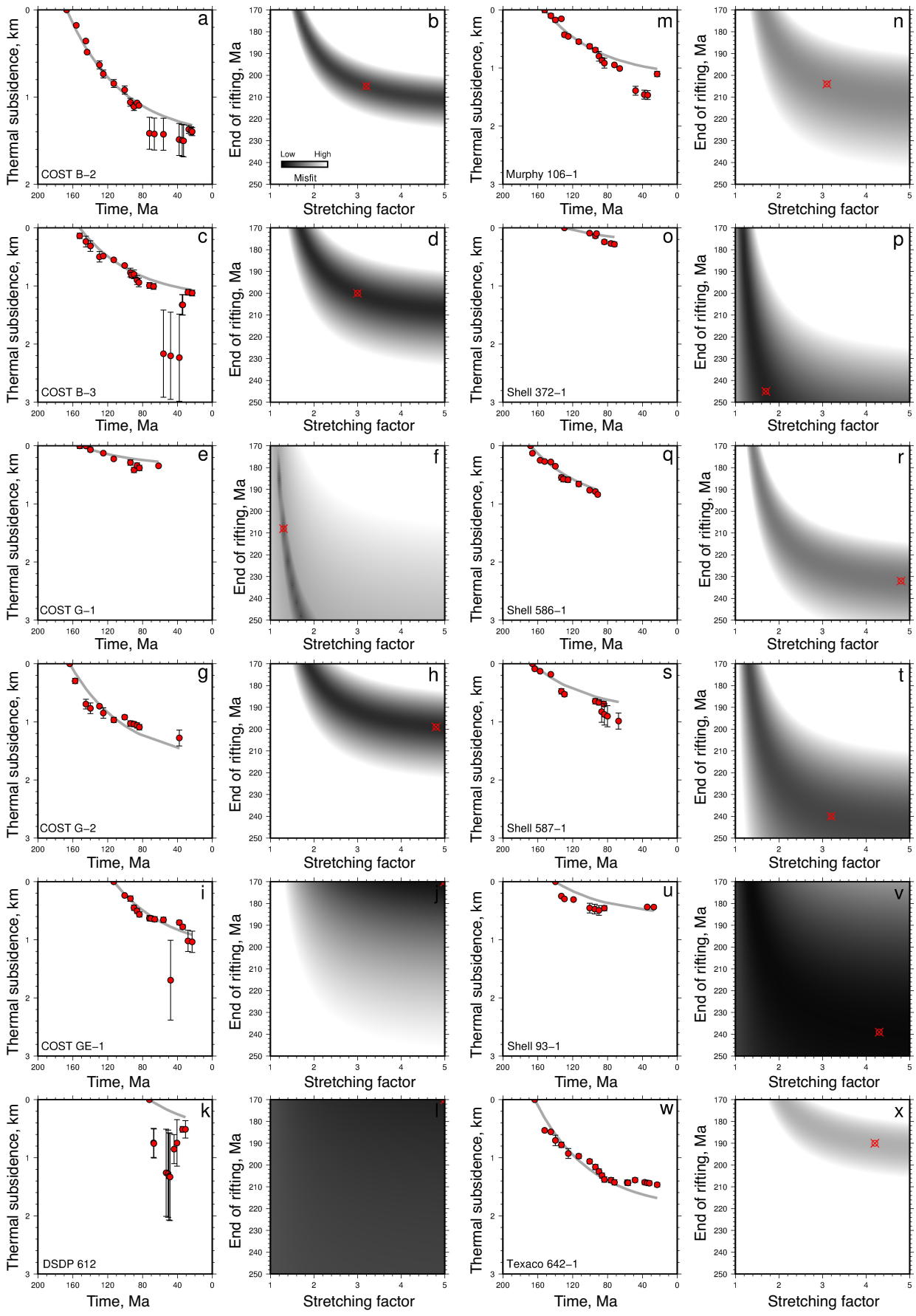
a
b
m
n
c
d
o
p
e
f
q
r
g
h
s
t
i
j
u
v
k
l
w
x
Thermal subsidence, km
Time, Ma
End of rifting, Ma
Stretching factor
COST B–2
COST B–3
COST G–1
COST G–2
COST GE–1
DSDP 612
Murphy 106–1
Shell 372–1
Shell 586–1
Shell 587–1
Shell 93–1
Texaco 642–1
Low
High
Misfit

Figure 4.9: **Best-fitting instantaneous rifting subsidence histories.** (a) Pre-Neogene, post-rift subsidence history of COST B-2 well (see Figure 4.5). Red circles = decompacted, water-loaded and paleowater depth (PWD) corrected subsidence; error bars = PWD uncertainties. Gray curve = theoretical thermal subsidence with lowest misfit to observations (red cross in panel b). (b) Misfit between observed and theoretical thermal subsidence assuming instantaneous stretching. (c–x) Subsidence histories and misfit as a function of β and time of rifting for other wells along the eastern margin of North America.

Substituting $1.7 \leq \beta \leq 2.2$ and $170 \leq t_\circ \leq 200$ Ma into Equations 4.8 and 4.9 yields total water-loaded thermal subsidence since rifting of 1876 ± 281 m, which brackets post-rift subsidence recorded by backstripping of the COST B-2 well (grey dashed curve in Figure 4.5). Calculated Neogene to Recent (23–0 Ma) thermal subsidence is 31 ± 13 m. The proximity of the margin to the Appalachian mountains and thick lithosphere imaged in some shear wave tomographic models indicates that the lithosphere beneath this margin might have been thicker before stretching. If, for example, $l = 150$ km calculated Neogene water loaded subsidence is 71 ± 24 m. These values of calculated Neogene thermal subsidence are nearly an order of magnitude lower than observed values ($\sim$ 500–600 m; e.g. Figures 4.5).

4.3.6 Subsidence history

The analyses in this study differ from *Miller* (2005) in that residual subsidence is not assumed to be necessarily generated by eustasy. Water-loaded subsidence curve for the COST B-2 well is shown in Figure 4.5, and for all other wells in Figures 4.10 and 4.11. Cumulative water-loaded subsidence from 188 Ma to the present day is 2.4 km. Most of this subsidence can be attributed to post-rift thermal sag (e.g. Equations 4.8 & 4.9). The most significant departure from predicted post-rift subsidence is between 20–11 Ma when an additional $\sim$ 200–500 m of water-loaded subsidence is observed. *Flament et al.* (2013) also observed an increase in Neogene subsidence rates, which they show could be attributed to increased lithospheric strain (i.e. stretching) at $\sim$ 16 Ma or mantle convective drawdown (e.g. their Figures 6 & 7). Anomalous water-loaded Neogene subsidence, with rates of up to $\sim$ 50 m Ma^{-1} between $\sim$ 20–0 Ma, is observed for most wells in the the Baltimore Canyon Trough and for the Bethany Beach and Ancora wells onshore. The sparsely populated subsidence curves shown in Figures 4.10i-k are a result of scant post-Cretaceous stratigraphic information. These wells have high residual post-Cretaceous subsidence, which is broadly comparable to that recorded in the more completely sampled wells. However, the sparsity of reported Cenozoic stratigraphy means that Neogene subsidence rates are not well constrained and they are excluded from subsequent analyses. The age of stratigraphy

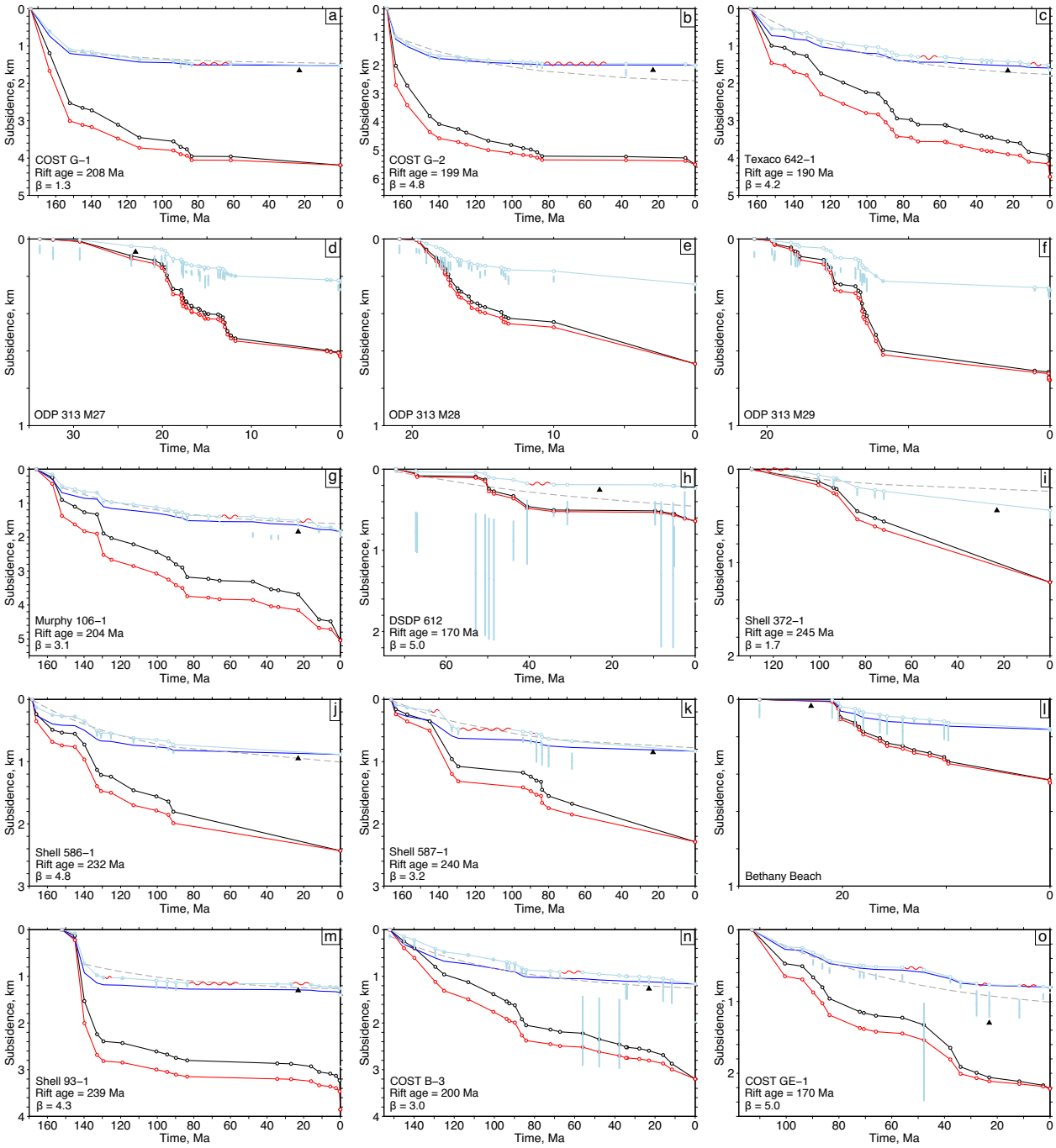

Figure 4.10: **History of passive margin subsidence** (a–o) Subsidence curves for wells on the Eastern North American passive margin (see yellow diamonds in Figure 4.3 for location). Wavy red curves represent unconformities. Annotation is same as for Figure 4.5b. Black/red/light blue curves = burial/decompacted/water-loaded subsidence curves. Light blue rectangles = water-loaded (tectonic) subsidence curves with added paleo-water depth uncertainties. Black triangles = onset of Neogene Period. Dashed lines = best-fitting thermal subsidence history calculated assuming instantaneous rifting. Best-fitting thermal subsidence curves are shown for wells with accurately matched pre-Neogene stratigraphy. Note that expected Neogene thermal subsidence is $O(10)$ m.

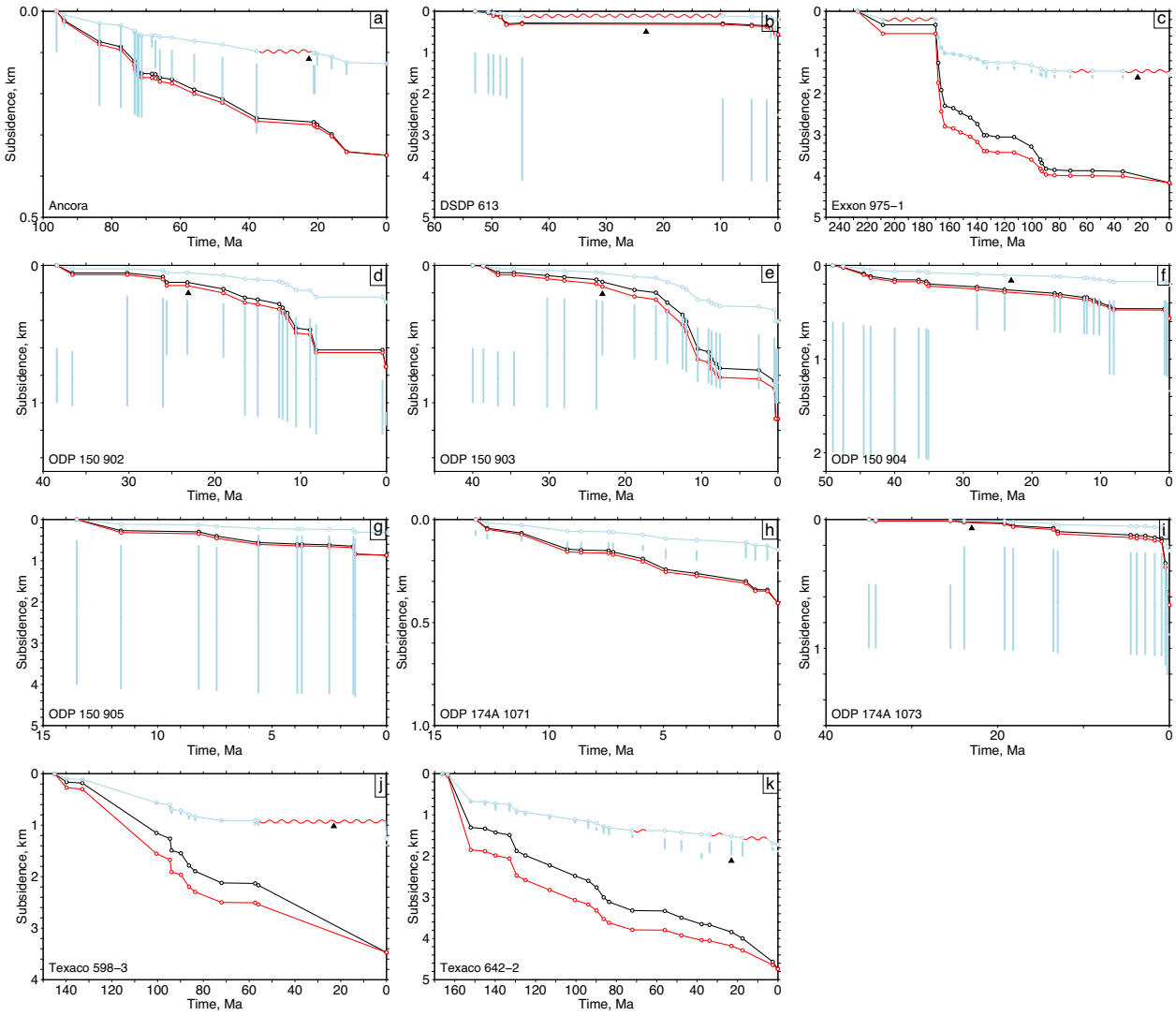

Figure 4.11: **History of passive margin subsidence (continued)**. (a–k) Subsidence curves for wells on the Eastern North American passive margin not shown in *Morris et al.* (2020) (see white diamonds in Figure 4.3 for location).

sampled during IODP Expedition 313 ages is determined by Sr isotopic chemistry and has a resolution of ±0.25–0.5 Ma (*Kominz et al.*, 2016). Backstripping of these wells shows that subsidence rates increased between 20 and 13 Ma (Figures 4.10e-g; *Kominz et al.*, 2016). In contrast, wells located on Georges Bank and the Southeast Georgia Embayment have $\lesssim$ 1 km of post-Santonian stratigraphy and almost no residual Neogene water-loaded subsidence (Figure 4.10a, b, o; Figure 4.11c).

It is important to acknowledge that some wells, especially those located in the deeper portions of the basin, have large paleo-water depth uncertainties. For example, wells ODP 150 905 and DSDP contain sedimentary deposits identified as 'bathyal', indicating a paleobathymetric range of 150–4000 m. This large uncertainty imposes a limitation on determining changes in subsidence rates from these wells.

Figure 4.12 shows the spatial patterns of total and Neogene water-loaded subsidence for all wells considered in this study. As predicted for a rifted continental margin, onshore and shallow wells record less total subsidence than deeper wells. Wells located off the continental shelf break showing under 1 km of total water-loaded subsidence (Figure 4.12a) are those which have not been drilled to syn-rift stratigraphy. Figure 4.12b highlights the anomalous Neogene subsidence of the BCT when compared with the adjacent continental margins.

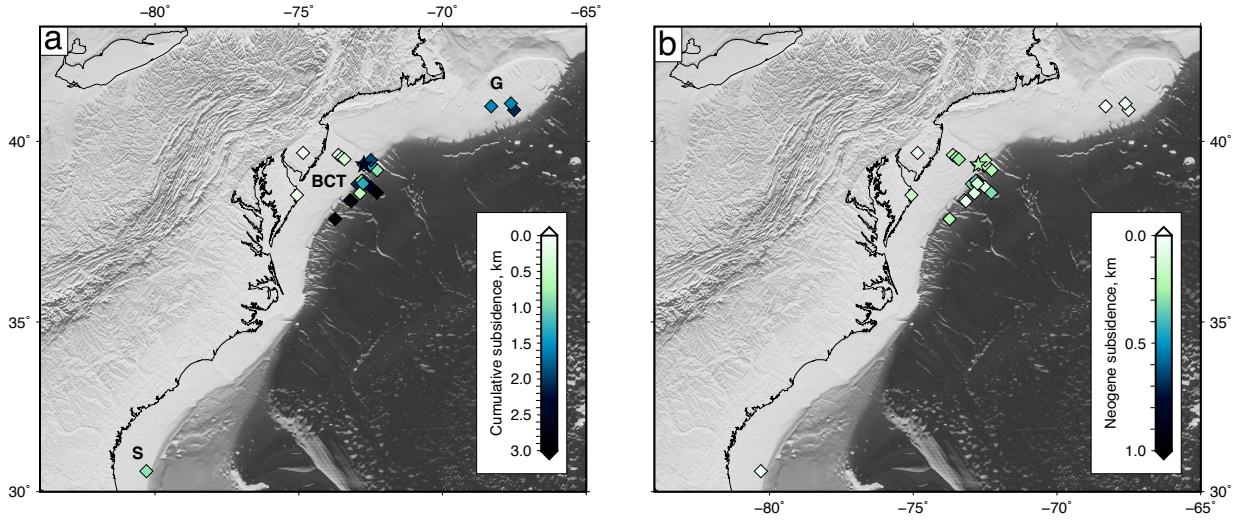

Figure 4.12: **Spatial patterns of tectonic subsidence**. (a) Coloured diamonds = total water-loaded subsidence calculated by backstripping wells along Eastern North America's passive margin (Figures 4.3, 4.10 & 4.11). COST B-2 well is identified as a star. BCT = Baltimore Canyon Trough; G = Georges Bank. (b) Neogene water-loaded subsidence. Highest Neogene subsidence is centred on the BCT.

4.3.7 Seismic reflection data

The stratigraphic architecture of the BCT might provide additional information about the history of the basin. Extensive seismic mapping of basin stratigraphy has been performed for the BCT, owing to the wealth of available data (e.g., *Fulthorpe et al.*, 1996; *Miller et al.*, 1998; *Fulthorpe and Austin Jr.*, 2008; *Miller et al.*, 2018; *Cosgrove et al.*, 2019). Based on these previous published interpretations, stratigraphy was mapped along the margin using four two-dimensional seismic reflection lines to highlight the large-scale stratigraphic architecture (Figures 4.4 & 4.14). Location of all seismic lines interpreted in this study are shown in Figure 4.13. These lines were chosen because of their proximity to backstripped wells, image fidelity and so that stratigraphy could be interpreted on dip and strike lines. Seismic segy data files were quality checked and visualised using segy.io software. The data display was scaled and standardised using the 99th percentile of the amplitudes for each profile.

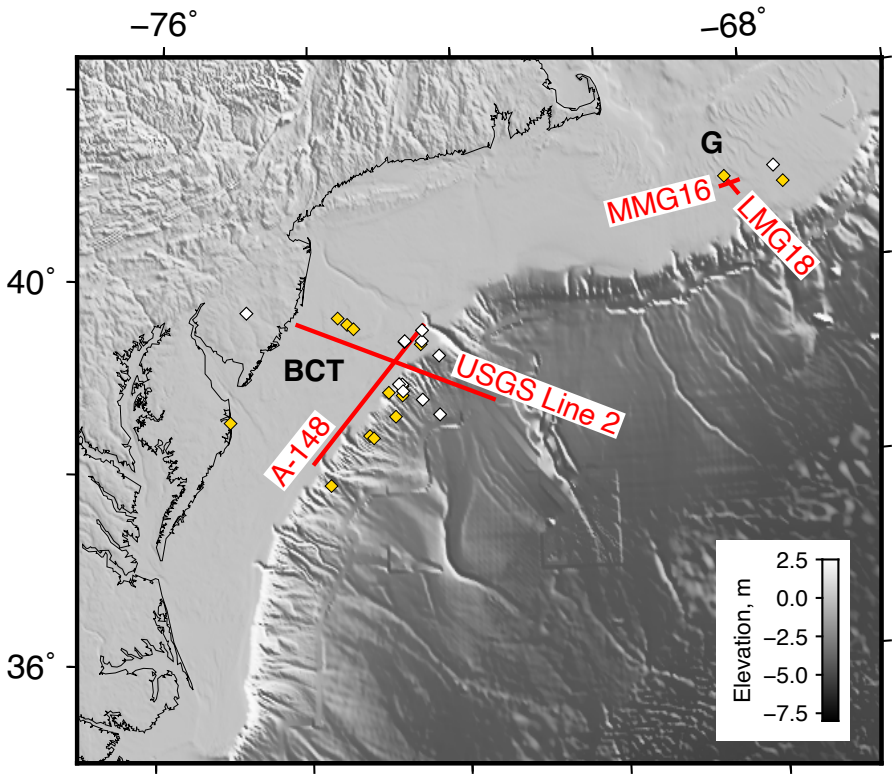

Figure 4.13: **Location of seismic profiles** (red lines) in the Baltimore Canyon Trough (BCT) and Georges Bank (G). Well locations shown for reference.

Data follows the American seismic wave polarity convention, where positive polarity or impedance contrast is represented by a positive amplitude. Seismic stratigraphy was tied to wells with accurate, biostratigraphically determined, ages. Age constraints from each well were converted from depth into two-way travel times using checkshot data and interval velocities provided in the well reports (Figure 4.5 and 4.6).

Seismic data and biostratigraphic correlations indicate that Neogene to Recent stratigraphy is up to ~ 1 s thick (two-way time; ~ 1 km, using velocities in Figure 4.5c) in the Baltimore Canyon Trough. Figure 4.14 shows a well-studied inline from the BCT, where both the syn- and post-rift sequences can be clearly identified. Strike line A-148, which intersects the trough, shows that Miocene to Recent stratigraphy is almost uniformly planar and > 1 s thick offshore New Jersey (Figure 4.15). In contrast seismic lines MMG16 and LMG81 on Georges Bank show that post-Santonian ($\lesssim 84$ Ma) stratigraphy is < 1 s thick (Figure 4.16 and 4.17). Well COST GE-1 on the bank indicates that its Miocene to Recent stratigraphy is < 100 m thick. Post-Jurassic stratigraphy of Georges Bank has a shallow gradient in strike and dip directions (Figure 4.16 and 4.17). In contrast, dip lines from the Baltimore Canyon

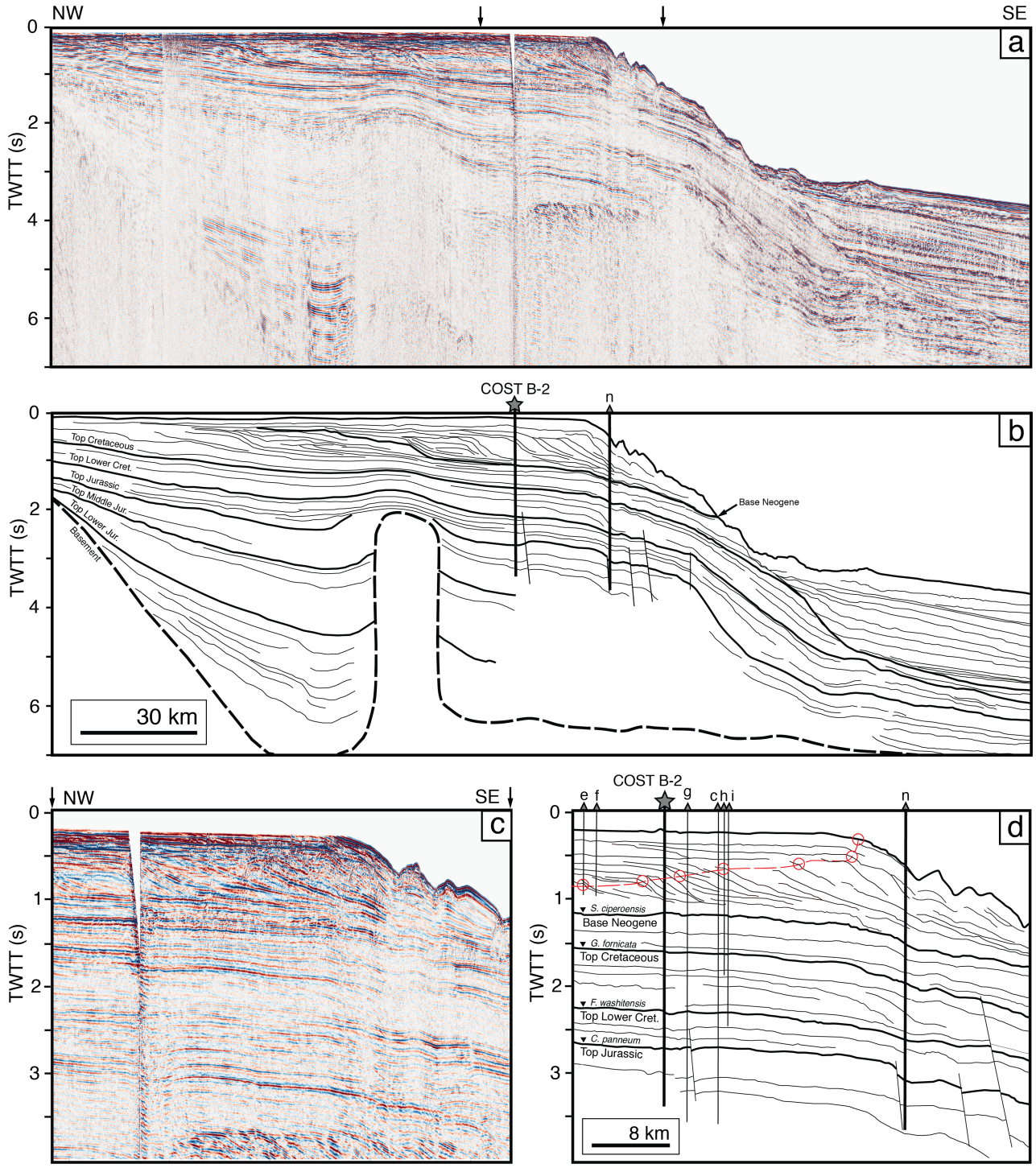

Figure 4.14: **Seismic stratigraphy of the New Jersey margin.** (a) Seismic line USGS Line 2 (Figure 4.3). Arrows = extent of zoomed-in image shown in panels (c) and (d). Negative reflectors are shown in red, positive in blue. (b) Interpreted stratigraphy. Annotated triangle, star and vertical lines = wells projected onto line (see Figure 4.3). Thick black curves = key stratigraphic horizons. Thin black curves are indicative of stratigraphic architecture. (c & d) Central portion of USGS Line 2 and interpreted stratigraphy. Annotated inverted triangles = last appearances of key biostratigraphic markers extracted from well reports (see e.g. Figure 4.4). Red circles and dashed curve = trajectory of clinoforms. Note ~ 1 s of Neogene stratigraphy, which contains prograding and aggrading clinoforms. Labelled triangles, star and vertical lines = wells projected onto transect (see Figure 4.3).

Trough show > 100 km of Miocene-Recent progradation and ∼ 0.25 s (∼ 250 m) of aggradation (Figure 4.14). These clinoforms prograde from close to the shoreline and are best developed in the northern part of the Baltimore Canyon Trough. Rapid increases in accommodation space offshore was coeval with increased sedimentary flux from onshore (*Poag and Sevon*, 1989).

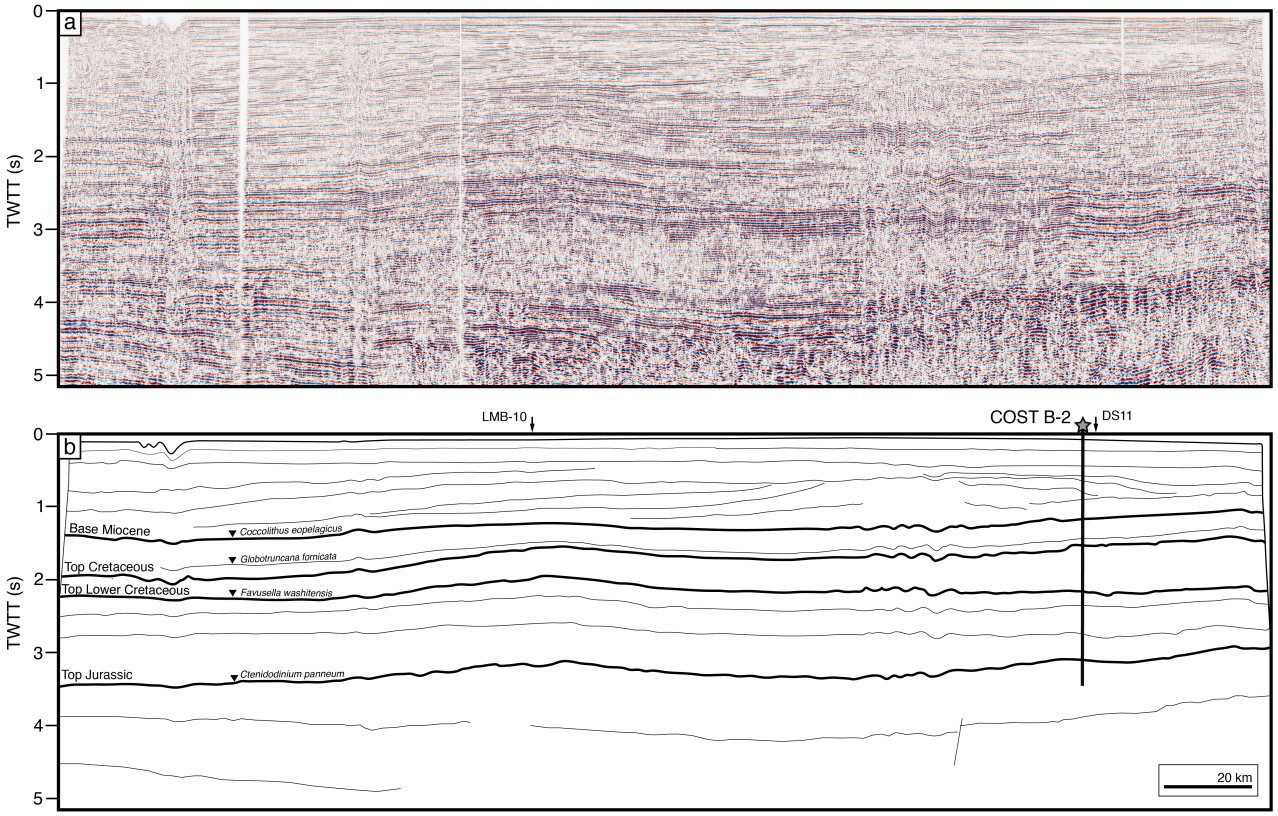

Figure 4.15: **Seismic strike line A-148, located offshore New Jersey.** See Figure 4.3 for location. (a) Uninterpreted seismic line. (b) Interpreted seismic line. Well COST G-1 was projected on to the line from 10 km to the north west. Major stratigraphic horizons are shown by the thick black curves. Annotations show last occurrence, ▼, occurrences of biota that constrain stratigraphic ages. Thin black lines show stratigraphic architecture.

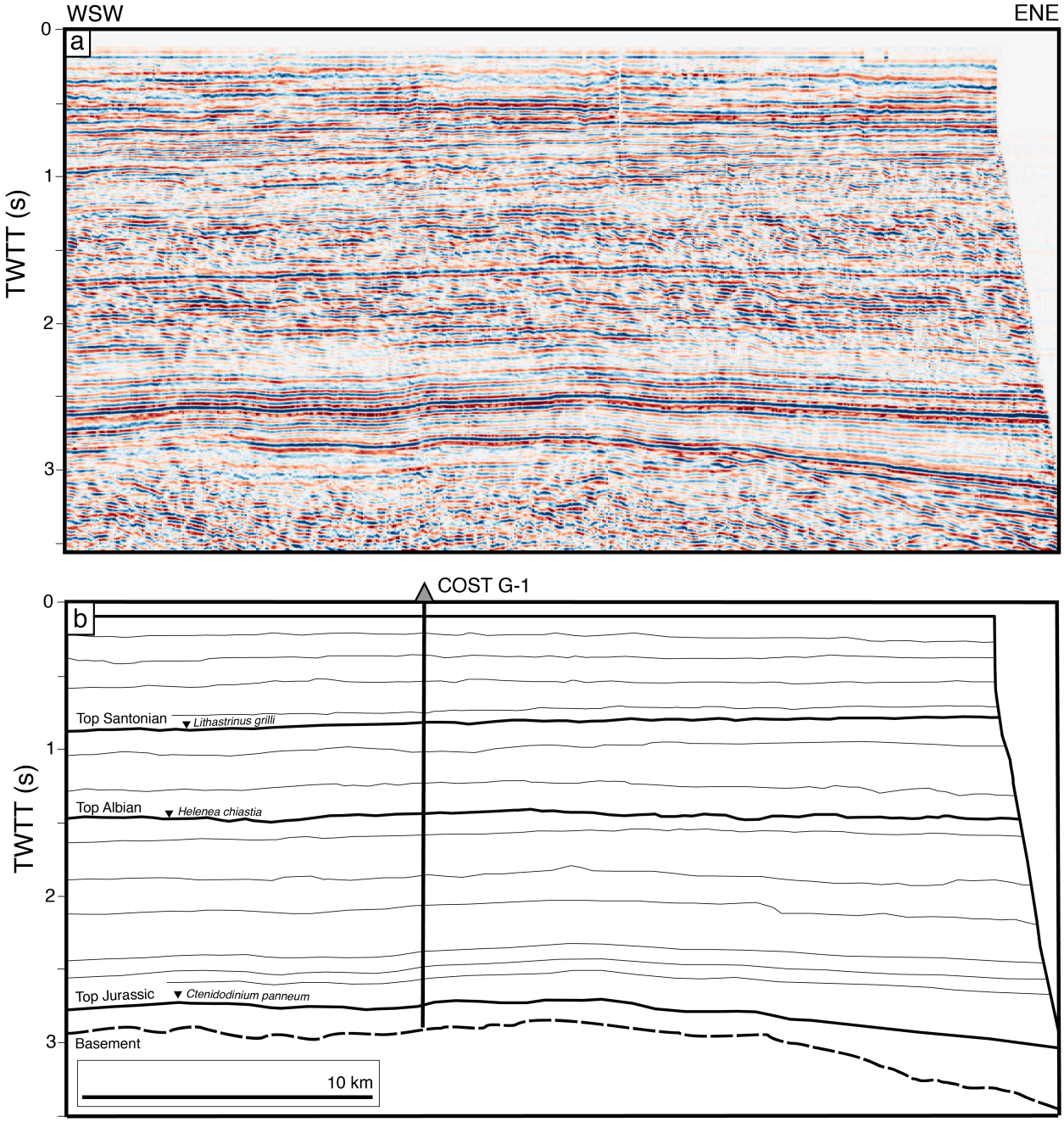

Figure 4.16: **Seismic line MMG16, located on Georges Bank.** (a) Uninterpreted seismic line. See Figure 4.3 for location of this line. (b) Interpreted seismic line. Note relatively thin post-Santonian (post-Mid Cretaceous) sedimentary packages compared to seismic data further south (e.g. line A-148; Figure 7).

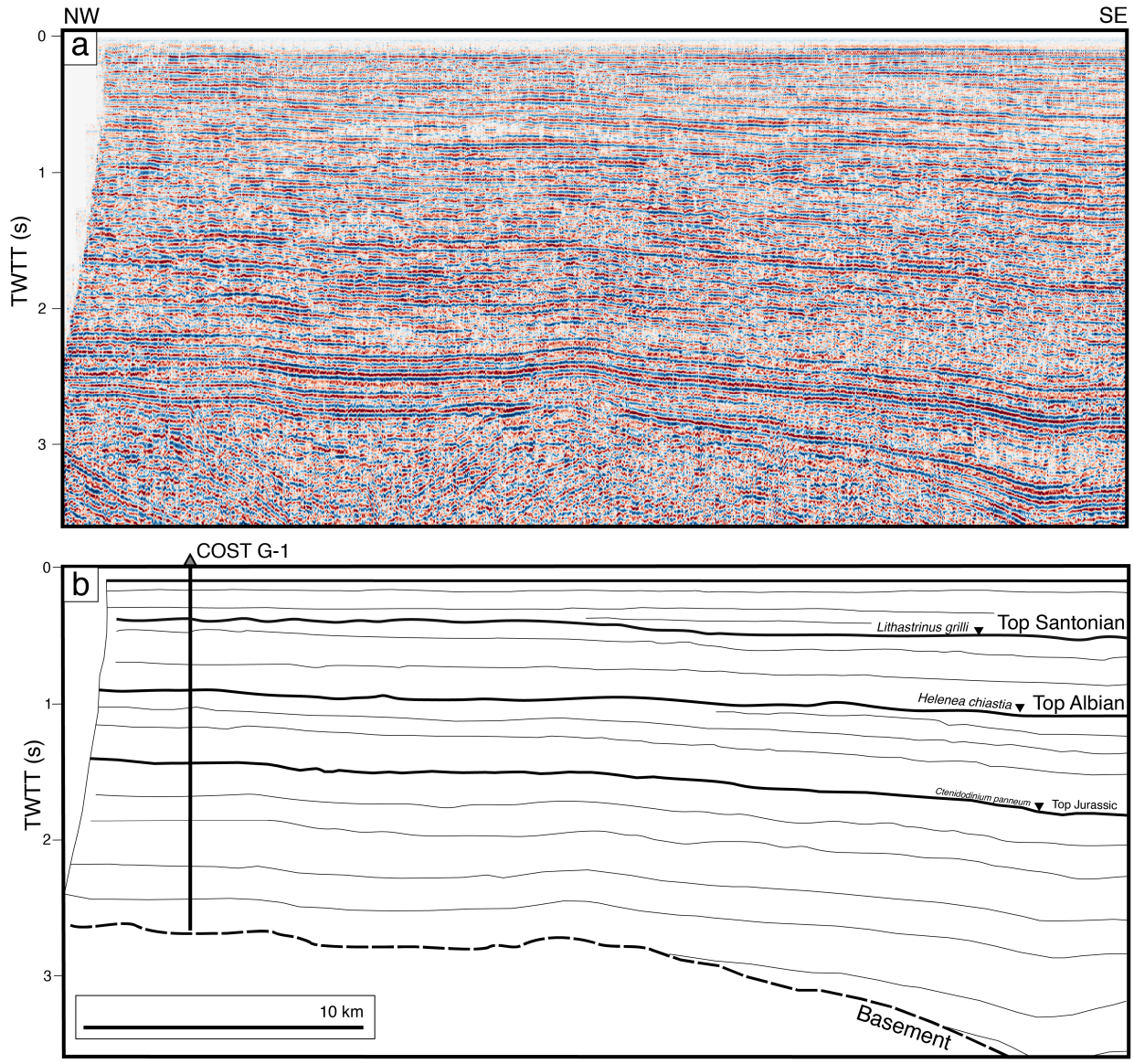

Figure 4.17: **Seismic line LMG18, located on Georges Bank.**(a) Uninterpreted seismic line. See Figure 4.3 for location of this line. (b) Interpreted seismic line.

4.3.8 Causes of subsidence in the Baltimore Canyon Trough

Up to ∼ 600 m of Neogene to Recent (∼ 20–0 Ma) water-loaded subsidence is recorded by backstripped wells centred on the Baltimore Canyon Trough. Seismic strike line A-148, which intersects the trough, shows that accumulation of Neogene sedimentary rock is up to ∼ 1 s (∼ 1 km) along at least ∼ 200 km of the margin offshore New Jersey. Miocene clinoforms, mapped on seismic dip lines, prograded > 100 km away from the coastline and then aggraded, which indicates an increase in Neogene accommodation space (e.g., seismic line USGS 2; *Greenlee et al.*, 1988; *Posamentier et al.*, 1988; *Poag and Sevon*, 1989; *Greenlee et al.*, 1992). In contrast, seismic mapping and backstripped

stratigraphy on the Georges Bank and the Southeast Georgia Embayment shows that Neogene subsidence and sedimentation rates were much lower. These observations imply that the relatively rapid Neogene to Recent subsidence observed in the Baltimore Canyon Trough is a local, rather than global (e.g. eustatic), phenomenon. The amplitude of water-loaded Neogene subsidence in the Baltimore Canyon Trough ($\sim$ 300 m, up to $\sim$ 600 m) also precludes glacio-eustasy as the mechanism for increased accommodation space along this margin. In the following section, I examine whether observed subsidence patterns could have been generated by flexure, lithospheric strain or sub-plate support.

A role for plate flexure or extension?

Variations in post-rift subsidence of the Baltimore Canyon Trough has been previously attributed to a flexural response to sediment loading (*Pazzaglia and Gardner*, 1994; *Kominz et al.*, 1998; *Vanderaveroet*, 2000; *Kominz et al.*, 2008; *Miller et al.*, 2013). I use a simple flexural model to examine whether loading could have generated the observed water-loaded subsidence patterns in the trough and its surroundings. The flexural model assumes that the lithosphere deflects as a semi-infinite plate in response to an end load. Maximum deflection, $w_\circ = V_\circ \alpha^3 / 4D$, where the flexural parameter, α, and flexural rigidity, D, are given by

$$\alpha = \left[\frac{4D}{g(\rho_m - \rho_w)} \right]^{\frac{1}{4}}, \qquad D = \frac{ET_e^3}{12(1-\sigma^2)}, \tag{4.11}$$

(e.g., *Turcotte and Schubert*, 2002). Gravitational acceleration, $g = 9.8$ m s^{-2}, mantle density, $\rho_m = 3300$ kg m^{-3}, water density, $\rho_w = 1000$ kg m^{-3}, Young's Modulus, E = 70 GPa, and Poisson's ratio $\sigma = 0.25$. The most obvious nearby large load is the Appalachian mountains. I estimate the width of foreland basins for a range of elastic thicknesses by calculating the position of forebulges, x_b, relative to the eastern edge of the Appalachian mountains using $x_b = 3\pi\alpha/4$ (*Turcotte and Schubert*, 2002). Figure 4.18 shows the distance to the forebulge from the eastern edge of the mountains for elastic thicknesses of 20–40 km (cf. *Watts and Ryan*, 1976; *Pazzaglia and Gardner*, 1994; *McKenzie*, 2010; *Audet*, 2014). These tests indicate that loading by the Appalachian mountains did not generate the observed Neogene subsidence. To produce a forebulge to the east of the Baltimore Canyon Trough requires an elastic thickness of $\gtrsim$ 100 km, which is much higher than that estimated from the admittance between gravity and topography along the margin ($\sim$ 15–40 km; *Watts and Ryan*, 1976; *McKenzie*, 2010; *Audet and Bürgmann*, 2011; *Audet*, 2014).

Another possible source of loading is sedimentary rock deposited on the margin. To generate the

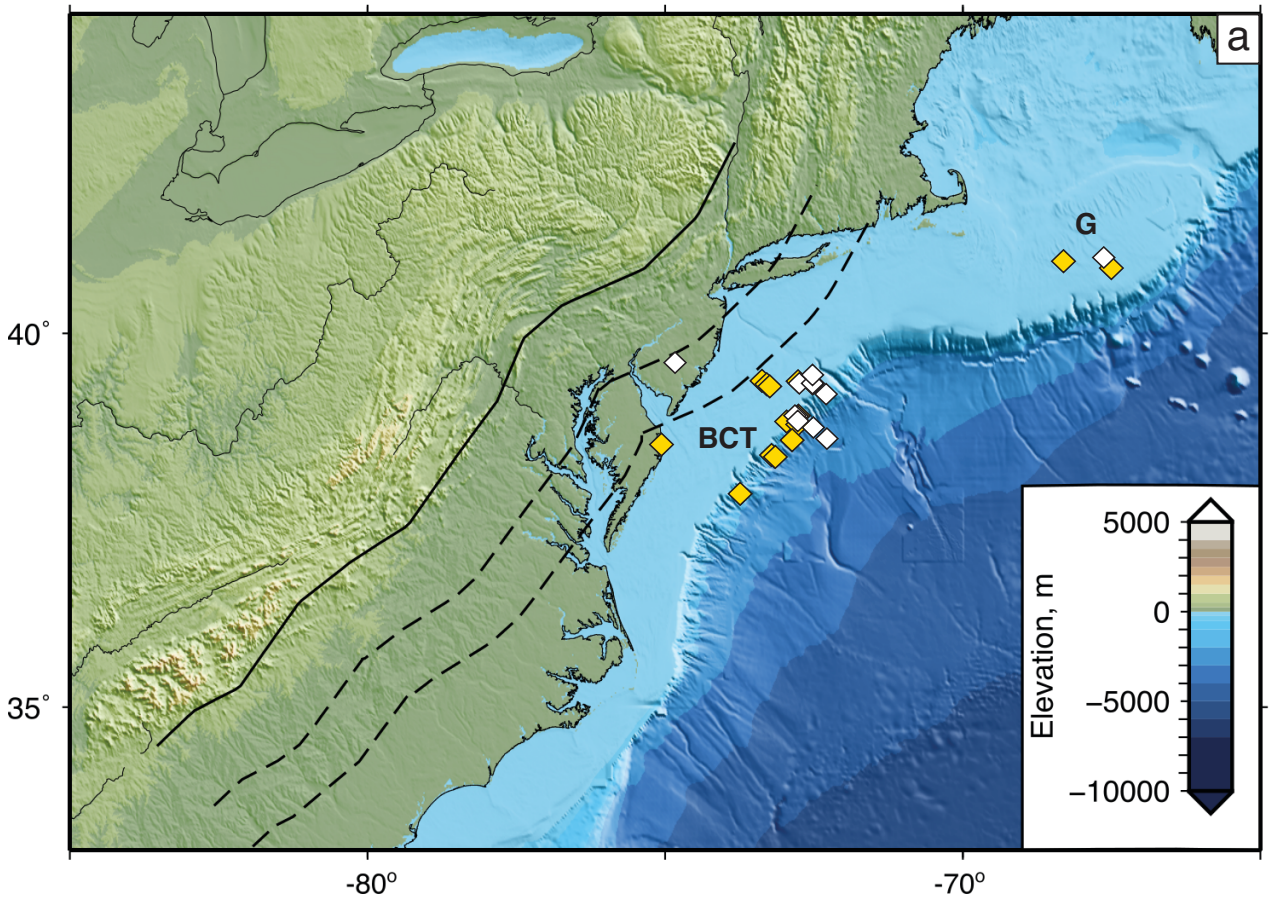

Figure 4.18: **Flexural analysis for an Appalachian load**. (a) Solid curve = eastern margin of the Appalachian mountains. Dashed curves show calculated distances to forebulge crests, which equal 128 and 216 km for elastic thicknesses T_e = 20 and 40 km, respectively. Note that all wells in this study (yellow/white diamonds) sit outboard of the calculated forebulge positions, except for the onshore Ancora well. BCT = Baltimore Canyon Trough, G = Georges Bank.

observed Neogene water-loaded subsidence ($\sim$ 550 m) by flexing a plate with an elastic thickness of 15 km requires a load, $V_\circ \sim 5.4 \times 10^{11}$ Pa per unit width (cf. *Watts and Ryan*, 1976; *Pazzaglia and Gardner*, 1994; *Audet*, 2014). If the load was generated by sedimentary rock and assumed to be ρglz, where l and z are the length and depth of the load, respectively, the volume of sedimentary rock required to generate the observed water loaded subsidence can be calculated. If the density of sedimentary rock is 1500 kg m^{-3} (equivalent to sedimentary rock with 64% porosity, 2400 kg m^{-3} solid grain density, 1000 kg m^{-3} pore fluid density; *Pazzaglia and Gardner*, 1994), the calculated volume of sedimentary rock required is 3.7×10^7 m^3. If I assume unit width and a 1 km thick Neogene sedimentary pile, the length of the required load is 37 km. If an infinite plate is used to model the deflection then the load required is approximately twice as large. Assuming a sedimentary infill density of 2400 kg m^{-3}, the required length is 23 km. If the elastic thickness is taken to be 30 km, the load length increases to 78 km. A difficulty with proposing such a model for generating the observed

water-loaded subsidence of the Baltimore Canyon is that such a load does not appear to exist nearby.

Another way to generate relatively rapid Neogene subsidence could be increasing lithospheric strain rates (stretching). Inversion of the subsidence history of the COST B-2 well indicates that Neogene strain rates of up to ~ 5 Ga^{-1} are required to generate observed subsidence patterns (*Flament et al.*, 2013). However, seismic lines in the Baltimore Canyon Trough do not show obvious faulting, or Neogene stratigraphic growth, which precludes lithospheric extension as an important mechanism for generating subsidence at this time. An obvious next step is to investigate the role sub-lithospheric support might play in generating lithospheric subsidence.

Sub-plate support

Several geodynamic models predict post-Cretaceous dynamic topography along the east coast of North America (e.g., *Moucha et al.*, 2008; *Spasojević et al.*, 2008; *Flament et al.*, 2013; *Liu*, 2015). Most of these models use broadly similar techniques to convert seismic tomographic models into predictions of mantle flow. Many predict dynamic support of the margin at wavelengths in excess of 1000 km. *Moucha et al.* (2008) calculated dynamic uplift of 100–200 m over the past 30 Ma. In contrast, *Spasojević et al.* (2008) estimated 100–200 m of dynamic drawdown over the same period and *Müller et al.* (2008) propose subsidence of 105–385 m since 70 Ma. *Flament et al.* (2013)'s model predicts 580 m of subsidence since 80 Ma, and ~ 30 m since 15 Ma, whilst *Rowley* (2013) estimate uplift of +10–20 m since 3 Ma. Dynamic uplift or subsidence along this margin is usually attributed to subduction of the cold, dense, relict Farallon slab, which is generally thought to reside in the lower mantle ($\gtrsim 670$ km depth; see e.g. *Rowley*, 2013; *Liu*, 2015).

Instead, I suggest that long wavelength free-air gravity anomalies, residual ocean age-depth measurements, and the stratigraphic and subsidence history of the margin suggest that Neogene dynamic drawdown was centred on the Baltimore Canyon Trough, and extended not more than ~ 500 km away from it (e.g. Figures 4.1 & 4.12). These observations indicate that the shallow upper mantle beneath the lithosphere might be playing an important role in generating dynamic support of the the margin (e.g. Figure 4.1; *Colli et al.*, 2016; *Hoggard et al.*, 2017; *Lodhia et al.*, 2018; *Roberts et al.*, 2018).

My approach to investigating the role the upper mantle plays in supporting topography along the margin makes use of the isostatic calculations described in Chapter 2. The presence of a cooler, denser asthenospheric mantle beneath the basin is suggested by the low shear wave velocity anomaly at shallow mantle depths (Figure 4.1b *Schaeffer and Lebedev*, 2013), and can provide a plausible

explanation for the observed drawdown. Assuming the lithospheric thickness of the passive margin has not changed since rifting in the Jurassic, the equations outlined in Section 2.5 simplify to

$$S = \frac{h\alpha\overline{T}}{1 - \alpha T_\circ}, \tag{4.12}$$

where S is excess subsidence, h is thickness of the anomalously hot or cool layer, here assumed to be 200 km, α is thermal expansivity, $\overline{T}$ is average negative excess temperature, $T_\circ$ is background temperature, which I set to 1333 ± 30°C (e.g. *Rudge et al.*, 2008). The calculated excess subsidence caused by cold thermal anomalies between 0 and -250°C, for a variable asthenospheric layer thickness, is shown in Figure 4.19. Layer thickness, h, is likely to be $\sim$ 200 km, based on the thickness of a high shear-wave velocity anomaly beneath the BCT, estimated from *Schaeffer and Lebedev* (2013). The blue box shows shows the range of temperatures anomalies that could generate the observed Neogene subsidence in the BCT for a cool layer of $\sim$ 200 km. Note that layers of thickness $<$ 200 km require unreasonably large changes in temperature to generate the observed $\sim$ 300–600 m of observed water-loaded subsidence. These calculations suggest that an asthenospheric layer with temperatures 100°C cooler than ambient mantle temperature can explain the observed subsidence.

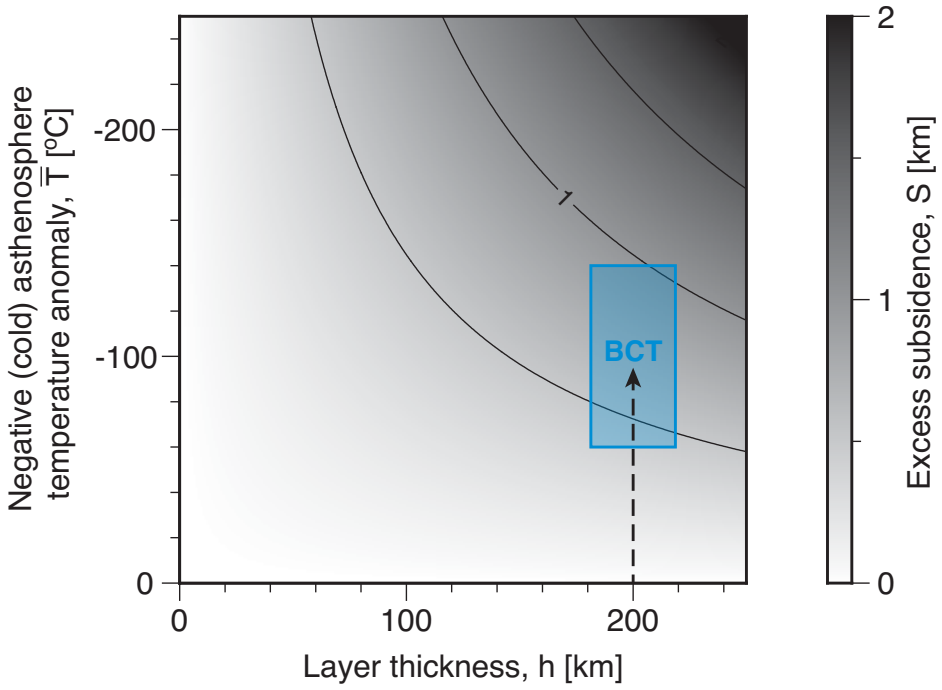

Figure 4.19: **Trade-off between average excess temperature, $\overline{T}$, and mantle layer thickness, h.** Blue box denotes range of temperature anomaly that could explain the observed subsidence of the BCT.

Implications for eustasy

Eustatic sea level estimates are often calculated at supposedly tectonically stable passive margins (e.g., *Vail et al.*, 1977; *Miller*, 2005). It is now generally accepted that dynamic topography can generate lithospheric vertical motions on space and time scales that overlap with estimates of eustasy (e.g., *Hager and Richards*, 1989; *Lovell*, 2010; *Hoggard et al.*, 2017; *Mitrovica et al.*, 2020). Most efforts to quantify the effect of sub-plate support for estimates of eustasy have focused on results obtained by geodynamic models of mantle convection (e.g., *Moucha et al.*, 2008; *Kominz et al.*, 2016; *Austermann et al.*, 2017). Instead, I show how geophysical and stratigraphic observations (e.g. gravity, seismic, backstripped wells) can be combined with simple isostatic calculations to constrain wavelengths and amplitudes of dynamic support at passive margins. The results indicate that a cool upper mantle has drawn down a $\sim$ 1000 km-long stretch of Eastern North America's passive margin by up to $\sim$ 600 m (in water-loaded space). Drawdown of the margin during the last $\sim$ 23 Ma has been centred close to the Baltimore Canyon Trough. I note that the wavelength of calculated drawdown is smaller than many geodynamic predictions. The cause of this discrepancy is probably, in part, because most geodynamic models do not include the shallow upper mantle in their calculations of mantle flow. Given that the mantle has a Rayleigh number of $\sim 10^6$–10^8, the vertical motions of passive margins are expected to be affected by dynamic uplift and drawdown on a range of spatial and temporal scales. Some of these scales are akin to long term sea level changes, complicating the interpretation of sea level curves derived from 'stable' continental margins (of the order 10^1–10^2 m, 10^{-1}–10^2 Ma).

In summary, backstripping of 27 wells showed that Neogene water-loaded subsidence was up to $\sim$ 600 m in the BCT. This subsidence history cannot be readily explained by post-rift thermal subsidence, post-rift stretching or flexure. In contrast, Neogene subsidence of the adjacent continental shelf, on the Georges Bank and Southeast Georgia Embayment, can be explained by simple post-rift lithospheric cooling. Seismic lines in the Baltimore Canyon Trough and Georges Bank show thick ($\sim$ 1 km) and thin ($<$ 200 m) Neogene sequences, respectively. Progradational and aggradational Neogene clinoforms in the Baltimore Canyon Trough reflect rapid generation of accommodation space and subsequent filling between $\sim$ 20–0 Ma. The amplitude of subsidence and its spatial localisation rules out eustasy as the sole contributor to the generation of accommodation space. Correlation with free-air gravity anomalies, shear wave tomography velocities and isostatic calculations indicate that temperature variations in the uppermost convecting mantle are able to generate sufficient density anomalies to drawdown the New Jersey margin. The patterns of dynamic subsidence shown in this study are similar to observations

of ocean age-depth measurements, and suggest that the Baltimore Canyon Trough has been drawn down by up to ~ 600 m since ~ 20 Ma. Upper mantle convection appears to play an important role in generating accommodation space along passive margins, which may incorrectly have been interpreted as a signal of eustasy in the past.

The sedimentary record preserved at passive margins, which records the history of basin subsidence, can also be used as an indicator of uplift in adjacent onshore regions. Increased influx of clastic sediments to offshore basins provide a record of changes to the geomorphic evolution of the rivers draining to the margin. In the next section, I explore how the sedimentary record of the BCT, combined with landscape evolution modelling, can be used to investigate the history of uplift in the Appalachians.

4.4 Appalachian Uplift and Sedimentary Flux

In the previous section, I have used the stratigraphy recorded at individual wells to show that the accommodation space of the BCT has increased by $\sim 300-600$ m in Neogene times. The cause of this excess subsidence, not readily explained by simple thermal cooling of stretched lithosphere or glacio-eustatic sea-level changes, was attributed to sub-plate mantle drawdown induced by the presence of a cooler than normal upper mantle. One question that arises is whether this increase in basin subsidence is matched by a concurrent increase in the sediment influx from the adjacent Appalachian Highlands.

Changes in sediment accumulation rate in basins are often attributed to one of three factors: tectonic subsidence, sea level, or sediment flux from the source region. The first two are related to changes in base-level or accommodation space, whereas the latter is a function of the geomorphic evolution of the source region. It is generally agreed that the Appalachian Mountains have been a tectonically quiescent region since the establishment of a passive margin in the Late Jurassic (e.g. *Klitgord et al.*, 1988). The apparent agreement between the long-term and short-term measurements of denudation in the Appalachian Mountains has led to the idea of a 'steadily-decaying orogen', where the present day topography is the result of the slow and steady decay of a Paleozoic mountain range that once reached Himalayan-like elevations (e.g., *Pavich et al.*, 1985; *Boettcher and Milliken*, 1994; *Matmon et al.*, 2003; *Naeser et al.*, 2004; *Portenga et al.*, 2013; *Amidon et al.*, 2016). Figure 4.20 shows a compilation of low-temperature thermochronology closure ages, incision rates, catchment average erosion rates from cosmogenic ^{10}Be analysis, and uplift of the Appalachians and adjacent coastal plains. Linear denudation rates calculated from closure ages (using equation from chapter 3), as well as thermal

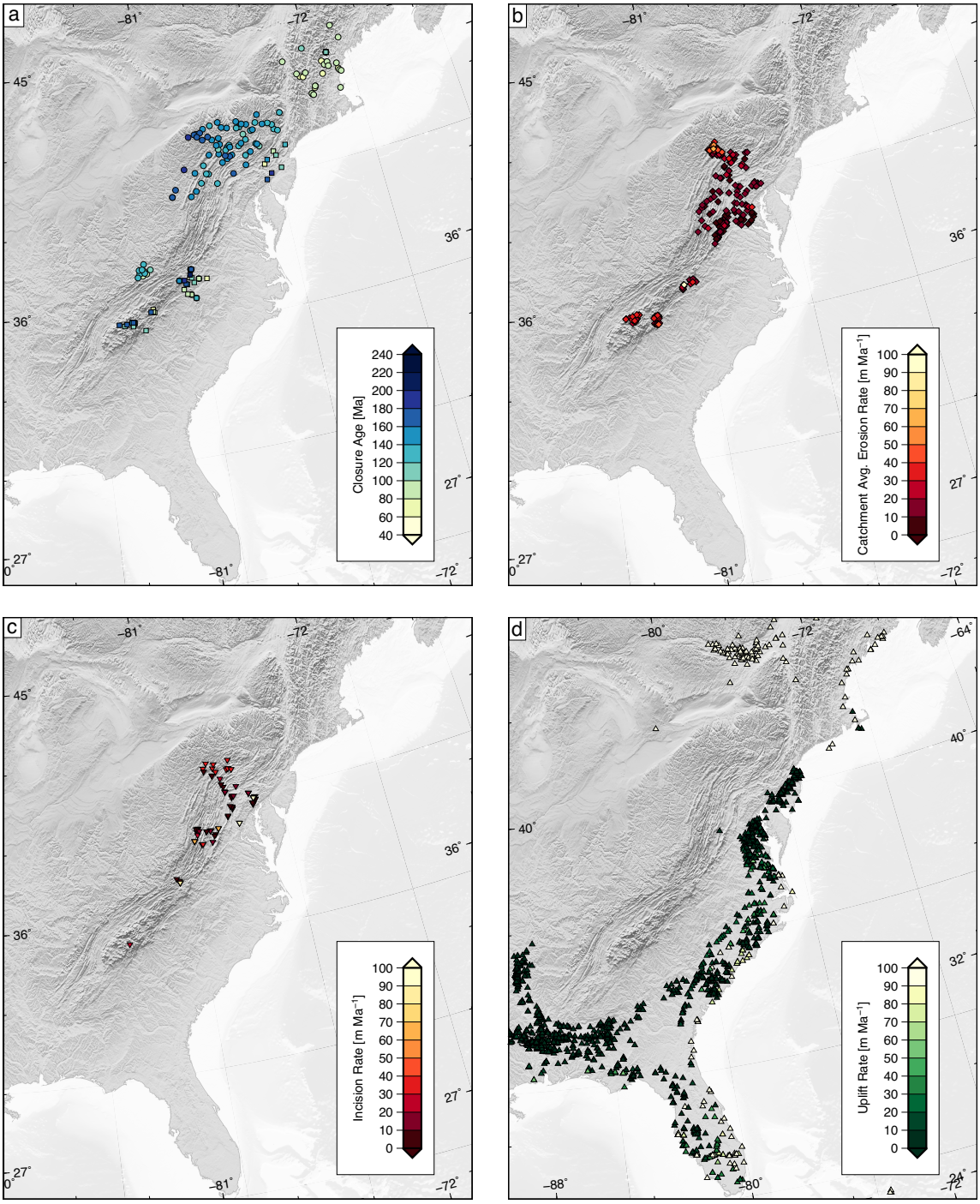

Figure 4.20: **Geomorphic constraints on the evolution of the Appalachian Mountains** and Atlantic Coastal Plain. (a) Apatite fission track and (U-Th)/He closure ages (*Zimmerman et al.*, 1975; *Blackmer et al.*, 1994; *Boettcher and Milliken*, 1994; *O'Sullivan and Lane*, 1997; *Spotila et al.*, 2004; *McKeon et al.*, 2014; *Amidon et al.*, 2016; *Shorten and Fitzgerald*, 2019); (b) Catchment average erosion rates (*Matmon et al.*, 2003; *Miller et al.*, 2013; *Duxbury et al.*, 2015; *Linari et al.*, 2017; Portenga et al., 2019); (c) Incision rates (*Pazzaglia and Gardner*, 1993; *Matmon et al.*, 2003; *Reusser et al.*, 2004; *Ward et al.*, 2005; *Hancock and Kirwan*, 2007; *Gallen et al.*, 2013; *Miller et al.*, 2013; *Portenga et al.*, 2013); (d) Uplift rates (PBDB derived rates, Chapter 2; *Rovere et al.*, 2014; Dowsett and Cronin, 1990).

modelling, suggest that long term exhumation rates are of similar order to the modern incision and erosion rates (Figure 4.20b,c). This idea of a steadily-eroding mountain range is at odds with the large sediment thicknesses of Middle Miocene age recorded in offshore wells of the BCT, which implies a significant increase in Neogene erosion rates.

On the other hand, the modelled uplift history shown in Chapter 3, derived from the inverse modelling of river profiles, suggests the Appalachian Mountains have been steadily uplifting since the Late Cretaceous, with a marked increase in uplift rates over the last 15 Ma in the southern and central ranges. Such changes in the uplift of source regions should predictably alter the observed sediment yield of rivers, and therefore the sediment accumulation history in depositional sinks. Landscape evolution models, such as the one described in Chapter 3, can be used to predict the sedimentary flux to basins as a function of a known uplift history, using a calibrated erosional model. In this way, a regional scale landscape evolution model of eastern North America, together with a well know history of sedimentary accumulation in the BCT, provides a practical method to test different hypotheses regarding the long-term geomorphic evolution of the Appalachian Mountains.

In this section, I explore whether forward modelling of landscape evolution using constraints from offshore sediment volumes and source-region erosion rates can give new insight into Late Cretaceous to Recent history of sedimentary flux to the Middle US Atlantic margin. Can the steady 'decay' of an initially high landscape, or modelled uplift of 300–500 m uplift over the last 20 Ma, as predicted by the inverse model, generate an order of magnitude increase in the sedimentary flux to the BCT? First, I review the existing record of sediment accumulation in the BCT, as it provides a proxy for the sediment flux to the margin. Estimates of sediment accumulation are then compared to predictions of sedimentary flux derived from the landscape evolution model (LEM) shown in Chapter 3, Section 3.6. The results presented in this section are part of an ongoing study, and the next steps are further discussed in Chapter 5.

4.4.1 Measuring sediment accumulation rate

The sediment accumulation recorded at each well can provide a proxy for sediment flux to the margin, and related to uplift or geomorphic processes onshore (e.g., Pinet and Souriau, 1988; *Milliman and Syvitski*, 1992; *Hovius*, 1998). Using the stratigraphic thicknesses and age constraints recorded in the individual well reports, sediment accumulation is calculated as the temporal rate of change in the thickness of the sediment column recorded at each well. To avoid a systematic bias towards

thicker sequences of younger sediments, a compaction correction was applied to each layer using equation 4.1 (e.g., *Einsele*, 1992; *Liu and Galloway*, 1993; Liu and Galloway, 1997). The compaction parameterisation used was that of *Watts and Thorne* (1984), where initial porosity, ϕ_o, is 0.52, and compaction wavelength, λ, is 3 km. Figures 4.21 and 4.22 show the Late Cretaceous to Recent

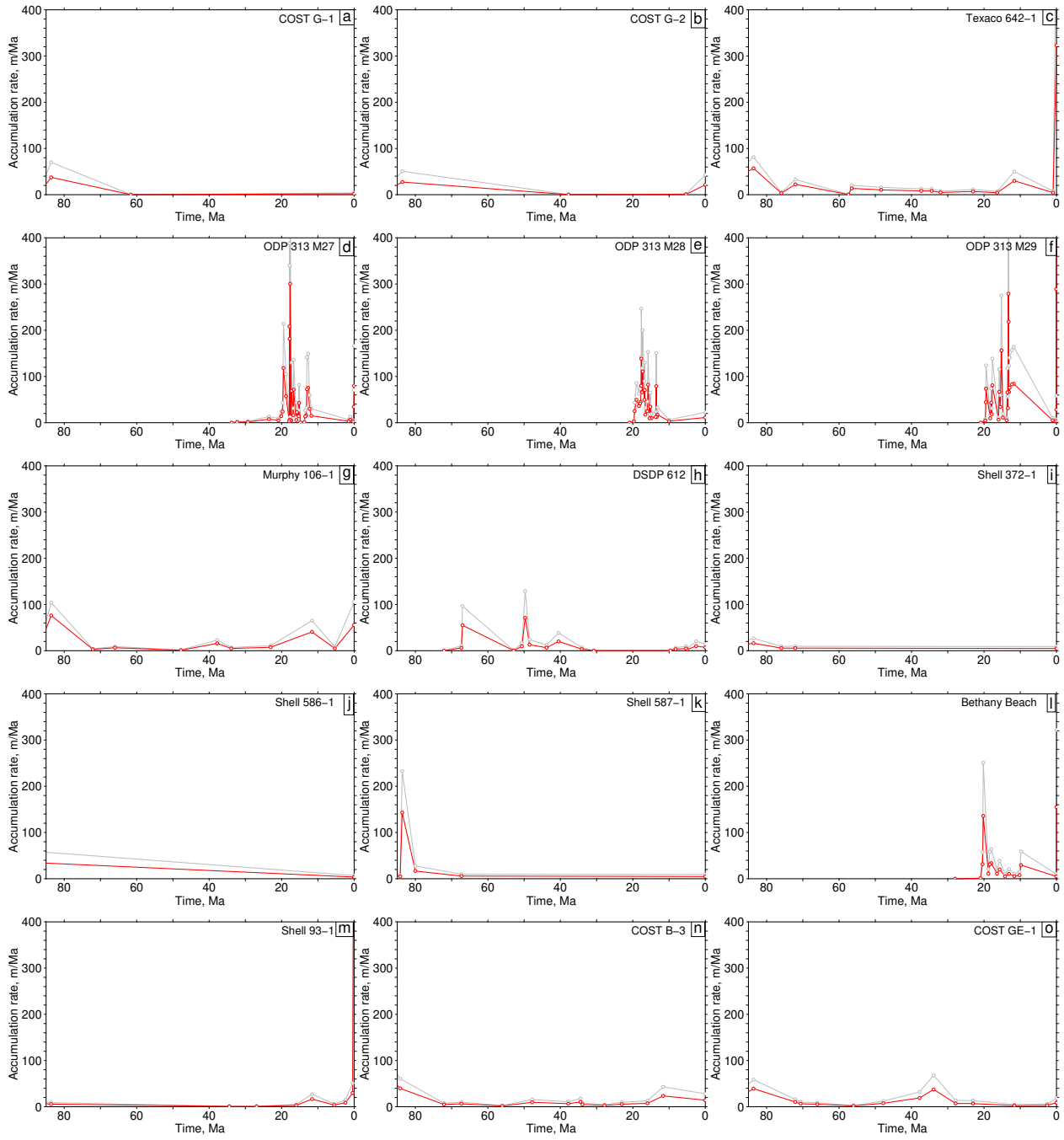

Figure 4.21: **Sediment accumulation rate at each well**, measured from reported thicknesses of sedimentary sequences and biostratigraphic ages (grey points). Solid sediment accumulation rate (red points) was calculated by subtracting the pore space, accounting for compaction, using the relationship described in equation 4.1 and the compaction parameterisation of *Watts and Thorne* (1984). No correction was made for unconformities, which will bias accumulation rates towards slower values.

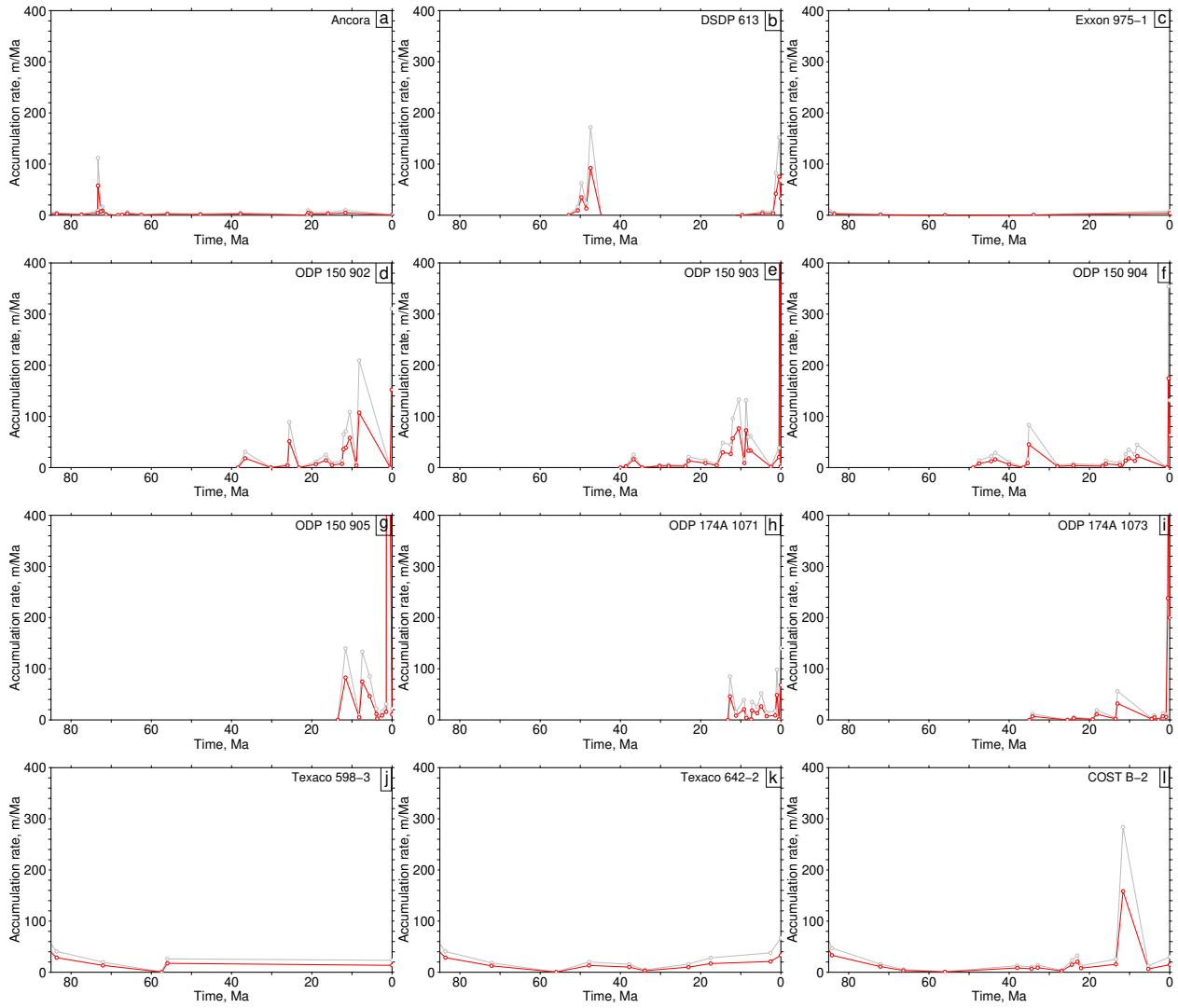

Figure 4.22: **Sediment accumulation rate at each well** (continued).

sediment accumulation for each well. The gray lines show the recorded thickness of sedimentary sequences accumulated at each well, and the red line shows the thicknesses at each well corrected for sediment compaction.

Most of the wells located within the BCT show a marked increase in the accumulation rates in the Middle Miocene, with changes of one to two orders of magnitude. Note that this increase in accumulation rate is coeval with the increase in water-loaded subsidence recorded in the wells (see Figure 4.10 and 4.11). Some wells, for example Shell 586-1 and Texaco 598-3, Figures 4.21j and 4.22j respectively, lack the temporal resolution in the stratigraphy to resolve any changes in accumulation

rate in Neogene times. Wells located on the Georges Bank, COST G-1, COST G-2 and Exxon 975-1, and on the Georgia Embayment, COST GE-1, do not show any significant increase in sediment accumulation during over the last 20 Ma. These wells also do not display a significant increase in water-loaded subsidence over the same time period.

There are inherent problems with using the sediment accumulation rates recorded at individual points as a proxy for sediment flux to whole basin. First, linear sedimentation rates derived from well data may be unrepresentative of the complexity of the depositional settings at passive margins (e.g., *Molnar*, 2004). Local variations in accommodation space caused by, for example, basement fault geometry, may cause lateral variability in the accumulation rate that is unrelated to the onshore sediment flux distribution. Secondly, sediment deposited during one time period can be reworked and redeposited as part of a younger sediment succession. Additionally, erosion can be localised, as is the case with submarine canyons, which can add to the lateral differences in accumulated sediment thicknesses. Finally, sedimentation rates are dependent upon the time scale of observation *McCave and Swift* (1976); *Sadler* (1981). This effect is well demonstrated by the wells lacking in temporal resolution over the last 20 Ma (e.g. Figures 4.21j and 4.22j).

Other methods exist for estimating the sedimentary flux to a basin. For example, *Petter et al.* (2013) related the geometry and stacking patterns of clinoforms, observed from seismic data, to sedimentary flux. This method cannot account for sediment re-worked and deposited in deeper, ocean floor portions of the basin. *Steckler et al.* (1999) estimated of sediment flux to the BCT based on down-dip cross-sectional areas of depositional sequences interpreted from seismic profiles tied to Ocean Drilling Program cores. This method, although it provides some improvement to the estimates from core only, still cannot fully account for variability along the strike of the basin.

Volumetric sedimentation rates provide the most robust estimate of the onshore sediment flux to a margin. It can account for spatial variability, especially if enough data is available such that sediment accumulated far from the basin main depocentre (e.g. on the abyssal plain) can be accounted for to some extent. Mapped sediment volumes can be used as proxy for the solid sediment flux from rivers as long as a correction for porosity is applied (e.g., Liu and Galloway, 1997). This method has been used by several researchers to estimate sediment flux on basinal and global scales at both short (k.y.) and long (m.y.) geologic time scales (e.g., *Hay et al.*, 1988; *Pazzaglia and Brandon*, 1996; Liu and Galloway, 1997; Walford et al., 2005; *Guillocheau et al.*, 2012; *Covault et al.*, 2013; *Pedersen et al.*, 2018). Volumetric estimates of sediment flux have formed the basis for many of the hypothesis

surrounding the evolution of the Appalachian Highlands and the BCT.

4.4.2 Assessment of sediment volumes

Sediment accumulation rates reported in the seminal work by *Poag and Sevon* (1989) provide a starting point for estimating sediment flux from the Appalachian Mountains to the BCT. Bulk volume of siliciclastic sediment for each of the stratigraphic intervals was determined from isopach maps, generated from interpretation of available well data and seismic reflection surveys. These isopach contour maps were digitised using QGIS software. The published isopach figures for each time slice were geo-referenced, and contour lines were individually traced to create a vector map of the contour lines where the thickness value of each line is an attribute. Next, using GRASS functionalities, the vector map was rasterised by creating a $1' \times 1'$ grid, where each grid cell is either a contour line cell (containing the sediment thickness value), or a fill cell. Using the r.surf.cont functionality, a linear interpolation between contour intervals is performed using a flood fill algorithm. Grid tests were performed by surface interpolation by fitting a regularised spline with tension, however it produced unwanted data artefacts in regions where the contour lines were too closely spaced. The best-fit isopach maps are shown in Figures 4.23 and 4.24.

A few key basin features can be picked out from the sediment thickness grids. The syn-rift sedimentation is well defined by localised, large thickness deposits from Aalenian to Callovian times. Development of a clear shelf-slope break can be observed from Santonian-Coniacian times. Low sediment accumulation rates from Upper Eocene to Lower Miocene times are followed by a significant volume increase from the Middle Miocene to Recent.

However, the *Poag and Sevon* (1989) data analysis has important shortcomings. First, the isopach maps were not depth-converted using an appropriate velocity model. The thickness of the sedimentary sequences, mapped on the seismic data in two-way travel time, were converted to depth using the simple assumption of 0.1 s = 100 m. This linear time-depth relationship overestimates the volume of sediment deposited at shallow depths and underestimates the volumes of older sediments, preserved deeper in the basin. For example, comparison of the linear time-depth conversion with an interval velocities curve from the COST B-2 well suggests sediments of Middle Miocene age deposited at depths of $\sim$ 450 m are overestimated by about 10%, while sediments of Callovian age are underestimated by at least factor of two. The time-depth relationships reported for wells in the BCT, shown in Figures 4.5 and 4.6, provides additional confirmation that a more careful approach to the depth-conversion of the

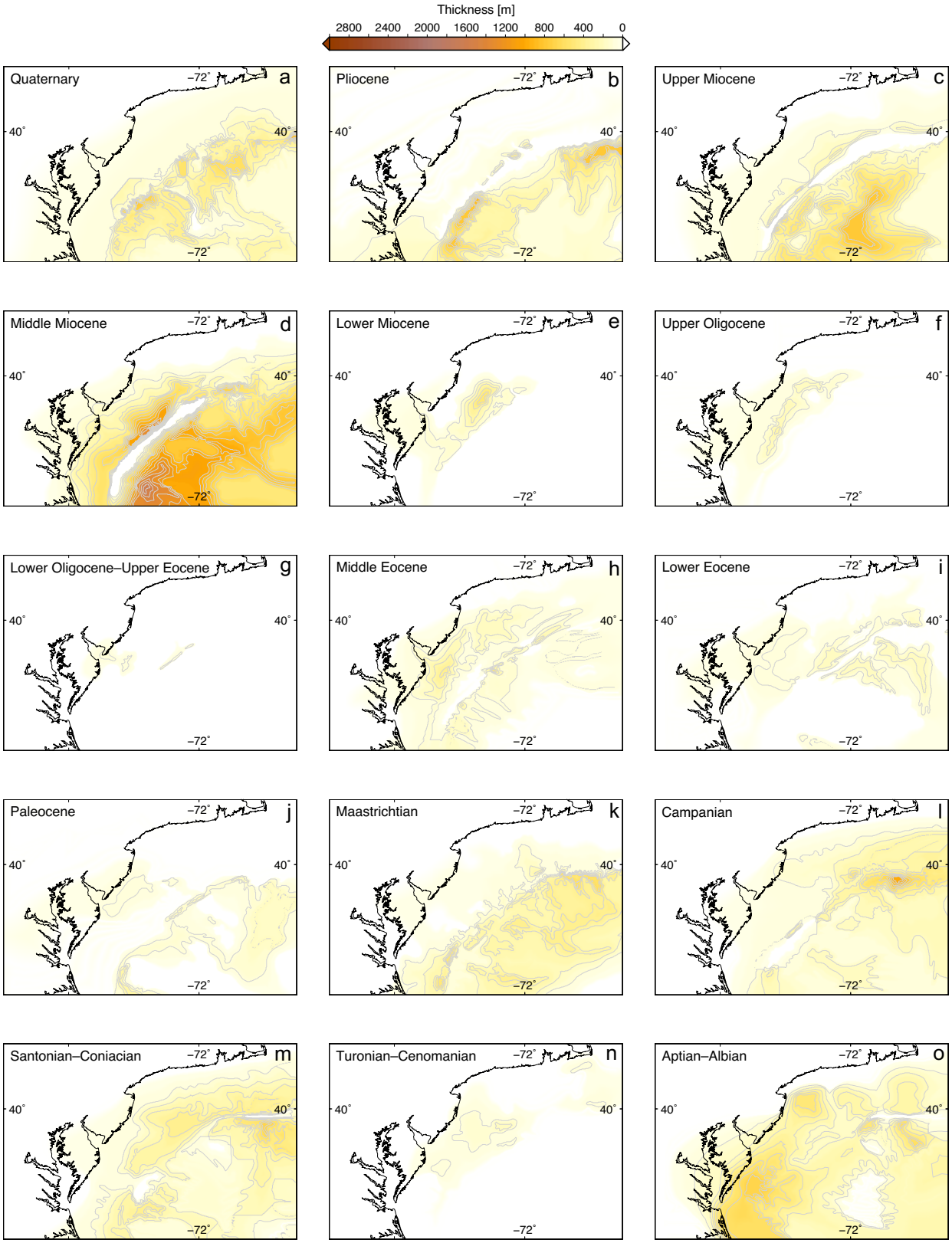

Figure 4.23: **Isopach maps of allostratigraphic units in the Baltimore Canyon Trough**, Salisbury Embayment, and Hatteras Basin as mapped by *Poag and Sevon* (1989). Grey lines show digitised isopach contour lines. 0 m thickness show regions of no deposition, erosional unconformities, or unit thicknesses too small to be resolved by the seismic reflection surveys.

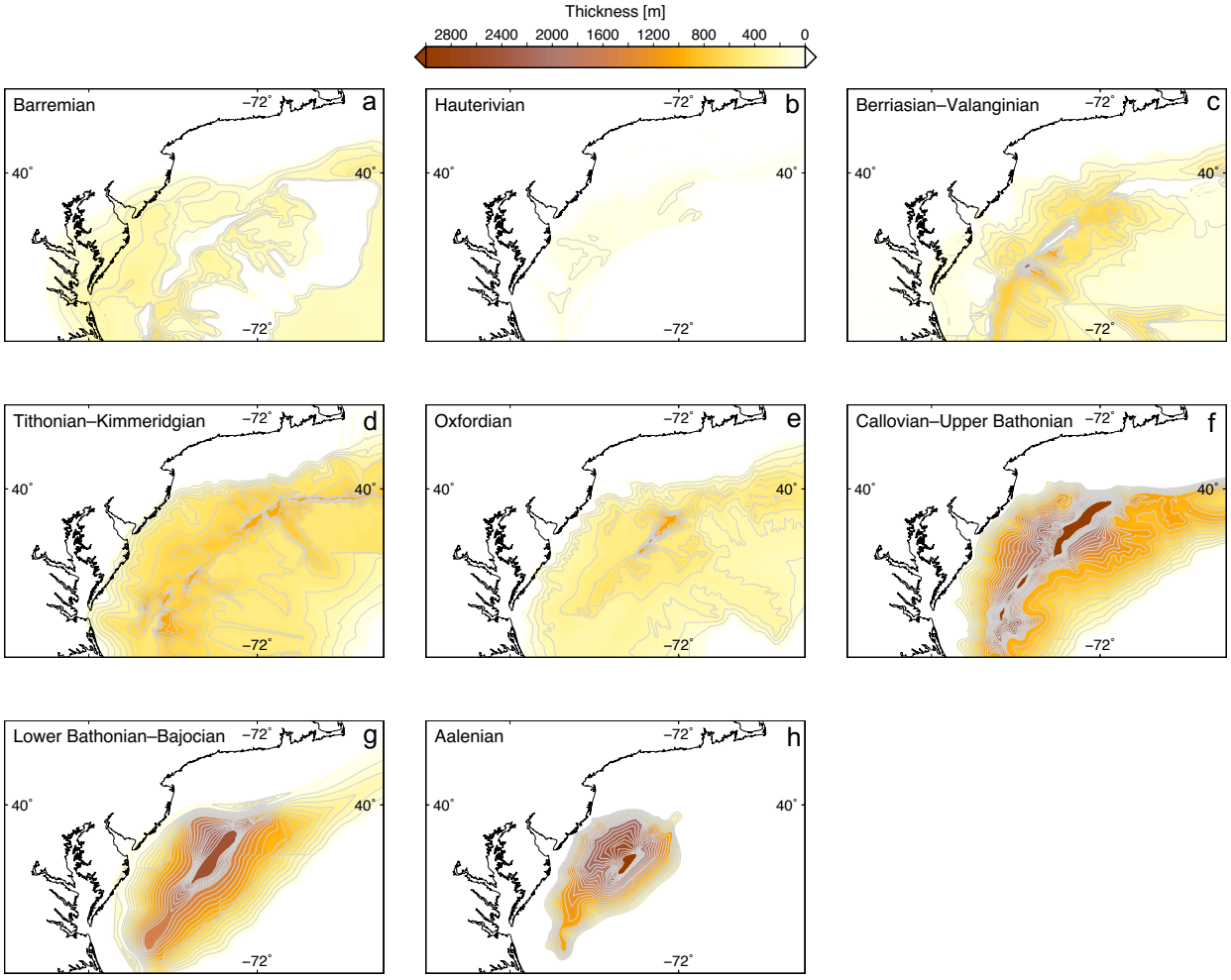

Figure 4.24: **Isopach maps of allostratigraphic units in the Baltimore Canyon Trough**, Salisbury Embayment, and Hatteras Basin as mapped by *Poag and Sevon* (1989) (continued).

isopach maps is required for a more accurate/precise estimate of the sediment volumes preserved in the BCT. Secondly, no correction for sediment compaction was applied to the volumes, which would also act to under-predict the volumes of older sediments in the basin. This shortcoming was recognised by *Pazzaglia and Brandon* (1996), who converted the sediment volumes into solid rock sediment volumes by applying a porosity correction to the volumes reported by *Scholle* (1977). However, the lateral variability in sediment thickness throughout the basin, shown in Figures 4.23 and 4.24, suggests that assuming a uniform porosity for each stratigraphic unit throughout the whole basin could result in erroneous solid sediment volumes. Thirdly, the geological timescale used by *Poag and Sevon* (1989) is the Decade of North America Geology (*Palmer*, 1983). This timescale has significantly different interval lengths, especially for Neogene and Jurassic periods, therefore the estimated volumetric flux will be different. For example, the *Palmer* (1983) scale identified the duration of the Oxfordian period as $\sim$ 5 Ma longer than *Gradstein et al.* (2012), 8 compared to 3.7 Ma, respectively. *Pazzaglia and*

Brandon (1996) also recognised this problem and corrected the ages to the timescale of *Cande and Kent* (1992), however this timescale has recently changed. For consistency, I calculated sedimentary flux using the sedimentary flux using the timescale of *Gradstein et al.* (2012). Finally, *Poag and Sevon* (1989) recognised that each allostratigraphic member, or depositional sequence, was separated by an erosional unconformity. As the duration of the unconformity cannot be accurately determined, they assumed a 1 Ma time gap between each depositional unit. However, it is unclear how this assumption was applied to the sediment accumulation rate calculations.

More detailed isopach maps, produced with more data, were published in *Poag* (1992) and *Poag and Ward* (1993), but the volumes recorded in each isopach map is not reported. One way of assessing the quality of the isopach maps from *Poag and Sevon* (1989) is to compare to the same data from *Poag and Ward* (1993). Figure 4.25 shows the comparison of the Middle Miocene isopach from *Poag and Sevon* (1989) and to the equivalent map from *Poag and Ward* (1993), which corresponds to the Phoenix Canyon allostratigraphic member. In general, the sediment accumulation patterns are similar: both show significant sediment storage within the continental shelf, an erosional hiatus where on the paleo-

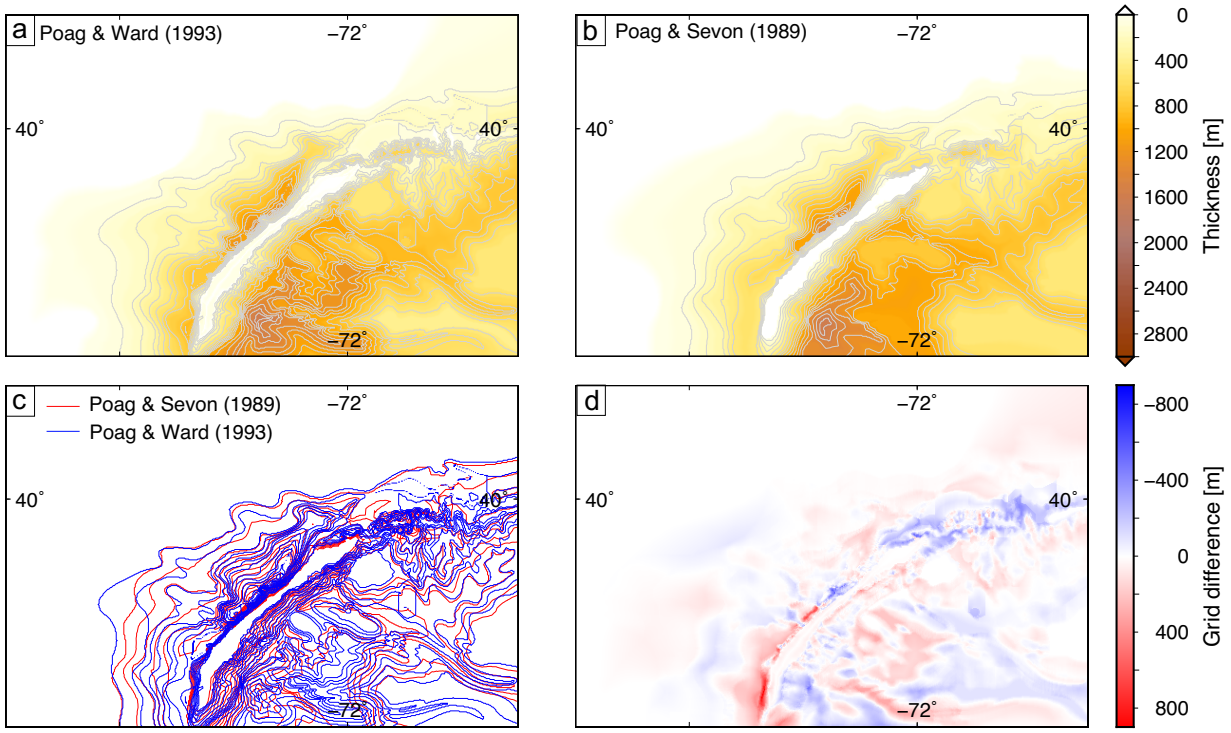

Figure 4.25: **Comparison of Middle Miocene isopach maps** from (a) *Poag and Sevon* (1989) and (b) *Poag and Ward* (1993) (Phoenix Canyon allostratigraphic member); (c) Isopach contour lines shown in (a) and (b); (d) Difference between isopachs shown in (a) and (b). Note that the maximum thickness difference is 900 m.

continental slope, and significant volumes accumulated in the abyssal plain in the southern portion of the region. However there are significant differences in the recorded thicknesses for the two isopach maps, by as much as 900 m as shown in Figure 4.25d. Surprisingly, the total volume recorded within these maps only differs by a relatively small amount (1.546×10^5 and 1.574×10^5 km^3 , from *Poag and Sevon* (1989) and *Poag and Ward* (1993), respectively). *Pazzaglia and Brandon* (1996) compared the volumes reported by *Poag and Sevon* (1989) and *Poag* (1992) and postulated that volumes agree within $\sim$ 20%. Despite being generated from the same well and seismic datasets, there are some discrepancies in the sedimentary fluxes. I examine these inconsistencies by systematically exploring the uncertainties.

One way to quantify the error in the sediment accumulation rate at each time interval is to compare the different estimates for the BCT from different sources. Figure 4.26 shows a comparison of the sediment flux reported in *Poag and Sevon* (1989), calculated from isopachs from *Poag and Sevon* (1989), the single Middle Miocene isopach from *Poag and Ward* (1993), and the volume from *Poag* (1992). For all datasets, sediment accumulation rate was re-calculated using the geological timescale

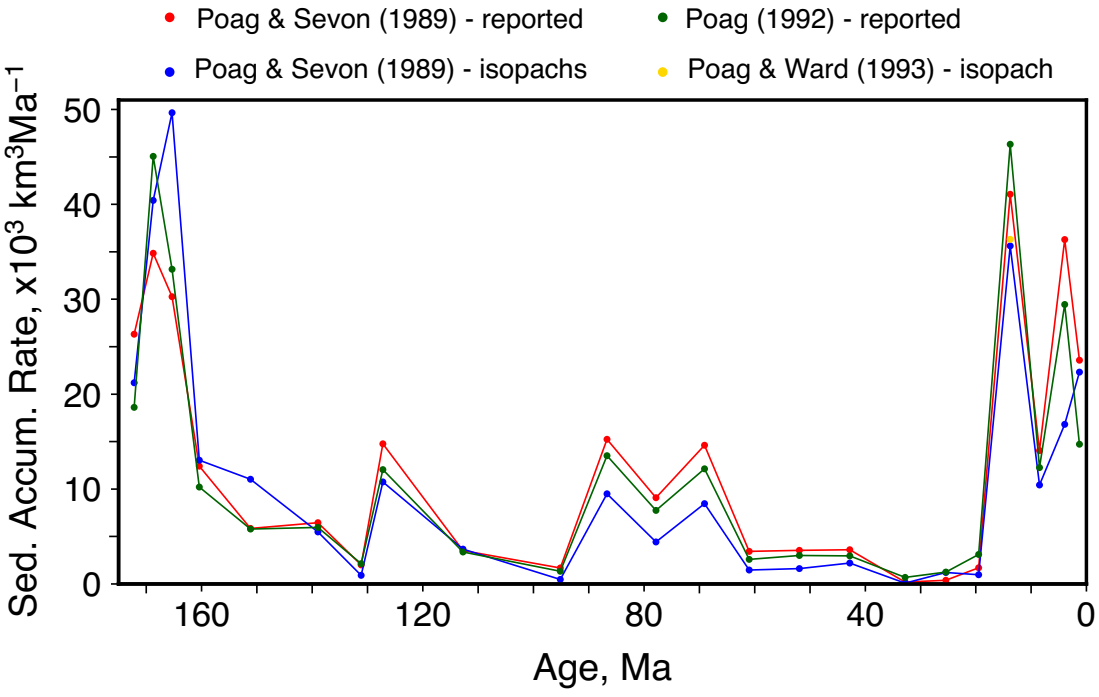

Figure 4.26: **Comparisons of sediment flux to the BCT**. Estimates of flux plotted as points to be comparable with original figure from *Poag and Sevon* (1989). Red = sediment accumulation rate reported by *Poag and Sevon* (1989), corrected for the (*Gradstein et al.*, 2012) timescale; Blue = rate calculated from digitised isopach grids from *Poag and Sevon* (1989); Green = rate reported in *Poag* (1992), corrected for the (*Gradstein et al.*, 2012) timescale; Yellow = rate calculated from the single digitised isopach from *Poag and Ward* (1993).

of *Gradstein et al.* (2012). No correction for porosity or compaction was applied, therefore the volumes represent the volumes observed in the seismic data.

In general, all datasets show a similar trend in the sediment accumulation rate history in the BCT (Figure 4.26). All reported histories of sediment accumulation show a peak in the Jurassic, corresponding to syn-rift deposits, a moderate increase in the Late Cretaceous, very low rates from Paleocene to Lower Miocene time, and a dramatic increase after the Middle Miocene. This similarity is perhaps unsurprising, all rates have been calculated from the same data. For exactly that reason, a better agreement between data might be expected, yet there are differences that cannot be systematically explained. For example, the rate calculated using the digitised Pliocene isopach map from *Poag and Sevon* (1989) (Figure 4.23) is significantly lower than that reported in their paper, differing by ~ 15 km^3 Ma^{-1}. As previously mentioned, the estimate from the *Poag and Sevon* (1989) Middle Miocene isopach is similar to the *Poag and Ward* (1993) estimate, but both are ~ 5 km^{3}Ma^{-1} lower than rates reported by *Poag and Sevon* (1989), and the ~ 5 km^3 Ma^{-1} lower still than *Poag* (1992). At each time interval, the standard deviation of the data is, on average, 30.9%.

The largest drawback of this dataset is that is that is records bulk volume, and a correction for pore space has not been performed. Even if the volumetrically derived fluxes were corrected for porosity, which should act to correct for an overprediction of younger volumes, significant flux increase in the Middle Miocene is still observed. For example, using a generous porosity estimate for Middle Miocene sediments of 50%, the the observed flux woud be reduced from ~ 40 to ~ 20 km^{3}Ma^{-1}. Despite the sizeable decrease, it is still an order of magnitude increase from a maximum 1.9 km^{3}Ma^{-1} in the Lower Miocene. Any model that attempts to predict the delivery of clastic sediments to the BCT basin must generate this order of magnitude increase in sediment accumulation rate at ~ 15 Ma.

Notwithstanding the limitations of each method, all estimates of sediment flux, whether point estimates from from individual wells, integrated cross-sectional area from a single seismic line (*Steckler et al.*, 1999), or from seismic volumes (*Poag and Sevon*, 1989; *Poag*, 1992; *Poag and Ward*, 1993; *Pazzaglia and Brandon*, 1996) show an order of magnitude increase in the sedimentation rates in the BCT during the Middle Miocene (~ 15 Ma). In the next section, I explore whether the landscape evolution model, described in Chapter 3, can generate the observed patterns of patterns of sediment flux to the BCT.

4.4.3 Sediment Flux Prediction from Landscape Evolution Modelling

Different explanations have been given to explain the Middle Miocene increase in sediment accumulated in the BCT, such as lowering of sea-level (*Miller et al.*, 1996), changes in climatic regimes (*Steckler et al.*, 1999), uplift of the Appalachian Mountains (*Poag and Sevon*, 1989), and drainage capture events in Appalachian rivers (*Moodie et al.*, 2017). In this section I explore the contribution of source region uplift to the Neogene increase in sediment flux to the BCT by comparing the observed sediment flux to that derived from a landscape evolution model (LEM). Here, I examine the assumption of a 'steadily decaying' origin, and investigate the extent to which the uplift history derived in Chapter 3 can explain the order of magnitude increase in the Middle Miocene offshore sediment accumulation rate in the BCT.

Model Setup

Three different scenarios are explored. (1) The model setup as described in Chapter 3, Section 3.6. Initial topography was seeded with the present-day DEM of North America scaled to 5% of the elevation. The model was then forced with the uplift history from the river profile inversion (Section 3.5). (2) An initial paleotopography that is allowed to steadily erode over the model time (82 Ma). The initial model elevation was generated by smoothing a present-day DEM of North America (ASTER) using a 500 km low-pass Gaussian filter. This model run is intended to explore the idea of an 'old decaying orogen', as is proposed for the Appalachians by several authors. (3) The LEM was seeded with the same paleotopography as in scenario (2), but forced with the uplift function from the inversion.

For all model scenarios, the erosional parameterisation was the same (as described in Chapter 3, Section 3.6). The Badlands landscape evolution model uses a detachment-limited stream power law formulation to compute erosion. Initial conditions are set with regular grid spacing of 10×10 km, which is used to generate a triangular irregular network grid, on which calculations are performed. Erosional parameters m and v are set to 0.4 and 0.9924×10^{-6} $m^{0.2}$ yr^{-1}, respectively. A diffusion coefficient $\kappa = 10^{-20}$ m^2 Ma^{-1} is assumed. Precipitation rate is set to 1 m a^{-1}. The modelled landscape is assumed to be purely erosive, in that all of the generated sediment is moved to the margin and no sediment is deposited on land. The full model description can be found in Chapter 3. This simple approach is a reasonable starting point, and I later consider other scenarios.

Modelling Results

Th model grid nodes containing the mouth of rivers flowing to the BCT were identified and defined as a swath, shown in Figure 4.27. For each model timestep, the sedimentary flux at each individual was extracted and summed, giving the total flux to the margin. The modelled sedimentary flux is converted from $m^3\ s^{-1}$ to $\times 10^3\ km^3\ Ma^{-1}$ in order to be compared with the volumes predicted from *Poag and Sevon* (1989) (Figure 4.26). It is important to note that model flux predictions are of solid sediment volumes, but the reported sediment flux are calculated from bulk volumes (i.e. including porosity). Figures 4.28, 4.29 and 4.30 show the model outputs for scenarios (1), (2) and (3), respectively. Figure 4.31 shows the predicted sedimentary flux to the BCT resulting from the three different model scenarios compared to the observed sediment accumulation history, the uplift history of the Appalachian Mountains from the inverse model, and the water-loaded subsidence history from the COST B-2 well.

Model (1), with 5% of the present-day DEM initial condition and forced with the uplift history from the river profile inversion, is shown by the red curve in Figure 4.31. This model fails to generate any significant variations in the sedimentary flux to the margin, with rates steadily increasing towards the present day but not surpassing $5 \times 10^3 km^3 Ma^{-1}$. Significant denudation of the topography only occurs after 23 Ma, as seen on Figure 4.28d, yet no concomitant increase in sediment flux is observed. Predicted sediment flux is not higher than $3 \times 10^3\ km^3 Ma^{-1}$. A steadily decaying initial topography, modelled in scenario (2), is shown by the blue curve. The model erodes most Appalachian topography

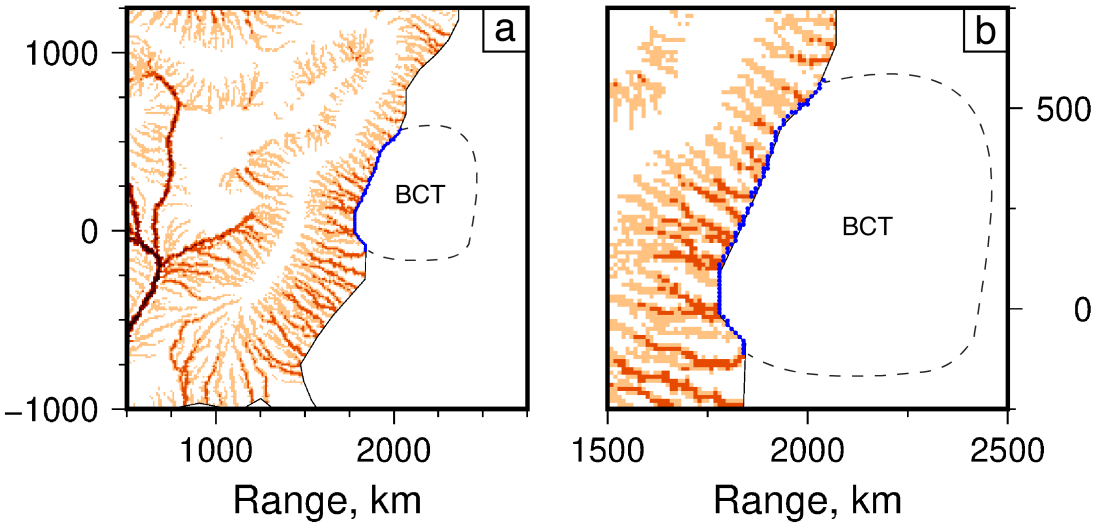

Figure 4.27: **Location of sedimentary flux swath profile.** (a) Swath profile (blue line) overlay on sedimentary flux grid. Dotted line shows approximate location of BCT deposits. (b) Zoom in of swath, showing location of individual points.

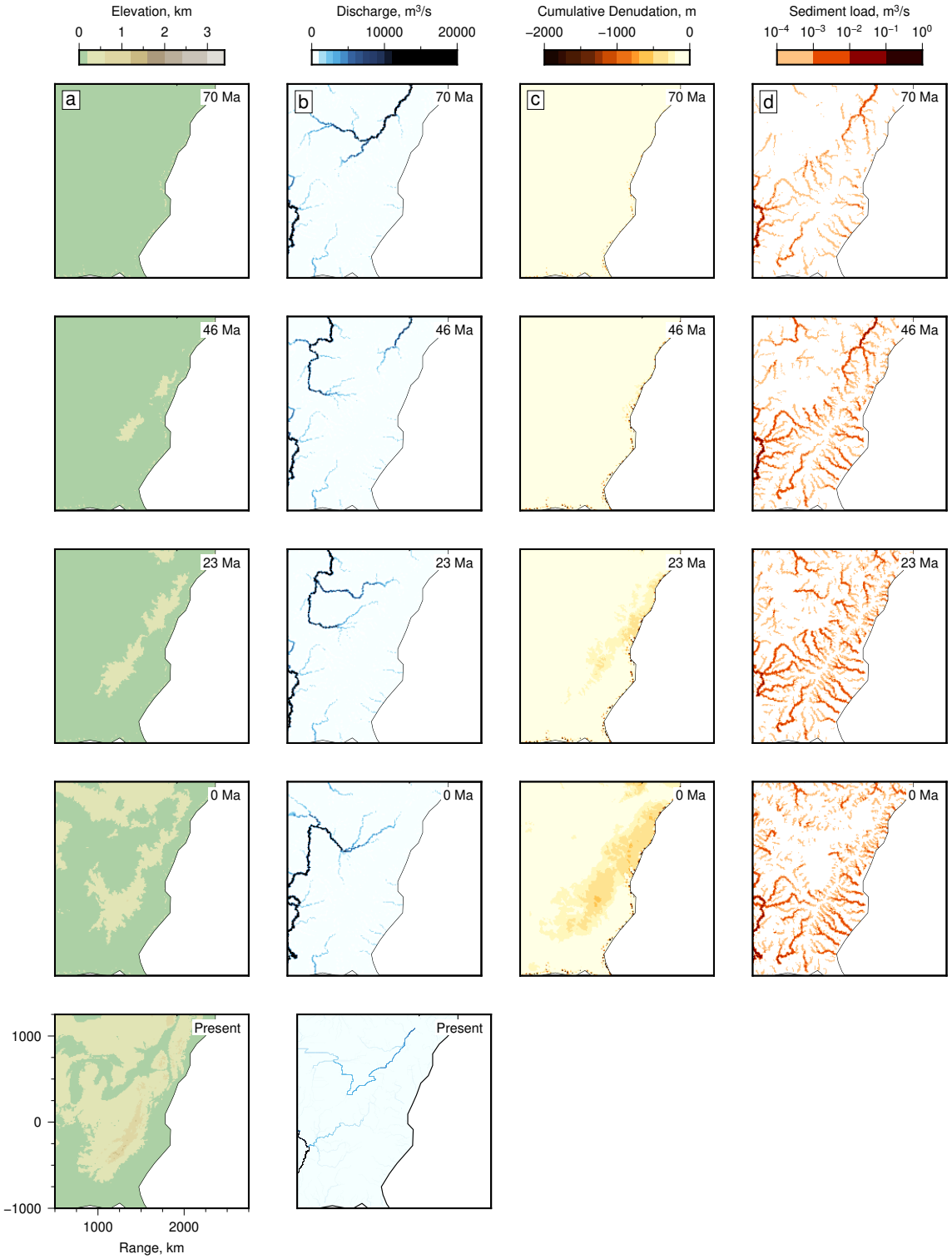

Figure 4.28: **Predicted landscape evolution of Appalachian Mountains** as shown in Figure 3.28, with 5% DEM initial condition. (a) Late Mesozoic and Cenozoic topographic evolution of eastern North America calculated using modified version of Badlands landscape evolution model (*Salles*, 2015). Model was forced using uplift history calculated by inverse modelling (Figure 3.18). Model resolution = 10 km. Lowest panel = present-day topography from ASTER GDEM database for comparison. (b) Calculated water discharge. Bottom panel = present-day discharge calculated using Esri flow-routing algorithms and ASTER GDEM database (see Figure 3.14 for annotation). (c) Calculated cumulative denudation (i.e. $\int \partial z \mathrm{dt}/\partial \mathrm{t}$). (d) Calculated sedimentary load (i.e. $\int \partial z \mathrm{dx}/\partial \mathrm{t}$).

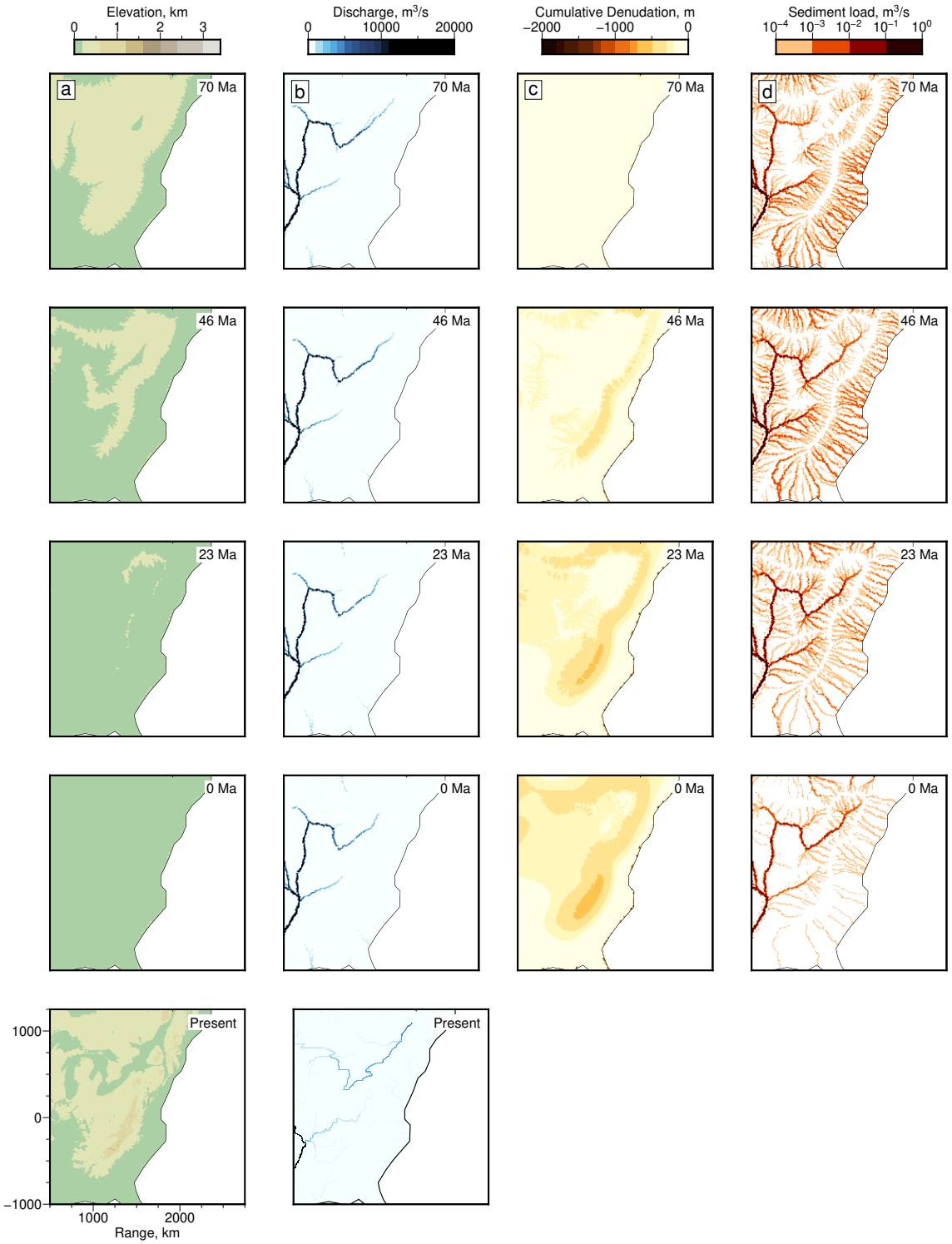

Figure 4.29: **Landscape evolution model for decaying topography.** Initial model elevation is a smooth present-day DEM of North America, which is allowed to erode with no additional uplift.

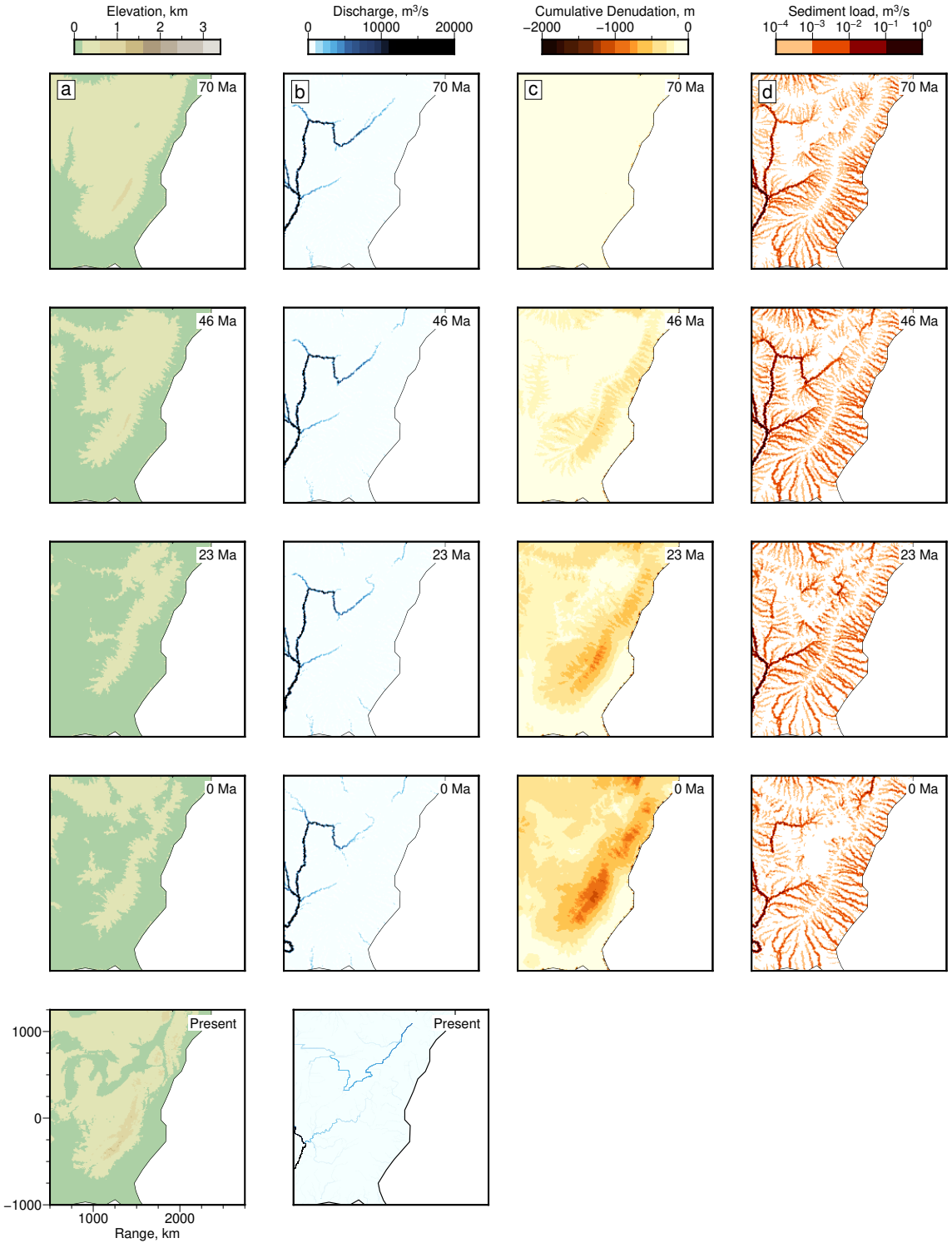

Figure 4.30: **Landscape evolution model with paleotopography and uplift.** Initial model elevation is a smooth present-day DEM of North America. Model was forced using uplift history calculated by inverse modelling (Figure 3.18).

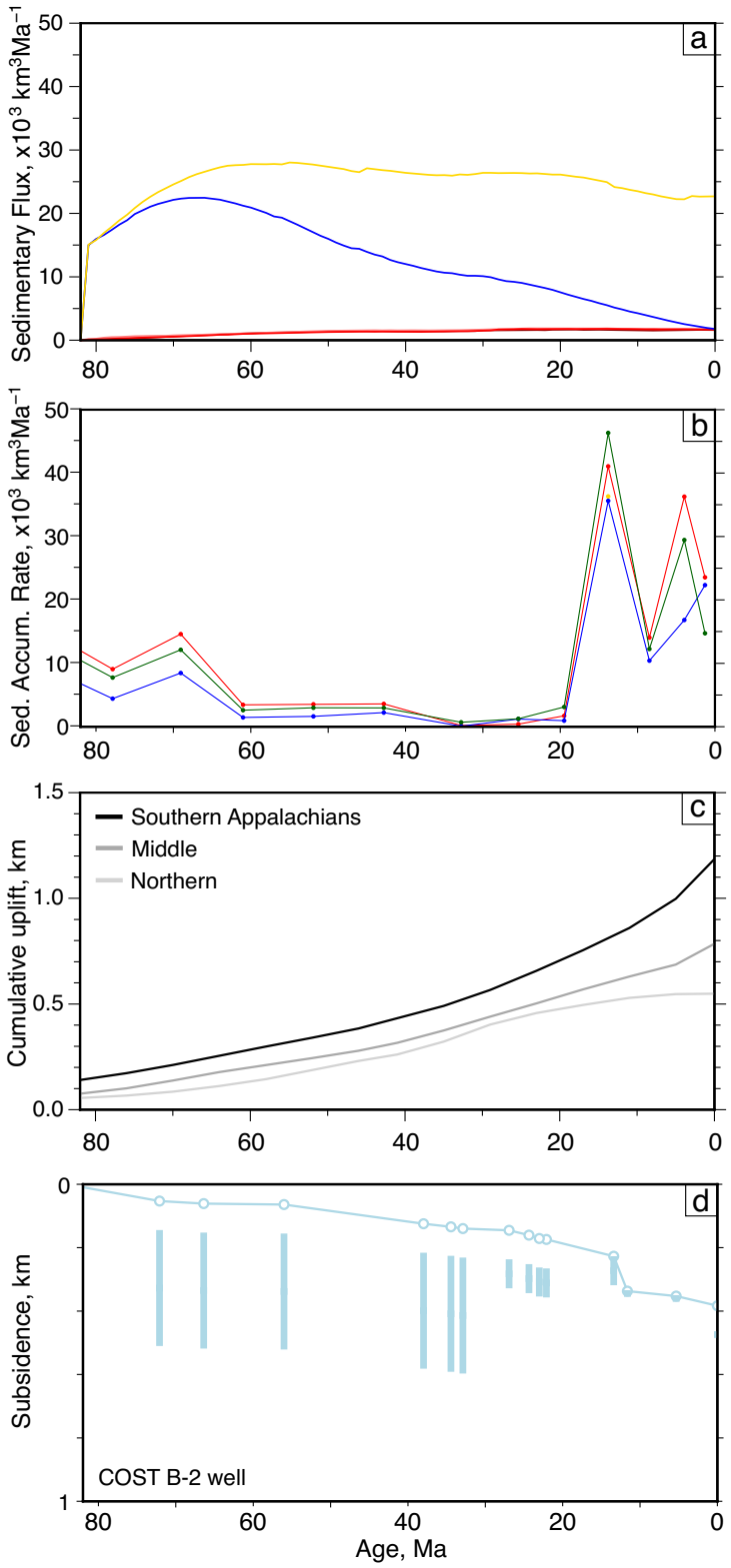

Figure 4.31: **Predicted and observed sedimentary flux, uplift and subsidence of the North American middle Atlantic margin** (a) Sedimentary flux from landscape evolution models over the last 82 Ma from the three presented model scenarios. Red curve = model (1), blue curve = model (2), yellow curve = model (3); (b) Sediment accumulation rate in BCT from mapped sediment volumes, Figure 4.26; (c) Uplift history of the Appalachian Mountains from inversion of river profiles, shown in Figures 3.18 & 3.20; (d) Campanian to Recent water-loaded subsidence history of the COST B-2 well, Figure 4.5.

to relatively flat elevations by 23 Ma, drainage patterns are fixed in space and time, total denudation follows the patterns of the original topography, and the sedimentary flux slowly decays over time. Model (2) predicts a peak in the flux at $\sim$ 70 Ma, and a steady decay to present-day flux similar to that predicted from scenario (1). Model (3) generates the highest denudation in the Appalachian Mountains, with a notable increase in the denudation of the Middle Appalachians in the last 23 Myr, although most denudation is focused in the southern portion of the mountain belt (Figure 4.30c). Predicted sedimentary flux is between 20 and 30 km^3Ma^{-1} throughout the model run time. Other than between 70–80 Ma, the model does not produce any significant, order of magnitude changes in the flux to the margin. Observed flux remains relatively constant over the Neogene period, with only a minor decrease in the Middle Miocene.

In summary, none of the model scenarios are capable of generating a 30–40 km^3Ma^{-1} increase in sedimentary flux to the BCT in the Neogene. Instead, all models predict a relatively stable flux of sediments to the basin, with either a steadily increasing or decreasing trend.

4.4.4 Causes for data-model mismatch

There are various possible reasons for the observed mismatch between the sediment accumulation rate and predicted sedimentary flux to the BCT. I will explore further two potential causes. First, I discuss whether the sediment accumulation data is representative of changes in the delivery of clastic sediments by rivers. Second, I consider whether the landscape evolution model is too simplistic.

External sources of sediment?

It is often inferred that Neogene clastic sedimentary rock hosted in the BCT was sourced from the Appalachian Mountains, generated as a consequence of enhanced erosion due to Miocene uplift, drainage capture events, or changes in climate (cf. *Poag and Sevon*, 1989; *Monteverde et al.*, 2008; *Moodie et al.*, 2017; *Steckler et al.*, 1999). One potential caveat is if the large volumes of Neogene sediment deposited in the BCT, particularly during the Middle Miocene, were sourced from several different regions, including areas outside the Atlantic margin. Interpretation of well-tied seismic sections across the Blake Plateau, offshore South Carolina, indicate an abbreviated Cenozoic sedimentary section, suggesting the continental shelf to the south of the BCT has been extensively scoured by the north-flowing Gulf Stream (*Pinet and Popenoe*, 1982, 1985; Dillon et al., 1990). If the sediments eroded off the Blake Plateau were subsequently deposited in the deeper portions of the BCT, a simple source-to-sink correlation of BCT sediments to Appalachian river sediment flux might not be so straightforward.

Additionally, quantifying how much sediment has been eroded from the BCT and deposited in sinks that lie outside of our study area provides an additional challenge. Correcting for these types of uncertainties, especially those relating to reworking, sediment bypass or alternative sediment sources, are intractable in an objective manner, and cannot be adequately tackled without a provenance analysis of basin sediments.

Is the model too simple?

The landscape evolution model purposefully did not include processes, other than uplift, that might play a key role in the geomorphic evolution of this region. Processes related to glacio-isostatic unloading or glacial erosion since the last glacial maximum were not considered. Effects of glacial erosion would be isolated to the northernmost sections of the model space in the Susquehanna River catchment, so probably reasonable to consider fluvial erosion only (*Clark and Ciolkosz*, 1988; *Braun*, 1989). However, modelling of glacial isostatic adjustments related to the demise of the Laurentide ice sheet suggests rivers in the Northern Appalachian Mountains might have been significantly affected by these processes (e.g., *Pico et al.*, 2019; *Ruetenik et al.*, 2019). I have also not considered changes in climate over the Neogene period, such as global cooling since the Middle Miocene (e.g., *Zachos et al.*, 2001). Changes in climate, particularly precipitation rates, can alter landscapes and erosion rates, however exactly how precipitation rates have varied in eastern North America over the Cenozoic is not known (*Molnar*, 2004; *Hoomehr et al.*, 2016). However, quantitative paleoclimatic reconstructions of the Middle Miocene Climactic Optimum using palinological analsysis from ODP wells drilled in the BCT suggest that the regional climate in the central Appalachian Mountains did not significantly change over that period. This suggests assuming a spatially and temporally uniform precipitation rate is a reasonable assumption, and changes in climate did not play a significant role in generating the increased sedimentary flux in the Middle Miocene. The LEM does not include short term active coastal and near-shore processes that reshape the deltas and shorelines and transport sediment off-the shelf into deeper water. As suggested by the sedimentation and erosional history of the Blake Plateau, coastal processes and marine currents might be important and key to explain the observed patterns of sedimentation (*Pinet and Popenoe*, 1985). The model is defined as being purely erosive, such that sediments are not allowed to deposit along the river flow length. Given the small volumes of onshore sediment deposition in present-day unglaciated Appalachian rivers, this assumption is probably reasonable (e.g., *Taylor and Kite*, 2006).

Finally, the LEM used in this study does not include a flexural response of the lithosphere to the

redistribution of surface loads. *Moucha and Ruetenik* (2017) modelled the evolution of the eastern margin of North America over the last 3.5 Ma using a LEM which solved for flexural-isostatic deformation on an thin, infinite elastic plate overlying an inviscid mantle. Their model was forced with a history of dynamic uplift and subsidence, and the resulting topography compared to the present day elevation of a well-studied Pliocene sea-level marker (Orangeburg Scarp). They concluded that the Pliocene to Recent deformation of the US East coast is the result of sup-plate support and flexural response to sediment loading/unloading, and that dynamic alone, without flexure, cannot explain the observed topographic patterns. It is therefore possible that, without including a flexural component to the LEM, the observed sedimentary flux to the BCT cannot be explained.

4.4.5 Implications for Neogene topographic growth of the Appalachian Mountains

Maximum Neogene sediment accumulation rate in BCT is 41×10^3 km^3 Ma^{-1}, deposited during the Middle Miocene. By applying a bulk correction for an average layer porosity of 50%, a conservative estimate, the the solid sediment flux is estimated as $\sim 20.5 \times 10^3$ km^3 Ma^{-1}. This value is a lower bound estimate of the flux. I acknowledge that re-picking the seismic data, depth converting using an appropriate velocity model, and basin-wide decompaction of sediment volumes would generate more accurate estimates.

The present-day area of Appalachian catchments draining to the BCT is $\sim 250 \times 10^3$ km^2. Combining these values of solid sedimentary flux and drainage area would imply an average, uniform denudation rate of 80 m Ma^{-1}, similar to the rates calculated by *Pazzaglia and Brandon* (1996). This rate is $\sim 40 - 60$ m Ma^{-1} higher than present fluvial incision rates, catchment average erosion rates, and long-term denudation rates from thermochronology (Figure 4.20). The predicted Appalachian denudation rate would be significantly higher if landscape denudation was not assumed to be uniform over the catchment area. Sustaining a uniform rate of 80 m Ma^{-1} over the duration of the Middle Miocene (4.34 Ma) would result in ~ 350 m of denudation over the central Appalachians and Coastal Plain. This value similar to the total uplift predicted by the inverse model over the last 20 Ma. It is then perhaps unsurprising that the uplift history shown in Chapter 3 could not predict the observed sediment flux to the BCT. Generation of such large incision rates would require a dramatic change during the Middle Miocene, either climate, tectonics, or mantle dynamics, and remains to be further explored.

Chapter 5

Discussion

5.1 General Conclusions

In Chapter 2, I addressed objectives 1 of this thesis by generating an inventory of 24,372 measurements of Cretaceous to Recent net uplift. The measurements were generated by combining records of Cretaceous to Recent marine rock in the Paleobiology Database (PBDB) with estimates of elevation, paleobathymetry, compaction, and global sea-level change. In some places the inventory is sufficiently dense that wavelengths and amplitudes of regional uplift can be constrained (e.g., western North America). In other places, sparse measurements provide useful bounds on topographic evolution (e.g., Borborema province, Brazil). Less than 1% of the records in the PBDB required manual modification to correct erroneously located samples. A larger effort was required to check the quality of paleo-water depth and paleoenvironment records. To address objective 2 of the thesis, I combines points from western North America and the Borborema province with seismological observations and simple isostatic calculations to investigate the origins of topography in western North America and northeast Brazil. In these regions, post-Cretaceous net uplift has amplitudes up to ~ 1 km at wavelengths of $100 - 1000$ km. The results indicate that spot measurements of uplifted marine rock aid understanding of sub-continental mantle dynamics and mantle-surface interactions. The inventory of uplift measurements might also provide useful constraints on paleo-environmental, -climatic and -biologic evolution.

Chapter 3 uses these biostratigraphic constraints on net uplift to investigate the large-scale evolution of the North American landscape from the Late Cretaceous to present-day. Uplift measurements from the paleobioloigcal database is supplemented by including outcrops of regressive (marine to terrestrial)

stratigraphic sequences. Average uplift rates estimated from fossil and stratigraphic data suggest that, following the retreat of the Western Interior Seaway at $\sim$ 80 Ma, western North America experienced staged uplift of up to 3 km. The Yukon, Appalachian Mountains and Mexico mostly underwent Neogene uplift. I addressed thesis objective 3 by inverting 4161 longitudinal river profiles, assuming a simplified version of the widely used stream power relationship, I have generated a smooth spatio-temporal uplift history that fills the gaps between spot stratigraphic and biostratigraphic constraints. Mapped drainage planforms indicate that North American rivers flow radially from large-scale swells, which have wavelengths of the order 100–1000 km. The principal swells are centred on the Colorado-Columbia-Rocky Mountains plateaus, Yukon, Appalachians and Mexico where sub-plate dynamic support is important. Predicted regional uplift rates of the Colorado-Columbia-Rocky Mountains plateaus increased from $\sim$ 0.02 mm a^{-1} between 80 and 50 Ma to $\sim$ 0.1 mm a^{-1} between 30 Ma and the present day. To address objective 4, to estimate denudation and to examine sensitivities of drainage patterns to tectonic forcing I parameterized the Badlands landscape evolution model using the inverted uplift history. The results of this forward simulation are compared with a synthesis of independent estimates of denudation from thermochronometric studies, and with continent-wide provenance analyses.

Several significant implications are apparent. First, substantial compilations of stratigraphic observations can be used to gauge uplift and denudation rates at large length and timescales. Secondly, drainage patterns can be inverted by assuming a simplified version of the stream power relationship despite the apparent complexity of eroding landscapes. This modelling approach provides a useful and reproducible way of constraining uplift histories on continental scales. Finally, measured and calculated uplift and denudation histories are consistent with Cenozoic sub-plate support which seems to have played a defining role in generating the North American landscape, especially at wavelengths greater than a few tens of kilometres.

In Chapter 4, I focused on the evolution of the eastern margin of North America. To address objective 5, a subsidence history for the Baltimore Canyon Trough Basin was calculated by backstripping of twenty seven wells along the margin. Results showed that Neogene water-loaded subsidence was up to $\sim$ 600 m in the basin. This subsidence history cannot be readily explained by post-rift thermal subsidence, post-rift stretching or flexure. In contrast, Neogene subsidence of the adjacent continental shelf, on the Georges Bank and Southeast Georgia Embayment, can be explained by simple post-rift lithospheric cooling. Seismic lines in the Baltimore Canyon Trough and Georges Bank show thick

($\sim$ 1 km) and thin ($<$ 200 m) Neogene sequences, respectively. Progradational and aggradational Neogene clinoforms in the Baltimore Canyon Trough reflect rapid generation of accommodation space and subsequent filling between $\sim$ 20–0 Ma. The amplitude of subsidence and its spatial localisation rules out eustasy as the sole contributor to the generation of accommodation space. Correlation with free-air gravity anomalies, shear wave tomography velocities and isostatic calculations indicate that temperature variations in the uppermost convecting mantle are able to generate sufficient density anomalies to drawdown the New Jersey margin. The patterns of sub-plate driven subsidence are similar to observations of ocean age-depth measurements, and suggest that the Baltimore Canyon Trough has been drawn down by up to $\sim$ 600 m since $\sim$ 20 Ma. Upper mantle convection appears to play an important role in generating accommodation space along this passive margin.

Finally, I addressed objective 6 by examining the sediment accumulation history in the Baltimore Canyon Trough, and how it might be linked to Neogene uplift of the Appalachian Mountains. The thickness of sedimentary sections recorded at each well shows that the Middle Miocene increase in water-loaded subsidence was accompanied by an order of magnitude increase in sediment accumulation rate in the basin. Notwithstanding the uncertainties in the data, volumetric estimates of sediment accumulation also suggest the rate of sediment delivered to the basin dramatically increased in Neogene times. If the source of sediment is solely the erosion of the Appalachian Mountains by eastward-draining catchments, this increase in sediment accumulation implies an increased source region erosion rates. I use the landscape evolution model from Chapter 3, forced by different uplift histories and initial conditions, to investigate possible causes of increased sedimentary flux. Of the modelled scenarios, whether a steadily eroding paleo-landscape in the absence of uplift, or forced with the uplift history derived in Chapter 3, none could generate the observed increase in sedimentary flux to the Baltimore Canyon Trough. These results suggest the large volumes Middle Miocene sediment might not be sourced from the Appalachian Mountains, or my models are too simplistic to model the observed increase in sediment flux.

5.2 Cross-cutting Themes

Several themes arise that are common to the three research chapters of this dissertation, which I further discuss in the sections below. First is the use of different methods to measure vertical motions, where each has their own advantages and caveats. Second, although constraining histories of vertical motion of the Earth's surface through space and time is important for a number of reasons, I have

used it as a means to understand the contributions of sub-plate processes to the growth of continental topography. To do so, measurements of surface uplift were made on length-scales > 100 km, where signals of mantle convection may be detected. Thirdly, I have explored existing databases, and re-visited published data, to generate new constraints on sub-plate support. Finally, I focused on North America as the main case-study for assessing the success of the three methods because of its vast spatial extent, the presence of continental-scale marine sedimentary deposits, the presence of large fluvial catchments draining most of the landmass, and the availability of big data inventories. The size and diversity of geological terranes of the North American continent has resulted in a rich history of publications, which has allowed the compilation of data covering a large geographical area. In other parts of the world, as is exemplified in Chapter 2 by the Borborema Province, the available data is more sparse.

5.2.1 Different methods for measuring vertical motions of the Earth's surface

Paleobiological databases

The first methodology, described in Chapter 2, makes use of paleobiological information recorded in an existing database to measure the net uplift of continents from the Late Cretaceous to Recent. This method makes use of geological 'big data' to measure global surface uplift at scales pertinent to mantle convection, and is useful because marine fossils have been extensively identified and mapped around the globe. Mapping uplift using this methodology is only possible because of the recent effort of the paleontological community, who have expended much time and effort to generate the Paleobiology Database, and have made the data easily accessible. These point measurements of surface uplift could have been significantly limited if not for the database.

Notwithstanding the global coverage and advantages of the method, there are instances where it cannot be used to reliably measure net continental uplift. For example, the measurements cannot resolve changes in surface uplift when the uncertainty outweighs the signal. For example, deep marine fossils have an inherently large range in of paleo-water depth uncertainties. This uncertainty can be even larger when required to correct for the compaction of very large thicknesses of underlying sediments. My work underlines the need for recording precise estimates of paleo-water depths, particularly for the PBDB. Many of the marine fossil assemblages in the PBDB are recorded generically as 'marine'. In these cases, additional work is required to independently constrain the paleo-water depth range of the deposit, which makes using the database not so straightforward. I wish to stress the general problem

that is attributing quantitative paleo-water depth estimates to descriptions of paleoenvironments, and my work provides one way of tackling this issue.

Additionally, the precision of the methodology decreases when used to measure net uplift since periods before the Cretaceous. In principle, one could measure uplift further back in time than the Cretaceous, but there are two major drawbacks to doing so. First, the method is limited to where continents have been inundated by marine waters, and the Mid to Late Cretaceous was the last time continental interiors were flooded on a large scale. Secondly, the completeness of the sedimentary record is more unknown the further back in time, thus increasing the methodological uncertainty to the point that it does not provide any insightful information.

As was done for the North American continent in Chapter 3, compilations of marine to terrestrial transitions recorded in outcropping sedimentary sequences, or markers of paleo-strandlines (e.g., *Lillegraven and Ostresh Jr.*, 1990), could be compiled to compliment measurements from the PBDB. The difficulty in increasing this database is that paleo-sea level or paleobathymetric markers are often qualitatively, rather than quantitatively recorded in the geological literature. Additionally, it relies on the existence of high-resolution geological maps, extensive sedimentological descriptions of the outcropping units and their lateral variability, and a well-established regional chronostratigraphy. All these requirements were met by the sedimentary deposits of the western interior of North America, but is not the case for all regions of the globe.

Fluvial inverse and forward modelling

The second method I used to investigate continental vertical motions is the inverse and forward modelling of fluvial erosion. These methods make use of quantitative relationships between uplift, erosion and the spatio-temporal evolution of rivers through the stream power law. Inversion of river longitudinal profiles for uplift is not uncontroversial, and the major pitfalls of the methodology have been outlined in Section 3.5. There is no general agreement on the value of erosional parameters or their relative importance when modelling rivers at continental-scales. This issue is pertinent to both forward and inverse models. Inverting river profiles for an uplift history, in the manner performed in this study, requires the assumption that drainage patterns have remained fixed over time. This assumption has been highly debated, especially in light of the recent publications that use the stream power law equation to infer drainage divide instability (e.g., *Willett et al.*, 2014). It also does not account for the role of changes in climate or the effect of glacial erosion, both of which have been

known to affect landscapes in quite dramatic ways (e.g., *Wickert*, 2016).

The primary advantage of inverting longitudinal river profiles for a best-fitting, smooth uplift rate history is that it can be performed on any landscape that is drained by rivers. This generally circumvents the limitation of measuring uplift from paleobiological data, as it is not limited to regions where marine sedimentary rock is preserved. Secondly, it is not limited to any spatial scale, as long as the model resolution is appropriate to the length-scales of interest. For example, the shapes of river profiles can be used to investigate the uplift history in smaller regions shaped by active slip of individual faults, or larger areas where epeirogenic uplift driven by mantle convection has driven surface uplift. Both forward and inverse modelling of rivers make testable predictions that can be compared to geological data, as well as fill in the gaps between spot measurements of uplift, denudation or topographic change, as has been done in Chapter 3. Different datasets were used to assess the resulting inverse and forward models, and a discussion of how the model-data fit could be improved is warranted.

The rock uplift history from the inversion was compared to net uplift calculated from paleobiological and stratigraphic data, which generated broadly a good fit between model and observations. Despite the generally good fit of the data when errors are included, the model still show some discrepancies with respect to some data points (i.e., not all points fall exactly on the 1:1 line). There are a few reasons that could account for this discrepancy. First, the maximum uplift that can be modelled by the inverse model is limited by the highest elevation of the river profiles, yet the actual rock uplift a region has experienced must have been higher as the interfluve regions stand higher than the river valleys. This is a model limitation and might explain why some data points are under-predicted by the model.Secondly, the erodibility value used was calibrated using a single incision measurement from the Colorado River, which is difficult to reconcile for a model that spans a whole continent. It is then perhaps unsurprising that some data points are better fit by models that use a different erodibility value (v). By varying the value of v by a factor of 2 reduces the global fit of the model to the data, but better matches parts of the dataset that were previously showed a larger misfit. For simplicity, the model assumes a temporally and spatially uniform erodibility value, and including a spatially variable v might possibly reduce the misfit between model and data. Finally, the model resolution and imposed smoothness might not capture smaller-scale processes, such as faulting, that might be responsible for spatially abrupt increases in uplift. These smaller scale processes would be captured by the stratigraphic offset of the data, but not the model. However, as previously discussed in Chapter

3, the global best-fit to the data is achieved by a moderate smoothing parameter.

The predicted denudation history from the landscape evolution model was compared to denudation estimates from low-temperature thermochronology data (AFTA, A-He), and sedimentary flux to sediment volumes from isopach maps of the Gulf of Mexico Basin. Although the model matched most data points within error, all the data appears to be systematically under-predicted by the model, with the data-model mismatch increasing for younger samples. Therefore the model does not predict sufficient denudation of North America. The model also predicts an overall increasing sedimentary flux to the Gulf of Mexico over the Cenozoic, matching the overall data trend, but fails to produce the large peak in sediment accumulation associated with the deposition of the Wilcox Group in Paleocene-Eocene times. Here I explore several reasons for the resulting data-model mismatch.

Firstly, the lack of a high initial topography in forward model will systematically under-predict both the maximum denudation and early spikes in sedimentary flux. It is important to emphasise that the uplift history modelled by the inversion inversion, which drives the landscape evolution model, does not make predictions about the initial topography of North America and does not preclude the existence of higher paleo-topography in Cretaceous times. Rather it only predicts small amounts of uplift in Cretaceous times, which is likely an under-prediction due to the reduced coverage at these time-steps. The result from the inversion is an uplift history, and the model makes no prediction about the initial topography of North America. The forward landscape evolution models were run using an initial topography with extremely low initial elevation and relief. Additionally, the forward model was forced with negligible uplift from 82 to $\sim$ 65 Ma. The combination of a small initial topography and little initial uplift mean the model would not have sufficient erosive power to generate a larger denudation and, consequently, a larger flux of sediments in the early time-steps. The importance of initial topography to the predicted sedimentary flux from the Badlands model is highlighted in Chapter 4, Section 4.4, where the predicted flux is shown to increase by multiple orders of magnitude with the inclusion of an initial topography. Secondly, as discussed for the mismatch between the observed and predicted uplift, the limit on maximum predicted uplift imposed by the elevation of the head of river catchment will also systematically decrease the predicted denudation and sedimentary flux, irrespective of the temporal model coverage. Finally, as reviewed in Chapter 3, the sensitivity of AFTA and A-He data to short-wavelength processes and the smooth nature of the landscape evolution model means there will be an inherent mismatch between the data and model.

In this dissertation, I have shown that this type of inverse modelling of river longitudinal profiles

can generate uplift histories that are broadly in agreement with independent geological constraints. These models can provide useful, first order estimates of the timing and spatial distribution of uplift on continents. Combining these uplift histories with forward landscape evolution models, as well as other datasets, provides a pragmatic way of exploring how the Earth's surface evolves over time.

Subsidence analysis

Lastly, I used the well-known method of backstripping to look at the negative vertical motions of the Earth's surface, i.e. subsidence, along the eastern passive margin of North America. Models that focus on the tectonic causes of subsidence have successfully described observed subsidence patterns in many rift basins, and allowed for critical insight into the formation of these geological features (e.g., *McKenzie*, 1978). The success of these kinematic models of basin evolution have allowed the geoscientific community to explore possible causes for the departure of observed subsidence from these models. For example, *Kominz et al.* (1998), *Miller* (2005), and others, have explained departures from the expected model behaviour at the New Jersey margin as a consequence of eustatic sea-level changes. In contrast, the geodynamic modelling community has emphasised the importance of sub-plate processes in the evolution of passive margins, and that there is 'no such thing as a stable continental platform' (e.g., *Moucha et al.*, 2008). One solution to reconcile these two approaches would be to correct eustatic sea-level curves using predictions from geodynamic models (e.g., *Kominz et al.*, 2016). However, geodynamic models are variable in their predictions of timing, amplitude and polarity of vertical motions, making such corrections not straightforward (e.g., *Müller et al.*, 2008; *Moucha et al.*, 2008; *Spasojević et al.*, 2008; *Flament et al.*, 2013; *Steinberger et al.*, 2019).

For the Baltimore Canyon Trough, I explain departures from the expected post-rift thermal subsidence as caused by sub-plate processes. The timing, magnitude and wavelength of the observed subsidence patterns are better explained by an increased in subsidence caused by the presence of cooler than average asthenospheric mantle, rather than changes in eustatic sea level. Despite the apparent success of this methodology, also adopted by *Czarnota et al.* (2013) and *Lodhia et al.* (2018), it has significant limitations, which I outline in turn. First, the observable patterns of subsidence are limited by the temporal resolution. For example, some of the wells did not report any age constraints for the Cenozoic, making it difficult to infer changes in subsidence or sedimentation. Secondly, the lack of adequate age constraints on the timing of rifting, and it's duration, limit the accuracy and precision of the model of tectonic subsidence. This information is crucial for an adequate parameterisation of a rift model that can predict the rate and amount of expected post-rift thermal cooling of a margin, which forms the

basis for identifying anomalous subsidence events (*McKenzie*, 1978). This is the case for the BCT, where no wells drilled have reached the basement, and is an issue pertinent to identifying both sub-plate support and eustatic sea level changes from subsidence curves. Thirdly, similar to using marine fossils to constrain uplift histories of continents (Chapter 2), uncertainty in paleo-water depth are the major sources of error. Large ranges in paleo-water depth estimates make it difficult to confidently pick out signals that are of the same magnitude as the uncertainty. This is particularly problematical for deep-sea deposits, where the uncertainty is very large and often difficult to constrain (e.g., bathyal environments). Finally, subsidence analysis provides no insight into periods of basin uplift. If such periods of uplift have occurred, they can be recorded as unconformities, but the exact timing and magnitude of events cannot be constrained. In some cases, subsidence analysis can be combined with other in information contained in well data, such as porosity-depth relationships, to infer denudation and large-scale epeirogenic uplift of passive margins (e.g., *Walford and White*, 2005).

5.2.2 What about tectonics?

Different geological processes can generate vertical motions of the Earth's surface, and in this dissertation I have chosen to focus on the role of sub-plate support in generating topography, specifically thermal anomalies in the shallow asthenospheric mantle. Despite not being explicitly addressed, I recognise tectonic structures exert a first order control on the evolution of large tracts of continental topography. For example, 'Laramide' thrust faults with kilometre-scale displacements, as picked out by stratigraphic offsets, have played a principal role in the development of the Rocky Mountains and the formation of intramontane flexural basins (e.g., *Cross*, 1986; *DeCelles*, 2004). Rifting of the North Atlantic exerted a primary control on the development of the Baltimore Canyon Trough Basin, where crustal thinning by normal fault displacement determined the timing and patterns of maximum subsidence (*Steckler and Watts*, 1978; *Grow et al.*, 1988). The methods I employed to quantify vertical motions of the Earth's surface can be, and have been, extensively used to understand rates of structural growth related to tectonic deformation (*Sclater and Christie*, 1980; *Nicol et al.*, 1997; *Woodward et al.*, 1997; *Whittaker et al.*, 2008; *Boulton and Whittaker*, 2009; *Seeber et al.*, 2006). These methods can also be used to look at regions where both tectonics and mantle dynamics exert principal controls on the evolution of topography (e.g., *Schildgen et al.*, 2012; *Rodríguez Tribaldos et al.*, 2017).

A key challenge is to determine the spatial scale of interest, and what methods are appropriate to the problem at hand. All of the methods I used to look at large-scale processes could also be used to resolve at local changes in vertical motion. However the resolution required to tackle smaller-scale

problems is significantly higher, which requires a more detailed approach. When trying to answer geodynamic or macro-scale tectonic questions, it is important to generate enough observations that span the spatial and temporal scales of interest. For example, within a single measurement of net uplift using the PBDB, there is too much complexity in the processes governing the exact measurement such that it cannot provide significant insight on lager scale geodynamic or tectonic problems. Conversely, it is crucial to understand how local processes might scale up to affect measurements of vertical on a larges scale. A key example of this dilemma is the role of lithology in controlling the shapes of rivers, and how lithologically-controlled erosion rates might shape landscape evolution on an orogen scale (e.g., Campforts et al., 2020). Determining rock strengths of individual lithologies, and how they relate to the shapes of rivers, can only be achieved through fieldwork (i.e., small scale studies). But, to meaningfully resolve how lithology scales up to continental length-scales requires large numbers of small-scale studies that can be brought together to understand the big picture. These considerations emphasise the importance of the work presented in this dissertation, which have made much use of large data compilations over a range of temporal and spatial scales.

5.3 Future Work

In this section I will discuss three possible lines of future research arising from the results of this dissertation.

First, the inventory of net uplift, presented in Chapter 2, may be used to constrain uplift histories in other regions, and explore how these relate to the evolution of tectonic and sub-plate processes. One particular area of interest is northern Africa, particularly the evolution of the Hoggar and Tibesti domes. Mantle temperature estimates from geochemical inverse modelling of major elements in volcanic rocks from the Tibesti province suggest that sub-plate temperature is a primary control in the generation of mafic volcanism in the region (*Ball et al.*, 2019). The presence of thermally-induced volcanism, combined with the occurrence of low shear-wave velocity anomalies beneath the region, suggest that asthenospheric buoyancy anomalies might play a significant role in generating the observed topographic swell (*Schaeffer and Lebedev*, 2013; *Ball et al.*, 2019). The uplift history of this regions has mostly been described in terms of ages of magmatic eruptions (e.g., *Deniel et al.*, 2015). From the distribution of Cretaceous marine deposits, *Sahagian* (1988) recognised that the Tibesti region has been uplifted in post-Cenomanian times, but did not further constrain the magnitude or timing of Cenozoic surface uplift. Using the database developed in Chapter 2, the net uplift measured

using the PBDB hosts Late Cretaceous–Paleocene marine fossils that would provide novel constraints on the timing of topographic growth of the region.

Secondly, following from the results of Chapter 4, it is possible that the subsidence histories at passive margins around the world can be jointly used to investigate the time-dependent behaviour of mantle convection. Recent work by *Austermann et al.* (2017) and (*Hoggard et al.*, 2016) highlight the importance of global-scale datasets for investigating mantle behaviour. Generating a global dataset of passive margin subsidence by backstripping published well reports, such as those from the Ocean Drilling Project, and compiling published data (e.g., *Czarnota et al.*, 2013; *Lodhia et al.*, 2018), could provide key constraints on the tempo and amplitude of global mantle convection as expressed at passive margins. Such a study could provide important constraints on the rate of mantle convection on timescales longer than glacial-interglacial cycles. Following one of the general themes of this dissertation, compiling the results from existing studies to generate an initial database would provide a starting point. Additionally, publicly available well databases such as the International Ocean Drilling Data Archive could help populate the dataset, as well as identify regional gaps.

Finally, building on the second part of Chapter 4, it is clear that Neogene uplift of the Appalachians, and whether or not it is required to explain the increase in sediment flux to the Baltimore Canyon Trough, is still an unresolved problem. A key challenge is to reconcile the histories of erosion from modelling with those observed in the sedimentary record of passive margins. For the specific case of the eastern margin of North America, there are two possible routes to follow. The first is to obtain accurate sediment accumulation estimates from the Baltimore Canyon Trough. This requires the re-interpretation of seismic data, depth conversion using an appropriate velocity model, and a spatially variable porosity correction. Using modern software and techniques, and with the inclusion of additional wells, it would be possible to improve the accuracy and precision of the original estimates of *Poag and Sevon* (1989). Having well-constrained sediment thickness maps, and a formal analysis of the data resolution, would also allow 3D backstripping, as well as reconstruction of basin-floor geometries over time. A second route is to further explore the parameter space of the landscape evolution model. In this dissertation, I looked at three possible model scenarios using a simple parameterisation of the erosional model. Different uplift histories and initial conditions could be tested, as well as the inclusion of different model features, such as the flexural response of the lithosphere to the redistribution of surface loads. Additionally, the landscape evolution model can be used to predict the stratigraphic evolution of the margin (e.g., *Salles et al.*, 2018). These predictions can be directly compared to

sediment thickness maps. Other methods of predicting sediment flux, such as the BQART model, could be included in the analysis. In this light, I wish to highlight the importance of well constrained geological observations for the assessment of landscape evolution models: the success of a model is only as good as the data used to test it. Finally, sediment provenance studies of the Middle Miocene deep-sea sedimentary deposits of the basin might shed light on the origin of these sediments, and whether they can indeed be attributed to a pulse in erosion of the Appalachians or transported from the south by the Gulf Stream.

Bibliography

Aciego, S.M., DePaolo, D.J., Kennedy, B.M., Lamb, M.P., Sims, K.W., and Dietrich, W.E. (2007). Combining ^{3}He cosmogenic dating with U–Th/He eruption ages using olivine in basalt, *Earth and Planetary Science Letters*, *254*(3–4), 288–302, doi:10.1016/j.epsl.2006.11.039.

Adegoke, O.S., Oyebamiji, A.S., Edet, J.J., Osterloff, P.L., and Ulu, O.K., eds. (2017). Foraminifera and Calcareous Nannofossil Biostratigraphy of the Niger Delta, Chapter 5 - Paleoenvironmental Synthesis, Elsevier, Oxford, UK, 129–144.

Ainsworth, N.R., Riley, L., Bailey, H.W., and Gueinn, K.J. (2014). Cretaceous–Tertiary stratigraphy of the Labrador Shelf, *Riley Geoscience Ltd.*, commissioned by Nalcor Energy, http://www.nalcorenergy.com/ OILGAS/labrador-biostratigraphy.asp

Allen, J.R.L. (1970). Sediments of the modern Niger delta: a summary and review, *in* Morgan, J. P. eds. Deltaic Sedimentation, Modern and Ancient, *Special Publications of SEPM*, pp. 138.

Allen, P.A., and Allen, J.R. (2005). Basin Analysis – Principles and Analysis, 2nd edition. Blackwell Science Ltd, p.73.

Allen, G.H., Barnes, J.B., Pavelsky, T.M., and Kirby, E. (2013). Lithologic and tectonic controls on bedrock channel form at the northwest Himalayan front, *Journal of Geophysical Research: Earth Surface*, *118*(3), 1806–1825, doi:10.1002/jgrf.20113.

Amante, C., and Eakins, B.W. (2009). ETOPO1 1 Arc-minute global relief model: procedures, data sources and analysis: NOAA Technical Memorandum NESDIS NGDC-24, National Geophysical Data Center, NOAA, *10*, V5C8276M.

Amidon, W.H., Roden-Tice, M., Anderson, A.J., McKeon, R.E., and Shuster, D.L. (2016). Late Cretaceous unroofing of the White Mountains, New Hampshire, USA: An episode of passive margin rejuvenation?, *Geology*, *44*(6), 415–418, doi:10.1130/G37429.1.

Anderson, R.S., and Anderson, S.P. (2010). Geomorphology: The mechanics and chemistry of landscapes: Cambridge University Press.

Antonioli, L., Thiago, L.K., Rodrigues, M.A.C, and Dino, R. (1999). Análise palinoestratigráfica dos sedimentos Aptianos da Bacia do Parnaíba, aflorantes na região de Codó, MA, *Boletim de Resumos do Congresso Brasileiro de Paleontologia*, Abstracts, *16*, 18–19.

Arai, M., and Coimbra, J.C. (1990). Análise paleoecológica do registro das primeiras ingressões marinhas na Formação Santana (Cretáceo Inferior da Chapada do Araripe), 1° *Simpósio da Bacia do Araripe e Bacias Interiores do Nordeste - Atas. SBG*, Crato-CE, Brazil, p. 225–240.

Arai, M. (2009). Paleogeografia do Atlântico Sul no Aptiano: um novo modelo a partir de dados micropaleontológicos recentes, *Boletim de Geociências – Petrobras*, *17*2, 331–351.

Armitage, J. J., and P. A. Allen (2010), Cratonic basins and the long-term subsidence history of continental interiors, *Journal of the Geological Society London.*, *167*(1), 61–70, doi:10.1144/0016-76492009-108.

Armitage, J.J., Whittaker, A.C., Zakari, M., and Campforts, B. (2018). Numerical modelling of landscape and sediment flux response to precipitation rate change, *Earth Surface Dynamics*, *6*, 77–99, doi:10.5194/esurf-6-77-2018.

Arnould, M., Coltice, N., Flament, N., Seigneur, V., and Müller, R.D. (2018). On the scales of dynamic topography in whole-mantle convection models, *Geochemistry, Geophysics, Geosystems*, *19*(9), 3140–3163, doi:10.1029/2018GC007516.

Arthur, M.A., and Sageman, B.B. (2004). Sea-level control on source-rock development: Perspectives from the Holocene Black Sea, the Mid-Cretaceous Western Interior Basin of North America, and the Late Devonian Appalachian Basin, *SEPM Special Publication*, *82*, 35–59.

Athy, L.F. (1930). Density, porosity, and compaction of sedimentary rocks, *AAPG Bulletin*, *14*1, 1–24.

Attal, M., Tucker, G.E., Whittaker, A.C., Cowie, P.A., and Roberts, G.P. (2008). Modelling fluvial incision and transient landscape evolution: Influence of dynamic channel adjustment, *Journal of Geophysical Research: Earth Surface*, *113*, 1–16, doi:10.1029/2007JF000893.

Assine, M.L. (1994). Paleocorrentes e paleogeografia da Bacia do Araripe, nordeste do Brasil, *Revista Brasileira de Geociências*, 244, 223–232.

Assine, M.L. (2007). Bacia do Araripe, *Boletim de Geociências da Petrobras, Rio de Janeiro*, *15*2, 371–389.

Audet, P., Bürgmann, R., (2011). Toward mapping the effective elastic thickness of planetary lithospheres from a spherical wavelet analysis of gravity and topography, *Nature Geoscience*, *4*, 48–82.

Audet, P. (2014). Toward mapping the effective elastic thickness of planetary lithospheres from a spherical wavelet analysis of gravity and topography, *Physics of the Earth and Planetary Interiors*, *226*, 48–82, doi:10.1016/j.pepi.2013.09.011.

Ault, A.K., Flowers, R.M., and Bowring, S.A. (2013). Phanerozoic surface history of the Slave craton, *Tectonics*, *32*(5), 1066–1083, doi:10.1002/tect.20069.

Austermann, J., Mitrovica, J.X., Huybers, P., and Rovere, A. (2017). Detection of a dynamic topography signal in last interglacial sea-level records, *Science Advances*, *3*(7), doi:10.1126/sciadv.1700457.

Ávila, P., and Dávila, F.M. (2020). Lithospheric thinning and dynamic uplift effects during slab window formation, southern Patagonia (45°–55° S), *Journal of Geodynamics*, *133*, 101689, doi:10.1016/j.jog.2019.101689.

Awater, T. (1970). Implications of plate tectonics for the Cenozoic tectonic evolution of Western North America, *GSA Bulletin*, *81*, 3513–3536, doi:10.1130/0016-7606(1970)81[3513:IOPTFT]2.0.CO;2.

Baldwin, J.A., Whipple, K.X., and Tucker, G. E. (2003). Implications of the shear stress river incision model for the timescale of postorogenic decay of topography, *Journal of Geophysical Research: Solid Earth*, *108*(B3), doi:10.1029/2001JB000550.

Ball, P.W., White, N.J., Masoud, A., Nixon, S., Hoggard, M.J., Maclennan, J., Stuart, F.M., Oppenheimer, C., and Kröpelin, S. (2019). Quantifying asthenospheric and lithospheric controls on mafic magmatism across North Africa, *Geochemistry, Geophysics, Geosystems*, *20*, 3520–3555, doi:10.1029/2019GC008303.

Barbosa, J.A., Neumann, V.H., Lima Filho, M., Souza, E.D., and Moraes, M.D. (2007). Estratigrafia da faixa costeira Recife-Natal (Bacia da Paraíba e Plataforma de Natal), NE Brasil, *Estudos Geológicos*, *17*(2), 3–30.

Bailey, I.W., Miller, M.S., Liu, K., and Levander, A., (2012). VS and density structure beneath the Colorado Plateau constrained by gravity anomalies and joint inversions of receiver function and phase velocity data, *Journal of Geophysical Research: Solid Earth*, *117*(B2), doi:10.1029/2011JB008522.

Barnett-Moore, N., Flament, N., Heine, C., Butterworth, N., and Müller, R.D. (2014). Cenozoic uplift of south Western Australia as constrained by river profiles, *Tectonophysics*, *622*, 186–197, doi:10.1016/j.tecto.2014.03.010.

Barton, P.J. (1986). The relationship between seismic velocity and density in the continental crust—a useful constraint?, *Geophysical Journal International*, *87*(1), 195–208, doi:10.1111/j.1365-246X.1986.tb04553.x.

Bartow, J.A. (1991). Cenozoic evolution of the San Joaquin Valley, California, *U.S. Geological Survey Professional Paper 1501*, 1–40.

Baynes, E., Lague, D., Attal, M., Gangloff, A., Kirstein, L.A., and Dugmore, A. J. (2018). River self-organisation inhibits discharge control on waterfall Migration, *Sci. Rep.*, *8*, 1–8, doi:10.1038/s41598-018-20767-6.

Beavan, N.R., and Russell, A.P. (1999). An Elasmobranch Assemblage from the Terrestrial-Marine Transitional Lethbridge Coal Zone (Dinosaur Park Formation: Upper Campanian), Alberta, Canada, *Journal of Paleontology*, *73*(3), 494–503, doi:10.1017/S0022336000028006.

Beaumont, C., Jamieson, R.A., Nguyen, M.H., and Lee, B. (2001). Himalayan tectonics explained by extrusion of a low-viscosity crustal channel coupled to focused surface denudation, *Nature*, *414*(6865), 738–742, doi:10.1038/414738a.

Becker, T.W., Faccenna, C., O'Connell, R.J., and Giardini, D. (1999). The development of slabs in the upper mantle: Insights from numerical and laboratory experiments, *Journal of Geophysical Research: Solid Earth*, *104*(B7), 15207–15226, doi:10.1029/1999JB900140.

Becker, T.W., Faccenna, C., Humphreys, E.D., Lowry, A.R., and Miller, M.S. (2014). Static and dynamic support of western United States topography, *Earth and Planetary Science Letters*, *402*(C), 234–246, doi:10.1016/j.epsl.2013.10.012.

Behling, R.E., Kite, J.S., Springer, T.C., Cenderelli, D.A., and Stuckenrath, R. (1993). Buried organic-rich sediments in unglaciated Appalachian Highlands: a stratigraphic model for finding pre-Late Wisconsin paleoenvironmental data, *Abstracts with Programs-Geological Society of America*, *25*, 60.

Benson, R.N., and Doyle, R.G. (1988). Chapter 5: Early Mesozoic rift basins and the development of the United States middle Atlantic continental margin, *in* Manspeizer, W. (ed.), Triassic-Jurassic

Rifting: Continental Breakup and the Origin of the Atlantic Ocean and Passive Margins, *Developments in Geotectonics*, *22*, 99–127, doi:10.1016/B978-0-444-42903-2.50010-5.

Berggren, W.A., (1974). Paleocene benthonic foraminiferal biostratigraphy, biogeography, and paleoecology of Libya and Mali, *Micropaleontology*, *20*, 449–465, doi:10.2307/1485130.

Bessin, P., Guillocheau, F., Robin, C., Braun, J., Bauer, H., and Schroëtter, J. (2017). Quantification of vertical movement of low elevation topography combining a new compilation of global sea-level curves and scattered marine deposits (Armorican Massif, western France), *Earth and Planetary Science Letters*, *470*, 25–36, doi:10.1016/j.epsl.2017.04.018.

Best, M.G., Barr, D.L., Christiansen, E.H., Gromme, S., Deino, A.L., and Tingey, D.G. (2009). The Great Basin Altiplano during the middle Cenozoic ignimbrite flareup: Insights from volcanic rocks, *International Geology Review*, *51*(7-8), 589–633, doi:10.1080/00206810902867690.

Bétard, F. (2010). Uplift and denudation history at low-elevation passive margins: Insights from morphostratigraphic analysis in the SE Armorican Massif along the French Atlantic margin, *Comptes Rendus Geoscience*, *342*, 215–222, doi:10.1016/j.crte.2010.02.004.

Bierman, P., and Steig, E.J., (1996). Estimating rates of denudation using cosmogenic isotope abundances in sediment, *Earth Surface Processes and Landforms*, *21*(2), 125–139, doi:10.1002/(SICI)1096-9837(199602)21:2<125::AID-ESP511>3.0.CO;2-8.

Binnie, A., Dunai, T.J., Binnie, S.A., Victor, P., González, G., and Bolten, A. (2016). Accelerated late quaternary uplift revealed by ^{10}Be exposure dating of marine terraces, Mejillones Peninsula, northern Chile, *Quaternary Geochronology*, *36*, 12–27, doi:10.1016/j.quageo.2016.06.005.

Bishop, P. (2007). Long-term landscape evolution: linking tectonics and surface processes, *Earth Surface Processes and Landforms*, *32*(3), 329–365, doi:10.1002/esp.1493.

Bjerager, M., Surlyk, F., Lykke-Andersen, H., Thibault, N., and Stemmerik, L. (2010). Danian cool-water coral reefs in southern Scandinavia localised over seafloor highs, *Marine and Petroleum Geology*, *27*, 455–466, doi:10.1016/j.marpetgeo.2009.09.008.

Bjerrum, C.J., and Dorsey, R.J. (1995). Tectonic controls on deposition of Middle Jurassic strata in a retroarc foreland basin, Utah-Idaho trough, western interior, United States, *Tectonics*, *14*4, 962–978, doi:10.1029/95TC01448.

Blackmer, G.C., Omar, G.I., and Gold, D.P. (1994). Post-Alleghanian unroofing history of the Appalachian Basin, Pennsylvania, from apatite fission track analysis and thermal models, *Tectonics*, *13*, 1259–1276, doi:10.1029/94TC01507.

Blisniuk, P.M., and Stern, L.A. (2005). Stable isotope paleoaltimetry: A critical review, *American Journal of Science*, *305*(10), 1033–1074, doi:10.2475/ajs.305.10.1033.

Blum, M., and Pecha, M. (2014). Mid-Cretaceous to Paleocene North American drainage reorganization from detrital zircons, *Geology*, *42*(7), 607–610, doi:10.1130/G35513.1.

Blum, M.D., Milliken, K.T., Pecha, M.A., Snedden, J.W., Frederick, B.C., and Galloway, W.E. (2017). Detrital-zircon records of Cenomanian, Paleocene, and Oligocene Gulf of Mexico drainage integration and sediment routing: Implications for scales of basin-floor fans, *Geosphere*, *13*(6), 2169–2205, doi:10.1130/GES01410.1.

Boettcher, S.S., and Milliken, K.L. (1994). Mesozoic-Cenozoic Unroofing of the Southern Appalachian Basin: Apatite Fission Track Evidence from Middle Pennsylvanian Sandstones, *The Journal of Geology*, *102*(6), 655–668, doi:10.1086/629710.

Bond, G. (1976). Evidence for continental subsidence in North America during the Late Cretaceous global submergence, *Geology*, *4*, 557–560, doi:10.1130/0091-7613(1976)4<557:EFCSIN>2.0.CO;2.

Bond, G.C., Kominz, M.A., Steckler, M.S., and Grotzinger, J.P. (1989). Role of thermal subsidence, flexure and eustasy in the evolution of early Paleozoic passive-margin carbonate platforms, *in* Crevello, P.D.,Wilson, J.L., Sarg J.F., and Read, J.F., eds., Controls on Carbonate Platform and Basin Development, *Society for Sedimentary Geology Special Publication*, *44*, 39–61, doi:10.2110/pec.89.44.0039.

Bonnet, S. (2009). Shrinking and splitting of drainage basins in orogenic landscapes from the migration of themain drainage divide, *Nature Geoscience*, *2*(11), 766–771, doi:10.1038/ngeo666.

Bonnet, S., and Crave, A. (2003). Landscape response to climate change: Insights from experimental modeling and implications for tectonic versus climatic uplift of topography, *Geology*, *31*(2), 123–126, doi:10.1130/0091-7613(2003)031<0123:LRTCCI>2.0.CO;2.

Boulton, S.J., and Whittaker, A.C. (2009). Quantifying the slip rates, spatial distribution and evolution of active normal faults from geomorphic analysis: Field examples from an oblique-extensional graben, southern Turkey, *Geomorphology*, *104*(3-4), 299–316, doi:10.1016/j.geomorph.2008.09.007.

Boyden, J.A., Müller, R.D., Gurnis, M., Torsvik, T.H., Clark, J.A., Turner, M., Ivey-Law, H., Watson, R.J., and Cannon, J.S., (2011). Next-generation plate-tectonic reconstructions using GPlates, *in Geoinformatics: Cyberinfrastructure for the Solid Earth Sciences*, 95–113, Cambridge University Press, Cambridge, UK.

Braun, D.D. (1989). Glacial and periglacial erosion of the Appalachians, *Geomorphology*, *2*(1-3), 233–256, doi:10.1016/0169-555X(89)90014-7.

Braun, J. (2002). Quantifying the effect of recent relief changes on age-elevation relationships, *Earth and Planetary Science Letters*, *200*, 331–343, doi:10.1016/S0012-821X(02)00638-6.

Braun, J., and Sambridge, M. (1997). Modelling landscape evolution on geological time scales: a new method based on irregular spatial discretization, *Basin Research*, *9*(1), 27–52, doi:10.1046/j.1365-2117.1997.00030.x.

Brigaud, B., Vincent, B., Pagel, M., Gras, A., Noret, A., Landrein, P., and Huret, E. (2018). Sedimentary architecture, depositional facies and diagenetic response to intracratonic deformation and climate change inferred from outcrops for a pivotal period (Jurassic/Cretaceous boundary, Paris Basin, France), *Sedimentary geology*, *373*, 48–76, doi:10.1016/j.sedgeo.2018.04.011.

Brocard, G.Y., and Van Der Beek, P. (2006). Influence of incision rate, rock strength, and bedload supply on bedrock river gradients and valley-flat widths: Field-based evidence and calibrations from western Alpine rivers (southeast France), *Geological Society of America Special Paper*, *398*(07), 101–126, doi:10.1130/2006.2398(07).

Brocard, G.Y., Willenbring, J.K., Miller, T.E., and Scatena, F.N. (2016). Relict landscape resistance to dissection by upstream migrating knickpoints, *Journal of Geophysical Research: Earth Surface*, *121*(6), 1182–1203, doi:10.1002/2015JF003678.

Browning, J.V., Miller, K.G., McLaughlin, P.P., Kominz, M.A., Sugarman, P.J., Monteverde, D., Feigenson, M.D., and Hernandez, J.C. (2006). Quantification of the effects of eustasy, subsidence, and sediment supply on Miocene sequences, mid-Atlantic margin of the United States, *GSA Bulletin*, *118*(5/6), 567–588, doi:10.1130/B25551.1.

Browning, J.V., Miller, K.G., Sugarman, P.J., Kominz, M.A., McLaughlin, P.P., Kulpecz, A.A., and Feigenson, M.D. (2008). 100 Myr record of sequences, sedimentary facies and sea level change from

Ocean Drilling Program onshore coreholes, US mid-Atlantic coastal plain, *Basin Research*, *20*(2), 227–248, doi:10.1111/j.3565-2117.2008.00360.x.

Buehler J.S., and Shearer, P.M. (2016). Uppermost mantle seismic velocity structure beneath USArray, *Journal of Geophysical Research*, *121*, doi:10.1002/2016JB013265.

Burke, K., and Gunnell, Y. (2008). The African erosion surface: A continental-scale synthesis of geomorphology, tectonics, and environmental change over the past 180 million years, *Geological Society of America, Volume 201*, doi:10.1130/2008.1201.

Burov, E., and Cloetingh, S.A.P.L. (1997). Erosion and rift dynamics: new thermomechanical aspects of post-rift evolution of extensional basins, *Earth and Planetary Science Letters*, *150*(1–2), 7–26, doi:10.1016/S0012-821X(97)00069-1.

Bustin, R.M. (1991), Organic maturity in the western Canada sedimentary basin, *International Journal of Coal Geology*, *19*, 319–358, doi:10.1016/0166-5162(91)90026-F.

Campforts, B., and G. Grovers (2015). Keeping the edge: A numerical method that avoids knickpoint smearing when solving the stream power law, *Journal of Geophysical Research: Earth Surface*, *120*, 1189–1205, doi:10.1002/2014JF003376

Campos Neto, O.D.A., Lima, W.S., and Cruz, F.G. (2007). Bacia de Sergipe-Alagoas, *Boletim de Geociências da Petrobras*, *15*(2), 405–415.

Cande, S.C., and Kent, D.V. (1992). A new geomagnetic polarity time scale for the Late Cretaceous and Cenozoic, *Journal of Geophysical Research: Solid Earth*, *97*(B10), 13917–13951, doi:10.1029/92JB01202.

Cao, W., Zahirovic, S., Flament, N., Williams, S., Golonka, J., and Müller, R.D. (2017), Improving global paleogeography since the late Paleozoic using paleobiology, *Biogeosciences*, *14*(23), 5425–5439, doi:10.5194/bg-14-5425-2017.

Carena, S., Bunge, H.-P., and Friedrich, A.M., (2019). Analysis of geological hiatus surfaces across Africa in the Cenozoic and Implications for the timescales of convectively-maintained topography, *Canadian Journal of Earth Sciences*, doi:10.1139/cjes-2018-0329.

Case, G.R., and Schwimmer, D.R., (1988). Late Cretaceous Fish from the Blufftown Formation (Campanian) in Western Georgia, *Journal of Paleontology*, *62*(2), 290–301, doi:

Cassel, E.J., Calvert, A.T., and Graham, S.A. (2009). Age, geochemical composition, and distribution of Oligocene ignimbrites in the northern Sierra Nevada, California: Implications for landscape morphology, elevation, and drainage divide geography of the Nevadaplano, *International Geology Review*, *51*(7-8), 723–742, doi:10.1080/00206810902880370.

Castelltort, S., Whittaker, A.C., and Vergés, J. (2015). Tectonics, sedimentation and surface processes: From the erosional engine to basin deposition, *Earth Surface Processes and Landforms*, *40*(13), 1839–1846, doi:10.1002/esp.3769.

Cather, S.M., Connell, S.D., Chamberlin, R.M., McIntosh, W.C., Jones, G.E., Potochnik, A.R., Lucas, S.G., and Johnson, P.S. (2008). The Chuska erg: Paleogeomorphic and paleoclimatic implications of an Oligocene sand sea on the Colorado Plateau, *GSA Bulletin*, *120*(1-2), 13–33, doi:10.1130/B26081.1.

Chamberlain, C.P., Mix, H.T., Mulch, A., Hren, M.T., Kent-Corson, M.L., Davis, S.J., Horton, T.W., and Graham, S.A. (2012). The cenozoic climatic and topographic evolution of the western north American Cordillera, *American Journal of Science*, *312*(2), 213–262, doi:10.2475/02.2012.05.

Champagnac, J.D., Molnar, P., Sue, C., and Herman, F. (2012). Tectonics, climate, and mountain topography modeling, *Journal of Geophysical Research: Solid Earth*, *119*(2), 1384–1424, doi:10.1002/2013JB010436.

Campforts, B., Vanacker, V., Herman, F., Vanmaercke, M., Schwanghart, W., Tenorio, G.E., Willems, P. and Govers, G. (2020). Parameterization of river incision models requires accounting for environmental heterogeneity: insights from the tropical Andes, *Earth Surface Dynamics*, *8*(2), 447–447, doi:10.5194/esurf-8-447-2020.

Channer, M.A., Ricketts, J.W., Zimmerer, M., Heizler, M., and Karlstrom, K.E. (2015). Surface uplift above the Jemez mantle anomaly in the past 4 Ma based on $^{40}Ar/^{39}Ar$ dated paleoprofiles of the Rio San Jose, New Mexico, USA, *Geosphere*, *11*(5), 1384–1400, doi:10.1130/GES01145.1.

Chapin, C.E., Wilks, M., and Mcintosh, W.C. (2004). Space-time patterns of Late Cretaceous to present magmatism in New Mexico – comparison with Andean volcanism and potential for future volcanism, *New Mexico Bureau of Geolology and Mineral Resources Bulletin*, *160*, 13–40.

Chapman, D.S., Keho, T.H., Bauer, M.S., and Picard, M.D. (1984). Heat flow in the Uinta

Basin determined from bottom hole temperature (BHT) data, *Geophysics*, *49*(4), 453–466, doi:10.1190/1.1441680.

Clayton, L., Moran, S.R., Bluemle, P., and Carlson, C.G. (1980). Geologic Map of North Dakota, *U.S. Geological Survey*, Scale 1:500,000.

Clark, G.M., and Ciolkosz, E.J. (1988). Periglacial geomorphology of the Appalachian Highlands and Interior Highlands south of the glacial border – a review, *Geomorphology*, *1*(3), 191–220, doi:10.1016/0169-555X(88)90014-1.

Cloetingh, S., Gradstein, F.M., Kooi, H., Grant, A.C., Kaminski, M., (1990). Plate reorganization: a cause of rapid late Neogene subsidence and sedimentation around the North Atlantic?, *Journal of the Geological Society*, *147*(3), 495–506, doi:10.1144/gsjgs.147.3.0495.

Cloetingh, S., and Haq, B.U. (2015). Inherited landscapes and sea level change, *Science*, *347*(6220), doi:10.1126/science.1258375.

Clouzet, P., Masson, Y., and Romanowicz, B. (2018). Box tomography: first application to the imaging of upper-mantle shear velocity and radial anisotropy structure beneath the North American continent, *Geophysical Journal International*, *213*(3), 1849–1875, doi:10.1093/gji/ggy078.

Coates, A.G., and Kauffman, E.G. (1973). Stratigraphy, paleontology and paleoenvrionment of a Cretaceous coral thicket, Lamy, New Mexico, *Journal of Paleontology*, *47*(5), 953–968.

Cobban, W.A., Walaszczyk, I., Obradovich, J.D., and McKinney, K.C. (2006). A USGS zonal table for the Upper Cretaceous Middle Cenomanian–Maastrichtian of the Western Interior of the United States based on Ammonites, Inoceramids, and Radiometric ages, *Technical report*.

Coimbra, J.C., Arai, M., and Carreño, A.L., (2002). Biostratigraphy of Lower Cretaceous microfossils from the Araripe basin, northeastern Brazil, *Geobios*, *35*, 687–698, doi:10.1016/S0016-6995(02)00082-7.

Cole, R.D., Young, R.G., and Willis, G.G. (1997). Prairie Canyon Member, a new unit of the Upper Cretaceous Mancos Shale, West-Central Colorado and East-Central Utah, *Utah Geological Survey Miscellaneous Publications*, *97*(4), p. 23.

Colgan, J.P., and Henry, C.D. (2009). Rapid middle Miocene collapse of the Mesozoic orogenic plateau in north-central Nevada, *International Geology Review*, *51*(9-11), 920–961, doi:10.1080/00206810903056731.

Colli, L., Ghelichkhan, S., and Bunge, H.P. (2016). On the ratio of dynamic topography and gravity anomalies in a dynamic Earth, *Geophysical Research Letters*, *43*(6), 2510–2516, doi:10.1002/2016GL067929.

Conrad, C.P., and Gurnis, M. (2003). Seismic tomography, surface uplift, and the breakup of Gondwanaland: Integrating mantle convection backwards in time, *Geochemistry, Geophysics, Geosystems*, *4*(3), 1031, doi:10.1029/2001GC000299.

Conrad, C.P., and Husson, L. (2009). Influence of dynamic topography on sea level and its rate of change, *Lithosphere*, *1*(2), 110–120, doi:10.1130/L32.1.

Copley, A., and McKenzie, D. (2007), Models of crustal flow in the India-Asia collision zone, *Geophysical Journal International*, *169*(2), 683–698, doi:10.1111/j.1365-246X.2007.03343.x.

Cornet, B., Olsen, P.E. (1985). A summary of the biostratigraphy of the Newark Supergroup of Eastern North America with comments on Early Mesozoic provinciality, *in* Simposio Sobre Floras del Triassico Tardio, su Fitogeografia y Paleoecologia, *III Congreso Latinoamericano de Paleontologia, Memoria*, 61–81., Mexico.

Cosgrove, G.I., Hodgson, D.M., Mountney, N.P., and McCaffrey, W.D. (2019). High-resolution correlations of strata within a sand-rich clinothem using grain fabric data, offshore New Jersey, USA, *Geosphere*, *15*(4), 1291–1322, doi:10.1130/GES02046.1.

Courtillot, V., Davaille, A., Besse, J., and Stock, J. (2003). Three distinct types of hotspots in the Earth's mantle, *Earth and Planetary Science Letters*, *205*(3), 295–308, doi:10.1016/S0012-821X(02)01048-8.

Cousminer, H.L. (1983). Late Triassic dinoflagellate cycts date Georges Bank deep marine sediments as Rhaeto-Norian, *Proc. Am. Assoc. Stratigr. Palynol.*, *2*.

Cousminer, H.L., and Steinkraus, W.E. (1988). COST G-2 Well: biostratigraphy and implications for the origin of the Atlantic passive margin, *in* Manspeizer (ed.), Triassic-Jurassic Rifting: Continental Breakup and the Origin of the Atlantic Ocean and Passive Margins, *Developments in Geotectonics*, *22*, 167–184, Elsevier, Amsterdam.

Covault, J.A., Craddock, W.H., Romans, B.W., Fildani, A., and Gosai, M. (2013). Spatial and temporal variations in landscape evolution: Historic and longer-term sediment flux through global catchments, *The Journal of Geology*, *121*(1), doi:10.1086/668680.

Crameri, F., Lithgow-Bertelloni, C.R., and Tackley, P.J. (2017). The dynamical control of subduction parameters on surface topography, *Geochemistry, Geophysics, Geosystems*, *18*(4), 1661–1687, doi:10.1002/2017GC006821.

Croissant, T., and Braun, J. (2014). Constraining the stream power law: A novel approach combining a landscape evolution model and an inversion method, *Earth Surface Dynamics*, *2*, 155–166, doi:10.5194/esurf-2-155-2014.

Crosby, A.G., and McKenzie, D. (2009). An analysis of young ocean depth, gravity and global residual topography, *Geophysical Journal International*, *178*(3), 1198–1219, doi:10.1111/j.1365-246X.2009.04224.x.

Crosby, A.G., McKenzie, D., and Sclater, J.G. (2006). The relationship between depth, age and gravity in the oceans, *Geophysical Journal International*, *166*(2), 553–573, doi:10.1111/j.1365-246X.2006.03015.x.

Crosby, B.T., and Whipple, K.X. (2006). Knickpoint initiation and distribution within fluvial networks, 236 waterfalls in the Waipaoa River, North Island, New Zealand, *Geomorphology*, *82*, 16–38, doi:10.1016/j.geomorph.2005.08.023.

Cross, T.A. (1986). Tectonic Controls of Foreland Basin Subsidence and Laramide Style Deformation, Western United States, doi:10.1002/9781444303810.ch1.

Cross, T.A., and Piliger, R.H. (1978). Tectonic controls of late Cretaceous sedimentation, western interior, USA, *Nature*, *247*, 653–657, doi:10.1038/274653a0.

Crough, S.T., and Thompson, G.A. (1976). Numerical and approximate solutions for lithospheric thickening and thinning, *Earth and Planetary Science Letters*, *31*(3), 397–402, doi:10.1016/0012-821X(76)90121-7.

Custódio, M.A., Quaglio, F., Warren, L.V., Simões, M.G., Fürsich, F.T., Perinotto, J.A.J., and Assine, M.L. (2017). The transgressive-regressive cycle of the Romualdo Formation (Araripe Basin): Sedimentary archive of the Early Cretaceous marine ingression in the interior of Northeast Brazil, *Sedimentary Geology*, *359*, 1–15, doi:10.1016/j.sedgeo.2017.07.010.

Czarnota, K., Hoggard, M.J., White, N.J., and Winterbourne, J. (2014). Spatial and temporal patterns of Cenozoic dynamic topography around Australia, *Geochemistry, Geophysics, Geosystems*, *14*, 634–658, doi:10.1029/2012GC004392.

Czarnota, K., Roberts, G.G., White, N.J., and Fishwick, S. (2014). Spatial and temporal patterns of Australian dynamic topography from river profile modelling, *Journal of Geophysical Research: Solid Earth*, *119*(2), 1384–1424, doi:10.1002/2013JB010436.

Davies, J.H., and von Blanckenburg, F. (1995). Slab breakoff: a model of lithosphere detachment and its test in the magmatism and deformation of collisional orogens, *Earth and Planetary Science Letters*, *129*(4), 85–102, doi:10.1016/0012-821X(94)00237-S.

Davies, R.B., Casey, D.M., Horbury, A.D., Sarland, P.R., and Simmons, M.D. (2002). Early to Mid-Cretaceous mixed carbonate-siliciclastic shelfal systems: Examples, issues and models from the Arabian Plate, *Geoarabia*, *7*(3), 541–598.

Davies, D.R., Valentine, A.P., Kramer, S.C., Rawlinson, N., Hoggard, M.J., Eakin, C.M., and Wilson, C.R. (2019). Earth's multi-scale topographic response to global mantle flow, *Nature Geoscience*, *12*(10), 845–850, doi:10.1038/s41561-019-0441-4.

Davis, W.M., (1899). The Geographical Cycle, *Geographical Journal*, *14*(5), 481–504, doi:10.1086/521238.

Dávila, F.M., and Lithgow-Bertelloni, C. (2015). Dynamic uplift during slab flattening, *Earth and Planetary Science Letters*, *425*, 34–43, doi:10.1016/j.epsl.2015.05.026.

Dean, C.D., Collins, D.S., van Cappelle, M., Avdis, A., and Hampson, G.J. (2019). Regional-scale paleobathymetry controlled location, but not magnitude, of tidal dynamics in the Late Cretaceous Western Interior Seaway, USA, *Geology*, *47*(11), 1083–1087, doi:10.1130/G46624.1.

DeCelles, P.G. (1994). Late Cretaceous-Paleocene synorogenic sedimentation and kinematic history of the Sevier thrust belt, northeast Utah and southwest Wyoming, *GSA Bulletin*, *106*(1), 32–56.

DeCelles, P. G. (2004), Late Jurassic to Eocene evolution of the Cordilleran thrust belt and foreland basin system, Western U.S.A., *American Journal of Science*, *304*(February), 105–168, doi:10.2475/ajs.304.2.105.

DeCelles, P.G., Robinson, D.M., and Zandt, G. (2002). Implications of shortening in the Himalayan fold-thrust belt for uplift of the Tibetan Plateau, *Tectonics*, *21*(6), 12–1, doi:10.1029/2001TC001322.

Delaunay, J. (1934). Sur la sphère vide. A la mémoire de Georges Voronoï, *Bulletin de l'Académie des Sciences de l'URSS. Cl. Sci. Math. 6*, 793–800.

de Matos, R.M.D. (1992). The northeast Brazilian rift system, *Tectonics*, *11*(4), 766–791, doi:10.1029/91TC03092.

Deng, T., and Ding, L. (2015). Paleoaltimetry reconstructions of the Tibetan Plateau: progress and contradictions, *National Science Review*, *2*(4), 417–437, doi:10.1093/nsr/nwv062.

Deniel, C., Vincent, P.M., Beauvilain, A., and Gourgaud, A. (2015). The Cenozoic volcanic province of Tibesti (Sahara of Chad): major units, chronology, and structural features, *Bulletin of Volcanology*, *77*(9), 74, doi:10.1007/s00445-015-0955-6.

Densmore, A.L., and Hovius, N. (2000). Topographic fingerprints of bedrock landslides, *Geology*, *28*(4), 371–374, doi: 10.1130/0091-7613(2000)28<371:TFOBL>2.0.CO;2.

DiBiase, R.A., Whipple, K.X., Lamb, M.P., and Heimsath, A.M. (2014). The role of waterfalls and knickzones in controlling the style and pace of landscape adjustment in the western San Gabriel Mountains, California, *GSA Bulletin*, *127*(3-4), 539–559, doi:10.1130/B31113.1.

Dickie, K., Keen, C.E., Williams, G.L., and Dehler, S.A. (2011). Tectonostratigraphic evolution of the Labrador margin, Atlantic Canada, *Marine and Petroleum Geology*, *28*, 1663–1675, doi:10.1016/j.marpetgeo.2011.05.009.

Dickinson, W.R., and Snyder, W.S. (1978). Plate tectonics of the Laramide orogeny, *in* Matthews III, V. (ed.), Laramide Folding Associated with Basement Block Faulting Western United States, *Geological Society of America Memoir 151.*

Dickinson, W.R., Klute, M.A., Hayes, M.J., Janecke, S.U., Lundin, E.R., Mckittrick, M.A., and Olivares, M.D. (1988). Paleogeographic and paleotectonic setting of Laramide sedimentary basins in the central Rocky Mountain region, *GSA Bulletin*, *100*(7), 1023–1039, doi:10.1130/0016-7606(1988)100<1023:PAPSOL>2.3.CO;2.

Dickinson, W.R. (2004). Evolution of the North American Cordillera, *Annual Review of Earth and Planetary Science*, *32*(1), 13–45, doi:10.1146/annurev.earth.32.101802.120257.

Dillon, W.P., Poag, C.W., Klitgord, K.O., Battuello, P.A., and Trehu, A.M. (1990). Evolution of the Blake Plateau basin from rift basin to carbonate platform to present eroded continental borderland, *AAPG Bulletin*, 74(CONF-900605–).

Dodson, M.H. (1973), Closure temperatures in cooling geological and petrological systems, *Contributions in Mineralogy and Petrology*, *40*, 259–274.

Dorsey, R.J., Housen, B.A., Janecke, S.U., Fanning, C.M., and Spears, A.L.F. (2011). Stratigraphic record of basin development within the San Andreas fault system: Late Cenozoic Fish Creek – Vallecito basin, southern California, *GSA Bulletin*, *123*(5–6), 771–793, doi:10.1130/B30168.1.

Dorsey, R.J., O'Connell, B., McDougall, K., and Homan, M.B. (2018). Punctuated sediment discharge during Early Pliocene birth of the Colorado River: Evidence from regional stratigraphy, sedimentology, and paleontology, *Sedimentary Geology*, *363*, 1–33, doi:10.1016/j.sedgeo.2017.09.018.

Dowsett, H.J. and Cronin, T.M. (1990). High eustatic sea level during the middle Pliocene: Evidence from the southeastern US Atlantic Coastal Plain, *Geology*, *18*, 435–438, doi:10.1130/0091-7613(1990)018<0435:HESLDT>2.3.CO;2.

Duller, R.A., Whittaker, A.C., Swinehart, J.B., Armitage, J.J., Sinclair, H.D., Bair, A., and Allen, P.A. (2012). Abrupt landscape change post-6 Ma on the central Great Plains, USA, *Geology*, *40*(10), 871–874, doi:10.1130/G32919.1.

Durand, S., Debayle, E., Ricard, Y., Zarioli, C., Lambotte, S. (2017). Confirmation of a change in the global shear velocity pattern at around 1,000 km depth, *Geophysical Journal International*, *211*(3), 1628–1639, doi:10.1093/gji/ggx405.

Duxbury, J., Bierman, P.R., Portenga, E.W., Pavich, M.J., Southworth, S. and Freeman, S.P. (2015). Erosion rates in and around Shenandoah National Park, Virginia, determined using analysis of cosmogenic ^{10}Be, *American Journal of Science*, *315*(1), 46–76, doi:10.2475/01.2015.02.

Dyman, T.S., Cobban, W.A., Fox, J.E., Hammond, R.H., Nichols, D.J., Perry Jr., W.J., Porter, K.W., Rice, D.D., Setterholm, D.R., Shurr, G.W., Tysdal, R.G., Harley, J.C., and Campen, E.B. (1994). Cretaceous frocks from Southwestern Montana to Southwestern Minnesota, Northern Rocky Mountains and Great Plains Region, *in* Shurr, G.W., Ludvigson, G.A., and Hammond, R.H. (eds.), Perspectives on the eastern margin of the Cretaceous Western Interior Basin, *Geological Society of America, Special Paper 287*.

El-Azabi, M., and El-Araby, A. (2007). Depositional framework and sequence stratigraphic aspects of the Coniacian–Santonian mixed siliciclastic/carbonate Matulla sediments in Nezzazat and Ekma blocks, Gulf of Suez, Egypt, *Journal of African Earth Sciences*, *47*, 179–202, doi:10.1016/j.jafrearsci.2007.02.002.

El-Sorogy, A.S., Ismail, A., Youssef, M., and Nour, H. (2016). Facies development and paleoenvironment of the Hajajah Limestone Member, Aruma Formation, central Saudi Arabia, *Journal of African Earth Sciences*, *124*, 355–364, doi:10.1016/j.jafrearsci.2016.09.037.

Eaton, J.G., Kirkland, J.I., Hutchison, J.H., Denton, R., O'Neill, R.C., and Parrish, J.M. (1997). Non-marine extinction across the Cenomanian-Turonian boundary, southwestern Utah, with a comparison to the Cretaceous-Tertiary extinction event, *GSA Bulletin*, *109*(5), 560-567, doi:10.1130/0016-7606(1997)109<0560:NEATCT>2.3.CO;2.

Eberth, D.A., and Brinkman, D.B. (1997). Paleoecology of an estuarine, incised-valley fill in the Dinosaur Park Formation (Judith River Group, Upper Cretaceous) of southern Alberta, Canada, *Palaios*, *12*, 43–58, doi:10.2307/3515293.

Eicher, D.L. (1969). Paleobathymetry of Cretaceous Greenhorn sea in eastern Colorado, *AAPG Bulletin*, *53*(5), 1075–1090, doi:10.1306/5D25C81B-16C1-11D7-8645000102C1865D.

Einsele, G. (1992). *Sedimentary basins: evolution, facies, and sediment budget*, Springer-Verlag, New York, NY, 628 p.

Elder, W.P. (1987). The paleoecology of the Cenomanian-Turonian (Cretaceous) stage boundary extinctions at Black Mesa, Arizona, *Palaios*, *2*(1), 24–40, doi:10.2307/3514570.

Elderbak, K., and Leckie, M. (2016). Paleocirculation and foraminiferal assemblages of the Cenomanian–Turonian Bridge Creek Limestone bedding couplets: Productivity vs. dilution during OAE2, *Cretaceous Research*, *60*, 52–77, doi:10.1016/j.cretres.2015.11.009.

Elliott, J., Walters, R., and Wright, T. (2016). The role of space-based observation in understanding and responding to active tectonics and earthquakes, *Nature Communications*, *7*, 13844, doi:10.1038/ncomms13844.

Elston, D.P., and Young, R.A. (1991). Cretaceous-Eocene (Laramide) landscape development and Oligocene-Pliocene drainage reorganization of Transition Zone and Colorado Plateau, Arizona, *Journal of Geophysical Research*, *96*(B7), 12,389–12,406, doi:10.1029/90JB01978.

England, P., and Molnar, P. (1990). Surface uplift, uplift of rocks, and exhumation of rocks, *Geology*, *18*, 1173–1177, doi:10.1130/0091-7613(1990)018<1173:SUUORA>2.3.CO;2.

Epis, R.C., and Chapin, C.E. (1975). Geomorphic and tectonic implications of the Post-Laramide, Late Eocene erosion surface in the southern Rocky Mountains, *in* Curtis, B.F. (ed.), Cenozoic History of the Southern Rocky Mountains, 45–74, *Geological Society of America Memoir 144*, Socorro, NM.

Ericksen, M.C., and Slingerland, R. (1990). Numerical simulations of tidal and wind-driven circulation in the Cretaceous Interior Seaway of North America, *GSA Bulletin*, *102*(11), 1499–1516, doi:10.1130/0016-7606(1990)102<1499:NSOTAW>2.3.CO;2.

Faccenna, C., and Becker, T.W. (2020). Topographic expressions of mantle dynamics in the Mediterranean, *Earth-Science Reviews*, 103327, doi:10.1016/j.earscirev.2020.103327.

Fan, M., and Carrapa, B. (2014). Late Cretaceous-early Eocene Laramide uplift, exhumation, and basin subsidence in Wyoming: Crustal responses to flat slab subduction, *Tectonics*, *33*(4), 509–529, doi:10.1002/2012TC003221.

Farley, K.A. (2002). (U-Th)/He Dating: Techniques, Calibrations, and Applications, *Reviews in Mineralogy and Geochemistry*, *47*(1), 819–844, doi:10.2138/rmg.2002.47.18.

Feng, J., Buffler, R.T., and Kominz, M.A. (1994). Laramide orogenic influence on late Mesozoic-Cenozoic subsidence history, western deep Gulf of Mexico basin, *Geology*, *22*(4), 359–362, doi:10.1130/0091-7613(1994)022<0359:LOIOLM>2.3.CO;2.

Fenneman, N. (1928). Physiographic Divisions of the United States, *Annals of the Association of American Geographers*, *18*(4), 261–353.

Ferrari, L., Valencia-Moreno, M., and Bryan, S. (2007). Magmatism and tectonics of the Sierra Madre Occidental and its relation with the evolution of the western margin of North America, *in* Alaniz-Álvarez, S.A., and Nieto-Samaniego, Á.F. (eds.), Geology of México: Celebrating the Centenial of the Géological Society of Mexico, *Geological Society of America Special Paper 422*, 1–39, doi:10.1130/2007.2422(01).

Ferrari, L., López-Martínez, M., Aguirre-Díaz, G., and Carrasco-Núñez, G. (1999). Space-time patterns of Cenozoic arc volcanism in central Mexico: From the Sierra Madre Occidental to the Mexican Volcanic Belt, *Geology*, *27*(4), 303–306, doi:10.1130/0091-7613(1999)027<0303:STPOCA>2.3.CO;2.

Ferrari, L., López-Martínez, M., and Rosas-Elguera, J. (2002). Ignimbrite flare-up and deformation in

the southern Sierra Madre Occidental, western Mexico: Implications for the late subduction history of the Farallon plate, *Tectonics*, *21*(4), 1–25, doi:10.1029/2001TC001302.

Ferrari, L., Orozco-Esquivel, T., Manea, V., and Manea, M. (2012). The dynamic history of the Trans-Mexican Volcanic Belt and the Mexico subduction zone, *Tectonophysics*, *522-523*(April), 122–149, doi:10.1016/j.tecto.2011.09.018.

Finnegan, N.J., Schumer, R., and Finnegan, S. (2014). A signature of transience in bedrock river incision rates over timescales of $10^4 - 10^7$ years, *Nature*, *505*(7483), 391–394, doi:10.1038/nature12913.

Fitton, J.G., James, D., and Leeman, W.P. (1991). Basic magmatism associated with Late Cenozoic extension in the western United States: Compositional variations in space and time, *Journal of Geophysical Research*, *96*(B8), 13693, doi:10.1029/91JB00372.

Fjeldskaar, W. (1994). Viscosity and thickness of the asthenosphere detected from the Fennoscandian uplift, *Earth and Planetary Science Letters*, *126*(4), 399–410, doi:10.1016/0012-821X(94)90120-1.

Flament, N., Gurnis, M., and Müller, R.D. (2013). A review of observations and models of dynamic topography, *Lithosphere*, *5*2, 189–210, doi:10.1130/L245.1.

Flament, N., Gurnis, M., Müller, R.D., Bower, D.J., and Husson, L. (2015). Influence of subduction history on South American topography, *Earth and Planetary Science Letters*, *430*, 9–18, doi:10.1016/j.epsl.2015.08.006.

Flowers, R.M., Wernicke, B.P., and Farley, K.A. (2008). Unroofing, incision, and uplift history of the southwestern Colorado Plateau from apatite (U-Th)/He thermochronometry, *GSA Bulletin*, *120*(5-6), 571–587, doi:10.1130/B26231.1.

Flowers, R.M., Ault, A.K., Kelley, S.A., Zhang, N., and Zhong, S. (2012). Epeirogeny or eustasy? Paleozoic-Mesozoic vertical motion of the North American continental interior from thermochronometry and implications for mantle dynamics, *Earth and Planetary Science Letters*, *317-318*, 436–445, doi:10.1016/j.epsl.2011.11.015.

Flowers, R.M., and Farley, K.A. (2012). Apatite ^{4}He/^{3}He and (U-Th)/He Evidence for an Ancient Grand Canyon, *Science*, *338*, 1616–1619, doi:10.1126/science.1229390.

Forte, A.M., Peltier, W.R., Dziewonski, A.M., and Woodward, R.L. (1993). Dynamic surface topography: A new interpretation based upon mantle flow models derived from seismic tomography, *Geophysical Research Letters*, *20*(3), 225–228, doi:10.1029/93GL00249.

Forte, A.M. (2000). Seismic-Geodynamic Constraints on Mantle Flow: Implications for Layered Convection, Mantle Viscosity, and Seismic Anisotropy in the Deep Mantle, *in* Karato, S.I., Forte, A., Liebermann, R., Masters, G., and Stixrude, L. (eds.) *Earth's Deep Interior: Mineral Physics and Tomography From the Atomic to the Global Scale*, American Geophysical Union–Geophysical Monograph Series, *117*, doi:10.1029/GM117p0003.

Forte, A.M., Mitrovica, J.X., Moucha, R., Simmons, N.A., and Grand, S.P. (2007). Descent of the ancient Farallon slab drives localized mantle flow below the New Madrid seismic zone, *Geophysical Research Letters*, *34*(4), doi:10.1029/2006GL027895.

Forte, A.M., Moucha, R., Simmons, N.A., Grand S.P., and Mitrovica, J.X. (2009). Deep-mantle contributions to the surface dynamics of the North American continent, *Tectonophysics*, *481*(1–4), 3–15, doi:10.1016/j.tecto.2009.06.010.

Forte, A.M., Quéré, S., Moucha, R., Simmons, N. A., Grand, S.P., Mitrovica, J.X., and Rowley, D.B. (2010). Joint seismic–geodynamic-mineral physical modelling of African geodynamics: A reconciliation of deep-mantle convection with surface geophysical constraints, *Earth and Planetary Science Letters*, *295*(3–4), 329–341, doi:10.1016/j.epsl.2010.03.017.

Forte, A.M., and Whipple, K.X. (2018). Criteria and tools for determining drainage divide stability, *Earth and Planetary Science Letters*, *493*, 102–117, doi:10.1016/j.epsl.2018.04.026.

Fox, M., Herman, F., Willett, S.D., and May, D.A. (2014). A linear inversion method to infer exhumation rates in space and time from thermochronometric data, *Earth Surface Dynamics*, *2*(1), 47–65, doi:10.5194/esurf-2-47-2014.

Fox, M., Goren, L., May, D.A., and Willett, S.D. (2014). Inversion of fluvial channels for paleorock uplift rates in Taiwan, *Journal of Geophysical Research: Earth Surface*, *119*(9), 1853–1875, doi:10.1002/2014JF003196.

Freitas, B.T., Almeida, R.P., Carrera, S.C., Figueiredo, F.T., Turra, B.B., Varejão, F.G., and Assine, M.L. (2017). Aptian sedimentation in the Recôncavo-Tucano-Jatobá Rift System and its tectonic and paleogeographic significance, *Journal of South American Earth Science*, *80*, 460–481, doi:10.1016/j.sames.2017.10.001.

French, S., Lekic, V., and Romanowicz, B. (2013). Waveform tomography reveals channeled flow at the base of the oceanic lithosphere, *Science*, *342*(6359), 277–230, doi:10.1038/355437a0.

French, S.W., and Romanowicz, B.A. (2014). Whole-mantle radially anisotropic shear velocity structure from spectral-element waveform tomography, *Geophysical Journal International*, *199*(3), 1303–1327, doi:10.1093/gji/ggu334.

Fulthorpe, C.S., Mountain, G.S., and Miller, K.G. (1996). Chapter 14: Mapping Noegene Depositional Geometries, New Jersey Continental Slope, Leg150 Drilling Area, *in* Mountain, G.S., Miller, K.G., Blum, P., Poag, C.W., and Twichell, D.C. (eds.), *Proceedings of the Ocean Drilling Program, Scientific Results*, Vol. 150.

Fulthorpe, C.S., Austin, J.S., and Mountain, G.S. (1999). Buried fluvial channels off New Jersey: Did sea-level lowstands expose the entire shelf during the Miocene?, *Geology*, *27*(3), 203–206, doi:10.1130/0091-7613(1999)027<0203:BFCONJ>2.3.CO;2.

Fulthorpe, C.S., and Austin Jr, J.A. (2008). Assessing the significance of along-strike variations of middle to late Miocene prograding clinoformal sequence geometries beneath the New Jersey continental shelf, *Basin Research*, *20*(2), 269–283,doi:10.1111/j.1365-2117.2008.00350.x.

Gaherty, J.B., and Hager, B.H. (1994). Compositional vs. thermal buoyancy and the evolution of subducted lithosphere, *Geophysical Research Letters*, *21*(2), 141–144, doi:10.1029/93GL03466.

Gallagher, K., and Lambeck, K. (1989). Subsidence, Sedimentation and Sea-level Changes in the Eromanga Basin, Australia, *Basin Research*, *2*, 115–131, doi:10.1111/j.1365-2117.1989.tb00030.x.

Gallagher, K. (1995). Evolving temperature histories from apatite fission-track data, *Earth and Planetary Science Letters*, *136*(3-4), 421–435, doi:10.1016/0012-821X(95)00197-K.

Gallagher, K. (2012). Transdimensional inverse thermal history modeling for quantitative thermochronology, *Journal of Geophysical Research: Solid Earth*, *117*(2), doi:10.1029/2011JB008825.

Gallen, S.F., Wegmann, K.W., and Bohnenstiehl, D.W.R. (2013). Miocene rejuvenation of topographic relief in the southern Appalachians, *GSA Today*, *23*(2), 4–10, doi:10.1130/GSATG163A.1.

Gallen, S.F. (2018). Lithologic controls on landscape dynamics and aquatic species evolution in post-orogenic mountains, *Earth and Planetary Science Letters*, *493*, 150–160, doi:10.1016/j.epsl.2018.04.029.

Galloway, W., Ganey-Curry, P., Li, X., and Buffler, R.T. (2000). Cenozoic depositional history of the Gulf of Mexico basin, *Am. Assoc. Pet. Geol. Bull.*, *84*(11), 1743–1774, doi:10.1306/110801720476.

Galloway, W.E. (2001). Cenozoic evolution of sediment accumulation in deltaic and shore-zone depositional systems, Northern Gulf of Mexico Basin, *Marine and Petroleum Geology*, *18*(10), 1031–1040, doi:10.1016/S0264-8172(01)00045-9.

Galloway, W.E. (2008). Depositional Evolution of the Gulf of Mexico Sedimentary Basin, *in* Miall, A.D. (ed.) *Sedimentary Basins of the World*, *Vol. 5*, 505–549, Elsevier, doi:10.1016/S1874-5997(08)00015-4.

Galloway, W.E., Whiteaker, T.L., and Ganey-Curry, P. (2011). History of Cenozoic North American drainage basin evolution, sediment yield, and accumulation in the Gulf of Mexico basin, *Geosphere*, *7*(4), 938–973, doi:10.1130/GES00647.1.

Gameil, M., El-Sorogy, A.S., and Al-Kahtany, K. (2020). Solitary corals of the Campanian Hajajah Limestone Member, Aruma Formation, Central Saudi Arabia, *Historical Biology*, *32*(1), 1–17, doi:/10.1080/08912963.2018.1461217.

Gani, R.M., Ranson, A., Cross, D.B., Hampson, G.J., Gani, N.D., and Sahoo, H. (2015). Along-strike sequence stratigraphy across the Cretaceous shallow marine to coastal-plain transition, Wasatch Plateau, Utah, U.S.A., *Sedimentary Geology*, *325*, 59–70, doi:10.1016/j.sedgeo.2015.05.003.

Gans, P.B., and Miller, E.L. (1983). Style of mid-Tertiary extension in east-central Nevada, *Geological excursions in the overthrust belt and metamorphic core complexes of the Intermountain region*, Utah Geological and Mineral Survey Special Studies, *59*, 107–139.

Garcia, G., Assine, M.L., and Soares, U.M. (2014). Modelagem estratigráfica do intervalo Cenomaniano-Turoniano, formações Açu e Jandaíra, na borda sudoeste da Bacia Potiguar, *Boletim de Geociências – Petrobras*, *22*(1), 29–50.

Garcia, X., Julià, J., Nemocón, A.M., and Neukirch, M. (2019). Lithospheric thinning under the Araripe Basin (NE Brazil) from a long-period magnetotelluric survey: Constraints for tectonic inversion, *Gondwana Research*, *68*, 174–184, doi:10.1016/j.gr.2018.11.013

Garzione, C.N., Quade, J., DeCelles P.G., and English, N.B. (2000). Predicting paleoelevation of Tibet and the Himalaya from δ18O vs. altitude gradients in meteoric water across the Nepal Himalaya, *Earth and Planetary Science Letters*, *181*(1), 215–229, doi:10.1016/S0012-821X(00)00252-1.

Ghosh, P., Garzione, C.N., and Eilet, J.M. (2006). Rapid Uplift of the Altiplano Revealed Through ^{13}C–^{18}O Bonds in Paleosol Carbonates, *Science*, *311*(5760), 511–515, doi:10.1126/science.1119365.

Gibson, T.G., and Bybell, L.M. (1981). Facies changes in the Hatchetigbee Formation in Alabama-Georgia and the Wilcox-Claiborne Group unconformity, *Gulf Coast Association of Geological Societies Transactions*, *31*, 301–306.

Gilbert, G.K. (1877). *Report on the Geology of the Henry Mountains*, U.S. Department of the Interior, Geological Survey of the Rocky Mountains.

Gill, J.R., Cobban, W.A., and Schultz, L.G. (1972). Stratigraphy and Composition of the Sharon Springs Member of the Pierre Shale in Western Kansas, *US Geological Survey Professional Paper 728*.

Gleadow, A.J.W., and Brown, R.W. (1999). Fission track thermochronology and the long-term denudational response to tectonics, *in* Summerfield, M.J. (ed.), *Geomorphology and Global Tectonics*. Wiley, New York, 57–75, (2000).

Glotzbach, C. (2015). Deriving rock uplift histories from data-driven inversion of river profiles, *Geology*, *43*, 467–470, doi:10.1130/G36702.1.

Goddéris, Y., and François, L.M. (1995). The Cenozoic evolution of the strontium and carbon cycles: relative importance of continental erosion and mantle exchanges, *Chemical Geology*, *126*(2), 169–190, doi:10.1016/0009-2541(95)00117-3.

Gohn, G.S. (1988). Late Mesozoic and early Cenozoic geology of the Atlantic Coastal Plain: North Carolina to Florida, *in* Sheridan, R.E., and Grow, J.A. (eds.), *The Atlantic Continental Margin*, DNAG Geology of North America Volume I-2, Geological Society of America, Boulder, CO, doi:10.1130/DNAG-GNA-I2.

Goldhammer, R.K. (1997). Compaction and decompaction algorithms for sedimentary carbonates, *Journal of Sedimentary Geology*, *67*(1), 26–35, doi:10.1306/D42684E1-2B26-11D7-8648000102C1865D.

Goes, S., Armitage, J., Harmon, N., Smith, H., and Huismans, R. (2012). Low seismic velocities below mid-ocean ridges: attenuation versus melt retention, *Journal of Geophysical Research: Solid Earth*, 117(B12), doi:10.1029/2012JB009637.

Gómez, J., Schobbenhaus, C., and Montes, N.E., compilers (2019). Geological Map of South America 2018, scale 1:5 000 000, *Commission for the Geological Map of the World (CGMW)*, Colombian Geological Survey and Geological Survey of Brazil, Paris, FR.

Goren, L., Willett, S.D., Herman, F., and Braun, J. (2014). Coupled numerical-analytical approach to landscape evolution modeling, *Earth Surface Processes and Landforms*, *39*(4), 522–545, doi:10.1002/esp.3514.

Gradstein, F.M., Ogg, J.G., Schmitz, M.B., and Ogg, G.M. (eds.) (2012). *The geologic time scale*, Elsevier, Oxford, UK.

Gran, K.B., Finnegan, N., Johnson, A.L., Belmont, P., Wittkop, C., and Rittenour, T. (2013). Landscape evolution, valley excavation, and terrace development following abrupt postglacial base-level fall, *GSA Bulletin*, *125*(11–12), 1851–1864, doi:10.1130/B30772.1.

Gray, G.G., Pottorf, R.J., Yurewicz, D.A., Mahon, K.I., Pevear, D.R., and Chuchla, R.J. (2001). Chapter 7: Thermal and chronological record of syn- to post-Laramide burial and exhumation, Sierra Madre Oriental, Mexico, *in* Bartolini, C., Buffler, R.T., and Cantu-Chapa, A. (eds.), *The Western Gulf of Mexico Basin: Tectonics, Sedimentary Basins, and Petroleum Systems*, AAPG Memoir 75, 159–181.

Green, P.F., Duddy, I.R., Gleadow, A.J., and Lovering, J.F. (1989). Apatite Fission-Track Analysis as a Paleotemperature Indicator for Hydrocarbon Exploration, *in* Naeser, N.D., and McCulloh, T.H. (eds.), *Thermal History of Sedimentary Basins*, Springer, New York, doi:10.1007/978-1-4612-3492-0_11.

Greene, J., Tominaga, M., Miller, N.C., Hutchinson, D., and Karl, M.R. (2017). Refining the formation and early evolution of the Eastern North American Margin: new insights from multiscale magnetic anomaly analyses, *Journal of Geophysical Research: Solid Earth*, *122*(11), 8724–8748, doi:10.1002/2017JB014308.

Greenlee, S.M., Devlin, W.J., and Miller, K. (1992). Integrated sequence stratigraphy of Neogene deposits, New Jersey continental shelf and slope: comparison with the Exxon model, *GSA Bulletin*, *104*(11), 1403–1411, doi:10.1130/0016-7606(1992)104<1403:ISSOND>2.3.CO;2.

Greenlee, S.M., Schroeder, F.W., and Vail, P.R. (1988). Seismic stratigraphic and geohistory analysis of Tertiary strata from the continental shelf off New Jersey; Calculation of eustatic fluctuations from stratigraphic data, *in* Sheridan, R.E., and Grow, J.A. (eds.), *The Atlantic Continental Margin*, DNAG Geology of North America Volume I-2, Geological Society of America, Boulder, CO, doi:10.1130/DNAG-GNA-I2.

Greenwood, D.R., and Wing, S.L. (1995). Eocene continental climates and latitudinal temperature gradients, *Geology*, *23*, 1044–1048, doi:10.1130/0091-7613(1995)023<1044:ECCALT>2.3.CO;2.

Gregory, K.M., and Chase, C.G. (1992). Tectonic significance of paleobotanically estimated climate and altitude of the late Eocene erosion surface, Colorado, *Geology*, *20*, 581–585, doi:10.1130/0091-7613(1992)020<0581:TSOPEC>2.3.CO;2.

Grow, J.A., Hutchinson, D.R., Klitgord, K.D., Dillon, W.P., and Schlee, J.S. (1983). Representative multichannel seismic profiles over the US Atlantic margin, *in* Bally, A.W. (ed.), Seismic Expression of Structural Styles: A Picture and Work Atlas, *AAPG Studies in Geology*, *15*(2), 1–19, US Geological Survey.

Grow, J., Klitgord, K., and Schlee, J. (1988). Structure and evolution of Baltimore Canyon Trough, *in* Sheridan, R.E., and Grow, J.A. (eds.), *The Atlantic Continental Margin*, DNAG Geology of North America Volume I-2, Geological Society of America, Boulder, CO, doi:10.1130/DNAG-GNA-I2.269.

Guillocheau, F., Rouby, D., Robin, C., Helm, C., Rolland, N., De Veslud, C.L.C., and Braun, J. (2012). Quantification and causes of the terrigeneous sediment budget at the scale of a continental margin: A new method applied to the Namibia–South Africa margin, *Basin Research*, *24*(1), 3–30, doi:10.1111/j.1365-2117.2011.00511.x.

Gurnis, M. (1990). Bounds on global dynamic topography from Phanerozoic flooding of continental platforms, *Nature*, *344*, 754–756, doi:10.1038/344754a0.

Gurnis, M. (1993). Phanerozoic marine inundation of continent driven by dynamic topography above subducting slabs, *Nature*, *364*, 590–593, doi:10.1038/364589a0.

Gurnis, M., Mitrovica, J.X., Ritsema, J., and van Heijst, H.J. (2000). Constraining mantle density structure using geological evidence of surface uplift rates: The case of the African Superplume, *Geochemistry, Geophysics Geosystems*, *1*(7), doi:10.1029/1999GC000035.

Hack, J.T. (1975). Dynamic equilibrium and landscape evolution: Theories of Landform Development, *Publications in Geomorphology*, *1*, 87–102.

Hager, B.H., Clayton, R.W., Richards, M.A., Comer, R.P., and Dziewonski, A.M. (1985). Lower mantle heterogeneity, dynamic topography and the geoid, *Nature*, *313*(6003), 541–545, doi:10.1038/313541a0.

Hager, B.H., and Richards, M.A. (1989). Long-Wavelength Variations in Earth's Geoid: Physical Models and Dynamical Implications, *Philosophical Transactions of the Royal Society of London. Series A, Mathematical and Physical Sciences*, *328*(1599), 309–327, doi:10.1098/rsta.1989.0038.

Hampson, G.J., (2010). Sediment dispersal and quantitative stratigraphic architecture across an ancient shelf, *Sedimentology*, *57*, 96–141, doi:10.1111/j.1365-3091.2009.01093.x.

Hancock, G. and Kirwan, M. (2007). Summit erosion rates deduced from ^{10}Be: Implications for relief production in the central Appalachians, *Geology*, *35*(1), 89–92, doi:10.1130/G23147A.1.

Haq, B.U., Hardenbol, J., and Vail, P.R. (1987). The new chronostratigraphic basis of Cenozoic and Mesozoic sea level cycles, Special Publication, *Cushman Foundation for Foraminiferal Research*, *24*, 7–13.

Haq, B.U., and Al-Qahtani, A.M. (2005). Phanerozoic cycles of sea-level change on the Arabian Platform, *GeoArabia*, *10*(2), 127–160.

Harel, M.A., Mudd, S.M., and Attal, M. (2016). Global analysis of the stream power law parameters based on worldwide 10Be denudation rates, *Geomorphology*, *268*, 184–196, doi:10.1016/j.geomorph.2016.05.035.

Hartley, R., Roberts, G.G., White, N., and Richardson, C. (2011). Transient convective uplift of an ancient buried landscape, *Nature Geoscience*, *4*, 562–565, doi:10.1038/ngeo1191.

Hay, W.W., Sloan, J.L., and Wold, C.N. (1988). Mass/age distribution and composition of sediments on the ocean floor and the global rate of sediment subduction, *Journal of Geophysical Research: Solid Earth*, *93*, 14933–14940, doi:10.1029/JB093iB12p14933.

He, M., Zhong, G., Liu, X., Liu, L., Shen, X., Wu, Z., and Huang, K. (2017). Rapid post-rift tectonic subsidence events in the Pearl River Mouth Basin, northern South China Sea margin, *Journal of Asian Earth Sciences*, *147*, 271–283, doi:10.1016/j.jseaes.2017.07.024.

Heaman, L.M., Kjarsgaard, B.A., and Creaser, R.A. (2004). The temporal evolution of North American kimberlites, *Lithos*, *76*, 377–397, doi:10.1016/j.lithos.2004.03.047.

Heine, C., Yeo, L.G., and Müller, R.D. (2015). Evaluating global paleoshoreline models for the Cretaceous and Cenozoic, *Australian Journal of Earth Sciences*, *62*(3), 275–287, doi:10.1080/08120099.2015.1018321.

Heller, P.L., Wentworth, C.M., and Poag, C.W. (1982). Episodic post-rift subsidence of the United States Atlantic continental margin, *GSA Bulletin*, *93*, 379–390, doi:10.1130/0016-7606(1982)93<379:EPSOTU>2.0.CO;2.

Heller, P.L., and Paola, C. (1989). The paradox of Lower Cretaceous gravels and the initiation of thrusting in the Sevier orogenic belt, United States Western Interior, *GSA Bulletin*, *101*(6), 864–875, doi:10.1130/0016-7606(1989)101<0864:TPOLCG>2.3.CO;2.

Heller, P.L., Mathers, G., Dueker, K., and Foreman, B. (2013). Far-traveled latest Cretaceous-Paleocene conglomerates of the Southern Rocky Mountains, USA: Record of transient Laramide tectonism, *GSA Bulletin*, *125*(3-4), 490–498, doi:10.1130/B30699.1.

Heller, P.L., and Liu, L. (2016). Dynamic topography and vertical motion of the U.S. Rocky Mountain region prior to and during the Laramide orogeny, *GSA Bulletin*, *128*(5-6), 973–988, doi:10.1130/B31431.1.

Henry, C.D., Hinz, N.H., Faulds, J.E., Colgan, J.P., John, D.A., Brooks, E.R., Cassel, E.J., Garside, L.J., Davis, D.A., and Castor, S.B. (2012). Eocene-Early Miocene paleotopography of the Sierra Nevada-Great Basin-Nevadaplano based on widespread ash-flow tuffs and paleovalleys, *Geosphere*, doi:10.1130/GES00727.1.

Herman, F., and Braun, J. (2006). Fluvial response to horizontal shortening and glaciations: A study in the Southern Alps of New Zealand, *Journal of Geophysical Research: Earth Surface*, *111*(1), 1–23, doi:10.1029/2004JF000248.

Herman, F., Seward, D., Valla, P.P., Carter, A., Kohn, B., Willet, S.D., and Ehlers, T.A. (2013). Worldwide acceleration of mountain erosion under a cooling climate, *Nature*, *504*, 423–426, doi:10.1038/nature12877.

Hettinger, R.D., and Roberts, L.N. (2005). Lewis total petroleum system of the Southwestern Wyoming province, Wyoming, Colorado, and Utah, *Petroleum Systems and Geologic Assessment of Oil and Gas in the Southwestern Wyoming Province, Wyoming, Colorado, and Utah*, *US Geological Survey Digital Data Series DDS–69–D*, 43.

Hilton, R.G., Galy, A., Hovius, N., Horng, M.J., and Chen, H. (2011). Efficient transport of fossil organic carbon to the ocean by steep mountain rivers: An orogenic carbon sequestration mechanism, *Geology*, *39*(1), 71–74, doi:10.1130/G31352.1.

Hintze, L.F. (1980). Geologic map of Utah, *Utah Geological and Mineral Survey*, Scale 1:500,000. Salt Lake City, Utah.

Hintze, L., and Kowallis, B. (2009). Geologic history of Utah, *Brigham Young University Geology Studies Special Publication 9*, Brigham Young University, Salt Lake City, UT.

Hoffmann, G., Schneider, B., Mechernich, S., Falkenroth, M., Dunai, T., and Preusser, F. (2020). Quaternary uplift along a passive continental margin (Oman, Indian Ocean), *Geomorphology*, *350*, 106870, doi:10.1016/j.geomorph.2019.106870.

Hoggard, M.J., White, N., and Al-Attar, D. (2016). Global dynamic topography observations reveal limited influence of large-scale mantle flow, *Nature Geoscience*, *9*, 456, doi:10.1038/ngeo2709.

Hoggard, M.J., Winterbourne, J., Czarnota, K., White, N. (2017). Oceanic residual depth measurements, the plate cooling model, and global dynamic topography, *Journal of Geophysical Research: Solid Earth*, *122*(3), 2328–2372, doi:10.1002/2016JB013457.

Holmes, A. (1965). Principles of Physical Geology, London, Nelson, 1288 p.

Hook, S.C., Mack, G.H., and Cobban, W.A. (2012). Upper Cretaceous stratigraphy and biostratigraphy of south-central New Mexico, *in* Spencer, L.G., McLemore, V.T., Lueth, V.W., Spielmann, J.A., and Krainer, K. (eds.), *Geology of Warm Springs region: New Mexico Geological Society 63rd Annual Fall Field Conference Guidebook*, 580 p.

Hoomehr, S., Schwartz, J.S., and Yoder, D.C. (2016). Potential changes in rainfall erosivity under GCM climate change scenarios for the southern Appalachian region, USA, *Catena*, *136*, 141–151, doi:10.1016/j.catena.2015.01.012.

Hosman, R.L. (1996). Regional stratigraphy and subsurface geology of Cenozoic deposits, Gulf Coastal Plain, south-central United States, *U.S. Geological Survey Professional Paper 1416-G*, 1–35.

Hovius, N. (1998). Controls on sediment supply by large rivers, *Relative Role of Eustasy, Climate and Tectonism in Continental Rocks, SEPM Special Publication*, *59*, 3–16

Howard, A.D., and Kerby, G. (1983). Channel changes in badlands, *GSA Bulletin 94*, 739–752, doi:10.1130/0016-7606(1983)94<739:CCIB>2.0.CO;2.

Howard, A.D. (1994). A detachment-limited model of drainage basin evolution, *Water Resources Research 30*, 2261–2285, doi:10.1029/94WR00757.

Humphreys, E.D. (1995). Post-Laramide removal of the Farallon slab, western United States, *Geology*, *23*(13), 987–990, doi:10.1130/0091-7613(1995)023<0987:PLROTF>2.3.CO;2.

Humphreys, E.D., Hessler, E., Dueker, K., Farmer, G.L., Erslev, E., and Atwater, T. (2003). How Laramide-age hydration of North American lithosphere by the Farallon slab controlled subsequent activity in the western United States, *International Geology Review*, *45*(7), 575–595, doi:10.2747/0020-6814.45.7.575.

Huntington, K.W., Wernicke, B.P., and Eiler, J.M. (2010). Influence of climate change and uplift on Colorado Plateau paleotemperatures from carbonate clumped isotope thermometry, *Tectonics*, *29*(3), 1–19, doi:10.1029/2009TC002449.

Husson, L. (2006). Dynamic topography above retreating subduction zones, *Geology*, *34*(9), 741–744, doi:10.1130/G22436.1.

Immenhauser, A.. (2009). Estimating palaeo-water depth from the physical rock record, *Earth-Science Reviews*, *96*, 107–139, doi:10.1016/j.earscirev.2009.06.003.

Japsen, P., Green, P.F., Bonow, J.M., Hinchey, A.M., and Wilton, D.H.C. (2016). Burial and exhumation history of the Labrador-Newfoundland margin: first observations, *Geological Survey of Denmark and Greenland Bulletin*, *35*, 91-94, doi:10.34194/geusb.v35.4947.

Jardim de Sá, E., Matos, R.M.D., Morais Neto, J., Saadi, A., and Pessoa Neto, O. (1999). Epirogenia Cenozóica na Província Borborema: síntese e discussão sobre os modelos de deformação associados, *Proceedings of the VII Simpósio Nacional de Estudos Tectônicos, Sociedade Brasileira de Geologia, Lençóis, Brazil*, 58–61.

Jardim de Sá, E.F., Souza, Z.S., Vasconcelos, P.M., Saadi, A., Galindo, A.C., Lima, M.G., and Oliveira, M.J.R. (2005). Marcos Temporais para a Evolução Cenozóica do Planalto da Borborema, *X Simpósio Nacional de Estudos Tectônicos – IV International Symposium on Tectonics - Abstracts, Sociedade Brasileira de Geologia, Curitiba, Brazil*, 160–162.

Jarvis, G.T., and McKenzie, D.P. (1980). Sedimentary basin formation with finite extension rates, *Earth and Planetary Science Letters*, *48*, 42–52, doi:10.1016/0012-821X(80)90168-5.

Jarvis, A., Reuter, H.I., Nelson, A., and Guevara, E. (2008). Hole-filled SRTM for the globe Version 4, available from the *CGIAR-CSI SRTM 90m Database* (http://srtm. csi. cgiar. org), *15*, 25–54.

Jeletzky, J.A. (1971). Marine Cretaceous biotic province and paleogeography of western and arctic Canada: illustrated by a detailed study of ammonites, *Geological Survey of Canada*, *70*, 1–92.

Johnson, S.Y. (1992). Phanerozoic evolution of sedimentary basins in the Uinta-Piceance Basin region, northwestern Colorado and northeastern Utah, U. S. Geological Survey Bulletin 1787–FF, US Department of the Interior, US Geological Survey.

Johnson, K.R., Nichols, D.J., and Hartman, J.H. (2002). Hell Creek Formation: a 2001 synthesis, *in*, Hartman, J.H., Johnson, K.R., and Nichols, D.J. (eds.), The Hell Creek Formation and the Cretaceous-Tertiary boundary in the northern Great Plains: An integrated continental record of the end of the Cretaceous, *Geological Society of America Special Paper 361*, Boulder, CO., 503–510.

Johnson, R.C. (2003). Chapter 10: Depositional framework of the Upper Cretaceous Mancos Shale and the lower part of the Upper Cretaceous Mesaverde Group, western Colorado and eastern Utah, *in* USGS Uinta-Piceance Assessment Team Eds. *Petroleum Systems and Geologic Assessment of Oil and Gas in the Uinta–Piceance Province, Utah and Colorado*, *United States Geological Survey, Digital Data Series DDS-69-B.*

Johnston, S.T. (2001). The Great Alaskan Terrane Wreck: Reconciliation of paleomagnetic and geological data in the Northern Cordillera., *Earth and Planetary Science Letters*, *193*, 259–272, doi:10.1016/S0012-821X(01)00516-7.

Kansas Geological Survey, (2008). Surficial Geology of Kansas, *Kansas Geological Survey*, Map M-118, Scale 1:500,000.

Karlstrom, K.E., Crow, R.S., Crossey, L.J., Coblentz, D., and Van Wijk, J.W. (2008). Model for tectonically driven incision of the younger than 6 Ma Grand Canyon, *Geology*, *36*(11), 835–838, doi:10.1130/G25032A.1.

Karlstrom, K.E., Coblentz, D., Dueker, K., Ouimet, W., Kirby, E., Van Wijk, J.W., Schmandt, B., Kelley, S.A., Lazear, G., Crossey, L.J., Crow, R.S., Aslan, A., Darling, A., Aster, R., MacCarthy, J., Hansen, S.M., Stachnik, J., Stockli, D.F., Garcia, R.V., Hoffman, M., McKeon, R., Feldman, J., Heizler, M., and Donahue, M.S. (2012). Mantle-driven dynamic uplift of the Rocky Mountains and Colorado Plateau and its surface response: Toward a unified hypothesis, *Lithosphere*, *4*(1), 3–22, doi:10.1130/L150.1.

Karlstrom, K.E., Lee, J.P., Kelley, S.A., Crow, R.S., Crossey, L.J., Young, R.A., Lazear, G., Beard, L.S., Ricketts, J.W., Fox, M., and Shuster, D.L. (2014). Formation of the Grand Canyon 5 to 6 million years ago through integration of older palaeocanyons, *Nature Geoscience*, *7*(3), 239–244, doi:10.1038/ngeo2065.

Karlstrom, K.E., Crossey, L.J., Embid, E., Crow, R., Heizler, M., Hereford, R., Beard, L.S., Ricketts, J.W., Cather, S., and Kelley, S. (2017). Cenozoic incision history of the Little Colorado River: Its role in carving Grand Canyon and onset of rapid incision in the past ca. 2 Ma in the Colorado River System, *Geosphere*, *13*(1), 49–81, doi:10.1130/GES01304.1.

Kass, M.S. (1999). Prognathodon stadtmani: (Mosasauridae) a new species from the Mancos Shale (Lower Campanian) of western Colorado, *in* Gillette, D. D. (ed.), Vertebrate Paleontology in Utah, *Utah Geological Survey Miscellaneous Publication*, *99*(1), 275–294.

Katz, M.E., Browning, J.V., Miller, K.G., Monteverde, D.H., Mountain, G.S., and Williams, R.H. (2013). Paleobathymetry and sequence stratigraphic interpretations from benthic foraminifera: Insights on New Jersey shelf architecture, IODP Expedition 313, *Geosphere*, *9*(6), 1488–1513, doi:10.1130/GES00872.1.

Kauffman, E.G., and Caldwell, W.G.E. (1993). The Western Interior Basin in space and time, *Geological Association of Canada, Special Paper 39*, 1–30.

Keller, G., Adatte, T., Stinnesbeck, W., Luciani, V., Karoui-Yaakoub, N., and Zaghbib-Turki, D. (2002). Paleoecology of the Cretaceous-Tertiary mass extinction in planktonic foraminifera, *Palaeogeography, Palaeoclimatology, Palaeoecology*, *178*, 257–297, doi:10.1016/S0031-0182(01)00399-6.

Kelley, S.A., and Chapin, C.E. (1995). Apatite fission-track thermochronology of the southern Rocky Mountain - Rio Grande rift - western High Plains province, *in* Geology of the Santa Fe region, *New Mexico Geological Society 46th Annual Field Conference Guidebook*, 87–96.

Ketcham, R.A. (2005). Forward and inverse modeling of low-temperature thermochronometry data, *Rev. Mineral. Geochemistry*, *58*(1), 275–314, doi:10.2138/rmg.2005.58.11.

Kidwell, S.M., Powars, D.S., Edwards, L.E., and Vogt, P.R. (2015). Miocene Stratigraphy and Paleoenvironments of the Calvert Cliffs, Maryland *in* Brezinski, D.K., Halka, J.P., and Ortt Jr., R.A. (eds.), Tripping from the Fall Line, Field Guide, *Geological Society of America*, *40*, 231–279, doi:10.1130/2015.0040(08).

Kirby, E., and Whipple, K. (2001). Quantifying differential rock-uplift rates via stream profile analysis, *Geology*, *29*, 415–418, doi:10.1130/0091-7613(2001)029<0415:QDRURV>2.0.CO;2.

Kirkland, J.I. (1996). Paleontology of the Greenhorn cylcothem (Cretaceous: late Cenomanian to middle Turonian) at Black Mesa, northeastern Arizona, *New Mexico Museum of Natural History and Science Bulletin*, *9*, 1–131.

Kitoh, A. (2004). Effects of mountain uplift on East Asian summer climate investigated by a coupled atmosphere–ocean GCM. *Journal of Climate*, *17*(4), 783–802, doi:10.1175/1520-0442(2004)017<0783:EOMUOE>2.0.CO;2.

Klitgord, K.D., Hutchinson, D.R., and Schouten, H. (1988). Structural and tectonic framework, *in* Sheridan, R.E., and Grow, J.A. (eds.), *The Atlantic Continental Margin*, DNAG Geology of North America Volume I-2, Geological Society of America, Boulder, CO, doi:10.1130/DNAG-GNA-I2.

Klöcking, M., White, N.J., Maclennan, J., McKenzie, D., and Fitton, J.G. (2018)a. Quantitative Relationships Between Basalt Geochemistry, Shear Wave Velocity, and Asthenospheric Temperature Beneath Western North America, Geochemistry, Geophysics, Geosystems, *19*(9), 3376–3404, doi:10.1029/2018GC007559.

Klöcking, M., Rodríguez Tribaldos, V., Hoggard, M., White, N., Maclennan, J., and Rezende Guimarães, A. (2018)b. Linking uplift and volcanism of the Borborema Province, northeast Brazil, *in* EGU General Assembly Conference Abstracts, v. 20, p. 9966.

Klöcking, M., Hoggard, M., Rodríguez Tribaldos, V., Richards, F.D., Rezende Guimarães, A., Maclennan, J., and White, N. (2020). A tale of two domes: Neogene to recent volcanism and dynamic uplift of northeast Brazil and southwest Africa, *Earth and Planetary Science Letters*, *547*, doi:10.1016/j.epsl.2020.116464.

Kominz, M.A., Miller, K.G., and Browning, J.V. (1998). Long-term and short-term global Cenozoic sea-level estimates, *Geology*, *26*(4), 311–314, doi:10.1130/0091-7613(1998)026<0311:LTASTG>2.3.CO;2.

Kominz, M.A., Browning, J.V., Miller, K.G., Sugarman, P.J., Mizintseva, S., and Scotese, C.R. (2008). Late Cretaceous to Miocene sea-level estimates from the New Jersey and Delaware coastal plain coreholes: An error analysis, *Basin Research*, *20*(2), 211–226, doi: 10.1111/j.1365-2117.2008.00354.x.

Kominz, M.A., Miller, K.G., Browning, J.V., Katz, M.E., Mountain, G.S. (2016). Miocene relative sea level on the New Jersey shallow continental shelf and coastal plain derived from one-dimensional backstripping: a case for both eustasy and epeirogeny, *Geosphere*, *12*(5), 1437–1456, doi:10.1130/GES01241.1.

Kooi, H., and Beaumont, C. (1996). Large-scale geomorphology: Classical concepts reconciled and integrated with contemporary ideas via a surface processes model, *Journal of Geophysical Research*, *101*(B2), 3361–3386, doi:10.1029/95JB01861.

Koppes, M.N., and Montgomery, D.R. (2009). The relative efficacy of fluvial and glacial erosion over modern to orogenic timescales, *Nature Geoscience*, *2*, 644–647, doi:10.1038/ngeo616.

Kotthoff, U., Greenwood, D.R., McCarthy, F.M.G., Müller-Navarra, K., Prader, S., and Hesselbo, S.P. (2014). Late Eocene to middle Miocene (33 to 13 million years ago) vegetation and climate development on the North American Atlantic Coastal Plain (IODP Expedition 313, Site M0027), *Climate of the Past*, *10*, 1523–1539, doi:10.5194/cp-10-1523-2014.

Kroh, A., and Menkveld-Gfeller, U. (2006). Echinoids from the Belpberg Beds (Obere Meeresmolasse, Middle Burdigalian) in the area of Bern (Switzerland), *Eclogae geologicae Helvetiae*, *99*, 193–203, doi:10.1007/s00015-006-1185-x.

Kutzbach, J.E., Guetter, P.J., Ruddiman, W.F., and Prell, W.L. (1989). Sensitivity of climate to late Cenozoic uplift in southern Asia and the American west: numerical experiments, *Journal of Geophysical Research*, *94*(D15), 18393–18407, doi:10.1029/JD094iD15p18393.

Lachenbruch, A.H. and Morgan, P. (1990). Continental extension, magmatism and elevation; formal relations and rules of thumb, *Tectonophysics*, *174*(1-2), 39–62, doi:10.1016/0040-1951(90)90383-J.

Lague, D., Crave, A., and Davy, P. (2003). Laboratory experiments simulating the geomorphic response to tectonic uplift, *Journal of Geophysical Research: Solid Earth*, *108*(B1), doi:10.1029/2002JB001785.

Lague, D. (2014). The stream power river incision model: Evidence, theory and beyond, *Earth Surface Processes and Landforms*, *39*(1), 38–61, doi:10.1002/esp.3462.

Lambeck, K., and Chappell, J. (1988). Sea level change through the Last Glacial Cycle, *Science*, *292*(5517), 679–686, doi:10.1126/science.1059549.

Landman, N.H., and Cobban, W.A. (2003). Ammonites from the upper part of the Pierre Shale and Fox Hills Formation of Colorado, *American Museum Novitates*, 2003(3388), 1–45, doi:10.1206/0003-0082(2003)388<0001:AFTUPO>2.0.CO;2.

Laske, G., Masters, G., Ma, Z., and Pasyanos, M. (2013). Update on CRUST1.0–A 1-degree global model of Earth's crust, *Geophysical Research Abstracts*, *v.* 15, p. 2658, Vienna, Austria: EGU General Assembly.

Lambeck, K., Smither, C., and Johnston, P. (1998). Sea-level change, glacial rebound and mantle viscosity for northern Europe, *Geophysical Journal International*, *134*(1), 102–144, doi:10.1046/j.1365-246x.1998.00541.x.

Leckie, R.M., Schmidt, M.G. Finkelstein, D., and Yuretich, R. (1991). Paleoceanographic and paleoclimatic interpretations of the Mancos Shale (Upper Cretaceous), Black Mesa Basin, Arizona *in* Nationa, J.D., and Eaton, J.G. (eds.), Stratigraphy, Depositional Environments, and Sedimentary Tectonics of the Western Margin, Cretaceous Western Interior Seaway, *Geological Society of America Special Paper 260.*

Le Pichon, X., and Sibuet, J. (1981). Passive margins: a model of formation, *Journal of Geophysical Research: Solid Earth*, *86*(B5), 3708–3720, doi:10.1029/JB086iB05p03708.

Le Stunff, Y., and Ricard, Y. (1995). Topography and geoid due to lithospheric mass anomalies, *Geophysical Journal International*, *122*(3), 982–990, doi:10.1111/j.1365-246X.1995.tb06850.x.

Levander, A., and Miller, M.S. (2012). Evolutionary aspects of lithosphere discontinuity structure in the Western U.S., *Geochemistry, Geophysics, Geosystems*, *13*(1), 1–22, doi:10.1029/2012GC004056.

Levandowski, W., Jones, C.H., Butcher, L.A., and Mahan, K.H. (2018). Lithospheric density models reveal evidence for Cenozoic uplift of the Colorado Plateau and Great Plains by lower-crustal hydration, *Geosphere*, *14*(3), 1–15, doi:10.1130/GES01619.1.

Lillegraven, J.A., and Ostresh, L.M. (1988). Evolution of Wyoming Early Cenozoic topography and drainage patterns, *Natl. Geogr. Res.*, *4*(3), 303–327.

Linari, C.L., Bierman, P.R., Portenga, E.W., Pavich, M.J., Finkel, R.C., and Freeman, P.H.T. (2017). Rates of erosion and landscape change along the Blue Ridge escarpment, southern Appalachian Mountains, estimated from in situ cosmogenic ^{10}Be, *Earth Surface Processes and Landforms*, *42*, 928–940, doi:10.1002/esp.4051.

Lisker, F., Ventura, B. and Glasmacher, U.A. (2009). Apatite thermochronology in modern geology, *Geological Society, London, Special Publication 324*, 1–23, doi:10.1144/SP324.1.

Lithgow-Bertelloni, C., and Gurnis, M. (1997). Cenozoic subsidence and uplift of continents from time-varying dynamic topography, *Geology*, *25*(8), 735–738, doi:10.1130/0091-7613(1997)025<0735:CSAUOC>2.3.CO;2.

Lithgow-Bertelloni, C., and Silver, P.G. (1998). Dynamic topography, plate driving forces and the African superswell, *Nature*, *395*, 345–348, doi:10.1038/26212.

Liu, X., and Galloway, W.E. (1993). Sediment accumulation rate: problems and new approach, *in* Armentrout, J.M., Bloch, R., Olson, H.C., and Perkins, B.F. (eds.), Rates of geological processes—tectonics, sedimentation, eustasy and climate, implications for hydrocarbon exploration, *Proceedings of the Fourteenth Annual Research Conference, Gulf Coast Section SEPM*, 101–107.

X. Liu, and Galloway, W.E. (1997). Quantitative Determination of Tertiary Sediment Supply to the North Sea Basin, *AAPG Bulletin*, *81*(9), 1482–1509, doi:10.1306/3B05BB28-172A-11D7-8645000102C1865D.

Liu, L. (2014). Rejuvenation of Appalachian topography caused by subsidence-induced differential erosion, *Nature Geoscience*, *7*, 518–523, doi:10.1038/ngeo2187.

Liu, L. (2015). The ups and downs of North America: Evaluating the role of mantle dynamic topography since the Mesozoic, *Reviews of Geophysics*, *53*(3), 1022–1049, doi:10.1002/2015RG000489.

Liu, S., and Nummedal, D. (2004). Late Cretaceous subsidence in Wyoming: Quantifying the dynamic component, *Geology*, *32*(5), 397–400, doi:10.1130/G20318.1.

Liu, L., Spasojević, S., and Gurnis, M. (2008). Reconstructing Farallon plate subduction beneath North America back to the Late Cretaceous, *Science*, *322*(January), 934–938, doi:10.5061/dryad.5t110.

Liu, L., and Gurnis, M. (2010). Dynamic subsidence and uplift of the Colorado Plateau, *Geology*, *38*(7), 663–666, doi:10.1130/G30624.1.

Levander, A., Schmandt, B., Miller, M.S., Liu, K., Karlstrom, K.E., Crow, R.S., Lee, C-T.A., and Humphreys, E.D. (2011). Continuing Colorado plateau uplift by delamination-style convective lithospheric downwelling, *Nature*, *472*(7344), 461–465, doi:10.1038/nature10001.

Lodhia, B.H., Roberts, G.G., Fraser, A.J., Fishwick, S., Goes, S., and Jarvis, J. (2018). Continental margin subsidence from shallow mantle convection: Example from West Africa, *Earth and Planetary Science Letters*, *481*, 350–361, doi:10.1016/j.epsl.2017.10.024.

Loget, N., and Van Den Driessche, J. (2009). Wave train model for knickpoint migration, *Geomorphology*, *106*(3-4), 376–382, doi:10.1016/j.geomorph.2008.10.017.

Love, J.D., and Christiansen, A.C. (1985). Geologic map of Wyoming, *U.S. Geological Survey*, 1:500,000.

Love, J.D., Christiansen, A.C., and Ver Ploeg, A.J. (1993). Stratigraphic chart showing Phanerozoic nomenclature for the state of Wyoming, *Wyoming State Geological Survey*, Map Series 41.

Lovell, B. (2010). A pulse in the planet: regional control of high-frequency changes in relative sea level by mantle convection: *Journal of the Geological Society, London*, *167*, 637–648, doi:10.1144/0016-76492009-127.

Luke, J.C. (1972). Mathematical models for landform evolution, *Journal of Geophysical Research*, *77*(14), 2460–2464, doi:10.1029/JB077i014p02460.

Luz, R.M.N., Julià, J., and do Nascimento, A.F. (2015)a. Crustal structure of the eastern Borborema Province, NE Brazil, from the joint inversion of receiver functions and surface wave dispersion: Implications for plateau uplift, *Journal of Geophysical Research: Solid Earth*, *120*, 3848–3869, doi:10.1002/2015JB011872.

Luz, R.M.N., Julià, J., and do Nascimento, A.F. (2015)b. Bulk crustal properties of the Borborema Province, NE Brazil, from P-wave receiver functions: Implications for models of intraplate Cenozoic uplift, *Tectonophysics*, *644*, 81–91, doi:0.1016/j.tecto.2014.12.017.

Lynds, R.M., and Slattery, J.S. (2017). Correlation of the Upper Cretaceous strata of Wyoming, *Wyoming State Geological Survey*.

Machado Júnior, D.L., Dehira, L.K., Carneiro, C.R., and Almeida, F.F.M. (1990). Reconstruções paleoambientais do Juro-Cretáceo no nordeste Brasileiro, *Revista Brasileira de Geociências*, *19*(4), 470–485.

Mackey, B.H., Scheingross, J.S., Lamb, M.P., and Farley, K.A. (2014). Knickpoint formation, rapid propagation, and landscape response following coastal cliff retreat at the last interglacial sea-level highstand: Kaua'i, Hawai'i, *GSA Bulletin*, *126*(7-8), 925–942, doi:10.1130/B30930.1.

Magara, K. (1980). Comparison of Porosity-Depth Relationships of Shale and Sandstone, *Journal of Petroleum Geology*, *3*(2), 175–185, doi:10.1111/j.1747-5457.1980.tb00981.x.

Magnavita, L.P., Davison, I., and Kusznir, N.J. (1994). Rifting, erosion and uplift history of the Recôncavo-Tucano-Jatobá Rift, northeast Brazil, *Tectonics*, *13*(2), 367–388, doi:10.1029/93TC02941.

Manspeizer, W. (1988). Triassic-Jurassic rifting: Continental Breakup and the Origin of the Atlantic Ocean and Passive Margins, *Developments in Geotectonics Volume 22*, doi:10.1016/B978-0-444-42903-2.50002-6.

Markwick, P.J. (2019). Palaeogeography in exploration, *Geological Magazine*, *156*(2), 366–407 doi:10.1017/S0016756818000468.

Marques, F.O., Nogueira, F.C.C., Bezerra, F.H.R., and De Castro, D.L. (2014). The Araripe Basin in NE Brazil: An intracontinental graben inverted to a high-standing horst, *Tectonophysics*, *630*, 251–264, doi:10.1016/j.tecto.2014.05.029.

Martill, D.M. (1988). Preservation of fish in the Cretaceous Santana Formation of Brazil, *Palaeontology*, *31*(1), 1–18.

Martin, J.E., Sawyer, J.F., Fahrenbach, M.D., Tomhave, D.W., and Schulz, L.D. (2004). Geologic Map of South Dakota, *South Dakota Geological Survey*, Scale 1:500,000.

Márquez, A., Oyarzun, R., Doblas, M., and Verma, S.P. (1999). Alkalic (ocean-island basalt type) and calc-alkalic volcanism in the Mexican volcanic belt: A case for plume-related magmatism and propagating rifting at an active margin?, *Geology*, *27*(1), 51–54, doi:10.1130/0091-7613(1999)027<0051:AOIBTA>2.3.CO;2.

Matmon, A., Bierman, P.R., Larsen, J., Southworth, S., Pavich, M., and Caffee, M. (2003). Temporally and spatially uniform rates of erosion in the southern Appalachian Great Smoky Mountains, *Geology*, *31*(2), 155–158, doi:10.1130/0091-7613(2003)031<0155:TASURO>2.0.CO;2.

Matmon, A., Bierman, P.R., Larsen, J., Southworth, S., Pavich, M., Finkel, R., and Caffee, M. (2003). Erosion of an ancient mountain range, the Great Smoky Mountains, North Carolina and Tennessee, *American Journal of Science*, *303*, 817–855, doi:10.2475/ajs.303.9.817.

McCave, I.N., and Swift, S.A. (1976). A physical model for the rate of deposition of fine-grained sediments in the deep sea, *GSA Bulletin*, *87*(4), 541–546, doi:10.1130/0016-7606(1976)87<541:APMFTR>2.0.CO;2.

McDonough, K.J., and Cross, T.A. (1991). Late Cretaceous sea level from a paleoshoreline, *Journal of Geophysical Research: Solid Earth*, *96*(B4), 6591–6607, doi:10.1029/91JB00281.

McKenna, M.C., and Love, J.D. (1972). High-level strata containing Early Miocene mammals on the Bighorn Mountains, Wyoming, *American Museum Novitates*, *2490*, 31.

McKenzie, D. (1978). Some remarks on the development of sedimentary basins, *Earth and Planetary Science Letters*, *40*(1), 25–32, doi:10.1016/0012-821X(78)90071-7.

McKenzie, D. (2003). Estimating T_e in the presence of internal loads, *Journal of Geophysical Research: Solid Earth*, *108*(B9), 1–21, doi:10.1029/2002JB001766.

McKenzie, D., Jackson, J., and Priestley, K. (2005). Thermal structure of oceanic and continental lithosphere, *Earth and Planetary Science Letters*, *233*(3-4), 337–349, doi:10.1016/j.epsl.2005.02.005.

McKenzie, D. (2010). The influence of dynamically supported topography on estimates of T_e, *Earth and Planetary Science Letters*, *295*, 127–138, doi:10.1016/j.epsl.2010.03.033.

McKeon, R.E., Zeitler, P.K., Pazzaglia, F.J., Idleman, B.D., and Enkelmann, E. (2014). Decay of an old orogen: Inferences about appalachian landscape evolution from low-temperature thermochronology, *GSA Bulletin*, *126*(1-2), 31–46, doi:10.1130/B30808.1.

McLaurin, B.T., and Steel, R.J. (2000). Fourth-order nonmarine to marine sequences, middle Castlegate Formation, Book Cliffs, Utah, *Geology*, *28*(4), 359–362, doi:10.1130/0091-7613(2000)28>359:FNTMSM<2.0.CO;2.

McMillan, M.E., Angevine, C.L., and Heller, P.L. (2002). Postdepositional tilt of the Miocene-Pleistocene Ogallala Group on the western Great Plains: Evidence of Late Cenozoic uplift of the Rocky Mountains, *Geology*, *30*, 63–66, doi:10.1130/0091-7613(2002)030<0063:PTOTMP>2.0.CO;2.

McMillan, M.E., Heller, P.L., and Wing, S.L. (2006). History and causes of post-Laramide relief in the Rocky Mountain orogenic plateau, *GSA Bulletin*, *118*(3-4), 393–405, doi:10.1130/B25712.1.

McNab, F., Ball, P.W., Hoggard, M.J., and White, N.J. (2018). Neogene uplift and magmatism of

Anatolia: Insights from drainage analysis and basaltic geochemistry, *Geochemistry, Geophysics, Geosystems*, *19*(1), 175–213, doi:10.1002/2017GC007251.

McQuarrie, N., and Chase, C.G. (2000). Raising the Colorado Plateau; discussion and reply, *Geology*, *28*(8), 767–768, doi:10.1130/0091-7613(2000)028<0091:RTCP>2.0.CO;2.

Menezes, M.R.F., Morais Neto, J.M., Szatmari, P., and York, D. (2003). Relações cronológicas entre o vulcanismo Macau e a Formação Serra do Martins com base na datação Ar/Ar do plug basáltico "Serrote Preto" (RN, Nordeste do Brasil), *IX Simpósio Nacional de Estudos Tectônicos - IIII International Symposium on Tectonics - Annals,Búzios, Brazil*, 246–249.

Menke, W., Skryzalin, P., Levin, V., Harper, T., Darbyshire, F., and Dong T., (2016). The Northern Appalachian Anomaly: A modern asthenospheric upwelling, *Geophysical Research Letters*, *43*, 10173–10179, doi:10.1002/ 2016GL070918.

Merewether, E.A., Cobban, W.A., and Obradovich, J.D. (2011). Biostratigraphic Data from Upper Cretaceous Formations–eastern Wyoming, Central Colorado, and Northeastern New Mexico, *U.S. Geological Survey Scientific Investigations Map 3175*, 2 sheets, pamphlet, 10 p.

Merewether, E.A., and McKinney, K.C. (2015). Composite biostratigraphic outcrop sections for Cretaceous Formations along a south-trending transect from northwestern Montana to northwestern New Mexico, *USGS*, *1258*, 20151, 087.

Merritts, D., Eby, R., Harris, R., Edwards, R.L., and Chang, H. (1999). Variable rates of Late Quaternary surface uplift along the Banda Arc-Australian plate collision zone, eastern Indonesia, *Geological Society, London, Special Publications*, *146*(1), 213–224, doi:10.1144/GSL.SP.1999.146.01.12.

Meyer, B., Tapponnier, P., Bourjot, L., Metivier, F., Gaudemer, Y., Peltzer, G., Shunmin, G. and Zhitai, C. (1998). Crustal thickening in Gansu-Qinghai, lithospheric mantle subduction, and oblique, strike-slip controlled growth of the Tibet plateau, *Geophysical Journal International*, *135*(1), 1–47, doi:10.1046/j.1365-246X.1998.00567.x.

Miller, K.G., Liu, C., and Feigenson, M.D. (1996). Oligocene to Middle Miocene Sr-Isotopic Stratigraphy of the New Jersey Continental Slope, *Proceedings from the Ocean Drilling Program, Scientific Results*, *150*, 97–114.

Miller, K.G., Mountain, G.S., Browning, J.V., Kominz, M., Sugarman, P.J., Christie-Blick, N., Katz, M., and Wright, J. D. (1998). Cenozoic Global Sea Level, Sequences, and the New Jersey Transect:

Results from Coastal Plain and Continental Slope Drilling, *Reviews of Geophysics*, *36*(4), 569–601, doi:10.1029/98RG01624.

Miller, K.G., Sugarman, P.J., Browning, J.V., McLaughlin, P.P., Benson, R.N., Hernández, J.C., Ramsey, K.W., Baxter, S.J., Feigenson, M.D., Aubry, M.-P., Monteverde, D.H., Cramer, B.S., Katz, M.E., McKenna, T.E., Strohmeier, S.A., Pekar, S.F., Uptegrove, J., Cobbs, G., Cobbs III, G., Curtin, S.E., (2003). Bethany Beach site, In *Proceedings of the Ocean Drilling Program, Initial Reports*, Vol.174AX (Suppl.), 1–85.

Miller, K.G., Kominz, M.A., Browning, J.V., Wright, J.D., Mountain, G.S., Katz, M.E., Sugarman, P.J., Cramer, B.S., Christie-Blick, N., and Pekar, S.F. (2005). The Phanerozoic Record of Global Sea-Level Change, *Science*, *310*(5752), 1293–1298, doi:10.1126/science.1116412.

Miller, K.G., Mountain, G.S., Wright, J.D., and Browning, J.V. (2011). A 180-million-year record of sea level and ice volume variations from continental margin and deep-sea isotopic records, *Oceanography*, *24*(2), 40–53.

Miller, S.R., Sak, P.B., Kirby, E., and Bierman, P.R. (2013). Neogene rejuvenation of central Appalachian topography: Evidence for differential rock uplift from stream profiles and erosion rates, *Earth and Planetary Science Letters*, *369-370*, 1–12, doi:10.1016/j.epsl.2013.04.007.

Miller, K.G., Browning, J.V., Sugarman, P.J., Monteverde, D.H., Andreasen, D.C., Lombardi, C., Thornburg, J., Fan, Y., and Kopp, R.E. (2017). Lower to Mid-Cretaceous Sequence Stratigraphy and Characterization of CO_2 Storage Potential in the Mid-Atlantic US Coastal Plain, *Journal of Sedimentary Research*, *87*(6), 609-629, doi:10.2110/jsr.2017.33.

Miller, K.G., Lombardi, C.J., Browning, J.V., Schmelz, W.J., Gallegos, G., Mountain, G.S., and Baldwin, K.E. (2018). Back to basics of sequence stratigraphy: early Miocene and mid-Cretaceous examples from the New Jersey paleoshelf, *Journal of Sedimentary Research*, *88*(1), 148–176, doi:10.2110/jsr.2017.73.

Milliken, K.T., M.D. Blum, J.W. Snedden, and W.E. Galloway (2018). Application of fluvial scaling relationships to reconstruct drainage basin evolution and sediment routing for the Cretaceous and Paleocene of the Gulf of Mexico, *Geosphere*, *14*(2), 749–767, doi:10.1130/GES01374.1.

Milliman, J.D., and Syvitski, J.P. (1992). Geomorphic/tectonic control of sediment discharge to the

ocean: the importance of small mountainous rivers, *The journal of Geology*, *100*(5), 525–544, doi:10.1086/629606.

Milliman, J., and Farnsworth, K. (2011). River Discharge to the Coastal Ocean: A Global Synthesis, *Cambridge University Press*, Cambridge, U.K, doi:10.5670/oceanog.2011.108.

Missimer, T.M., and Maliva, R.G. (2017). Late Miocene fluvial sediment transport from the southern Appalachian Mountains to southern Florida: An example of an old mountain belt sediment production surge, *Sedimentology*, *64*(7), 1846–1870, doi:10.1111/sed.12377.

Mitchell, S.G., Matmon, A., Bierman, P.R., Enzel, Y., Caffee, M., and Rizzo, D. (2001). Displacement history of a limestone normal fault scarp, northern Israel, from cosmogenic ^{36}Cl, *Journal of Geophysical Research: Solid Earth*, *106*(B3), 4247–4264, doi:10.1029/2000JB900373.

Mitrovica, J.X., Beaumont, C., and Jarvis, G.T. (1989). Tilting of continental interiors by the dynamical effects of subduction, *Tectonics*, *8*(5), 1079–1094, doi:10.1029/TC008i005p01079.

Mitrovica, J.X., Milne, G.A. (2002). On the origin of late Holocene sea-level highstands within equatorial ocean basins, *Quaternary Science Reviews*, *21*(20), 2179–2190, doi:10.1016/S0277-3791(02)00080-X.

Mitrovica, J.X., Austermann, J., Coulson, S., Creveling, J.R., Hoggard, M.J., Jarvis, G.T., and Richards, F.D. (2020). Dynamic Topography and Ice Age Paleoclimate, *Annual Review of Earth and Planetary Sciences*, *48*, 585–621, doi:10.1146/annurev-earth-082517-010225.

Mix, H.T., Mulch, A., Kent-Corson, M.L., and Chamberlain, C.P. (2011). Cenozoic migration of topography in the North American Cordillera, *Geology*, *39*(1), 87–90, doi:10.1130/G31450.1.

Molnar, P., and England, P. (1990). Late Cenozoic uplift of mountain ranges and global climate change: chicken or egg?, *Nature*, *346*(6279), 29–34, doi:10.1038/346029a0.

Molnar, P., (2004). Late Cenozoic increase in accumulation rates of terrestrial sediment: how might climate change have affected erosion rates? *Annual Review of Earth and Planetary Science 32*, 67–89, doi:10.1146/annurev.earth.32.091003.143456.

Molnar, P., England, P.C., and Jones, C.H. (2015). Journal of Geophysical Research: Solid Earth, *Journal of Geophysical Research*, *120*, 1932–1957, doi:10.1002/2014JB011724.

Moodie, A. J., Pazzaglia, F. J., and Berti, C. (2018). Exogenic forcing and autogenic processes on continental divide location and mobility, *Basin Research*, *30*(2), 344–369, doi:10.1111/bre.12256.

Monteverde, D.H., Mountain, G.S., and Miller, K.G. (2008). Early Miocene sequence development across the New Jersey margin, *Basin Research*, *20*, 249–267, doi:10.1111/j.1365-2117.2008.00351.x.

Montgomery, D.R., and López-Blanco, J. (2003). Post-Oligocene river incision, southern Sierra Madre Occidental, Mexico, *Geomorphology*, *55*(1-4), 235–247, doi:10.1016/S0169-555X(03)00142-9.

Morais Neto, J., Hegarty, K.A., Karner, G.D., and Alkmim, F.F.D. (2009). Timing and mechanisms for the generation and modification of the anomalous topography of the Borborema Province, northeastern Brazil, *Marine and Petroleum Geology*, *26*(7), 1070–1086, doi:10.1016/j.marpetgeo.2008.07.002.

Morgan, P., and Swanberg, C.A. (1985). On the Cenozoic uplift and tectonic stability of the Colorado Plateau, *Journal of Geodynamics*, *3*(1–2), 39–63, doi:10.1016/0264-3707(85)90021-3.

Morris, M., Fernandes, V.M., and Roberts, G.G. (2020). Extricating dynamic topography from subsidence patterns: Examples from Eastern North America's passive margin, *Earth and Planetary Science Letters*, *530*, 115840, doi:10.1016/j.epsl.2019.115840.

Morrison, R.B. (1991). Quaternary stratigraphic, hydrologic, and climatic history of the Great Basin, with emphasis on Lakes Lahontan, Bonneville, and Tecopa, *Quaternary Nonglacial Geology: Conterminous US*, *2*, 283–320, doi:10.1002/2014JB011724.

Moucha, R., Forte, A.M., Mitrovica, J.X., Rowley, D.B., Quéré, S., Simmons, N.A., and Grand, S.P. (2016). Dynamic topography and long-term sea-level variations: There is no such thing as a stable continental platform, *Earth and Planetary Science Letters*, *271*(1–4), 101–108, doi:10.1016/j.epsl.2008.03.056.

Moucha, R., Forte, A.M., Rowley, D.B., Mitrovica, J.X., Simmons, N.A., and Grand, S.P. (2008)b. Mantle convection and the recent evolution of the Colorado Plateau and the Rio Grande Rift valley, *Geology*, *36*(6), 439–442, doi:10.1130/G24577A.1.

Moucha, R., and Ruetenik, G.A. (2017). Interplay between dynamic topography and flexure along the US Atlantic passive margin: Insights from landscape evolution modeling, *Global and Planetary Change*, *149*, 72–78, doi:10.1016/j.gloplacha.2017.01.004.

Moulik, P., Ekstrom, G. (2014). An anisotropic shear velocity model of the Earth's mantle using normal modes, body waves, surface waves and long-period wave-forms, *Geophysical Journal International*, *199*(3), 1713–1738, doi:10.1093/gji/ggu356.

Mountain, G.S., Damuth, J.E., Lorenzo, J.M., and Fulthorpe, C.S. (1996). Origin, reburial, and significance of a Middle Miocene canyon, New Jersey contiental slope, *Proceedings of the Ocean Drilling Program, Scientific Results*, *150*, 283–292.

Müller, R.D., Sdrolias, M., Gaina, C., Steinberger, B., and Heine, C. (2008). Long-term sea-level fluctuations driven by ocean basin dynamics, *Science*, *319*(5868), 1357–1362, doi:10.1126/science.1151540.

Müller, R.D., Hassan, R., Gurnis, M., Flament, N., and Williams, S.E., (2018). Dynamic topography of passive continental margins and their hinterlands since the Cretaceous, *Gondwana Research*, *53*, 225–251, doi:10.1016/j.gr.2017.04.028.

Naeser, N.D., Naeser, C.W., Southworth, C.S., Morgan, B.A., and Schultz, A.P. (2004). Paleozoic to Recent Tectonic and Denudation History of Rocks in the Blue Ridge Province, Central and Southern Appalachians–Evidence from Fission-Track Thermochronology, *Geological Society of America, Abstracts with Programs*, *36*(2).

Naeser, C.W., Naeser, N.D., Newell, W.L., Southworth, S., Edwards, L.E., and Weems, R.E. (2016). Erosional and depositional history of the Atlantic passive margin as recorded in detrital zircon fission-track ages and lithic detritus in Atlantic Coastal Plain sediments, *American Journal of Science*, *316*(2), 110–168, doi:10.2475/02.2016.02.

Nassichuk, W.W., and McIntyre, D.J. (1995). Cretaceous and Tertiary fossils discovered in kimberlites at Lac de Gras in the Slave Province, Northwest Territories, *Geological Survey of Canada Geological Survey of Canada Current Research*, *B*, 109–114.

Nereson, A., Stroud, J., Karlstrom, K., Heizler, M., and McIntosh, W. (2013). Dynamic topography of the western Great Plains: Geomorphic and $^{40}Ar/^{39}Ar$ evidence for mantle-driven uplift associated with the Jemez lineament of NE New Mexico and SE Colorado, *Geosphere*, *9*(3), 521–545, doi:10.1130/GES00837.1.

Newton, E.T. (1892). Note on an iguanodont tooth from the lower Chalk ("Totternhoe Stone"), near Hitchin, *Geological Magazine, new series*, *3*(9), 49–50.

Nicol, A., Walsh, J., Watterson, J., and Underhill, J.R. (1997). Displacement rates of normal faults, *Nature*, *390*, 157–159, doi:10.1038/36548.

Nurkowski, J.R. (1984). Coal quality, coal rank variation and its relation to reconstructed overburden, Upper Cretaceous and Tertiary plains coals, Alberta, Canada, *AAPG Bulletin*, *68*(3), 285–295, doi:10.1306/AD460A12-16F7-11D7-8645000102C1865D.

Obradovich, J.D., and Cobban, W.A. (1975). A time-scale for the Late Cretaceous of the Western Interior of North America, *Geological Association of Canada Special Paper 13*, 31–54.

Ojeda, H.A.O. (1983). Estrutura e evolução das bacias mesozóicas emersas da margem continental brasileira, *Revista Brasileira de Geociências*, *13*(2), 71–83.

O'Leary, M.A., Bouaré, M.L., Claeson, K.M., Heilbronn, K., Hill, R.V., McCartney, J., Sessa, J.A., Sissoko, F., Tapanila, L., Wheeler, E., and Roberts, E.M. (2019). Stratigraphy and Paleobiology of the Upper Cretaceous-Lower Paleogene Sediments from the Trans-Saharan Seaway in Mali, *Bulletin of the American Museum of Natural History*, *436*, 1–183, doi:10.1206/003-0090.436.1.1.

Olesen, J. (1991). Foraminiferal biostratigraphy and paleoecology of the Mancos Shale (Upper Cretaceous), southwestern Black Mesa, Arizona, *in* Nationa, J., and Eaton J.G. (eds.), Stratigraphy, Depositional Environments, and Sedimentary Tectonics of the Western Margin, Cretaceous Western Interior Seaway, *Geological Society of America Special Paper, 260*, 153–166.

Oliveira, R.G., and Medeiros, W.E. (2012). Evidences of buried loads in the base of the crust of Borborema Plateau (NE Brazil) from Bouguer admittance estimates, *Journal of South American Earth Sciences*, *37*, 60–76, doi:10.1016/j.jsames.2012.02.004.

Olson, H.C., and Keckie, R.M. (2003). Foraminifera as proxies for sea-level change on siliciclastic margins, *SEPM Special Publication*, *74*, 5–19, doi:10.2110/pec.03.75.0005.

Olsson, R.K., Gibson, T.G., Hansen, H.J., and Owens, J.P. (1988). Geology of the northern Atlantic coastal plain: Long Island to Virginia, *in* Sheridan, R.E., and Grow, J.A. (eds.), *The Atlantic Continental Margin*, DNAG Geology of North America Volume I-2, Geological Society of America, Boulder, CO, doi:10.1130/DNAG-GNA-I2.

Lillegraven, J.A., and Ostresh Jr., L.M. (1990). Late Cretaceous (earliest Campanian/Maastrichtian) evolution of western shorelines of the North American Western Interior Seaway in relation to known mammalian faunas, *in* Bown, T.M., and Rose, K.D. (eds.), Dawn of the age of mammals in the

northern part of the Rocky Mountain Interior, North America, *Geological Society of America Special Paper 243*, 1–30.

O'Sullivan, P.B., and Currie, L.D. (1996). Thermotectonic history of Mt Logan, Yukon Territory, Canada: Implications of multiple episodes of middle to late Cenozoic denudation, *Earth and Planetary Science Letters*, *144*, 251–261, doi:10.1016/0012-821X(96)00161-6.

O'Sullivan, P.B., and Lane, L.S. (1997). Early Tertiary thermotectonic history of the northern Yukon and adjacent Northwest Territories, Arctic Canada, *Canadian Journal of Earth Sciences*, *34*(10), 1366–1378, doi:10.1139/e17-109.

Palmer, K.V., and Brann, D.C. (1965). Catalogue of the Paleocene and Eocene mollusca of the southern and eastern United States. Part 1. Pelecypoda–Amphineura–Peteropoda–Scaphopoda and Cephalopoda, *Bulletins of American Paleontology*, *48*, 1–471.

Palmer, A.R. (1983). *The Decade of North America Geology 1983 Geologic Time Scale*, Geological Society of America, Boulder, CO.

Pang, M., and Nummedal, D. (1995). Flexural subsidence and basement tectonics of the Cretaceous Western Interior basin, United States, *Geology*, *23*(2), 173–176, doi:10.1130/0091-7613(1995)023<0173:FSABTO>2.3.CO;2.

Parker, R.L. (1994), Geophysical Inverse Theory, *Princeton University Press*.

Parnell-Turner, R., White, N.J., McCave, I.N., Henstock, T.J., Murton, B., and Jones, S.M. (2015). Architecture of North Atlantic contourite drifts modified by transient circulation of the Icelandic mantle plume, *Geochemistry, Geophysics, Geosystems*, *16*, 3414–35, doi:10.1002/2015GC005947.

Parsons, B., and Sclater, J.G. (1977). An analysis of the variation of ocean floor bathymetry and heat flow with age, *Journal of Geophysical Research*, *82*(5), 803–827, doi:10.1029/JB082i005p00803.

Paul, J.D., Roberts, G.G., and White, N. (2014). The African landscape through space and time, *Tectonics*, *33*(6), 898–935, doi:10.1002/2013TC003479.

Pavich, M.J., Brown, L., Valette-Silver, J.N., Klein, J., and Middleton, R. (1985). ^{10}Be analysis of a Quaternary weathering profile in the Virginia Piedmont, *Geology*, *13*(1), 39–41, doi:10.1130/0091-7613(1985)13<39:BAOAQW>2.0.CO;2.

Pazzaglia, F.J., and Gardner, W. (1994). Late Cenozoic flexural deformation of the middle U.S. Atlantic passive margin, *Journal of Geodynamics*, *99*(B6), 12,143–12,157, doi:10.1029/93JB03130.

Pazzaglia, F.J., and Brandon, M.T. (1996). Macrogeomorphic evolution of the post-Triassic Appalachian mountains determined by deconvolution of the offshore basin sedimentary record, *Basin Research*, *8*(3), 1–24, doi:10.1046/j.1365-2117.1996.00274.x.

Pazzaglia, F.J., and Gardner, T.W. (1993). Fluvial terraces of the Susquehanna River, *Geomorphology*, *8*, 83–113, doi:10.1016/0169-555X(93)90031-V.

Pedersen, V.K., Braun, J., and Huismans, R.S. (2018). Eocene to mid-Pliocene landscape evolution in Scandinavia inferred from offshore sediment volumes and pre-glacial topography using inverse modelling, *Geomorphology*, *303*, 467–485, doi:doi.org/10.1016/j.geomorph.2017.11.025.

Pedoja, K., Ortlieb, L., Dumont, J.F., Lamothe, M., Ghaleb, B., Auclair, M., and Labrousse, B. (2006). Quaternary coastal uplift along the Talara Arc (Ecuador, Northern Peru) from new marine terrace data, *Marine Geology*, *228*(1-4), 73–91, doi:10.1016/j.margeo.2006.01.004.

Pedoja, K., Husson, L., Johnson, M.E., Melnick, D., Witt, C., Pochat, S., Nexer, M., Delcaillau, B., Pinegina, T., Poprawski, Y., and Authemayou, C. (2014). Coastal staircase sequences reflecting sea-level oscillations and tectonic uplift during the Quaternary and Neogene, *Earth-Science Reviews*, *132*, 13–38, doi:10.1016/j.earscirev.2014.01.007.

Peel, F.J., Travis, C.J., and Hossback, J.R. (1995). Genetic structural provinces and salt tectonics of the Cenozoic offshore U.S. Gulf of Mexico: a preliminary analysis, *in* Jackson, M.P.A., Roberts, D.G., and Snelson, S. (eds.), Salt tectonics a Global. Perspective, 153–175, *AAPG Memoir*.

Pekar, S.F., Miller, K.G., and Kominz, M.A. (2000). Reconstructing the stratal geometry of latest Eocene to Oligocene sequences in New Jersey: resolving a patchwork distribution into a clear pattern of progradation, *Sedimentary Geology*, *134*(1-2), 93–109, doi:10.1016/S0037-0738(00)00015-4.

Pekar, S.F., Christie-Blick, N., Miller, K.G.,and Kominz, M.A. (2003). Quantitative constraints on the origin of stratigraphic architecture at passive continental margins: Oligocene sedimentation in New Jersey, USA, *Journal of Sedimentary Research*, *73*(2), 227–245, doi:10.1306/090402730227.

Pereira, P.A., Cassab, R.C.T., and Barreto, A.M.F. (2016). Cassiopidae gastropods, influence of Tethys Sea of the Romualdo Formation (Aptian–Albian), Araripe Basin, Brazil, *Journal of South American Earth Sciences*, *70*, 211–223, doi:10.1016/j.jsames.2016.05.005.

Perrigo, A., Hoorn, C., and Antonelli, A. (2019). Why mountains matter for biodiversity, *Journal of Biogeography*, *47*(2), 315–325, doi:10.1111/jbi.13731.

Pessoa Neto, O.C., Soares, U.M., Silva, J.G.F., Roesner, E.H., Florencio, C.P., and Souza, C.A.V. (2007). Bacia Potiguar, *Boletim de Geociências – Petrobras*, *15*(2), 357–369.

Petter, A.L., Steel, R.J., Mohrig, D., Kim, W., and Carvajal, C. (2013). Estimation of the paleoflux of terrestrial-derived solids across ancient basin margins using the stratigraphic record, *GSA Bulletin*, *125*(3-4), 578–593, doi:10.1130/B30603.1.

Peulvast, J., and Bétard, F. (2015). A history of basin inversion, scarp retreat and shallow denudation: The Araripe basin as a keystone for understanding tong-term landscape evolution in NE Brazil, *Geomorphology*, *233*, 20–40, doi:10.1016/j.geomorph.2014.10.009.

Peyton, S.L., and B. Carrapa (2013). An overview of low-temperature thermochronology in the Rocky Mountains and its application to petroleum system analysis, *in* Knight, C., and Cuzella, J. (eds.), Application of structural methods to Rocky Mountain hydrocarbon exploration and development, *AAPG Studies in Geology*, *65*, 37–70, doi:10.1306/13381689St653578.

Pico, T., Mitrovica, J.X., Perron, J.T., Ferrier, K.L., and Braun, J. (2019). Influence of glacial isostatic adjustment on river evolution along the US mid-Atlantic coast, *Earth and Planetary Science Letters*, *522*, 176–185, doi:10.1016/j.epsl.2019.06.026.

Pinet, P. R., and Popenoe, P. (1982). Blake Plateau: Control of Miocene sedimentation patterns by large-scale shifts of the Gulf Stream axis, *Geology*, *10*(5), 257–259, doi:10.1130/0091-7613(1982)10<257:BPCOMS>2.0.CO;2.

Pinet, P.R., and Popenoe, P. (1985). Shallow seismic stratigraphy and post-Albian geologic history of the northern and central Blake Plateau, *Geological Society of America Bulletin*, *96*(5), 627–638, doi:10.1130/0016-7606(1985)96<627:SSSAPG>2.0.CO;2.

Pinet, P., and Souriau, M. (1988). Continental erosion and large-scale relief, *Tectonics*, *7*(3), 563–582, doi:10.1029/TC007i003p00563.

Plint, A.G., Tyagi, A., Hay, M.J., Varban, B.L., Zhang, H., and Roca, X. (2009). Clinoforms, paleobathymetry, and mud dispersal across the Western Canada Cretaceous foreland basin: evidence from the Cenomanian Dunvegan Formation and contiguous strata, *Journal of Sedimentary Research*, *79*(3), 144–161, doi:10.2110/jsr.2009.020.

Poag, C.W. (1992). US middle Atlantic continental rise: Provenance, dispersal, and deposition of Jurassic to Quaternary sediments, *Geologic Evolution of Atlantic Continental Rises*, Van Nostrand Reinhold, New York, 100, 156.

Poag, C.W., and Ward, L.W. (1993). Allostratigraphy of the U.S. Middle Atlantic Continental Margin–Characteristics, Distribution and Depositional History of Principal Unconformity-Bounded Upper Cretaceous and Cenozoic Sedimentary Units, *U.S. Geological Survey Professional Paper 1542*, 81 p.

Poag, C.W., and Sevon, W.D. (1989). A record of Appalachian denudation in postrift Mesozoic and Cenozoic sedimentary deposits of the U.S. Middle Atlantic continental margin, *Geomorphology*, *2*(1-3), 119–157, doi:10.1016/0169-555X(89)90009-3.

Portenga, E.W., Bierman, P.R., Rizzo, D.M., and Rood, D.H. (2013). Low rates of bedrock outcrop erosion in the Central Appalachian mountains inferred from in situ ^{10}Be, *GSA Bulletin*, *125*(1-2), 201–215, doi:10.1130/B30559.1.

Portenga, E.W., Bierman, P.R., Trodick Jr., C.D., Greene, S.E., DeJong, B.D., Rood, D.H., and Pavich, M.J. (2019). Erosion rates and sediment flux within the Potomac River basin quantified over millennial timescales using beryllium isotopes, *GSA Bulletin*, *131*(7-8), 1295–1311, doi:10.1130/B31840.1.

Posamentier, H.W., Jervey, M.T., and Vail, P.R. (1988). Eustatic controls on clastic deposition I – conceptual framework, *in* Sea-Level Changes: an Integrated Approach, *Special Publications of SEPM 42*, 125–154.

Prado, L.A.C., Pereira, P.A., Sales, A.M.F., and Barreto, A.M.F. (2016). Tafonomia dos Invertebrados do Sítio Canastra, Formação Romualdo, Cretáceo Inferior, Bacia do Araripe, Araripina, Pernambuco, Brasil, *Anuário do Instituto de Geociências*, *39*(2), 77–87.

Priestley, K., and McKenzie, D. (2006). The thermal structure of the lithosphere from shear wave velocities, *Earth and Planetary Science Letters*, *244*(1-2), 285–301, doi:10.1016/j.epsl.2006.01.008.

Priestley, K., and McKenzie, D. (2013). The relationship between shear wave velocity, temperature, attenuation and viscosity in the shallow part of the mantle, *Earth and Planetary Science Letters*, *381*, 78–91, doi:10.1016/j.epsl.2013.08.022.

Prince, P.S., and Spotila, J.A. (2013). Evidence of transient topographic disequilibrium in a landward

passive margin river system: Knickpoints and paleo-landscapes of the New River basin, southern Appalachians, *Earth Surface Processes and Landforms*, *38*(14), 1685–1699, doi:10.1002/esp.3406.

Pritchard, D., Roberts, G.G., White, N.J., and Richardson. C.N. (2009). Uplift histories from river profiles, *Geophysical Research Letters*, *36*(24), 1–5, doi:10.1029/2009GL040928.

Ramirez-Herrera, M.T., Kostoglodov, V., and Urrutia-Fucugauchi, J. (2011). Overview of recent coastal tectonic deformation in the Mexican subduction zone, *Pure and Applied Geophysics*, *168*(8-9), 1415–1433, doi:10.1007/s0024-010-0205-y.

Raymo, M.E. , Ruddiman, W.F., Philip N. Froelich; Influence of late Cenozoic mountain building on ocean geochemical cycles. Geology ; 16 (7): 649–653. doi: https://doi.org/10.1130/0091-7613(1988)016¡0649:IOLCMB¿2.3.CO;2

Raymo, M.E., and Ruddiman, W.F. (1992). Tectonic forcing of late Cenozoic climate, *Nature*, *359*(6391), 117–122, doi:10.1038/359117a0.

Read, J.F. (1985). Carbonate Platform Facies Models, *APPG Bulletin*, *69*(1), 1–21, doi:10.1306/AD461B79-16F7-11D7-8645000102C1865D.

Reed, J.C., Wheeler, J.O., Tucholke, B.E., Card, K.D., Davidson, A., Hoffman, P.F., Okulitch, A.V., Palmer, A.R., Sanford, B.V., Williams, G.K., Williams, H., Dixon, J., Embry, A.F., Holcombe, T.L., Laine, E.P., Mountain, G.S., Popenoe, P., and Wiley, T. (2005). Geologic map of North America: Geological Society of America, Continent-Scale Map 001, scale 1:5,000,000, *Geological Society of America*, Boulder-CO, USA.

Reilinger, R., McClusky, S., Paradissis, D., Ergintav, S., and Vernant, P. (2010). Geodetic constraints on the tectonic evolution of the Aegean region and strain accumulation along the Hellenic subduction zone, *Tectonophysics*, *488*(1–4), 22–30, doi:10.1016/j.tecto.2009.05.027.

Reiners, P.W., and Brandon, M.T. (2006). Using thermochronology to understand orogenic erosion, *Annual Review of Earth and Planetary Science*, *34*, 419–466, doi:10.1146/annurev.earth.34.031405.125202.

Rengers, F.K., and Tucker, G.E. (2014). Analysis and modeling of gully headcut dynamics, North American high plains, *Journal of Geophysical Research: Earth Surface*, *119*(5), 983–1003, doi:10.1002/2013JF002962.

Repasch, M., Karlstrom, K., Heizler, M., and Pecha, M. (2017). Birth and evolution of the Rio Grande fluvial system in the past 8 Ma: Progressive downward integration and the influence of tectonics, volcanism, and climate, *Earth-Science Reviews*, *168*, 113–164, doi:10.1016/j.earscirev.2017.03.003.

Reusser, L., Bierman, P., Pavich, M., Zen, E., Larssen, J. and Finkel, R. (2004). Rapid Late Pleistocene Incision of Atlantic Passive-Margin River Gorges, *Science*, *305*(5683), 499–502, doi:10.1126/science.1097780.

Reymer, A., and Schubert, G. (1984). Phanerozoic addition rates to the continental crust and crustal growth, *Tectonics*, *3*(1), 63–77, doi:10.1029/TC003i001p00063.

Ricard, Y., Richards, M., Lithgow-Bertelloni, C., and Le Stunff, Y. (1993). A geodynamic model of mantle density heterogeneity, *Journal of Geophysical Research: Solid Earth*, *98*(B12), 21895–21909, doi:10.1029/93JB02216.

Richard, S.M., Reynolds, S.J., Spencer, J.E., and Pearthree, P.A. (2000). Geologic Map of Arizona, *Arizona Geological Survey*, *Map 35*, 1 sheet, Scale 1:1,000,000.

Ritsema, J., Deuss, A., van Heijst, H.J., and Woodhouse, J.H. (2011). S40RTS: a degree-40 shear-velocity model for the mantle from new Rayleigh wave dispersion, teleseismic traveltime and normal-mode splitting function measurements, *Geophysical Journal International*, *184*(3), 1223–1236, doi:10.1111/j.1365-246X.2010.04884.x.

Roberts, L.N., and Kirschbaum, M.A. (1995). Paleogeography of the Late Cretaceous of the Western Interior of middle North America–Coal distribution and sediment accumulation, *U.S. Geological Survey Professional Paper 1561*, 115 p.

Roberts, G.G., and White, N. (2010). Estimating uplift rate histories from river profiles using African examples, *Journal of Geophysical Research: Solid Earth*, *115*(2), 1–24, doi:10.1029/2009JB006692.

Roberts, G.G., White, N.J., Martin-Brandis, G.L., and Crosby, A.G. (2012a), An uplift history of the Colorado Plateau and its surroundings from inverse modeling of longitudinal river profiles, *Tectonics*, *31*(4), 1–25, doi:10.1029/2012TC003107.

Roberts, G.G., Paul, J.D., White, N., and Winterbourne, J. (2012b), Temporal and spatial evolution of dynamic support from river profiles: A framework for Madagascar, *Geochemistry, Geophys. Geosystems*, *13*(4), 1–23, doi:10.1029/2012GC004040.

Roberts, G.G., White, N., Hoggard, M.J., Ball, P.W., and Meenan, C. (2018). A Neogene history of mantle convective support beneath Borneo, *Earth and Planetary Science Letters*, *496*, 142–158, doi:10.1016/j.epsl.2018.05.043.

Roberts, G.G., White, N.J., and Lodhia, B.H. (2019). Generation and scaling of longitudinal river profiles, *Journal of Geophysical Research: Earth Surface*, *124*(1), 137–153, doi:10.1029/2018JF004796.

Roberts, G.G. (2019). Scales of similarity and disparity between drainage networks, *Geophysical Research Letters*, *46*(7), 3781–3790, doi: 10.1029/2019GL082446.

Roberts, G.G., and Mannion, P.D. (2019). Timing and periodicity of Phanerozoic marine biodiversity and environmental change, *Scientific Reports*, *9*, 6116, doi:10.1038/s41598-019-42538-7.

Roden-Tice, M.K., Eusden, J.D., and Wintsch, R.P. (2012). Apatite fission-track evidence for the Cretaceous development of kilometer-scale relief and steady-state Tertiary topography in New England, *Geomorphology*, *141-142*, 114–120, doi:10.1016/j.geomorph.2011.12.029.

Rodrigues, R. (1995). A geoquimica orgânica da Bacia do Parnaíba, Doctoral Thesis, Universidade Federal do Rio Grande do Sul – UFRGS, 225 pp.

Rodríguez Tribaldos, V., White, N.J., Roberts, G.G., and Hoggard, M.J. (2017). Spatial and temporal uplift history of South America from calibrated drainage analysis, *Geochemistry, Geophysics, Geosystems*, *18*(6), 2321–2353, doi:10.1002/2017GC006909.

Roe, G.H., Whipple, K.X., and Fletcher, J.K. (2008). Feedbacks among climate, erosion, and tectonics in a critical wedge orogen, *American Journal of Science*, *308*(7), 815–842, doi:10.2475/07.2008.01.

Rogers, R.D., Kárason, H., and van der Hilst, R.D. (2002). Epeirogenic uplift above a detached slab in northern Central America, *Geology*, *30*(11), 1031–1034, doi:10.1130/0091-7613(2002)030<1031:EUAADS>2.0.CO;2.

Rohrman, M., van der Beek, P.A., Van Der Hilst, R.D., and Reemst, P. (2002). Timing and mechanisms of North Atlantic Cenozoic uplift: evidence for mantle upwelling, *Geological Society, London, Special Publications*, *196*(1), 27–43, doi:10.1144/GSL.SP.2002.196.01.03.

Rosenbloom, N.A., and Anderson, R.S. (1994). Hillslope and channel evolution in a marine terraced landscape, Santa Cruz, California, *Journal of Geophysical Research: Solid Earth*, *99*, 13–14, doi:10.1029/94JB00048.

Rossetti, D.F., and Santos Jr., A.E.A. (2004). Facies architecture in a tectonically-influenced estuarine incised valley fill of Miocene age, northern Brazil, *Journal of South American Earth Sciences*, *17*, 267–284, doi:10.1016/j.jsames.2004.08.003.

Rossetti, D.F., Bezerra, F.H.R., and Dominguez, J.M.L. (2013). Late Oligocene-Miocene transgressions along the equatorial and eastern margins of Brazil, *Earth-Science Reviews*, *123*, 87–112, doi:10.1016/j.earscirev.2013.04.005.

Rovere, A., Raymo, M.E., Mitrovica, J.X., Hearty, P.J., Leary, M.J.O., and Inglis, J.D. (2014). The mid-Pliocene sea-level conundrum: glacial isostasy, eustasy and dynamic topography, *Earth and Planetary Science Letters*, *387*, 27–33, doi:10.1016/j.epsl.2013.10.030.

Rowley, D.B. (2013). Sea level: Earth's dominant elevation–Implications for duration and magnitudes of sea level variations, *The Journal of Geology*, *121*(5), 445–454, doi:10.1086/671392.

Roy, M., Jordan, T.H., and Pederson, J.L. (2009). Colorado Plateau magmatism and uplift by warming of heterogeneous lithosphere., *Nature*, *459*(7249), 978–82, doi:10.1038/nature08052.

Royden, L., and Perron, J.T. (2013). Solutions of the stream power equation and application to the evolution of river longitudinal profiles, *Journal of Geophysical Research: Earth Surface*, *118*(2), 497–518, doi:10.1002/jgrf.20031.

Ruddiman, W.F., and Kutzbach, J.E. (1989). Forcing of late Cenozoic northern hemisphere climate by plateau uplift in southern Asia and the American West, *Journal of Geophysical Research: Atmospheres*, *94*(D15), 18409–18427, doi:10.1017/S0263593300020812.

Rudge, J.F., Champion, M.E.S., White, N., McKenzie, D., and Lovell, B. (2008). A plume model of transient diachronous uplift at the Earth's surface, *Earth and Planetary Science Letters*, *267*(1–2), 146–160, doi:10.1016/j.epsl.2007.11.040.

Rudge, J.F., Roberts, G.G., White, N.J., and Richardson, C.N. (2015). Uplift histories of Africa and Australia from linear inverse modeling of drainage inventories, *Journal of Geophysical Research: Earth Surface*, *120*(5), 894–914, doi:10.1002/2014JF003297.

Ruetenik, G., Moucha, R., and de Boer, B. (2019). Deformation in response to landscape evolution during glacial cycles on the US Atlantic passive margin, *Earth and Planetary Science Letters*, *526*, 115759, doi:10.1016/j.epsl.2019.115759.

Sadler, P.M. (1981). Sediment accumulation rates and the completeness of stratigraphic sections, *The Journal of Geology*, *89*(5), 569–584, doi:10.1086/628623.

Sageman, B.B (1989). The benthic boundary biofacies model: Hartland Shale Member, Greenhorn Formation (Cenomanian), Western Interior, North America, *Paleogeography, Paleoclimatology, Paleoecology*, *74*, 87–110, doi:10.1016/0031-0182(89)90021-7.

Sageman, B.S., and Bina, C.R. (1997). Diversity and Species Abundance Patterns in Late Cenomanian Black Shale Biofacies–Western Interior–U.S., *Palaios*, *12*, 449–466, doi:10.2307/3515383.

Sahagian, D. (1987). Epeirogeny and eustatic sea level changes as inferred from Cretaceous shoreline deposits: Applications to the central and western United States, *Journal of Geophysical Research: Solid Earth*, *92*, 4895–4904, doi:10.1029/JB092iB06p04895.

Sahagian, D. (1988). Epeirogenic motions of Africa as inferred from Cretaceous shoreline deposits, *Tectonics*, *7*(1), 125–138, doi:10.1029/TC007i001p00125.

Sahagian, D., and Jones, M. (1993). Quantified Middle Jurassic to Paleocene eustatic variations based on Russian Platform stratigraphy: Stage level resolution, *GSA Bulletin*, *105*(8), 1109–1118, doi.org/10.1130/0016-7606(1993)105<1109:QMJTPE>2.3.CO;2.

Sahagian, D., Pinous, O., Olferiev, A., and Zakharov, V. (1996). Eustatic Curve for the Middle Jurassic—Cretaceous based on Russian Platform and Siberian Stratigraphy: Zonal Resolution, *AAPG bulletin*, *80*(9), 1433–1458, doi:10.1306/64ED9A56-1724-11D7-8645000102C1865D.

Sahagian, D., and Proussevitch, A. (2007). Paleoelevation measurement on the basis of vesicular basalts, *Reviews in Mineralogy and Geochemistry*, *66*(1), 195–213, doi:10.2138/rmg.2007.66.8.

Salles, T. (2015). Badlands: A parallel basin and landscape dynamics model, *SoftwareX*, *5*, 195–202, doi:10.1016/j.softx.2016.08.005.

Salles, T., Flament, N., and Muller, D. (2017). Influence of mantle flow on the drainage of eastern Australia since the Jurassic Period, *Geochemistry, Geophysics, Geosystems*, *18*, 280–305, doi:10.1002/2016GC006617.

Salles, T., Ding, X., and Brocard, G. (2018). pyBadlands: A framework to simulate sediment transport, landscape dynamics and basin stratigraphic evolution through space and time, *PloS one*, *13*(4), e0195557, doi:10.1371/journal.pone.0195557.

Schaeffer, A.J., and Lebedev, S. (2013). Global shear speed structure of the upper mantle and transition zone, *Geophysical Journal International*, *149*, 417–449, doi:10.1093/gji/ggt095.

Schildgen, T.F., Ehlers, T.A., Whipp, D.M., van Soest, M.C., Whipple, K.X., and Hodges, K.V. (2009). Quantifying canyon incision and Andean Plateau surface uplift, southwest Peru: A thermochronometer and numerical modeling approach, *Journal of Geophysical Research: Earth Surface*, *114*, F04014, doi:10.1029/2009JF001305.

Schildgen, T.F., Cosentino, D., Caruso, A., Buchwaldt, R., Yıldırım, C., Bowring, S.A., Rojay, B., Echtler, H., and Strecker, M.R. (2012). Surface expression of eastern Mediterranean slab dynamics: Neogene topographic and structural evolution of the southwest margin of the Central Anatolian Plateau, Turkey, *Tectonics*, *31*(2), TC2005, doi:10.1029/2011TC003021.

Schildgen, T.F., Yıldırım, C., Cosentino, D., and Strecker, M.R. (2014). Linking slab break-off, Hellenic trench retreat, and uplift of the Central and Eastern Anatolian plateaus, *Earth-Science Reviews*, *128*, 147–168, doi:10.1016/j.earscirev.2013.11.006.

Schildgen, T.F., van der Beek, P.A., Sinclair, H.D., and Thiede, R.C. (2018). Spatial correlation bias in late-Cenozoic erosion histories derived from thermochronology, *Nature*, *559*(7712), 89–93, doi:10.1038/s41586-018-0260-6.

Schlee. J.S. (1981). Seismic stratigraphy of Baltimore Canyon Trough, *AAPG Bulletin*, *54*, 26–53, doi:10.1306/2F91976A-16CE-11D7-8645000102C1865D.

Schlunegger, F., Leu, W., and Matter, A. (1997). Sedimentary Sequences, Seismic Facies, Subsidence Analysis, and Evolution of the Burdigalian Upper Marine Molasse Group, Central Switzerland: AAPG Bulletin, v. 81 no. 7, p. 1185–1207, doi:10.1306/522B4A19-1727-11D7-8645000102C1865D.

Schøder, A.E., and Surlyk, F. (2020). Adaptive brachiopod morphologies in four key environments of the Late Cretaceous–Danian Chalk Sea of Northern Europe: A comparative study, *Cretaceous Research*, *107*, 104288, doi:10.1016/j.cretres.2019.104288.

Scholle, P. (1977). Geological Studies on the COST No. B-2 Well, U.S. Mid-Atlantic Outer Continental Shelf Area, *US Geological Survey Circular 750*, Arlington, VA.

Scholle, P. (2003). Geologic Map of New Mexico, *New Mexico Bureau of Geology and Mineral Resources*, Scale 1:500,000.

Schwimmer, D.R., Williams, G.D., Dobie, J.L., and Siesser, W.G. (1993). Late Cretaceous dinosaurs from the Blufftown Formation in western Georgia and eastern Alabama, *Journal of Paleontology*, *67*(2), 288–296.

Sclater, J.G., and Christie, P.A.F. (1980). Continental stretching: An explanation for the post-Mid-Cretaceous subsidence of the Central North Sea Basin, *Journal of Geophysical Research: Solid Earth*, *85*(B7), 3711–3739, doi:10.1029/JB085iB07p03711.

Scotese, C.R., and Golonka, J. (1992). Paleogeographic atlas: Paleomap Project, Arlington, Texas, Department of Geology, University of Texas at Arlington.

Seeber, L., Cormier, M.H., McHugh, C., Emre, O., Polonia, A., and Sorlien, C. (2006). Rapid subsidence and sedimentation from oblique slip near a bend on the North Anatolian transform fault in the Marmara Sea, Turkey, *Geology*, *34*(11), 933–936, doi:10.1130/G22520A.1

Seidemann, D.E., Masterson, W.D., Dowling, M.P., Turekian, K.K. (1984). K-Ar dates and $^{40}Ar/^{39}Ar$ age spectra for Mesozoic basalt flows of the Hartford Basin, Connecticut, and the Newark Basin, New Jersey, *GSA Bulletin*, *95*(5), 594–598, doi:10.1130/0016-7606(1984)95<594:KDAAAS>2.0.CO;2.

Self, R.P. (1977). Longshore variation in beach sands, Nautla Area, Veracruz, Mexico, *J. Sediment. Res.*, *47*(4), 1437–1443, doi:10.1306/212F7388-2B24-11D7-8648000102C1865D.

Setterholm, D.R. (1994). The Cretacous rocks of southwestern Minnesota: Reconstructions of a marine to nonmarine transition along the eastern margin of the Western Interior Seaway, *in* Shurr, G.W., Ludvigson, G.W., and Hammond, R.H. (eds.), Perspectives on the Eastern Margin of the Cretaceous Western Interior Seaway, *Geological Society of America Special Paper 287*, 97–110, Boulder, CO.

Shattuck, G.B. (1904). Geological and paleontological relations–with a review of earlier investigations, *Maryland Geological Survey.*

Shen, W., and Ritzwoller, M.H. (2016). Crustal and uppermost mantle structure beneath the United States, *Journal of Geophysical Research: Solid Earth*, *121*, 4306–4342, doi:10.1002/2016JB012887.

Sheridan, R.E., Musser, D., Glover III, L., Talwani, M., Ewing, J.I., Holbrook, W.S., Purdy, G.M., Hawman, R., Smithson, S., (1993). Deep seismic reflection data of EDGE US mid-Atlantic continental-margin experiment: implications for Appalachian sutures and Mesozoic rifting and magmatic underplating, *Geology*, *21*(6), 563–567, doi:10.1130/0091-7613(1993)021<0563:DSRDOE>2.3.CO;2.

Shimada, K. (2006). Marine vertebrates from the Blue Hill Shale member of the Carlile Shale (Upper Cretaceous: Middle Turonian) in Kansas, *in* Lucas, S.G., and Sullivan, R.M. (eds.), Late Cretaceous vertebrates from the Western Interior, New Mexico Museum of Natural History and Science Bulletin, *35*, p. 165–176.

Short, A.D. (2014). Australia's temperate carbonate coast: Sources, depositional environments and implications, *Geological Society London, Special Publications*, *388*(1), 389–405, doi:10.1144/SP388.5.

Shorten, C.M. and Fitzgerald, P.G. (2019). Post-orogenic thermal history and exhumation of the northern Appalachian Basin: Low-temperature thermochronologic constraints, *Basin Research*, *31*, 1017–1039, doi:10.1111/bre.12354.

Sklar, L., and Dietrich, W.E. (1998). River longitudinal profiles and bedrock incision models: Stream power influence of sediment supply, *in* Tinkler, K.J., and Wohl, E.E. (eds.), *Rivers Over Rock: Fluvial Processes in Bedrock Channels*, American Geophysical Union–Geophysical Monograph Series, doi:10.1029/GM107p0237.

Sklar, L.S., and Dietrich, W.E. (2001). Sediment and rock strength controls on river incision into bedrock, *Geology*, *29*(12), 1087–1090, doi:10.1130/0091-7613(2001)029<1087:SARSCO>2.0.CO;2.

Revised by Slone, J., Henry, C.D., Hopkins, M., and Ludington, S., original database by Zartman, R.E., Bush, C.A., and Abston, C. (2003). National Geochronological Database, *U. S. Geological Survey Open-file Report*, *03-236*, https://pubs.usgs.gov/of/2003/0236.

Sloss, L.L. (1963). Sequences in the cratonic interior of North America, *GSA Bulletin*, *74*(2), 93–114, doi:10.1130/0016-7606(1963)74[93:SITCIO]2.0.CO;2.

Smith, M.A., Amato, R.V., Furbush, M.A., Pert, D.M., Nelsom, M.E., Hendrix, J.S., Tamm, L.C., Wood Jr, G., Shaw, D.R. (1976). Geological and operational summary, COST No. B-2 well, Baltimore Canyon trough area, mid-Atlantic OCS, *Open-File Report 76-774*, United States Department of the Interior Geological Survey.

Smith, A.G., Smith, D.G., and Funnell, B.M. (1994). *Atlas of Mesozic and Cenozoic Coastlines*, 99 pp., Cambridge University Press.

Snyder, W.S., Dickinson, W.R., and Silberman, M.L. (1976). Tectonic implications of space-time patterns of Cenozoic magmatism in the Western United States, *Earth and Planetary Science Letters*, *32*, 91–106, doi:10.1016/0012-821X(76)90189-8.

Snyder, N.P., Whipple, K., Tucker, G., and Merritts, D. (2000). Landscape response to tectonic forcing: DEM analysis of stream profiles in the Mendocino triple junction region, northern California, *GSA Bulletin*, *112*(8), 1250–1263, doi:10.1130/0016-7606(2000)112<1250:LRTTFD>2.3.CO;2.

Spasojević, S., Liu, L., Gurnis, M., Müller, R.D. (2008). The case for dynamic subsidence of the U.S. East coast since the Eocene, *Geophysical Research Letters*, *35*(8), 1–6, doi:10.1029/2008GL033511.

Spasojević, S., Liu, L., and Gurnis, M. (2009). Adjoint models of mantle convection with seismic, plate motion, and stratigraphic constraints: North America since the Late Cretaceous, *Geochemistry, Geophysics, Geosystems*, *10*, Q05W02, doi:10.1029/2008GC002345.

Spasojević, S., and Gurnis, M. (2012). Sea level and vertical motion of continents from dynamic earth models since the Late Cretaceous, *AAPG Bulletin*, *96*(11), 2037–2064, doi:10.1306/03261211121.

Spencer, J.E. (1996). Uplift of the Colorado Plateau due to lithosphere attenuation during Laramide low-angle subduction, *Journal of Geophysical Research: Solid Earth*, *101*, 13,595, doi:10.1029/96JB00818.

Spotila, J.A., Bank, G.C., Reiners, P.W., Naeser, C.W., Naeser, N.D., and Henika, W.S. (2004). Origin of the Blue Ridge escarpment along the passive margin of Eastern North America, *Basin Research*, *16*, 41–63, doi:10.1111/j.1365-2117.2003.00219.x.

Steckler, M.S., and Watts, A.B., (1978). *Subsidence of the Atlantic-type continental margin off New York*, *Earth and Planetary Science Letters*, *41*(13), 1–13.

Steckler, M.S., Mountain, G.S., Miller, K.G., and Christie-Blick, N. (1999). Reconstruction of Tertiary progradation and clinoform development on the New Jersey passive margin by 2-D backstripping, *Marine Geology*, *154*(1-4), 399–420, doi:10.1016/S0025-3227(98)00126-1.

Steinberger, B. (2007). Effects of latent heat release at phase boundaries on flow in the Earth's mantle, phase boundary topography and dynamic topography at the Earth's surface, *Physics of the Earth and Planetary Interiors*, *164*(1-2), 2–20, doi:10.1016/j.pepi.2007.04.021.

Steinberger, B. (2016). Topography caused by mantle density variations: observation-based estimates and models derived from tomography and lithosphere thickness, *Geophysical Journal International*, *205*(1), 604–621, doi:10.1093/gji/ggw040.

Steinberger, B., Conrad, C.P., Tutu, A.O., and Hoggard, M.J., (2019). On the amplitude of dynamic topography at spherical harmonic degree two, *Tectonophysics*, 760, 221–228, doi:10.1016/j.tecto.2017.11.032.

Stephenson, S.N., Roberts, G.G., Hoggard, M.J., and Whittaker, A.C. (2014), A Cenozoic uplift history of Mexico and its surroundings from longitudinal river profiles, *Geochemistry, Geophysics, Geosystems*, *15*(12), 4734–4758, doi:10.1002/2014GC005425.

Stewart, D.B., and Lockhart, W.L. (2006). An Overview of the Hudson Bay Marine Ecosystem, *Canadian Technical Report of Fisheries and Aquatic Sciences*, *2586*.

Stone, D.S. (1993). Basement-involved thrust-generated folds as seismically imaged in the subsurface of the central Rocky Mountain foreland, *in* Schmidt, C.J., Chase, R.B., and Erslev, E.A., Laramide Basement Deformation in the Rocky Mountain Foreland of the Western United States, *Geological Society of America Special Paper 280*, doi:10.1130/SPE280.

Straume, E.O., Gaina, C., Medvedev, S., Hochmuth, K., Gohl, K., Whittaker, J.M., Abdul Fattah, R., Doornenbal, J.C. and Hopper, J.R. (2019). GlobSed: Updated total sediment thickness in the world's oceans, *Geochemistry, Geophysics, Geosystems*, *20*(4), 1756–1772, doi:10.1029/2018GC008115.

Stucky de Quay, G., Roberts, G.G., Watson, J.S., and Jackson, C.A.-L. (2017). Incipient mantle plume evolution: Constraints from ancient landscapes buried beneath the North Sea, *Geochemistry, Geophysics, Geosystems*, *18*, 973–993, doi:10.1002/2016GC006769.

Stucky de Quay, G., Roberts, G.G., Rood, D.H., and Fernandes, V.M. (2019). Holocene uplift and rapid fluvial erosion of Iceland: A record of post-glacial landscape evolution, *Earth and Planetary Science Letters*, *505*, 118–130, doi:10.1016/j.epsl.2018.10.026.

Suess, E. (1906). The Face of the Earth, Clarendon Press, Oxford, 556 p.

Sulser, H. Garcia-Ramso, D. Kursteiner, P., and Menkveld-Gfeller, U. (2010). Taxonomy and palaeoecology of brachiopods from the South-Helvetic zone of the Faneren region (Lutetian, Eocene, NE Switzerland), *Swiss Journal of Geosciences*, *103*, 257–272, doi:10.1007/S00015-010-0018-0.

Suppe, J., Chou, G.T., and Hook, S.C. (1992). Rates of folding and faulting determined from growth strata, *in* McClay, K.R. (ed.), *Thrust tectonics*, 105–121. Springer, Dordrecht.

Sutter, J.F., (1988). Innovative approaches to the dating of igneous events in the early Mesozoic basins of the eastern United States, *in* Froelich, A.J., and Robinson, G.R. (eds.), Studies of the Early Mesozoic Basins of the Eastern United States, *U.S. Geological Survey Bulletin 1776*, 194–200.

Tachikawa, T., Kaku, M., Iwasaki, A., Gesch, D., Oimoen, M., Zhang, Z., Danielson, J., Krieger, T., Curtis, B., Haase, J., Abrams, M., Crippen, R., and Carabajal, C. (2011). *ASTER Digital Elevation Model Version 2 - Summary of validation results.*

Tadono, T., Ishida, H., Oda, F., Naito, S., Minakawa, K., and Iwamoto, H. (2014). Precise Global DEM Generation by ALOS PRISM, *ISPRS Annals of the Photogrammetry, Remote Sensing and Spatial Information Sciences*, *2*(4), 71–76.

Tapanila, L., Roberts, E., Bouaré, M.L., Sissoko, F., and O'Leary, M.A. (2008). Phosphate taxonomy of bone and comprolite conglomerates: a case study from the Eocene of Mali, NW Africa, *Palaios*, *23*, 139–152, doi:10.2110/palo.2006.p06-113r.

Tapley, B., Ries, J., Bettadpur, S., Chambers, D., Cheng, M., Condi, F., Gunter, B., Kang, Z., Nagel, P., Pastor, R., and Pekker, T. (2005). GGM02 – An improved Earth gravity field model from GRACE, *Journal of Geodesy*, *79*, 467–478, doi:10.1007/s00190-005-0480-z.

Tapponnier, P., Zhiqin, X., Roger, F., Meyer, B., Arnaud, N., Wittlinger, G., and Jingsui, Y. (2001). Oblique stepwise rise and growth of the Tibet Plateau, *Science*, *294*(5547), 1671–1677, doi:10.1126/science.105978.

Taylor, J.P., and Fitzgerald, P.G. (2011). Low-temperature thermal history and landscape development of the eastern Adirondack Mountains, New York: Constraints from apatite fission-track thermochronology and apatite (U-Th)/He dating, *GSA Bulletin*, *123*(3-4), 412–426, doi:10.1130/B30138.1.

Taylor, S.B., and Kite, J.S. (2006). Comparative geomorphic analysis of surficial deposits at three central Appalachian watersheds: Implications for controls on sediment-transport efficiency, *Geomorphology*, *78*(1-2), 22–43, doi:10.1016/j.geomorph.2006.01.032.

Thompson, G.A., and Zoback, M.L. (1979). Regional geophysics of the Colorado Plateau, *Tectonophysics*, *61*(1-3), 149–181, doi:10.1016/0040-1951(79)90296-8.

Tintant, H., Lang, J., Moussa, B., Alzouma, K., and Dikouma, M. (2001). Nautiles Paléocènes du Niger, *Geobios*, *34*, 629–656, doi:10.1016/S0016-6995(01)80026-7.

Triezenberg, P.J., Hart, P.E., and Childs, J.R., (2016). National Archive of Marine Seismic Surveys (NAMSS): A USGS data website of marine seismic reflection data within the U.S. Exclusive Economic Zone (EEZ), *U.S. Geological Survey Data Release*, doi:10.5066/F7930R7P.

Tucker, G.E., and Slingerland, R. (1996). Predicting sediment flux from fold and thrust belts, *Basin research*, *8*(3), 329–349, doi:10.1046/j.1365-2117.1996.00238.x.

Turcotte, D.L., and Schubert, G. (2002). *Geodynamics*, 2nd edition. Cambridge University Press.

Tweto, O. (1979). Geologic Map of Colorado, *U.S. Geological Survey*, 1:500,000.

USGS Uinta-Piceance Assessment (UUPA) Team (2003). *Petroleum systems and geologic assessment of oil and gas in the Uinta-Piceance Province, Utah and Colorado*, 69-B, US Geological Survey.

Ussami, N., Molina, E.C., and Medeiros, W.E. (1999). Novos vínculos sobre a evolução térmica da margem continental leste do Brasil, *VII Simpósio Nacional de Estudos Tectônicos, Lençóis, Annals*, *S3*, 20–23.

Vail, P.R., Mitchum, R.M., and Thompson, S. (1977). Relative Changes of Sea Level from Coastal Onlap, in Payton, C.E. (ed.), Seismic Stratigraphy–Applications to Hydrocarbon Exploration, *AAPG Memoir*, *26*, 63–81.

Van Sickel, W., Kominz, M.A., Miller, K.G., and Browning, J.V. (2004). Late Cretaceous and Cenozoic sea-level estimates: backstripping analysis of borehole data, onshore New Jersey, *Basin Research*, *16*(4), 451–465, doi:10.1111/j.1365-2117.2004.00242.x.

Vanderaveroet, P. (2000). Miocene to Pleistocene clay mineral sedimentation on the New Jersey shelf, *Oceanologica Acta*, *23*(1), 25–36, doi:10.1016/S0399-1784(00)00102-X.

van Wijk, J.W., Baldridge, W.S., van Hunen, J., Goes, S., Aster, R., Coblentz, D.D., Grand, S.P., and Ni, J. (2010). Small-scale convection at the edge of the Colorado Plateau: Implications for topography, magmatism, and evolution of Proterozoic lithosphere, *Geology*, *38*, 611–614, doi:10.1130/G31031.1.

Voronoi, G. (1908). Nouvelles applications des paramètres continus à la théorie des formes quadratiques. Premier mémoire. Sur quelques propriétés des formes quadratiques positives parfaites, *Journal für die reine und angewandte Mathematik (Crelles Journal)*, *133*, 97–102, doi:10.1515/crll.1908.134.198.

Vuke, S.M., Porter, K.W., Lonn, J.D., and Lopez, D.A. (2007). Geologic map of Montana, *Montana Bureau of Mines and Geology Geologic Map A*, 62, 73, 1:500,000.

Wakabayashi, J., and Sawyer, T.L. (2001). Stream Incision, Tectonics, Uplift, and Evolution of Topography of the Sierra Nevada, California, *The Journal of Geology*, *109*(5), 539–562, doi:10.1086/321962.

Walford, H.L., and White, N.J. (2005). Constraining uplift and denudation of west African continental margin by inversion of stacking velocity data, *Journal of Geophysical Research: Solid Earth*, *110*(B4), doi:10.1029/2003JB002893.

Walford, H.L., White, N.J., and Sydow, J.C. (2005). Solid sediment load history of the Zambezi Delta, *Earth and Planetary Science Letters*, *238*(1-2), 49–63, doi:10.1016/j.epsl.2005.07.014.

Walker, J.F., Roberts, G.P., Cowie, P.A., Papanikolaou, I.D., Sammonds, P.R., Michetti, A.M., and Phillips, R.J. (2009). Horizontal strain-rates and throw-rates across breached relay zones, central Italy: Implications for the preservation of throw deficits at points of normal fault linkage, *Journal of Structural Geology*, *31*(10), 1145–1160, doi:10.1016/j.jsg.2009.06.011.

Wang, H., Wright, T.J., Liu-Zeng, J., and Peng, L. (2019). Strain rate distribution in south-central Tibet from two decades of InSAR and GPS, *Geophysical Research Letters*, *46*, 5170–5179, doi:10.1029/2019GL081916.

Ward, D.J., Spotila, J.A., Hancock, G.S., and Galbraith, J.M. (2005). New constraints on the late Cenozoic incision history of the New River, Virginia, *Geomorphology*, *72*, 54–72, doi:10.1016/j.geomorph.2005.05.002.

Watts, A.B., and Ryan, W.B. (1976). Flexure of the lithosphere and continental margin basins, *Developments in Geotectonics*, *12*(C), 25–44, doi:10.1016/B978-0-444-41549-3.50006-2.

Watts, A.B. (1982). Tectonic subsidence, flexure and global changes of sea level, *Nature*, *297*, 469–474, doi:10.1038/297469a0.

Watts, A.B. (1988). Gravity anomalies, crustal structure and flexure of the lithosphere at the Baltimore Canyon Trough, *Earth and Planetary Science Letters*, *89*(2), 221–238, doi:10.1016/0012-821X(88)90174-4.

Watts, A.B. (2001). *Isostasy and Flexure of the Lithosphere*, Cambridge University Press, Cambridge, UK.

Watts, A.B., and Steckler, M.S. (1979). Subsidence and Eustasy at the Continental Margin of Eastern North America, *in* Talwani, W.H., and Ryan, W.B.F. (eds.), Deep Drilling Results in the Atlantic Ocean: Continental Margins and Paleoenvironment, doi:10.1029/ME003p0218.

Watts, A.B., and Thorne, J. (1984). Tectonics, global changes in sea level and their relationship to stratigraphical sequences at the US Atlantic continental margin, *Marine Petroleum Geology*, *1*(4), 319–339, doi:10.1016/0264-8172(84)90134-X.

Weems, R.E., and Olsen, P.E. (1997). Synthesis and revision of groups within the Newark Supergroup, eastern North America, *GSA Bulletin*, *109*, 195–209, doi:10.1130/0016-7606(1997)109<0195:SAROGW>2.3.CO;2.

Weissel, J.K., and Seidl, M.A. (1998). Inland propagation of erosional escarpments and river profile evolution across the southeast Australian passive continental margin, *in* Tinkler, K.J., and Wohl, E.E. (eds.), *Rivers Over Rock: Fluvial Processes in Bedrock Channels*, American Geophysical Union–Geophysical Monograph Series, doi:10.1029/GM107p0189.

Wernicke, B.P. (1992). Cenozoic extensional tectonics of the U.S. Cordillera, *in* Burchfeil, B.C., Lipman, P.W., and Zoback, M.L. (eds.), *Cordilleran Orogen Conterminous U.S.*, DNAG Geology of North America Volume G-3, Geological Society of America, Boulder, CO, doi:10.1130/DNAG-GNA-G3.

Westaway, R., Bridgland, D., and White, M. (2006). The Quaternary uplift history of central southern England: evidence from the terraces of the Solent River system and nearby raised beaches, *Quaternary Science Reviews*, *25*(17-18), 2212–2250, doi:10.1016/j.quascirev.2005.06.005.

Whipple, K.X., and Tucker, G.E. (1999). Dynamics of the stream-power river incision model: Implications for height limits of mountain ranges, landscape response timescales, and research needs, *Journal of Geophysical Research: Solid Earth*, *104*(B8), 17661–17674, doi:10.1029/1999JB900120.

Whipple, K.X., and Meade, B.J. (2006). Orogen response to changes in climatic and tectonic forcing, *Earth and Planetary Science Letters*, *243*(1-2), 218–228, doi:10.1016/j.epsl.2005.12.022.

Whipple, K.X. (2009). The influence of climate on the tectonic evolution of mountain belts, *Nature Geoscience*, *2*(2), 97-104, doi:10.1038/ngeo413.

White, N., and McKenzie, D. (1988). Formation of the "steer's head" geometry of sedimentary

basins by differential stretching of the crust and mantle, *Geology*, *16*(3), 250–253, doi:10.1130/0091-7613(1988)016<0250:FOTSSH>2.3.CO;2.

White, N. (1994). An inverse method for determining lithospheric strain rate variation on geological timescales. *Earth and Planetary Science Letters*, *122*(3), 351–371, doi: 10.1016/0012-821X(94)90008-6 .

Whittaker, A.C., Cowie, P.A., Attal, M., Tucker, G.E., and Roberts, G. (2007). Bedrock channel adjustment to tectonic forcing: Implications for predicting river incision rates, *Geology*, *35*, 103–106, doi:10.1130/G23106A.1.

Whittaker, A.C., Attal, M., Cowie, P.A., Tucker, G.E., and Roberts, G. (2008). Decoding temporal and spatial patterns of fault uplift using transient river long profiles, *Geomorphology*, *100*(3-4), 506–526, doi:10.1016/j.geomorph.2008.01.018.

Whittaker, A.C. (2012). How do landscapes record tectonics and climate?, *Lithosphere*, *4*(2), 160–164, doi:10.1130/RF.L003.1.

Whittaker, A.C., and Boulton, S.J. (2012). Tectonic and climatic controls on knickpoint retreat rates and landscape response times, *Journal of Geophysical Research: Earth Surface*, *117*, 1–19, doi:10.1029/2011JF002157.

Wickert, A.D. (2016). Reconstruction of North American drainage basins and river discharge since the Last Glacial Maximum, *Earth Surface Dynamics*, *4*(4), 831–869, doi:10.5194/esurf-4-831-2016.

Willenbring, J.K., and Jerolmack, D.J. (2016). The null hypothesis: globally steady rates of erosion, weathering fluxes and shelf sediment accumulation during Late Cenozoic mountain uplift and glaciation, *Terra Nova*, *28*(1), 11–18, doi:10.1111/ter.12185.

Willett, S.D. (1999). Orogeny and orography: The effects of erosion on the structure of mountain belts, *Journal of Geophysical Research: Solid Earth*, *104*(B12), 28957–28981, doi:10.1029/1999JB900248.

Willett, S.D., Slingerland, R., and Hovius, N. (2001). Uplift, shortening, and steady state topography in active mountain belts, *American journal of Science*, *301*(4–5), 455–485, doi:10.2475/ajs.301.4-5.455.

Willett, S.D., McCoy, S.W., Perron, J.T., Goren, L., and Chen, C.Y. (2014). Dynamic Reorganization of River Basins, *Science*, *343*(6175), 1248,765–1248,765, doi:10.1126/science.1248765.

Willett, S.D., McCoy, S.W., and Beeson, H.W. (2018). Transience of the North American High Plains landscape and its impact on surface water, *Nature*, doi:10.1038/s41586-018-0532-1.

Wilson, D., Aster, R., Ni, J., Grand, S., West, M., Gao, W., Baldridge, W.S., and Semken, S. (2005). Imaging the seismic structure of the crust and upper mantle beneath the Great Plains, Rio Grande Rift, and Colorado Plateau using receiver functions, *Journal of Geophysical Research: Solid Earth*, *110*(5), 1–14, doi:10.1029/2004JB003492.

Winn, C., Karlstrom, K.E., Shuster, D.L., Kelley, S., and Fox, M. (2017). 6 Ma age of carving Westernmost Grand Canyon: Reconciling geologic data with combined AFT, (U–Th)/He and $^{4}He/^{3}He$ thermochronologic data, *Earth and Planetary Science Letters*, *474*, doi:10.1016/j.epsl.2017.06.051.

Winterbourne, J., White, N., and Crosby, A. (2014). Accurate measurements of residual topography from the oceanic realm, *Tectonics*, *33*(6), 982–1015, doi:10.1002/2013TC003372.

Withjack, M. (1979). A convective heat transfer model for lithospheric thinning and crustal uplift, *Journal of Geophysical Research: Solid Earth*, *84*(B6), 3008–3022, doi:10.1029/JB084iB06p03008.

Wobus, C.W., Whipple, K.X., Kirby, E., Snyder, N., Johnson, J., Spyropolou, K., Crosby, B., and Sheehan, D. (2006). Tectonics from topography: procedures, promise, pitfalls, *in* Willett, S.D., Hovius, N., Brandon, M.T., and Fisher, D.M. (eds.), Tectonics, Climate, and Landscape Evolution, *Geological Society of America Special Paper 398*, Penrose Conference Series, 55–74, doi:10.1130/2006.2398(04).

Wolfe, J.A., Forest, C.E., and Molnar, P. (1998). Paleobotanical evidence of Eocene and Oligocene paleoaltitudes in midlatitude western North America, *GSA Bulletin*, *110*(5), 664–678, doi:10.1130/0016-7606(1998)110<0664:PEOEAO>2.3.CO;2.

Woods, M.A (2015). Applied paleontology in the Chalk Group: Quality control for geological mapping and modelling and revealing new understanding, *Proceedings of the Geologists' Association*, *126*(6), 777–787, doi:10.1016/j.pgeola.2015.11.003.

Woodward, L.A., Anderson, O.J., and Lucas, S.G. (1997). Mesozoic stratigraphic constraints on Laramide right slip on the east side of the Colorado Plateau, *Geology*, *25*(9), 843–846, doi:10.1130/0091-7613(1997)025<0843:MSCOLR>2.3.CO;2.

Wyllie, M.R.J., Gregory, A.R., and Gardner, L.W. (1956). Elastic wave velocities in heterogeneous and porous media, *Geophysics*, *21*(1), p. 41–70, doi:10.1190/1.1438217.

Yang, T., and Gurnis, M. (2016). Dynamic topography, gravity and the role of lateral viscosity variations from inversion of global mantle flow, *Geophysical Supplements to the Monthly Notices of the Royal Astronomical Society*, *207*(2), 1186–1202, doi:10.1093/gji/ggw335.

Zachos, J., Pagani, M., Sloan, L., Thomas, E., and Billups, K. (2001). Trends, rhythms, and aberrations in global climate 65 Ma to present, *Science*, *292*(5517), 686–693, doi:10.1126/science.1059412.

Zhong, S., and Gurnis, M. (1994). Controls on trench topography from dynamic models of subducted slabs, *Journal of Geophysical Research: Solid Earth*, *99*(B8), 15683–15695, doi:10.1029/94JB00809.

Ziegler, A., Rowley, D., Lottes, A., Sahagian, D., Hulver, M., and Gierlowski, T. (1985). Paleogeographic interpretation: with an example from the mid-Cretaceous, *Annual Review of Earth and Planetary Science*, *13*, 385–425, doi:10.1146/annurev.earth.13.1.385.

Zimmerman, R.A., Reimer, G.M., Foland, K.A., and Faul, H. (1975). Cretaceous fission track dates of apatites from northern New England, *Earth and Planetary Science Letters*, *28*, 181–188, doi:10.1016/0012-821X(75)90225-3.

Zoback, M.L., Thompson, G.A., and Anderson, R.E. (1981). Cainozoic evolution of the state of stress and style of tectonism of the Basin and Range province of the western United States, *Philosophical Transactions of the Royal Society of London. Series A, Mathematical and Physical Sciences*, *300*(1454), 407–434, doi:10.1098/rsta.1981.0073.